Spin Currents
in
Metallic Nanostructures

Franz Dominik Czeschka

Abstract

A pure spin current, i.e., a flow of angular momentum without accompanying net charge current, is a key ingredient in the field of spintronics. In this thesis, we experimentally investigated two different concepts for pure spin current sources suggested by theory.

The first is based on a time-dependent magnetization precession which "pumps" a pure spin current into an adjacent non-magnetic conductor. Our experiments quantitatively corroborated important predictions expected theoretically for this approach, including the dependence of the spin current on the sample geometry and the microwave power. Even more important, we could show for the first time that the spin pumping concept is viable in a large variety of ferromagnetic materials and that it only depends on the magnetization damping. Therefore, our experiments established spin pumping as generic phenomenon and demonstrated that it is a powerful way to generate pure spin currents.

The second theoretical concept is based on the conversion of charge currents into spin currents in non-magnetic nanostructures via the spin Hall effect. We experimentally investigated this approach in H-shaped, metallic nanodevices, and found that the predictions are linked to requirements not realizable with the present experimental techniques, neither in sample fabrication nor in measurement technique. Indeed, our experimental data could be consistently understood by a spin-independent transport model describing the transition from diffusive to ballistic transport. In addition, the implementation of advanced fabrication and measurement techniques allowed to discover a new non-local phenomenon, the non-local anisotropic magnetoresistance.

Finally, we also studied spin-polarized supercurrents carried by spin-triplet Cooper pairs. We found that low resistance interfaces are a key requirement for further experiments in this direction.

Zusammenfassung

Spinströme, also reine Drehmomentströme bei verschwindendem Netto-Ladungsstrom, stellen ein Schlüsselkonzept im Bereich der Spintronik dar. Im Rahmen dieser Arbeit wurden zwei theoretische Vorschläge zur Erzeugung von Spinströmen experimentell untersucht.

Das erste Konzept basiert auf einer zeitlich variierenden Magnetisierung, die einen Spinstrom in einen benachbarten nichtmagnetischen Leiter "pumpt". Unsere Experimente konnten zentrale Vorhersagen der Spin-Pumpen-Theorie quantitativ bestätigen, im Besonderen die Abhängigkeit des Signals von der Probengeometrie und der Mikrowellenleistung. Wichtiger noch ist, dass wir zum ersten Mal zeigen konnten, dass das Spin-Pumpen-Konzept für unterschiedlichste ferromagnetische Materialien gültig ist und nur von der Dämpfung der Magnetisierung abhängt. Unsere Experimente haben gezeigt, dass das Spin-Pumpen ein generischer Effekt ist und damit eine leistungsfähige Methode zur Erzeugung reiner Spinströme.

Das zweite Konzept beruht auf der Umwandlung von Spin- in Ladungsstrom in nicht-magnetischen elektrischen Leitern mittels des Spin-Hall-Effektes. Wir haben diesen Ansatz experimentell in H-förmigen metallischen Nanostrukturen untersucht und konnten zeigen, dass die existierenden theoretischen Vorhersagen an Voraussetzungen geknüpft sind, die mit den derzeitigen experimentellen Techniken nicht zu erfüllen sind, weder im Bereich der Probenherstellung noch im Bereich der Messtechnik. Tatsächlich konnten unsere Messdaten mittels eines spinunabhängigen Transportmodells, das den Übergang von diffusivem zu ballistischem Transport beschreibt, vollständig erklärt werden. Außerdem hat die Implementierung von hochentwickelten Herstellungs- und Messmethoden die Entdeckung eines neuen nicht-lokalen Effektes ermöglicht, nämlich den des nicht-lokalen anisotropen Magnetwiderstandes.

Schließlich haben wir spinpolarisierte Supraströme untersucht, die aus Spin-Triplet Cooper-Paaren bestehen. Dabei haben wir herausgefunden, dass niedrige Grenzflächenwiderstände eine essenzielle Voraussetzung für weitere Experimente in dieser Richtung sind.

Contents

Appendices

Chapter 1

Introduction

The first electrical battery was discovered in 1799/1800 by A. Volta (1745-1827) and is nowadays known as the Voltaic pile [1, 2]. Originally, it consisted of galvanic cells connected in series, where one cell consists of a copper and a zinc disc separated by a brine soaked cardboard or cloth. It was the first convenient current source supplying a continuous electric current – long before the electric generator. This invention was the basis for many scientific advances in the 19th century, such as the discovery of the electrolysis (1800) or the investigation of electricity. Up to now, current sources are essential in everyday life.

In 1897, the elementary charged particles forming the electrical current from such current sources were discovered by J. J. Thomson [3]: the electrons. Due to their electric charge, electrons couple to electromagnetic fields. The occurring forces are the well known Coulomb and Lorentz forces. These interactions are the basis of conventional *electronics* omnipresent in our high-tech civilization.

In the 20th century, it finally became clear that electrons do not only possess mass and charge, but contain an internal degree of freedom, called spin. Ultimately, this resulted in a new research field named *spintronics* whose aim is to exploit the spin degree of freedom in new devices attaining an extended functionality. However, so far the spin property is mainly used for data storage in form of the magnetization orientation in ferromagnetic grains (e.g. in hard disks).

One prominent exception where the spin is used in dynamic systems, is spin transfer torque [4, 5, 6]: an electric current is sent through a ferromagnet and becomes spin-polarized, which means that an imbalance between spin-up and spin-down (the two quantum mechanical states of the spin) electrons is created. After passing a non-magnetic metal, the spin-polarized current impinges on a second ferromagnet, whose magnetization then can be switched due to its interaction with the transported spin angular momentum. Spin transfer torque thus allows to switch the magnetization of a ferromagnetic electrode without any external magnetic field. So far, however, high current densities (and nanoscale devices) are required for spin transfer torque, which results in strong heating of the devices. This heating is caused by the unneeded charge current which accompanies the spin actually required for the switching. Therefore, it would be highly advantageous if the spin transport could be decoupled from the charge degree of freedom: in other words, a current source which generates a pure spin current, that is a flow of spin angular momentum without accompanying charge current, would be ideal. Such a pure spin current is predicted to be dissipationless (Chapter 2).

The aim of this thesis was to experimentally study and compare fundamental properties of different spin current sources predicted theoretically. In the first instance, we experimentally investigated the so-called spin pumping concept, where a precessing magnetization emits a pure spin current into an adjacent non-magnetic conductor [7, 8] (Chapter 3). More precisely, we studied fundamental properties of this spin current source and in particular addressed the following key questions: (i) which types of ferromagnets can be used, (ii) how does the generation efficiency depend on the ferromagnetic properties, and (iii) what is the influence of the device geometry and the excitation power. Our experiments, for the first time, unambiguously demonstrated that spin pumping is possible from any ferromagnet, independent of the exchange mechanism, the saturation magnetization, the spin polarization, the charge carrier transport mechanism and the charge carrier polarity. The spin current magnitude is well described by a scaling relation within the entire investigated temperature range of $2\,\mathrm{K} \leq T \leq 290\,\mathrm{K}$ which allowed us to quantitatively corroborate the present spin pumping/inverse spin Hall effect theories [7, 8, 9, 10, 11, 12].

The second studied spin current source concept is based on the prediction that any charge current flowing in an electrical conductor with spin-orbit interaction generates a perpendicular pure spin current. This generation mechanism is predicted to be observable in H-shaped nanoscale devices [13, 14, 15]. To detect this effect in metallic nanostructures, we fabricated and studied intersecting metallic nanowires with wire widths and separations well below $100\,\mathrm{nm}$ (Chapter 4). This required the development of a highly optimized electron beam fabrication process and a sophisticated low-level, low-noise measurement setup. However, our experiments show that the requirements for the generation and detection of pure spin currents in purely non-magnetic devices are so severe that a reliable experimental detection is very difficult, if not impossible. However, during these measurements, we discovered a new effect, the non-local anisotropic magnetoresistance.

Spin-polarized supercurrents are discussed at the end of this thesis (Appendix A). In this part, we investigate the prerequisites for the generation of spin-triplet Cooper pairs and find that low resistance interfaces are the key requirement for further experiments.

To sum things up, the discovery of the conventional battery supplying a continuous flow of electrons (charge) revolutionized every day life. With the discovery of the electron's internal degree of freedom, the spin, a completely new research field evolved. Thereby, many well known physical effects related to for example carrier transport, tunneling processes or interface effects are now investigated including the spin degree of freedom. This already resulted in many new effects such as the discovery of the giant magnetoresistance which was awarded with the Nobel prize in physics in 2007 for Albert Fert and Peter Grünberg [16]. For spin electronics, a major step forward would be the availability of a new type of current source supplying a pure spin current, thus a pure flow of spin angular momentum without net charge current. Different concepts of such spin current sources are experimentally investigated in this thesis. We proved several predictions from theory and quantified various parameters crucial in spin transfer torque, spin pumping, and spin Seebeck effect [17] measurements.

The thesis is organized as follows: the next chapter (Chapter 2) gives a theoretical introduction to the concepts of spin currents and related phenomena. In Chapter 3, theory and experiment for a spin current source based on spin pumping are presented. Chapter 4 discusses theory and experiment of a spin current source based on nanoscale H-shaped devices made of a single electric conductor. The main part of this thesis concludes with a summary and an outlook (Chapter 5). Finally, the Appendices A and B include a brief discussion on our experiments related to spin-polarized supercurrents (Appendix A) and calculations which unambiguously discern DC voltages due to spin pumping from voltages due to microwave rectification (Appendix B).

Chapter 2

Spin currents – Theory

This theory chapter gives an introduction to the concepts of spin currents and related phenomena such as spin-orbit coupling and the spin Hall effect. We hereby focus on spin-1/2 particles and take in particular electrons with charge $-e$[1] as example. As mentioned in the introduction, electrons contain an internal degree of freedom, the spin. The spin is a quantum mechanical observable described by the spin angular momentum operator [18]

$$\mathbf{S} = \frac{\hbar}{2}\boldsymbol{\sigma},\tag{2.1}$$

where $\hbar$ is Planck's constant and $\boldsymbol{\sigma}$ is the vector of the Pauli spin matrices

$$\sigma_\mathrm{x} = \begin{pmatrix} 0 & 1 \\ 1 & 0 \end{pmatrix}, \qquad \sigma_\mathrm{y} = \begin{pmatrix} 0 & -\mathrm{i} \\ \mathrm{i} & 0 \end{pmatrix}, \qquad \sigma_\mathrm{z} = \begin{pmatrix} 1 & 0 \\ 0 & -1 \end{pmatrix}.\tag{2.2}$$

The two-component spin wave function can be written as [18]

$$|\Psi\rangle = a\,|\uparrow\rangle + b\,|\downarrow\rangle \equiv: \begin{pmatrix} a \\ b \end{pmatrix},\tag{2.3}$$

where a and b are complex numbers (normalized as $|a|^2 + |b|^2 = 1$), and $|\uparrow\rangle$ and $|\downarrow\rangle$ are the two eigenstates of $\mathbf{S}$ called "spin-up" and "spin-down" which correspond to the eigenvalues $\pm\hbar/2$, respectively. A direct consequence of the electron's spin (Eq. (2.1)) is a magnetic moment of [19]

$$\boldsymbol{\mu} = -g\mu_\mathrm{B}\frac{\mathbf{S}}{\hbar}\tag{2.4}$$

which is oriented antiparallel to $\mathbf{S}$ [20]. Here, g is the electron g-factor and $\mu_\mathrm{B} = \frac{e\hbar}{2m}$ the Bohr magneton.

2.1 Charge current and spin current

In this section, various properties of spin currents are derived and discussed in analogy to the well known charge currents. In the following, we consider a and b as position dependent functions resulting in the fact that the wave function of Eq. (2.3)

---

[1]In the following, we use e for the positive elementary charge and $-e$ for the negative one.

describes both spin and position. We now use the normalization $a^2 + b^2 = n_\uparrow + n_\downarrow = n$, where $n_\uparrow$ and $n_\downarrow$ denote the classic carrier densities for spin-up and spin-down particles and n is their sum. The charge density ρ_c and the spin density $\rho_{s,\hat{s}}$ for spins with a quantization axis along $\hat{s}$ can then be defined as [21, 22]

$$\rho_c = \langle \Psi | Q | \Psi \rangle, \qquad\qquad \rho_{s,\hat{s}} = \hat{s} \cdot \langle \Psi | \mathbf{S} | \Psi \rangle \qquad (2.5)$$

with the "charge operator" for an electron $Q = -e \mathbb{1}_2$ and the spin operator $\mathbf{S}$ from Eq. (2.1). Inserting Ψ from Eq. (2.3) and choosing, without loss of generality, $\hat{s} = (0, 0, 1)$ yields

$$\begin{aligned}
\rho_c(x) &= -e\langle \Psi | \Psi \rangle = -e\left(a^2 + b^2\right) & \rho_{s,\hat{s}}(x) &= \hat{s} \cdot \langle \Psi | \mathbf{S} | \Psi \rangle = \frac{\hbar}{2}a^2 - \frac{\hbar}{2}b^2 \\
&= -e\left(n_\uparrow + n_\downarrow\right), & &= \frac{\hbar}{2}\left(n_\uparrow - n_\downarrow\right).
\end{aligned} \qquad (2.6)$$

Multiplying the spin density with the carrier velocity $\mathbf{v}$ gives the spin current density $\mathbf{J}_s = \rho_{s,\hat{s}} \mathbf{v}$ in analogy to the relation between charge density and charge current density $\mathbf{J}_c = \rho_c \mathbf{v}$ [23]. Inserting the calculated densities of Eq. (2.6) and using the charge current densities for the two carrier species $\mathbf{J}_\uparrow = -e\, n_\uparrow\, \mathbf{v}_\uparrow$ and $\mathbf{J}_\downarrow = -e\, n_\downarrow\, \mathbf{v}_\downarrow$ give the charge and the spin current density as

$$\mathbf{J}_c = \left(\mathbf{J}_\uparrow + \mathbf{J}_\downarrow\right), \qquad\qquad \mathbf{J}_s = -\frac{\hbar}{2e}\left(\mathbf{J}_\uparrow - \mathbf{J}_\downarrow\right). \qquad (2.7)$$

Thus, $\mathbf{J}_c$ is given by the sum of the current densities of the two carrier species, whereas $\mathbf{J}_s$ by their difference[2]. The spin quantization axis of $\mathbf{J}_s$ is determined by the experimental environment and henceforth, the direction of $|\uparrow\rangle$ is referred to as the "spin orientation $\hat{s}$" of the spin current. The prefactor $-\hbar/2e$ in the spin current density reflects the fact that the electron is considered as angular momentum carrier $(\hbar/2)$ in $\mathbf{J}_s$, whereas it is seen as charge carrier $(-e)$ in $\mathbf{J}_c$. The spin current density is then given in units of $[\mathrm{A/m^2} \cdot \hbar/e]$, whereas $\mathbf{J}_c$, $\mathbf{J}_\uparrow$ and $\mathbf{J}_\downarrow$ are given in units of $[\mathrm{A/m^2}]$.

Of course, a separate treatment of the two spin states ($|\uparrow\rangle$ and $|\downarrow\rangle$) is only appropriate if the spin flip time is reasonably long in comparison to the momentum relaxation time ($\tau_{sf} \gg \tau_t$, see Sec. 2.4) [29, 30].

With Eq. (2.7), three types of currents can be distinguished: in Fig. 2.1(a), the current densities of both spin states $J_\uparrow$ and $J_\downarrow$ are equal. This corresponds to a net charge transport without accompanying spin transport which is called *pure charge current*. In general, this is the situation in a conventional, paramagnetic conductor without spin-orbit coupling. In Fig. 2.1(b), a situation is sketched, where one current density is larger than the other (here $J_\uparrow > J_\downarrow$). Hence, both charge and spin are transported. This case is called *spin-polarized current* and is the prevalent condition in ferromagnetic materials. In the third case (Fig. 2.1(c)), both current densities are equal in magnitude, but they propagate in opposite directions ($\mathbf{J}_\uparrow = -\mathbf{J}_\downarrow$). This results in a spin transport without accompanying net charge current and is called *pure spin current*. It corresponds to a pure flow of angular momentum.

---

[2]Note that the definition used here is based on the two channel model. There are more general approaches to define the spin current density as discussed in Refs. [24, 25, 26, 27, 28].
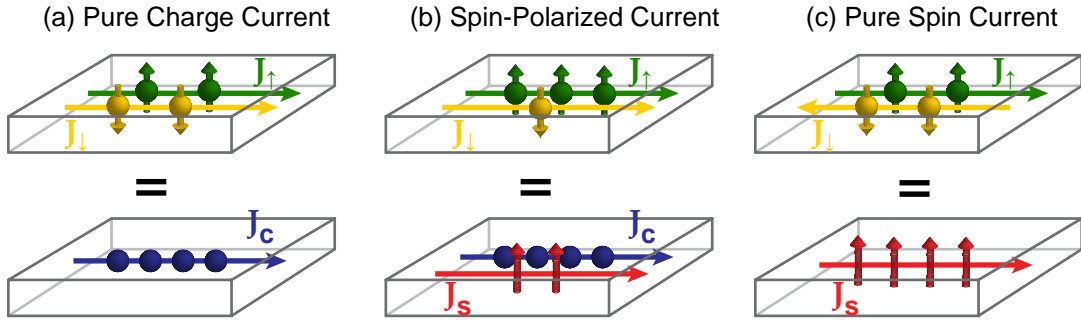
Figure 2.1: Currents. (a) Pure charge current. (b) Spin-polarized current. (c) Pure spin current. In analogy to [31].

In general, electron transport in a diffusive channel is the result of a difference in the electrochemical potential between two reservoirs [32, 33]. The force acting on an electron is then given by $\mathbf{F} = -\nabla\mu_{\uparrow(\downarrow)}$, where the (spin-resolved) electrochemical potential $\mu_{\uparrow(\downarrow)} = \mu_{\mathrm{ch},\uparrow(\downarrow)} - e\Phi$ consists of the (spin-resolved) chemical potential μ_{ch} and the (obviously spin-independent) electric potential Φ. For small deviations from equilibrium, $\mu_{\mathrm{ch},\uparrow(\downarrow)}$ can be written as $\mu_{\mathrm{ch},\uparrow(\downarrow)} = n_{\uparrow(\downarrow)}/\mathcal{N}_{\uparrow(\downarrow)}$, where $\mathcal{N}_{\uparrow(\downarrow)}$ is the (spin-resolved) density of states at the Fermi energy. From this, it becomes clear that electron transport can originate either from a spatial variation of $\mu_{\mathrm{ch},\uparrow(\downarrow)}$ via a gradient in the carrier density $n_{\uparrow(\downarrow)}$ (diffusion), or from an electric field $\mathbf{E} = -\nabla\Phi$ (drift)[3]. The resulting current densities are given by [32, 33]

$$\mathbf{J}_{\uparrow(\downarrow)} = \frac{\sigma_{\uparrow(\downarrow)}}{e}\nabla\mu_{\uparrow(\downarrow)} \tag{2.8}$$

with the spin-dependent electric conductivity $\sigma_{\uparrow(\downarrow)}$. In the steady state, the continuity equations for charge and spin current density are [34]

$$\nabla \cdot (\mathbf{J}_{\uparrow} + \mathbf{J}_{\downarrow}) = 0, \qquad \nabla \cdot (\mathbf{J}_{\uparrow} - \mathbf{J}_{\downarrow}) = e\frac{\delta n_{\uparrow}}{\tau_{\mathrm{sf},\uparrow}} - e\frac{\delta n_{\downarrow}}{\tau_{\mathrm{sf},\downarrow}}, \qquad (2.9)$$

where $\delta n_{\uparrow(\downarrow)} = n_{\uparrow(\downarrow)} - \bar{n}_{\uparrow(\downarrow)}$ is the deviation from the equilibrium carrier density, $\tau_{\mathrm{sf},\uparrow}$ the scattering time from spin-up to spin-down state, and $\tau_{\mathrm{sf},\downarrow}$ the scattering time for the inverse process. Equations (2.9) elucidate that the spin current is a not conserved quantity in contrast to the charge current. From these equations, the relations for the electrochemical potential describing charge and spin transport can be derived [34, 35, 36, 37, 38, 39]:

$$\nabla^2 (\sigma_{\uparrow}\mu_{\uparrow} + \sigma_{\downarrow}\mu_{\downarrow}) = 0, \qquad \nabla^2 (\mu_{\uparrow} - \mu_{\downarrow}) = \frac{1}{\lambda_{\mathrm{sd}}^2} (\mu_{\uparrow} - \mu_{\downarrow}), \qquad (2.10)$$

where the spin diffusion length λ_{sd} is linked to the diffusion constant and the spin flip scattering time (see Sec. 2.4). The difference between the electrochemical potentials

---

[3]In the linear response regime, diffusion and drift approach are related to each other via the Einstein relation $\sigma_{\uparrow(\downarrow)} = e^2 \mathcal{N}_{\uparrow(\downarrow)} D_{\uparrow(\downarrow)}$, where $D_{\uparrow(\downarrow)}$ is the (spin-resolved) diffusion constant.

of spin-up and spin-down charge carriers can be defined as *spin accumulation*

$$\mu_s = \mu_\uparrow - \mu_\downarrow. \tag{2.11}$$

In a normal metal, conductivity and diffusion constant are identical for both spin orientations ($\sigma_\uparrow = \sigma_\downarrow = \sigma$ and $D_\uparrow = D_\downarrow = D$). Therefore, with Eqs. (2.7) and (2.8), one obtains the relation between the electrochemical potential and the charge respective spin current density

$$\mathbf{J}_\mathrm{c} = \frac{\sigma}{\mathrm{e}} \nabla \left(\mu_\uparrow + \mu_\downarrow \right), \qquad\qquad \mathbf{J}_\mathrm{s} = -\frac{\hbar\sigma}{2e^2} \nabla \mu_\mathrm{s}. \tag{2.12}$$

This reveals the different origins: $\mathbf{J}_\mathrm{c}$ is caused by a gradient in the sum of $\mu_\uparrow$ and $\mu_\downarrow$, whereas $\mathbf{J}_\mathrm{s}$ originates from a gradient in the spin accumulation.

Dissipation of pure spin currents

Interestingly, it was predicted that pure spin currents are dissipationless [40, 41] which means that they are not inevitably tied to heat-generating processes. This prediction is based on the argument that spin currents are, in contrast to conventional currents, invariant under time reversal. Upon time reversal, velocity and spin reverse sign, whereas charge is invariant. Thus, a conventional charge current $\mathbf{J}_\mathrm{c} = \rho_\mathrm{c} \mathbf{v}$ transforms under time reversal into $\mathbf{J}_\mathrm{c} \to -\mathbf{J}_\mathrm{c}$, whereas a pure spin current $\mathbf{J}_\mathrm{s} = \rho_\mathrm{s} \mathbf{v}$ remains unchanged: $\mathbf{J}_\mathrm{s} \to \mathbf{J}_\mathrm{s}$ (Fig. 2.2).
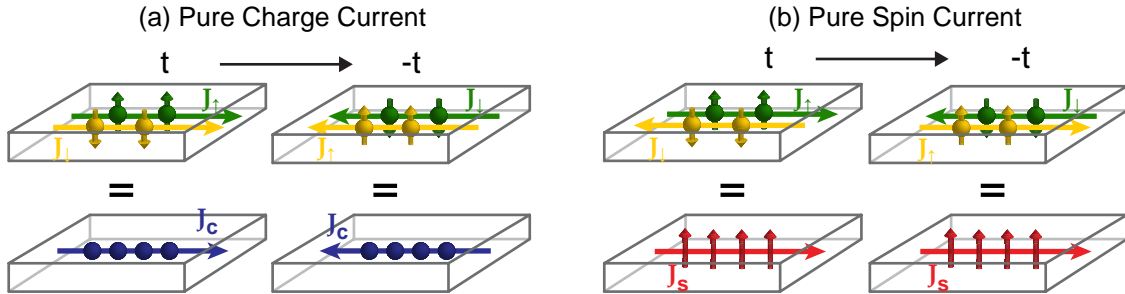
Figure 2.2: Effect of time reversal on (a) a pure charge current and (b) a pure spin current. Upon time reversal $t \to -t$, velocity $\mathbf{v} \to -\mathbf{v}$ and spin $\hat{\mathbf{s}} \to -\hat{\mathbf{s}}$ invert sign, whereas the charge $q \to q$ is invariant. This results in an inversion of the charge current $\mathbf{J}_\mathrm{c} \to -\mathbf{J}_\mathrm{c}$, whereas the pure spin current remains unchanged: $\mathbf{J}_\mathrm{s} \to \mathbf{J}_\mathrm{s}$.

The prediction that spin currents are dissipationless attracted a lot of interest, since this might allow to uncouple energy and/or information transport from heating. However, whether pure spin currents are dissipationless or not is the subject of controversial discussions and could not be experimentally proven yet[4]. If spin

---

[4]In the here introduced two channel model, a dissipationless spin current is hard to imagine, as the spin current is always linked to electron transport which generally is dissipative. Thus, very likely, dissipationless spin currents ought to be decoupled from charge carrier transport. First experiments in this direction were presented by Kajiwara *et al.* [42] who showed that a pure spin current can cross a magnetic insulator.

currents were dissipationless, they could, for example, be used to enhance the performance of processors: to overcome a main problem, cooling [43]. Spin currents might now enable to separate the regions of heat generation from those where the logic operations are performed. So, in high performance processors, pure spin currents could be used for the logic operations in the center of the device, but their generation, which is connected to heating, is located in the outer parts, where an efficient cooling is possible.

2.2 Spin-orbit interaction

Charge current and spin current are closely related to each other via a microscopic effect, the spin-orbit interaction (SOI). On the one hand, the SOI enables a conversion of a charge current into a spin current and vice versa. On the other hand, it is also one of the main origins of spin relaxation. In this section, only a brief overview of the different mechanisms responsible for the conversion of a charge into a spin current is given. Detailed information including mathematical derivations can be found in books and review articles, e.g., Refs. [44, 45, 46, 47, 48].

The physical origin of the spin-orbit interaction can be understood as follows: an electron moving with a velocity $\mathbf{v}$ in an external electric field $\mathbf{E}$ will feel a magnetic field $\mathbf{B} = (1/c^2)\mathbf{E} \times \mathbf{v}$ [45], where c is the velocity of light. As $\mathbf{B}$ is perpendicular to both $\mathbf{E}$ and $\mathbf{v}$, it is parallel to the orbital angular momentum $\mathbf{L}$ of the electron. The magnetic field $\mathbf{B}$ acts on the magnetic moment (antiparallel to $\mathbf{S}$) of the electron, such that the spin-orbit coupling can be written as $\lambda\mathbf{LS}$ with the coupling constant λ. The general Hamiltonian for the SOI is known as Pauli spin orbit term and can be derived from the Dirac equation. For an electron in a lattice potential, it is given by [44, 49]

$$H_{\text{SOI}} = -\frac{\hbar}{4m^2c^2}\,\boldsymbol{\sigma} \cdot \left(\mathbf{p} \times \nabla\widetilde{V}\right). \qquad (2.13)$$

Here, $\hbar$, m, c, $\boldsymbol{\sigma}$ and $\mathbf{p}$ are Planck's constant, the electron mass, the velocity of light, the vector of Pauli matrices (see Eq. (2.2)) and the electron momentum. The total potential $\widetilde{V} = V_{\text{c}} + V_{\text{ap}}$ can be split into a periodic crystal potential V_{c} and an aperiodic part V_{ap} containing the potential due to impurities, external electric fields, confinements, and boundaries [44].

There are three main mechanisms identified from semiclassical treatment of transport theory that are discussed in the following: the two extrinsic contributions "side-jump" and "skew scattering" being caused by impurity scattering and the "intrinsic" contribution, originating from the bandstructure (Fig. 2.3).

Skew scattering

In 1929, Mott found that spin carrying particles were asymmetrically scattered by a central potential [50]. The magnetic field $\mathbf{B}$ acting on an electron is inhomogeneous as the scattering potential and the electron velocity are space dependent. This generates a spin dependent force which is proportional to the gradient of the Zeeman energy $g\mu_{\text{B}}\mathbf{BS}/\hbar$ acting on the electron [45]. As the direction of the force depends
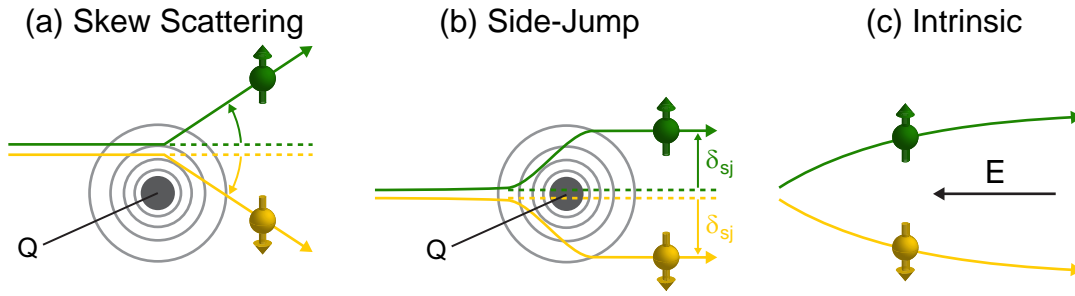
Figure 2.3: Spin-orbit interaction: (a) Skew scattering at an impurity with charge Q. (b) Side-jump scattering at an impurity with charge Q resulting in a spin dependent displacement δ_{sj}. (c) Intrinsic mechanism. All effects lead to a spin current transverse to the incoming particles. (a) and (b) are in analogy to [31] and (c) to [46].

on the spin orientation of the electron, spin-up and spin-down electrons are deflected in different directions as sketched in Fig. 2.3(a). Thus, the skew scattering leads to a conductivity σ_{ss} perpendicular to the incoming particles.

Side-jump scattering

The second extrinsic mechanism, side-jump scattering, originates from the anomalous form of the velocity operator in spin-orbit coupled systems [46]. Berger semiclassically interpreted this as a discontinuous, sideways displacement δ_{sj} of the center of mass of an electron wave package upon collision, where the shift direction depends on the spin orientation but not on the sign of the impurity potential (Fig. 2.3(b)) [51, 52]. The side-jump is superimposed to the skew scattering and leads to a conductivity σ_{sj} perpendicular to the incoming particles.

Intrinsic interaction

Besides the effects relying on impurity scattering, another SOI mechanism which is also present in ideal crystals was predicted. It is referred to as "intrinsic" or "Berry-phase" mechanism originating from the spin dependence of the so-called *anomalous velocity*. It was first proposed by Karplus and Luttinger [53] to explain the anomalous Hall effect and subsequently found by various other authors via different theoretical approaches as detailed in Refs. [54, 55, 56, 57]. In a semiclassical Boltzmann approach, the carrier velocity is then written as [49, 58]

$$\mathbf{v}_{k,\uparrow(\downarrow)} = \frac{1}{\hbar}\frac{\partial E_{\mathbf{k}}}{\partial \mathbf{k}} + e\mathbf{E} \times \mathbf{\Omega_k}, \tag{2.14}$$

where the first term is the "normal" velocity, thus the derivative of the band energy with respect to the crystal momentum $\mathbf{k}$. The second term, the anomalous contribution, is linear in the applied electric field $\mathbf{E}$ and contains the so-called Berry curvature $\mathbf{\Omega}$ [59]. It leads to a spin current perpendicular to the electric field $\mathbf{E}$ with conductivity σ_{int} as sketched in Fig. 2.3(c). The intrinsic effect was predicted to have a substantial influence in certain metals, e.g., for Pt, large effects were predicted [60]. More details can be found, for instance, in Refs. [49, 58].

2.3 The spin Hall effect and its inverse

In the previous section, several microscopic mechanisms generating a spin current perpendicular to the incoming particles were presented. These mechanisms can turn up as macroscopic effects. As in ferromagnets the numbers of spin-up and spin-down charge carriers at the Fermi edge are different, the previously discussed mechanisms lead to a spin-polarized current perpendicular to the charge carrier flow direction even if no external magnetic field is applied (Fig. 2.4(a)). This macroscopic effect is referred to as *anomalous Hall effect* and was discovered by E. H. Hall already in 1880. However, a microscopic understanding was established not until about 70 years later by Karplus and Luttinger [53].
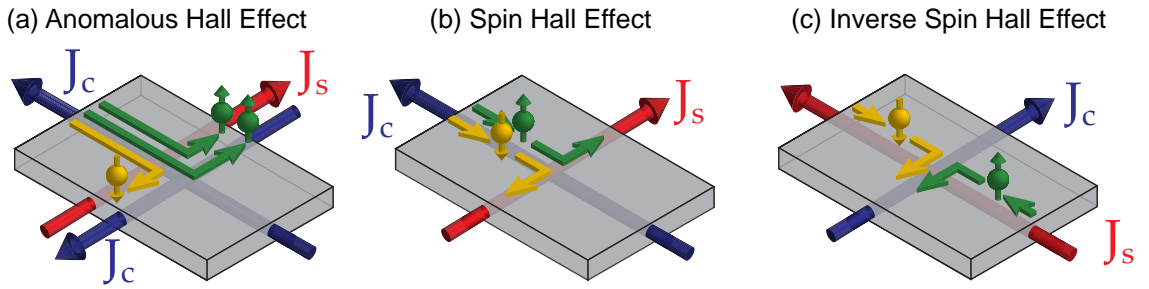
Figure 2.4: Macroscopic manifestations of the spin-orbit interaction: (a) The anomalous Hall effect in ferromagnets leads to a spin-polarized current perpendicular to an initial charge current. (b) The spin Hall effect in paramagnets generates a pure spin current transverse to an initial charge current. Its inverse process is shown in (c). The inverse spin Hall effect generates a charge current transverse to an initial spin current.

In paramagnetic conductors, the numbers of spin-up and spin-down charge carriers are equal. Thus, the same mechanisms generate a pure spin current perpendicular to an applied charge current (Fig. 2.4(b)). This conversion from charge current to spin current is called *spin Hall effect*. It was predicted by Dyakonov and Perel in 1971 [61], "rediscovered" by Hirsch in 1999 [13], and experimentally observed for the first time by Kato *et al.* in 2004 [62]. Also the inverse effect, namely the transformation of a pure spin current into a perpendicular charge current exists. It is called *inverse spin Hall effect* (Fig. 2.4(c)).

Hence, charge and spin current are closely related and can be transformed into each other by making use of the spin-orbit interaction. The contribution of the single mechanisms and how to experimentally distinguish between them is still under discussion [63, 64, 65].

As all mechanisms result in the same macroscopic effect, a perpendicular spin current, one can define the spin Hall conductivity σ_{SH} as the sum of the single conductivities: $\sigma_{\mathrm{SH}} = \sigma_{\mathrm{ss}} + \sigma_{\mathrm{sj}} + \sigma_{\mathrm{int}}$ [34]. Often, the *spin Hall angle* $\alpha_{\mathrm{SH}} = \sigma_{\mathrm{SH}}/\sigma$, the ratio of the spin Hall conductivity σ_{SH} and the electric conductivity σ is used. With this definition, the charge current generated by the inverse spin Hall effect and the spin current generated by the spin Hall effect can be written as

$$\mathbf{J}_{\mathrm{c}}^{\mathrm{ISH}} = \alpha_{\mathrm{SH}} \left(-\frac{2e}{\hbar} \right) J_{\mathrm{s}} \left[\hat{\mathbf{z}} \times \hat{\mathbf{s}} \right], \qquad\qquad \mathbf{J}_{\mathrm{s}}^{\mathrm{SH}} = \alpha_{\mathrm{SH}} \left(-\frac{\hbar}{2e} \right) J_{\mathrm{c}} \left[\hat{\mathbf{z}} \times \hat{\mathbf{s}} \right], \quad (2.15)$$

where $\hat{\mathbf{z}}$ is the direction of the initial current and $\hat{\mathbf{s}}$ the spin orientation of the spin current. From this equation, it can be seen that the crucial parameter determining the conversion efficiency between charge and spin current is the spin Hall angle. Therefore, huge efforts in theory and experiment have been undertaken to quantify this material specific quantity and investigate its dependence on various parameters as, e.g., band structure, impurity concentration or temperature [9, 10, 60, 64, 66, 67, 68, 69].

2.4 Relevant length scales

This section gives a short overview of different length scales relevant in the here studied metallic samples.

In a normal metal, the charge carriers (electrons) are usually considered to be particles which ballistically move between collisions. The mean distance between collisions (independent of the collision type: spin conserving or spin flipping) is called transport (momentum relaxation) mean free path λ_{t}. When defining a mean time between collisions τ_{t}, one can relate λ_{t} to the Fermi velocity v_{F}: $\lambda_{\mathrm{t}} = v_{\mathrm{F}}\tau_{\mathrm{t}}$. From the number of collisions while crossing a sample, two transport regimes can be discerned: the ballistic (few collisions) and the diffusive (many collisions) one.

In the ballistic limit, the spin-flip length λ_{sf} is – in analogy to the transport quantity λ_{t} – the mean distance between spin-flip scattering events which is given by $\lambda_{\mathrm{sf}} = v_{\mathrm{F}}\tau_{\mathrm{sf}}$, where τ_{sf} is the mean time between spin-flip collisions.

In the diffusive limit, the spin diffusion length λ_{sd} is used. It is the mean distance which electrons diffuse between spin-flip events and is related via the (charge) diffusion constant D to the spin-flip time: $\lambda_{\mathrm{sd}} = \sqrt{D\tau_{\mathrm{sf}}}$ [36]. This length scale is crucial for spin diffusion processes described by the spin diffusion equation (Eq. (2.10)).

The usual ordering of the different length scales is $\lambda_{\mathrm{t}} < \lambda_{\mathrm{sd}} < \lambda_{\mathrm{sf}}$.

In ferromagnets, the situation is more complex as the scattering processes and thus also the length scales are spin dependent. Here, we will not go into details, since the focus of this section is on non-magnetic metals. A detailed discussion both for normal metals and for ferromagnets can be found, e.g., in Ref. [70].

This concludes the theoretical introduction to spin currents and related effects. In the next chapter, we discuss "spin pumping" a method for the generation of pure spin currents.

Chapter 3

Spin pumping as a spin current source

In this chapter, we discuss spin pumping – the emission of a pure spin current from a ferromagnet into a normal metal due to a time-dependent magnetization – and its experimental realization. The concept of a "spin battery" emitting a pure spin current was suggested in 2002 by Y. Tserkovnyak, A. Brataas and G. E. W. Bauer [7, 8, 12]. They predicted that a precessing magnetization injects a pure spin current into an adjacent normal metal. To detect this effect, E. Saitoh *et al.* [71] suggested to use the inverse spin Hall effect (see Sec. 2.3) which generates from a spin current a charge current accessible with conventional electronics. Recently, in 2010, Mosendz *et al.* [9, 10] developed a theory to quantify the resulting DC voltage.

The chapter starts with a short description of the spin pumping effect and its detection principle, followed by a more detailed theory section. We also critically compare the DC voltage generated by spin pumping with the DC voltage caused by microwave rectification. The subsequent main part of the chapter deals with our measurement results on various heterostructures and their interpretation.

3.1 Overview

For our spin pumping measurements, we used ferromagnet/normal metal (F/N) heterostructures contacted for electrical measurements as sketched in Fig. 3.1. An incident microwave AC magnetic field in combination with a static magnetic field $\mathbf{H}_0$ (applied under an angle ϕ in the x-z-plane) causes a precession of the magnetization $\mathbf{M}$ (blue arrow in Fig. 3.1) around the effective magnetic field $\mathbf{H}_{\text{eff}}$ with a cone angle Θ. This angle becomes maximal under ferromagnetic resonance (FMR), the resonant absorption of electromagnetic waves by a ferromagnet. The rotating magnetization emits a pure spin current $\mathbf{J}_s$ (orange arrow) perpendicular to the interface with spin orientation $\hat{\mathbf{s}}$[1] (red arrow[2]) into the adjacent normal metal. Due to

---

[1]$\hat{\mathbf{s}}$ is antiparallel to the magnetic moment of the electron.

[2]For a magnetization relaxation, angular moment oriented in $\hat{\mathbf{x}}$-direction has to be added (red arrow inside the ferromagnet in Fig. 3.1) which corresponds to an emission of angular momentum in $-\hat{\mathbf{x}}$-direction. As magnetic moment and spin orientation are antiparallel, this equals an emission of a spin current with spin orientation $\hat{\mathbf{s}}$ in $\hat{\mathbf{x}}$-direction (red arrow in the normal metal).
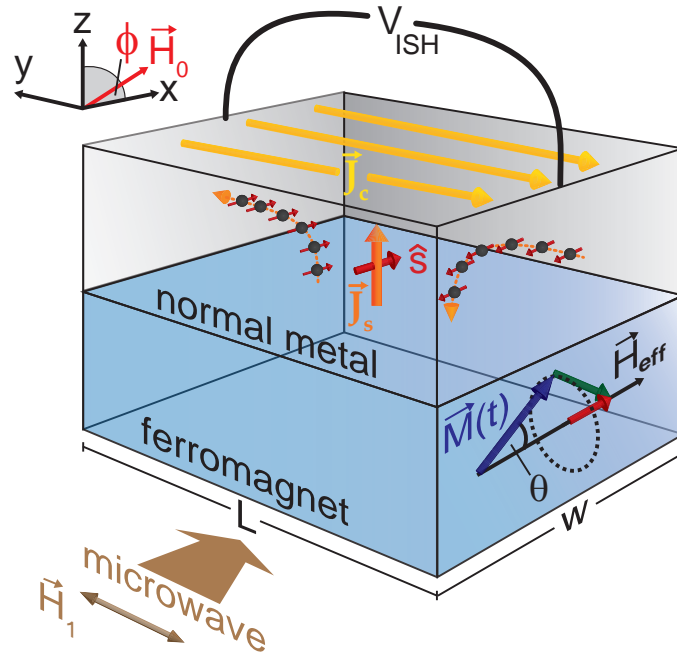
Figure 3.1: Sketch of the spin pumping measurement principle in a ferromagnet/normal metal heterostructure with length L and width w. A microwave magnetic field $\mathbf{H}_{\mathrm{MW}}$ in combination with a static magnetic field $\mathbf{H}_0$ drives a precession of the magnetization $\mathbf{M}$. This generates a pure spin current $\mathbf{J}_{\mathrm{s}}$ (orange arrow) across the ferromagnet/normal metal interface. Inside the normal metal, the spin current causes via the inverse spin Hall effect a charge current $\mathbf{J}_{\mathrm{c}}$ (yellow arrows) which generates a potential difference V_{ISH} owing to the open circuit condition. For details, see text.

the inverse spin Hall effect (see Sec. 2.3) inside the normal metal, the pure spin current generates a pure charge current $\mathbf{J}_{\mathrm{c}}$ (yellow arrows) perpendicular to both flow direction of $\mathbf{J}_{\mathrm{s}}$ and $\hat{\mathbf{s}}$. Under open circuit conditions, this charge current generates a potential difference V_{ISH} between the two sides of the sample which can be detected via the attached wires.

In a microscopic picture, the pure spin current $\mathbf{J}_{\mathrm{s}}$ injected into the normal metal corresponds to a flow of electrons with spin orientation $\hat{\mathbf{s}}$ along $\hat{\mathbf{x}}$ from the ferromagnet into the normal metal and an equal flow of electrons with opposite spin orientation, along $-\hat{\mathbf{x}}$, from the normal metal into the ferromagnet (Fig. 3.1). This results in a pure spin current without an accompanying net charge current across the interface. Theory [7, 8, 9, 12] predicts that the detected DC voltage V_{ISH} is closely related to the precession cone angle Θ of the magnetization. One key goal of this thesis was to quantitatively test this theoretical picture. Therefore, we performed ferromagnetic resonance spectroscopy in combination with simultaneous DC voltage measurements on various samples at different microwave power and at different temperatures.

3.2 Theory

In this theory section, a short introduction to FMR and spin transfer torque is given. Subsequently, the spin pumping effect and the spin current detection principle are discussed in detail. Finally, DC voltages generated by microwave rectification effects are treated.

3.2.1 Basics of the ferromagnetic resonance

In a quantum mechanic picture, a static external magnetic field $\mu_0\mathbf{H}_0$ leads to an energy splitting of the eigenstates of an isolated magnetic dipole μ_J, called Zeeman splitting. The corresponding energy eigenvalues, characterized by their magnetic quantum number m_J, are given by $E_J = -\mu_J\mu_0H_0 = g\mu_B m_J\mu_0 H_0$ with the g-factor g and the Bohr magneton μ_B. Irradiation of a radio frequency microwave magnetic field $\mu_0\mathbf{H}_1(t) = \mu_0\mathbf{H}_1 e^{-i\omega t}$ perpendicular to $\mathbf{H}_0$ can now induce magnetic dipole transitions (allowed if $\Delta m_J = \pm 1$) between energy eigenstates if the resonance condition

$$\hbar\omega = \Delta E = g\mu_B\mu_0 H_0 \tag{3.1}$$

is fulfilled (Fig. 3.2(a)). The corresponding resonant microwave absorption is called electron paramagnetic resonance (EPR) [19].
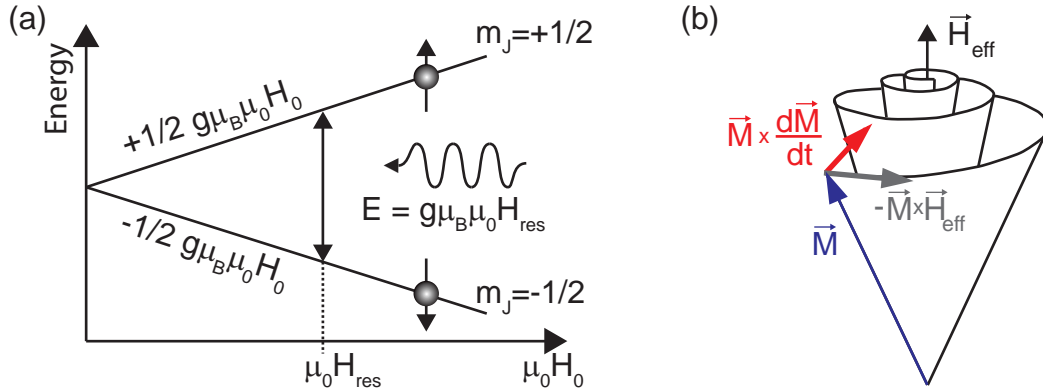
Figure 3.2: (a) Basic principle of EPR/FMR. The Breit-Rabi diagram illustrates how a radio frequency magnetic field can induce transitions between two energy eigenstates split by a static magnetic field. (b) Illustration of the magnetization relaxation after the radio frequency field is turned off. For details, see text.

We now turn from the quantum mechanic description of an isolated dipole to the classic limit for large quantum numbers. In ferromagnets, the magnetic moments are coupled via the exchange interaction, and therefore, the whole spin system with magnetization $\mathbf{M}$ can be considered as one macrospin. Ferromagnetic resonance (FMR) is the resonant absorption of electromagnetic waves in a ferromagnetic material [19] resulting in an excitation of this macrospin: the magnetization $\mathbf{M}$ precesses around an effective static magnetic field $\mathbf{H}_{\mathrm{eff}}$. The time-dependent evolution of the

magnetization orientation can be described by the Landau-Lifshitz-Gilbert (LLG) equation [72, 73, 74]

$$\frac{\partial \mathbf{M}}{\partial t} = -\gamma \left[\mathbf{M} \times (\mu_0 \mathbf{H}_{\text{eff}})\right] + \frac{\eta}{M_s}\left[\mathbf{M} \times \frac{\partial \mathbf{M}}{\partial t}\right] \tag{3.2}$$

with the saturation magnetization M_s, the gyromagnetic ratio $\gamma = g\mu_{\text{B}}/\hbar$, and the dimensionless phenomenological damping parameter η. The often used Gilbert damping parameter is defined as $\tilde{G} = \eta\gamma M_s$ [74]. The first term on the right of Eq. (3.2) describes the torque acting on the magnetization due to $\mathbf{H}_{\text{eff}}$. The second one accounts for the damping of the magnetization precession motion due to relaxation processes which tend to align the magnetization along $\mathbf{H}_{\text{eff}}$ (Fig. 3.2(b)). The damping term is important to quantify the energy absorption from the microwave field and determines the linewidth of the FMR.

The effective magnetic field $\mathbf{H}_{\text{eff}}$ in Eq. (3.2) consists of

$$\mathbf{H}_{\text{eff}} = \mathbf{H}_0 + \mathbf{H}_{\text{ex}} + \mathbf{H}_{\text{aniso}} + \mathbf{H}_1 \tag{3.3}$$

with the static external magnetic field $\mathbf{H}_0$, the exchange field $\mathbf{H}_{\text{ex}}$ which parametrizes the exchange interaction between the magnetic moments, the anisotropy field $\mathbf{H}_{\text{aniso}}$ taking into account the magneto-crystalline and shape anisotropy, and the radio frequency microwave magnetic field $\mathbf{H}_1$. A prominent application of FMR is the determination of $\mathbf{H}_{\text{aniso}}$ for different ferromagnetic films. More details of EPR and FMR are given, e.g., in Refs. [19, 75, 76].

3.2.2 Spin transfer torque

In 1996, Slonczewski [77] and Berger [78] predicted that a spin-polarized current can transfer angular momentum to the magnetization of a ferromagnet. This results in a torque and thus leads to an excitation or even a switching of the magnetization. In 1999, this prediction was experimentally observed for the first time in F/N/F pillars [4, 5, 6].

The transfer of angular momentum across a normal metal/ferromagnet interface is determined by the interface scattering properties and can be treated in the framework of magnetoelectronic circuit theory developed by Brataas *et al.* [79]. It can be understood in analogy to Andreev scattering at a normal metal/superconductor interface [80]. Let us consider a N/F bilayer, sketched in Fig. 3.3, for the simple case of a half metallic ferromagnet in which only electrons of one spin orientation can cross the interface and propagate. In the quantization system of the ferromagnetic magnetization, the incident spin-"right" electron from the normal metal is a linear combination of $|\uparrow\rangle$ and $|\downarrow\rangle$. The $|\downarrow\rangle$ state can cross the interface, whereas the $|\uparrow\rangle$ state cannot and is reflected[3]. A comparison of the angular momentum before ($|\rightarrow\rangle$) and after ($|\uparrow\rangle/\sqrt{2}$) the scattering process reveals a loss of transverse angular momentum which was absorbed in the ferromagnet and acts as torque T on the magnetization.

---

[3]Note that we do not use the nomenclature of Brataas *et al.* [79]. In this work, $|\uparrow\rangle$ and $|\downarrow\rangle$ represent the spin states and not the orientation of the electron's magnetic moment.
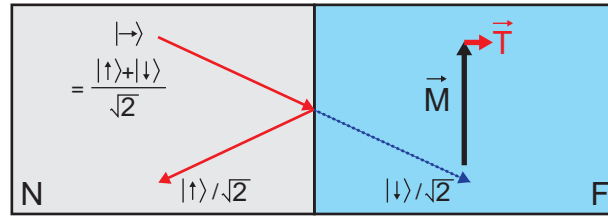
Figure 3.3: Transfer of transverse angular momentum from a spin current to a magnetization at a N/F interface (in analogy to [81][3]). For details, see text.

A second elementary scattering process, where a spin-"left" hole hits the interface from the left causes an identical spin transfer torque but cancels the charge current and the longitudinal momentum carried by the electron. The combination of both processes represents a spin-flip reflection (right → left) and is equivalent to a transverse polarized pure spin current that is completely absorbed at the interface. Thus, the angular momentum of the transverse spin current is transferred as torque **T** to the magnetization of the ferromagnet inducing a precession [81]. The efficiency of such an angular momentum transfer across an interface is governed by a parameter called spin mixing conductance $g^{\uparrow\downarrow}$ which is discussed in Sec. 3.2.3.

When relaxing the condition of a fully spin-polarized ferromagnet, also spins oriented transverse to the magnetization, represented as linear combination of the ferromagnet's eigenstates $|\uparrow\rangle$ and $|\downarrow\rangle$, can enter the ferromagnet. However, due to the exchange splitting, the components parallel and anti-parallel to the magnetization differ in energy and wave vector $k_{\mathrm{F}}^{\uparrow}$ and $k_{\mathrm{F}}^{\downarrow}$. This leads to a precession of the spin orientation around the direction of the magnetization **M** which results in a destructive interference of the spin component transverse to the magnetization [81]. The absorption of the transverse component happens within the ferromagnetic coherence length

$$\lambda_{\mathrm{c}} = \pi / \left(k_{\mathrm{F}}^{\uparrow} - k_{\mathrm{F}}^{\downarrow} \right) \tag{3.4}$$

which is for typical transition metals usually in the range of a few Å [81].

3.2.3 Spin pumping

We just saw that spin transfer torque, the transfer of angular momentum from a spin current in a normal metal into a ferromagnet, leads to an excitation of the magnetization. Also the inverse process is possible, namely that a time-dependent magnetization pumps a spin current into a normal metal. Indeed, this effect was suggested by Berger [78] and Tserkovnyak *et al.* [7] in analogy to the parametric pumping of charge carriers in mesoscopic systems [82, 83]. Parametric pumping is a push-pull process, where two parameters of a system periodically vary with a phase difference between them[4].

The generation of a spin current due to a time-dependent magnetization is illustrated in Fig. 3.4. A simplified density of states (DOS) of the conduction electrons

---

[4]For example, a periodic variation of two gate voltages can create a DC current through a quantum dot.
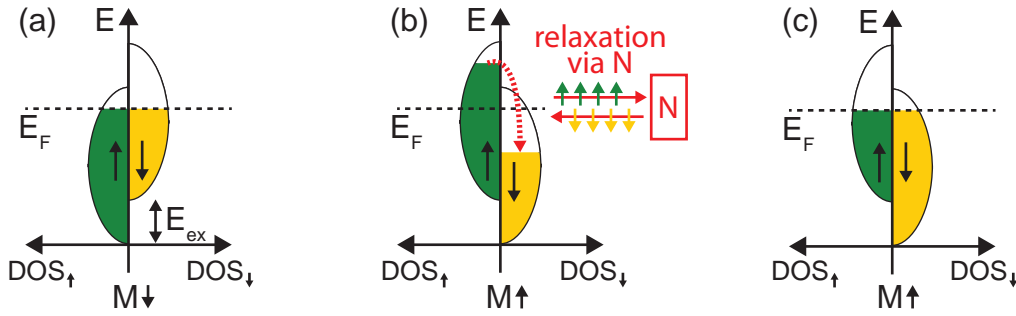
Figure 3.4: Principle of spin pumping. The conduction electron density of states of a ferromagnet for the two electron spin orientations is shown. (a) System in equilibrium. (b) A sudden magnetization switching requires spin relaxation. An additional spin relaxation channel is given via the emission of angular momentum (a pure spin current) into an adjacent normal metal. (c) After a certain time, equilibrium is restored [84].

in a ferromagnet, split into spin-up and spin-down states, is shown. The spin-up and spin-down bands are shifted with respect to each other by the exchange energy E_{ex}, and both bands are filled up to the Fermi energy E_{F}. A sudden switching of the magnetization orientation leads to a relative energy shift of the two spin bands (Fig. 3.4(b)). The electrons above the Fermi energy will relax via spin flip processes to fill the lower energy spin band (dashed arrow). If there is a normal metal in contact with the ferromagnet, an additional relaxation process, the emission of a pure spin current, can take place. This happens until the system is in equilibrium again (Fig. 3.4(c)) [84].

A periodical, sudden switching of the magnetization direction leads to an AC spin current. In the adiabatic limit, where the magnetization precesses slowly in comparison to the relaxation times of the system's electronic degrees of freedom, the x- and y-components of the magnetization vector act as the two push and pull parameters of the parametric pump. This generates the desired DC spin current [12].

Tserkovnyak *et al.* [7] proposed this effect as the origin of the enhanced damping observed in FMR experiments on N/F/N heterostructures [85]. Using time-dependent scattering theory, the authors calculated in the adiabatic approximation for ferromagnets thicker than the ferromagnetic coherence length λ_{c} (see Eq. (3.4)) that a precessing magnetization generates a pumped spin current

$$J_{\mathrm{s}}^{\mathrm{pump}}\hat{\mathbf{s}} = \frac{\hbar}{4\pi}\left(\mathrm{Re}(g^{\uparrow\downarrow})\hat{\mathbf{m}} \times \frac{\partial\hat{\mathbf{m}}}{\partial t} - \mathrm{Im}(g^{\uparrow\downarrow})\frac{\partial\hat{\mathbf{m}}}{\partial t}\right), \qquad (3.5)$$

where $\hat{\mathbf{s}}$ is the spin orientation and $\hat{\mathbf{m}}$ the unit vector of the magnetization. In FMR experiments, the first term of Eq. (3.5) ($\propto \mathrm{Re}(g^{\uparrow\downarrow})$) has the same form as the Gilbert term in Eq. (3.2) and thus leads to an additional damping of the magnetization precession, whereas the second term ($\propto \mathrm{Im}(g^{\uparrow\downarrow})$) acts as an additional field and results in a shift of the resonance position.

For conventional scattering processes, the transfer of angular momentum across an interface is governed by the real and imaginary part of the spin mixing conductance $g^{\uparrow\downarrow} = \sum_{nm}\left[\delta_{nm} - r_{nm}^{\uparrow}(r_{nm}^{\downarrow})^{*}\right]$ with the spin dependent reflection amplitudes $r_{nm}^{\uparrow}$

and $r^\downarrow_{nm}$ between transverse modes m and n in the normal metal at the interface to the ferromagnet [12]. $g^{\uparrow\downarrow}$ is a material combination dependent parameter that describes how a given spin accumulation transmits torque across a certain interface. It was introduced in the framework of magnetoelectronic circuit theory to describe the transport between non-collinear ferromagnets. Details can be found in Refs. [12, 79, 81]. The spin mixing conductance used in the following represents the number of transport channels per unit area for torque transport across an interface. For the simple case of an isotropic free electron gas, $g^{\uparrow\downarrow}$ can be calculated as [8]

$$g^{\uparrow\downarrow} = \frac{k_{\mathrm{F}}^2}{4\pi} \tag{3.6}$$

with the Fermi wave vector k_{F} of the normal metal. For real metals with a more complex Fermi surface, band-structure calculations are needed to determine $g^{\uparrow\downarrow}$. First principle band-structure calculations for conventional 3d-transition metal interfaces as Co/Cu, Fe/Cr or Fe/Au yield very small imaginary parts of $g^{\uparrow\downarrow}$ [86, 87]. However, comparable values of real and imaginary part were predicted for interfaces with half-metallic ferromagnets (Co_2MnSi/Cr and (Ga,Mn)As/Cr) [88] or ferromagnetic insulators [89]. In the following discussion, we concentrate on "conventional" ferromagnets and thus assume $\mathrm{Im}(g^{\uparrow\downarrow}) \ll \mathrm{Re}(g^{\uparrow\downarrow})$ such that the imaginary part in Eq. (3.5) can be neglected. Thus, Eq. (3.5) simplifies to

$$J_{\mathrm{s}}^{\mathrm{pump}}\hat{\mathbf{s}} = \frac{\hbar}{4\pi}\mathrm{Re}(g^{\uparrow\downarrow})\left[\hat{\mathbf{m}} \times \frac{\partial\hat{\mathbf{m}}}{\partial t}\right]. \tag{3.7}$$

Hence, the precessing magnetization of the ferromagnet generates a spin current proportional to the real part of $g^{\uparrow\downarrow}$ with spin orientation $\hat{\mathbf{s}}$ perpendicular to both $\hat{\mathbf{m}}$ and $\partial\hat{\mathbf{m}}/\partial t$ (Fig. 3.5). The magnitude of the DC component of the spin current is obtained by time averaging of Eq. (3.7) under the assumption of a circular magnetization precession[5] [9]. It reads

$$J_{\mathrm{s}}^{\mathrm{pump, circ}} = \frac{1}{2\pi}\frac{\hbar}{2}\omega\mathrm{Re}(g^{\uparrow\downarrow})\sin^2\Theta \tag{3.8}$$

with the microwave frequency ω and the precession cone angle Θ of the magnetization. Its spin orientation $\hat{\mathbf{s}}$ is parallel to $\mathbf{H}_{\mathrm{eff}}$, and $\sin^2\Theta$ is proportional to the area of the magnetization precession trajectory S indicated in Fig. 3.5.

In magnetic thin films, the demagnetization field can significantly influence the magnetization precession, changing it from circular to elliptical. Therefore, Ando $et\,al.$ [90] suggested to include the static and dynamic demagnetization fields into $\mathbf{H}_{\mathrm{eff}}$ of Eq. (3.2), originating from the static and dynamic components of the magnetization. This leads to a correction factor P for the magnitude of the effective spin current

$$J_{\mathrm{s}}^{\mathrm{pump, eff}} = P \cdot J_{\mathrm{s}}^{\mathrm{pump, circ}} \tag{3.9}$$

---

[5]For the moment, all anisotropy fields as the demagnetization field or the magneto-crystalline anisotropy fields are neglected.
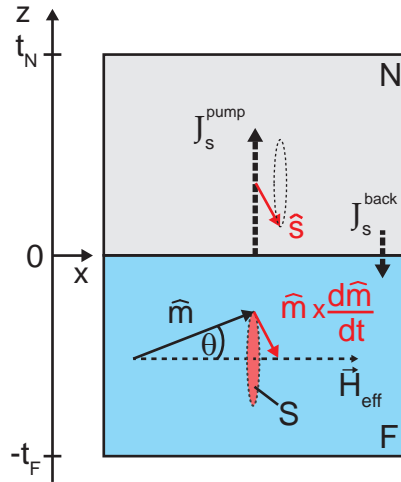
Figure 3.5: The magnetization precession in F pumps a spin current J_s^{pump} across the F/N interface which decays normal to the interface. The spin orientation $\hat{s}$ of the spin current is parallel to $\hat{m} \times (\partial\hat{m}/\partial t)$ and always has a component parallel to $\mathbf{H}_{\mathrm{eff}}$. There is also a backflow J_s^{back} into the ferromagnet.

with

$$P = \frac{2\omega \left[\gamma\mu_0 M_s \cos^2 \Phi_{\mathrm{M}} + \sqrt{(\gamma\mu_0 M_s)^2 \cos^4 \Phi_{\mathrm{M}} + (2\omega)^2} \right]}{(\gamma\mu_0 M_s)^2 \cos^4 \Phi_{\mathrm{M}} + (2\omega)^2}, \qquad (3.10)$$

where Φ_{M} is the angle between the magnetization orientation and its projection onto the film plane. A more detailed discussion of the influence of P on the measured signal is given in Sec. 3.4.8.

To summarize, spin pumping is the result of a periodic change in the spin dependent scattering matrix at the F/N interface due to magnetization precession. The precessing magnetization pumps a pure spin current, without any net charge current, across the interface. The spin current density is measured in units of torque per time and area. Moreover, spin injection into an adjacent conductive material does not suffer from a conductance mismatch [91] as the smallness of the mixing conductance for a ferromagnet/semiconductor interface is compensated by the small spin current that is necessary to saturate the spin accumulation [12].

3.2.4 Spin diffusion in a normal metal

The spin current transferred across the F/N interface creates a spin accumulation $\mu_s = \mu^\uparrow - \mu^\downarrow$ (see Eq. (2.11)) in the normal metal at the F/N interface. The vector orientation of $\boldsymbol{\mu}_s = \mu_s \cdot \hat{s}$ gives the spin orientation of the injected spin current. It is perpendicular to both $\hat{m}$ and $\partial\hat{m}/\partial t$ and thus has an AC and a DC component, where the latter is parallel to $\mathbf{H}_{\mathrm{eff}}$.

In the ballistic limit, the spin accumulation crosses the entire normal metal layer, gets fully reflected at the normal metal/vacuum interface and is reabsorbed by the ferromagnet without influencing the magnetization dynamics. In conventional, diffusive normal metals, the spin accumulation is not a conserved quantity, but it is

reduced by spin-flip processes (e.g., due to spin-orbit coupling or scattering on magnetic impurities) with the characteristic relaxation length λ_{sd} (see Sec. 2.4). The propagation of the spin accumulation along $\hat{\mathbf{z}}$ in the normal metal can be described by the one-dimensional spin diffusion equation [92]

$$\frac{\partial \mu_s}{\partial t} = D_{\mathrm{N}} \frac{\partial^2 \mu_s}{\partial z^2} - \frac{\mu_s}{\tau_{\mathrm{sf}}}, \tag{3.11}$$

where $\partial \mu_s / \partial t = i\omega_{\mathrm{M}} \mu_s$ and the normal metal diffusion constant $D_{\mathrm{N}} = v_{\mathrm{F}}^2 \tau_{\mathrm{t}}/3$ with the Fermi velocity v_{F} and the normal metal momentum scattering time τ_{t}. In the case of ferromagnetic resonance, the magnetization precession frequency ω_{M} equals the microwave frequency ω: $\omega_{\mathrm{M}} = \omega$. We consider the limit of strong spin-flip scattering $\omega \tau_{\mathrm{sf}} \ll 1$, where the left side of Eq.(3.11) can be neglected ($\partial \mu_s / \partial t \approx 0$). For the microwave frequency used in our setup ($\omega \approx 10^{11}\,\mathrm{s}^{-1}$) and for materials with a high atomic number as platinum used in our experiments, this condition is easily fulfilled [8].

The solution of the spin diffusion equation (Eq. (3.11)) depends on the boundary conditions. We demand continuity of the total spin current J_{s}^0 at the F/N interface ($z = 0$),

$$J_{\mathrm{s}}\left(z = 0\right)\hat{\mathbf{s}} = J_{\mathrm{s}}^0\,\hat{\mathbf{s}} = -\frac{\hbar}{2e}\frac{\sigma}{e}\left.\frac{\partial \mu_{\mathrm{s}}}{\partial z}\right|_{z=0}, \tag{3.12}$$

and a vanishing spin current at the normal metal/vacuum interface ($z = t_{\mathrm{N}}$):

$$J_{\mathrm{s}}\left(z = t_{\mathrm{N}}\right)\hat{\mathbf{s}} = 0 = -\frac{\hbar}{2e}\frac{\sigma}{e}\left.\frac{\partial \mu_{\mathrm{s}}}{\partial z}\right|_{z=t_{\mathrm{N}}}. \tag{3.13}$$

With these conditions, one obtains for the spin accumulation [8, 11]

$$\mu_{\mathrm{s}}(z) = \mu_{\mathrm{s}}^0 \frac{\cosh\left[\left(t_{\mathrm{N}} - z\right)/\lambda_{\mathrm{sd}}\right]}{\sinh\left[t_{\mathrm{N}}/\lambda_{\mathrm{sd}}\right]}. \tag{3.14}$$

Its decay with z causes a spin current, whose time-independent component is given by [9, 10]

$$J_{\mathrm{s}}\left(z\right) = J_{\mathrm{s}}^0 \frac{\sinh\left[\left(t_{\mathrm{N}} - z\right)/\lambda_{\mathrm{sd}}\right]}{\sinh\left[t_{\mathrm{N}}/\lambda_{\mathrm{sd}}\right]} \tag{3.15}$$

and depends on the ratio $t_{\mathrm{N}}/\lambda_{\mathrm{sd}}$. Figure 3.6 shows the magnitude of the spin current between the two interfaces ferromagnet/normal metal ($z = 0$) and normal metal/vacuum ($z = t_{\mathrm{N}}$) for different $t_{\mathrm{N}}/\lambda_{\mathrm{sd}}$ ratios. For $\lambda_{\mathrm{sd}} > t_{\mathrm{N}}$, an almost linear decay occurs, whereas for $\lambda_{\mathrm{sd}} \ll t_{\mathrm{N}}$ the spin current vanishes already close to the ferromagnet.

When determining J_{s}^0, one has to take into account that the spin accumulation μ_{s} at the F/N interface does not only lead to a spin current in the normal metal but also to a backflow of spins into the ferromagnet [11, 12]. Thus, the total spin current J_{s}^0 at the F/N interface propagating into the normal metal is reduced by $J_{\mathrm{s}}^{\mathrm{back}}$ and can be expressed as
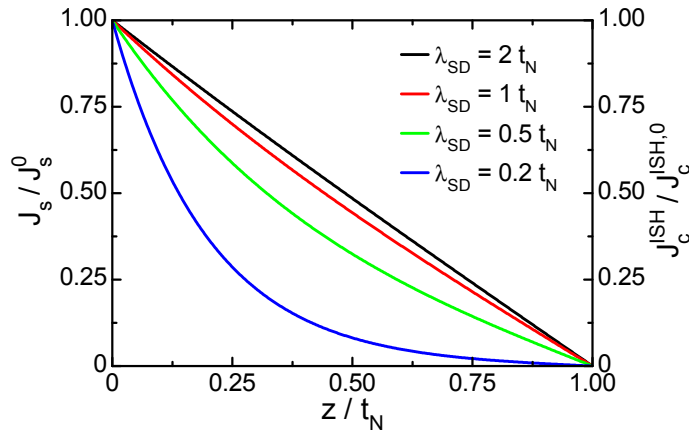
Figure 3.6: Decay of spin current and charge current with the distance from the ferromagnet/normal metal interface for different ratios of $t_{\mathrm{N}}/\lambda_{\mathrm{sd}}$.

$$J_{\mathrm{s}}^0 = J_{\mathrm{s}}^{\mathrm{pump}} - J_{\mathrm{s}}^{\mathrm{back}}.$$

This effect can be accounted for by replacing the spin mixing conductance of Eq. (3.5) by an effective $g^{\uparrow\downarrow}$ [8, 10]. This effective spin mixing conductance is used in the following.

3.2.5 Spin current detection via voltage measurements

As discussed in Sec. 2.3, spin currents generate charge currents via the inverse spin Hall effect. This mechanism was suggested as detection principle for the spin pumping effect by Saitoh *et al.* [71]. The inverse spin Hall effect is described by Eq. (2.15)

$$\mathbf{J}_{\mathrm{c}}^{\mathrm{ISH}} = \alpha_{\mathrm{SH}} \left(-\frac{2e}{\hbar} \right) J_{\mathrm{s}} \left[\hat{\mathbf{z}} \times \hat{\mathbf{s}} \right]$$

with the efficiency α_{SH}. The presence of the cross product reflects the symmetry of the inverse spin Hall effect, where the DC charge current is perpendicular to both the flow direction of the spin current (perpendicular to the interface, along $\hat{\mathbf{z}}$) and to the time-averaged spin orientation $\hat{\mathbf{s}}$, defined by the equilibrium orientation of $\mathbf{M}$ (Fig. 3.7).

Equation (2.15) reveals that the charge current $J_{\mathrm{c}}^{\mathrm{ISH}}(z)$ has the same z-dependence as $J_{\mathrm{s}}(z)$ and thus can be added as right axis to Fig. 3.6.

The calculation of the DC voltage resulting from the combination of spin pumping and inverse spin Hall effect is performed along the lines of Mosendz *et al.* [9, 10]. As our device is an open circuit (Fig. 3.7), the charge current caused by the inverse spin Hall effect leads to a charge accumulation at the borders of the sample. This generates, in analogy to, e.g., the Hall effects [93], a compensating electric field $\mathbf{E}_{\mathrm{comp}}$. If the sample is much larger in y-direction (length) than in z-direction (thickness), this field should be uniform over the whole sample thickness. Thus, the total current
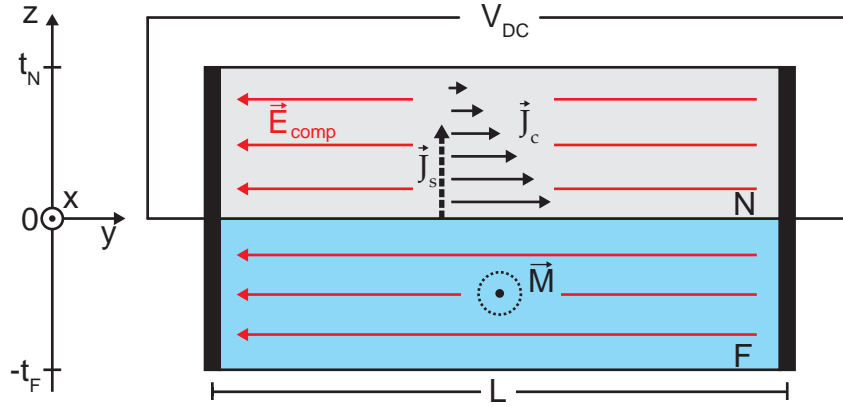
Figure 3.7: Magnetization precession generates a pure spin current $\mathbf{J}_\mathrm{s}$ which causes a charge current $\mathbf{J}_\mathrm{c}$ via the inverse spin Hall effect. Due to the open circuit condition, an electric field $\mathbf{E}_\mathrm{comp}$ compensating for the electron flow is created.

density $\mathbf{J}(z)$ is given by

$$\mathbf{J}(z) = \mathbf{J}_\mathrm{c}^\mathrm{ISH}(z) + \sigma_\mathrm{tot}\mathbf{E}_\mathrm{comp} \tag{3.16}$$

with the bilayer conductivity

$$\sigma_\mathrm{tot} = \frac{1}{R_\mathrm{tot}}\frac{L}{w(t_\mathrm{N}+t_\mathrm{F})} = \left(\frac{1}{R_\mathrm{N}}+\frac{1}{R_\mathrm{F}}\right)\frac{L}{w(t_\mathrm{N}+t_\mathrm{F})} = \frac{\sigma_\mathrm{N}t_\mathrm{N}+\sigma_\mathrm{F}t_\mathrm{F}}{t_\mathrm{N}+t_\mathrm{F}}. \tag{3.17}$$

Here, R_N, σ_N, t_N, R_F, σ_F and t_F are the resistance, the conductivity and the thickness of the N and F layer, respectively. Moreover, R_tot is the bilayer resistance, and L and w are the sample length (in y-direction) and width (in x-direction) as indicated in Figs. 3.1 and 3.7, respectively. The open circuit condition demands the overall current $\int \mathbf{J}(z)\,dz$ to be zero, leading to

$$0 = \int_{-t_\mathrm{F}}^{t_\mathrm{N}} \mathbf{J}_\mathrm{c}^\mathrm{ISH}(z)\,dz + \int_{-t_\mathrm{F}}^{t_\mathrm{N}} \sigma_\mathrm{tot}\mathbf{E}_\mathrm{comp}dz. \tag{3.18}$$

Taking into account that $\sigma_\mathrm{tot}\mathbf{E}_\mathrm{comp}$ is independent of z for $L \gg t_\mathrm{N}+t_\mathrm{F}$, and that the charge current is generated only in the normal metal, we obtain for the compensating electric field along the measurement direction y

$$E_\mathrm{comp} = \frac{-\int_0^{t_\mathrm{N}} J_\mathrm{c}^\mathrm{ISH}(z)\,dz}{(t_\mathrm{N}+t_\mathrm{F})\,\sigma_\mathrm{tot}}. \tag{3.19}$$

Solving the integral with $J_\mathrm{c}^\mathrm{ISH}$ from Eq. (2.15) and taking J_s from Eq. (3.15) results in

$$E_\mathrm{comp} = \frac{e\left[\alpha_\mathrm{SH}\lambda_\mathrm{SD}\tanh\frac{t_\mathrm{N}}{2\lambda_\mathrm{SD}}\right][\hat{\mathbf{z}}\times\hat{\mathbf{s}}]\,g^{\uparrow\downarrow}}{\sigma_\mathrm{F}t_\mathrm{F}+\sigma_\mathrm{N}t_\mathrm{N}}\nu_\mathrm{MW}P\sin^2\Theta. \tag{3.20}$$

The corresponding voltage $V_\mathrm{ISH} = E_\mathrm{comp}\cdot L$ between the left and right wire contact, generated by spin pumping in combination with the inverse spin Hall effect, is thus

given by[6]

$$V_{\mathrm{ISH}} = \frac{e \left[\alpha_{\mathrm{SH}} \lambda_{\mathrm{SD}} \tanh \frac{t_{\mathrm{N}}}{2\lambda_{\mathrm{SD}}} \right] g^{\uparrow\downarrow}}{\sigma_{\mathrm{F}} t_{\mathrm{F}} + \sigma_{\mathrm{N}} t_{\mathrm{N}}} \nu_{\mathrm{MW}} PL \sin^2 \Theta. \tag{3.21}$$

This equation has important implications on the experiments. V_{ISH} is proportional to the spin Hall angle α_{SH} determined by the conversion efficiency between spin and charge current, proportional to $g^{\uparrow\downarrow}$ given by the transfer of angular momentum across the F/N interface, proportional to the sample length L and to the $\sin^2 \Theta$, where Θ is the precession cone angle of the magnetization. The denominator is the sum of the conductivities of the single layers weighted by their thickness. This can be understood as a partial shorting of the generated voltage by the conductive layer stack. Several proportionalities predicted by Eq. (3.21) are experimentally verified in the following sections. In anticipation of these more detailed discussions, let us mention right away that Eq. (3.21) is quantitatively corroborated in experiment.

3.2.6 DC voltages due to microwave rectification

Besides spin pumping in combination with the inverse spin Hall effect, also other mechanisms for the generation of a DC voltage in conjunction with FMR have been suggested and were observed in experiment [94, 95, 96, 97]. In particular, microwave rectification effects related to the anisotropic magnetoresistance or the anomalous Hall effect are often superimposed onto the spin pumping signal if the sample is not located exactly in a node of the microwave electric field [9, 98]. Figure 3.8 displays the field configuration of a bilayer sample positioned at the center of a TE_{102} microwave cavity with the static magnetic field applied along $\hat{\mathbf{x}}$ ($\phi = 0°$). At the cavity center, an anti-node of the microwave magnetic field $\mathbf{H}_1$, oriented parallel $\hat{\mathbf{y}}$, and a node of the microwave electric field $\mathbf{E}_1$ are present. Thus, at the sample position, $\mathbf{H}_1$ is maximal, whereas $\mathbf{E}_1$ is minimal. In this configuration, no DC voltage should be generated via rectification effects. However, if the sample was positioned slightly off center, a microwave electric field oriented parallel $\hat{\mathbf{x}}$ would appear (Fig. 3.8). In this situation, a DC voltage can be created as the following discussion will show.

3.2.6.1 Homodyning by AMR and AHE

In ferromagnetic materials, nonlinear conduction effects may occur as the electric conductivity depends on the orientation of the current relative to the magnetization [94]. In a simple phenomenological description for a ferromagnetic, isotropic and monodomain sample, including AMR and AHE, the electric field inside the conductor takes the form [93]

$$\mathbf{E} = \rho_\perp \mathbf{J} + \frac{\Delta\rho}{M_{\mathrm{s}}^2}(\mathbf{J}{\cdot}\mathbf{M})\mathbf{M} + \mu_0 R_{\mathrm{A}}(\mathbf{J} \times \mathbf{M}). \tag{3.22}$$

Here, R_{A} is the anomalous Hall coefficient and $\Delta\rho = \rho_{||} - \rho_\perp$ is the so-called resistivity anisotropy with $\rho_{||}$ and $\rho_\perp$ being the diagonal components of the resistivity

---

[6]The cross product $[\hat{\mathbf{z}} \times \hat{\mathbf{s}}]$ in Eq. (3.20) is evaluated for the geometry depicted in Fig. 3.7. In this case, it results in a factor of one. Note that, e.g., other orientations of $\mathbf{M}$ (and thus $\hat{\mathbf{s}}$) result in other values, in particular an inversion of $\mathbf{M}$ leads to a sign change.
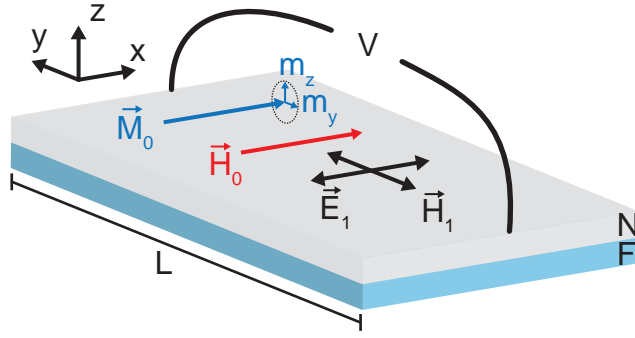
Figure 3.8: Electric and magnetic field configuration in spin pumping measurements. If the sample is positioned exactly at the center of the microwave cavity, the microwave electric field vanishes: $\mathbf{E}_1 = 0$. However, for the calculations in this section, we assume a finite value of $\mathbf{E}_1$.

tensor for two principal directions of the current density $\mathbf{J}$, parallel and perpendicular to $\mathbf{M}$. In Eq. (3.22), the effects of the applied static magnetic field are neglected as they are normally much smaller than the anomalous effects and only play a role at very large applied fields.

For the following analysis, magnetization $\mathbf{M}$ and current density $\mathbf{J}$ are split into static ($\mathbf{M}_0$ and $\mathbf{J}_0$) and dynamic ($\mathbf{M}_1$ and $\mathbf{J}_1$) parts:

$$\mathbf{M} = \mathbf{M}_0 + \mathbf{M}_1 \qquad \text{and} \qquad \mathbf{J} = \mathbf{J}_0 + \mathbf{J}_1. \tag{3.23}$$

As the precession amplitude is assumed to be small, we use the approximations $\mathbf{M}_0 \cdot \mathbf{M}_1 \approx 0$ and $|\mathbf{M}| \approx |\mathbf{M}_0| = M_s$. Inserting Eq. (3.23) into Eq. (3.22) results in

$$\mathbf{E} = \rho(\mathbf{J}_0 + \mathbf{J}_1) + \frac{\Delta\rho}{M_s^2}[(\mathbf{J}_0 + \mathbf{J}_1)(\mathbf{M}_0 + \mathbf{M}_1)] \cdot (\mathbf{M}_0 + \mathbf{M}_1) + \mu_0 R_A[(\mathbf{J}_0 + \mathbf{J}_1) \times (\mathbf{M}_0 + \mathbf{M}_1)] =$$

$$= \rho(\mathbf{J}_0 + \mathbf{J}_1) + \frac{\Delta\rho}{M_s^2}[(\mathbf{J}_0 \mathbf{M}_0)\mathbf{M}_0 + (\mathbf{J}_0 \mathbf{M}_1)\mathbf{M}_0 + (\mathbf{J}_1 \mathbf{M}_0)\mathbf{M}_0 + (\mathbf{J}_1 \mathbf{M}_1)\mathbf{M}_0 +$$

$$+ (\mathbf{J}_0 \mathbf{M}_0)\mathbf{M}_1 + (\mathbf{J}_0 \mathbf{M}_1)\mathbf{M}_1 + (\mathbf{J}_1 \mathbf{M}_0)\mathbf{M}_1 + (\mathbf{J}_1 \mathbf{M}_1)\mathbf{M}_1] +$$

$$+ \mu_0 R_A[\mathbf{J}_0 \times \mathbf{M}_0 + \mathbf{J}_0 \times \mathbf{M}_1 + \mathbf{J}_1 \times \mathbf{M}_0 + \mathbf{J}_1 \times \mathbf{M}_1]. \tag{3.24}$$

The terms containing $\mathbf{J}_0$, a constant current density, lead to a so-called photoresistance discussed in detail in Ref. [97]. In our setup, no DC current is applied and thus all parts comprising $\mathbf{J}_0$ are zero. Moreover, a photovoltage is exclusively created in terms simultaneously containing $\mathbf{J}_1$ and $\mathbf{M}_1$. When neglecting second order effects ($\mathbf{M}_1 \mathbf{M}_1 \approx 0$), Eq. (3.24) reduces to

$$\mathbf{E} = \frac{\Delta\rho}{M_s^2}[(\mathbf{J}_1 \mathbf{M}_1)\mathbf{M}_0 + (\mathbf{J}_1 \times \mathbf{M}_1) \times \mathbf{M}_0] + \mu_0 R_A(\mathbf{J}_1 \times \mathbf{M}_1) \tag{3.25}$$

with time-dependent and time-independent contributions. To extract the time-independent part relevant in DC measurements, a time averaging symbolized by $\langle\,\rangle$ is carried out. The time-independent electric field generated by microwave rectification can then be written as [94]

$$\mathbf{E}_{\mathrm{HD}} = \underbrace{\frac{\Delta\rho}{M_{\mathrm{s}}^2}[\langle\mathbf{J}_1\mathbf{M}_1\rangle\mathbf{M}_0 + \langle\mathbf{J}_1\times\mathbf{M}_1\rangle\times\mathbf{M}_0]}_{\propto\mathrm{AMR}} + \underbrace{\mu_0 R_{\mathrm{A}}\langle\mathbf{J}_1\times\mathbf{M}_1\rangle}_{\propto\mathrm{AHE}} \qquad (3.26)$$

with the first term proportional to the AMR ($\propto \Delta\rho$) and the second to the AHE ($\propto R_{\mathrm{A}}$). In the following, we call this DC electric field and the corresponding DC voltage *homodyne* electric field and voltage as their origin is the nonlinear interaction of the dynamic components of current density and magnetization, both varying at the same frequency.

The explicit expressions for E_{HD} and the DC voltage generated by homodyning for our measurement geometry are calculated in Appendix B.

3.2.6.2 Transformation behavior of the homodyne voltage under field inversion

To enable a comparison of the experimentally observed field dependence of the DC voltage with theory, the effect of an inversion of the external magnetic field $\mathbf{H}$ on Eq. (3.26) is discussed. Upon field inversion ($\mathbf{H} \to -\mathbf{H}$), both the static and the dynamic part of $\mathbf{M}$ invert: $\mathbf{M}_0 \to -\mathbf{M}_0$ and $\mathbf{M}_1 \to -\mathbf{M}_1$. The inversion of $\mathbf{M}_1$ can be justified as the sign of γ determines the precession direction of $\mathbf{M}$. Thus, a change from $\mathbf{M}_0 \to -\mathbf{M}_0$ also requires an inversion of $\mathbf{M}_1$. The same result is obtained when analyzing the high frequency susceptibility tensor in Appendix B. In contrast, $\mathbf{J}_1$, generated by the microwave field, is independent of the static magnetic field orientation: $\mathbf{J}_1 \to \mathbf{J}_1$. Inserting these relations into Eq. (3.26) yields

$$\mathbf{E}_{\mathrm{HD}}(-\mathbf{H}) = \frac{\Delta\rho}{M_{\mathrm{s}}^2}[\langle\mathbf{J}_1(-\mathbf{M}_1)\rangle(-\mathbf{M}_0)+\langle\mathbf{J}_1\times(-\mathbf{M}_1)\rangle\times(-\mathbf{M}_0)+\mu_0 R_{\mathrm{A}}\langle\mathbf{J}_1\times(-\mathbf{M}_1)\rangle =$$

$$= \underbrace{\frac{\Delta\rho}{M_{\mathrm{s}}^2}[\langle\mathbf{J}_1\mathbf{M}_1\rangle\mathbf{M}_0 + \langle\mathbf{J}_1\times\mathbf{M}_1\rangle\times\mathbf{M}_0]}_{\text{sign unchanged}} \underbrace{- \mu_0 R_{\mathrm{A}}\langle\mathbf{J}_1\times\mathbf{M}_1\rangle}_{\text{sign changed}}. \qquad (3.27)$$

A comparison with Eq. (3.26) shows that the part originating from the AMR remains unchanged under magnetic field inversion, whereas the part arising from the AHE reverses sign. This allows us to distinguish the different contributions to $\mathbf{E}_{\mathrm{HD}}$. Moreover, it is important to note that under magnetic field inversion, the calculated DC voltage generated by spin pumping (Eq. (3.21)) reverses sign. The different behavior of the term proportional to the AMR under field inversion and the different symmetry with respect to the resonance field of the term arising from the AHE will allow us to determine spin pumping and exclude microwave rectification as the origin of our experimental observations (see Sec. 3.4.2 and Appendix B).

This concludes the theoretical part of spin pumping as spin current source. In the following sections, our experiments in this field are discussed.

3.3 Experimental techniques and sample properties

First, the experimental setup and a typical measurement are explained. Subsequently, a brief overview of the different studied materials, their properties, and the actual sample fabrication is given.

3.3.1 Measurement technique

A sketch of the Bruker ESP300 setup used for FMR and spin pumping measurements is shown in Fig. 3.9(a). The microwave radiation with a fixed frequency of $\nu = 9.3\,\mathrm{GHz}$ (X-band) and a maximum power of $200\,\mathrm{mW}$ is generated by a Gunn diode and then transferred via waveguides and a circulator into a TE_{102} microwave resonator. Critical coupling between waveguide and resonator is achieved by a tunable iris. In tuned condition, the incident microwave is entirely absorbed within the resonator. If the sample is in resonance, it absorbs part of the radiation and thus detunes the cavity which leads to a partial reflection of the microwave radiation. The reflected part passes the circulator and is guided to the detector. A reference arm, connecting microwave source and detector, biases the detecting diode to improve sensitivity. Moreover, it enables to determine the phase of the microwave signal which allows to switch between absorption and dispersion experiments, corresponding to the measurement of the imaginary or the real part of the high-frequency susceptibility. All measurements within this thesis were performed in absorption.

The resonator is positioned between the poles of an electromagnet generating a DC magnetic field $0 \leq \mu_0 H_0 \leq 1\,\mathrm{T}$. $\mu_0 H_0$ is superimposed by a parallel AC magnetic field with a modulation frequency of $\nu_{\mathrm{mod}} = 100\,\mathrm{kHz}$ and a modulation amplitude of $0.4\,\mathrm{mT}$ or $0.8\,\mathrm{mT}$. A lock-in amplifier (Stanford Research SR830) which is sensitive
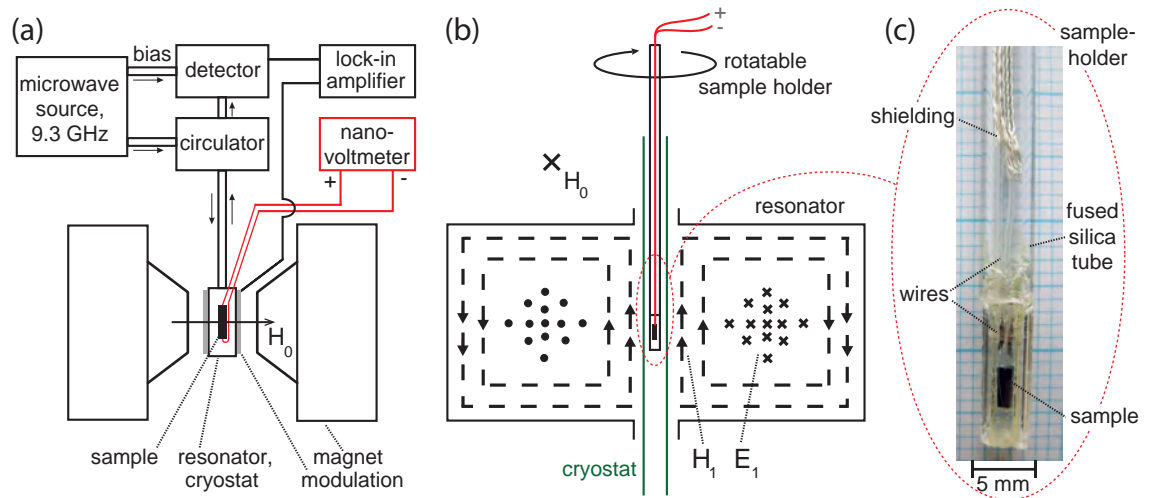
Figure 3.9: (a) Sketch of the measurement setup with microwave source, circulator, resonator, detector, lock-in amplifier, electromagnet and nanovoltmeter. (b) Sketch of the microwave resonator including field distribution, cryostat and rotatable sample holder. This sketch is rotated by 90° with respect to (a) [99]. (c) Photograph of the sample mounted on a fused silica sample holder with wires for DC measurements.
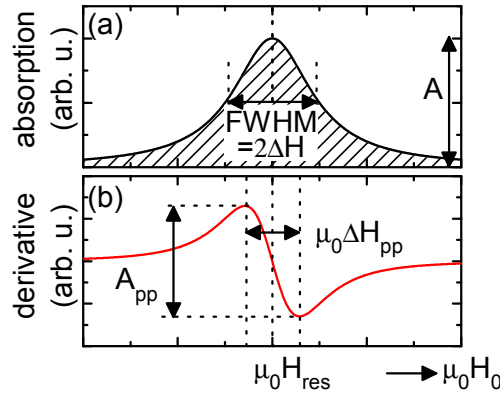
Figure 3.10: (a) Resonant absorption at $\mu_0 H_{\mathrm{res}}$ with a Lorentzian line shape, a full width at half maximum FWHM$=2\Delta H$, and an amplitude A. (b) First derivative of the Lorentzian absorption in (a) with peak-to-peak linewidth $\mu_0 \Delta H_{\mathrm{pp}}$ and amplitude A_{pp}.

only to signals modulated with ν_{mod} (and thus excludes random noise) is used for FMR signal detection. This measurement technique considerably improves detection sensitivity.

Figure 3.9(b) depicts a sketch of the resonator. The sample (black) is positioned at the center of the cavity in a node of the microwave electric field and an anti-node of the microwave magnetic field. It is surrounded by a He-flow cryostat which allows to adjust the sample temperature T between 2 K and 300 K.

The close up in Fig. 3.9(c) shows a photograph of a sample mounted on a fused silica sample holder. Great care was taken to position the sample surface exactly on the rotation axis of the holder. Up to four aluminum bond wires on the sample run into shielded coaxial wires that lead out of the cavity for DC measurements.

The DC voltage across the sample is detected via a Keithley Nanovoltmeter 2182. In all measurements, FMR and DC voltage are recorded simultaneously as a function of the static magnetic field $\mu_0 H_0$. Unless stated otherwise, the measurements are performed at a microwave power of 200 mW. This corresponds to $\mu_0 H_1 = 0.12$ mT as determined by separate paramagnetic resonance calibration experiments.

Due to the magnetic field modulation in combination with lock-in detection, the measured FMR signal does not correspond to a Lorentzian microwave absorption signal (Fig. 3.10(a)) but to its first derivative (Fig. 3.10(b)) [100]. The inflection point of the derivative of the Lorentzian function corresponds to the resonance field $\mu_0 H_{\mathrm{res}}$. From the difference in H_0 between maximum and minimum, referred to as peak-to-peak linewidth $\mu_0 \Delta H_{\mathrm{pp}}$, the precession cone angle of the magnetization at resonance Θ_{res} can be calculated as [101]

$$\Theta_{\mathrm{res}} = \frac{2H_1}{\sqrt{3}\Delta H_{\mathrm{pp}}} \tag{3.28}$$

with the microwave magnetic field H_1 at the sample position. The relation between the linewidth ΔH of the Lorentzian function and ΔH_{pp} of its derivative is given by

$$\Delta H_{\mathrm{pp}} = \frac{2}{\sqrt{3}}\Delta H. \tag{3.29}$$

3.3.2 Material properties and sample fabrication

The measurements presented in this chapter were performed with ferromagnet/ platinum (F/Pt) bilayer samples and with two types of tri-layer structures: ferromagnet 1/normal metal/ferromagnet 2 (F1/N/F2) and ferromagnet/normal metal 1/ normal metal 2 (F/N1/N2). For the F layer, Ni, Co, Fe, Co_2FeAl, Co_2FeSi, Fe_3O_4, and (Ga,Mn)As were used, and as normal metals Al or Pt were taken. In the following, some material properties relevant for the later experiments and their interpretation are briefly discussed. Furthermore, the respective fabrication method is stated.

$3d$-transition metal ferromagnets

Ni, Co and Fe exhibit band or itinerant ferromagnetism which originates from a spontaneous splitting of the energy bands in the crystal.

The polycrystalline films were deposited at the Walther-Meißner-Institute on oxidized silicon substrates via electron beam evaporation at a base pressure of 1×10^{-8} mbar.

Heusler compounds

Heusler compounds are ternary, intermetallic compounds with the chemical composition XYZ or X_2YZ where X and Y usually are transition metal elements and Z is a main group element [102, 103, 104]. This material class attracts a lot of attention as band structure calculations predict half-metallicity for certain compounds [105, 106, 107], making them interesting for spintronic applications. The compounds Co_2FeSi and Co_2FeAl, studied in this work are predicted to be half-metallic [108]. However, structural disorder, an important issue for Heusler compounds, destroys half-metallicity and drastically decreases spin polarization [109]. The mechanism of the ferromagnetic exchange interaction between the localized magnetic moments of the Co and Fe atoms is not clarified yet. For Co_2MnSi, one suggestion is that the magnetic moments of the Co and Mn atoms ferromagnetically couple via the direct exchange interaction [110, 111]. Another model comes to the conclusion that the localized magnetic moments are indirectly coupled via a RKKY interaction mediated by the free electrons of the system [112]. An overview on Co_2-based Heusler compounds can be found in Refs. [104, 113].

The epitaxial Heusler thin films studied within this thesis were prepared in the group of Andy Thomas by Inga-Mareen Imort at the University of Bielefeld. They were sputtered on (001)-oriented MgO single crystal substrates at an Ar pressure of 1.5×10^{-3} mbar followed by an annealing step in vacuum at 500°C [114].

Magnetite

For magnetite (Fe_3O_4) which exhibits a cubic inverse spinel structure at room temperature [115], half-metallicity is predicted [116]. Magnetite undergoes a structural phase transition, called Verwey transition, at $T_V \approx 120$ K [117] below which the crystal structure changes to monoclinic [118]. Among other things, this influences elec-

tric and magnetic properties (see e.g., Ref. [119]). For the charge transport above T_V, different models exist suggesting large polarons [120, 121], phonon-assisted electron hopping [122], or a superposition of small-polaron band and small-polaron hopping conduction [123] as the relevant mechanisms.

Epitaxial (001)- and (111)-oriented Fe_3O_4 films were grown at the Walther-Meißner-Institute via pulsed laser deposition in an argon atmosphere of $0.7\,\mu$bar with an energy density of $3.1\,\mathrm{J/cm^2}$ at a substrate temperature of $320°\,\mathrm{C}$ [124] on (001)-oriented MgO and (0001)-oriented Al_2O_3 substrates, respectively.

(Ga,Mn)As

$Ga_{1-x}Mn_xAs$ is one of the most widely studied dilute magnetic semiconductors with a Curie temperature of up to $190\,\mathrm{K}$ [125, 126, 127]. The ferromagnetism is achieved by doping GaAs with several percent of manganese atoms. This introduces both localized magnetic moments in the Mn $3d$-shell and itinerant holes as the Mn atoms are preferentially incorporated at Ga lattice sites [128]. As the origin of the exchange interaction, hopping of delocalized holes in the Mn-derived impurity band is suggested which mediates the ferromagnetic coupling of the Mn magnetic moments. This mechanism has been successfully described by a p-d exchange interaction in the Zener model. Further details can be found in Refs. [125, 129, 130] and references therein.

The $Ga_{1-x}Mn_xAs$ films studied within this thesis were grown in the group of Wolfgang Limmer by Wladimir Schoch at the University of Ulm. The films have a Mn concentration of $x = 0.04$ with respect to the Ga lattice sites and were grown via low temperature ($\sim 250\,°\mathrm{C}$) molecular beam epitaxy on semi-insulating (001)-oriented GaAs substrates. To improve crystalline quality a $30\,\mathrm{nm}$ thick high temperature GaAs buffer layer was grown prior to the actual (Ga,Mn)As deposition [131].

Normal metals

For most of the samples, Pt was used as normal metal as it acts as a good spin sink, due to its large spin flip probability $\epsilon \gtrsim 10^{-2}$ [8]. ϵ is defined as [8]

$$\epsilon = \frac{\tau_\mathrm{t}}{\tau_\mathrm{sf}} \tag{3.30}$$

with the momentum scattering time τ_t and the spin flip scattering time τ_sf. The large value of ϵ for Pt is due to its large atomic number ($Z = 78$) and the hybridization of the conduction electrons with the d orbitals leading to a large spin-orbit coupling and a large value of the spin Hall angle α_SH (see Sec. 2.3).

The second normal metal used, Al, is a less good spin sink ($\epsilon \lesssim 10^{-2}$ [8, 132]) which is mainly due to its small atomic number $Z = 13$. We used this material in tri-layer measurements as interlayer, separating the spin current generation in F from its detection in Pt.

The Pt films were deposited via electron beam evaporation at a base pressure of $1 \times 10^{-8}\,\mathrm{mbar}$ in the same chamber as the $3d$-transition metals.

The Al layer is deposited via Ar-ion sputtering at a pressure of 2.7×10^{-3} mbar. Note that the samples can be transferred between the electron-beam evaporation chamber and the sputtering chamber without breaking the vacuum.

Sample preparation

All ferromagnetic layers have a thickness of $t_\mathrm{F} = 10$ nm except for the (111)-oriented Fe_3O_4 film with $t_\mathrm{F} = 35$ nm and the (Ga,Mn)As films with $t_\mathrm{F} = 200$ nm, 175 nm, and 65 nm. As high-quality, transparent interfaces are crucial for spin pumping [133], all F layers used for bilayer structures were in situ covered with a 7 nm thick Pt layer, except the (Ga,Mn)As films which were covered after exposure to ambient atmosphere. The tri-layer samples were fabricated without breaking the vacuum.

Subsequently to the deposition, all samples were cut into rectangular bars (length $L = 3$ mm, width $w = 1$ mm or 2 mm) and contacted on the short sides via Al wedge bonding for electrical measurements as shown in Fig. 3.1.

3.4 Results and discussion

In this section, our spin pumping measurements are presented and discussed. We show that spin pumping is the origin of our DC signal, and that microwave rectification cannot explain our observations. Furthermore, some theory predictions concerning sample geometry and power dependence are experimentally proven. Subsequently, we show that the present theories for spin pumping are not limited to transition metal-based bilayers, but also apply to the ferromagnetic Heusler compounds Co_2FeAl and Co_2FeSi, the ferrimagnetic oxide spinel Fe_3O_4, and the dilute magnetic semiconductor (Ga,Mn)As. In addition, measurements taken not only at room temperature but down to 2 K and data taken at various angles of the external magnetic field are discussed. In this context, spin pumping from the spin wave excitations in (Ga,Mn)As/Pt is analyzed in detail. Finally, measurements on two types of heterostructures consisting of three different layers, F1/N/F2 and F/N1/N2, are discussed. The results of Secs. 3.4.7 and 3.4.9 were published on the preprint server and in Physical Review Letters [134, 135]. To simplify the notation, the static magnetic field H_0 is denoted as H in the following. We start with a phenomenological introduction to our measurements.

3.4.1 Experimental data

Figure 3.11 shows simultaneous measurements of FMR and DC voltage of a Ni/Pt bilayer for different orientations of the external magnetic field (in-plane: $\phi = 0°$ and 180°, and out-of-plane: $\phi = 90°$). The FMR traces of both in-plane orientations are
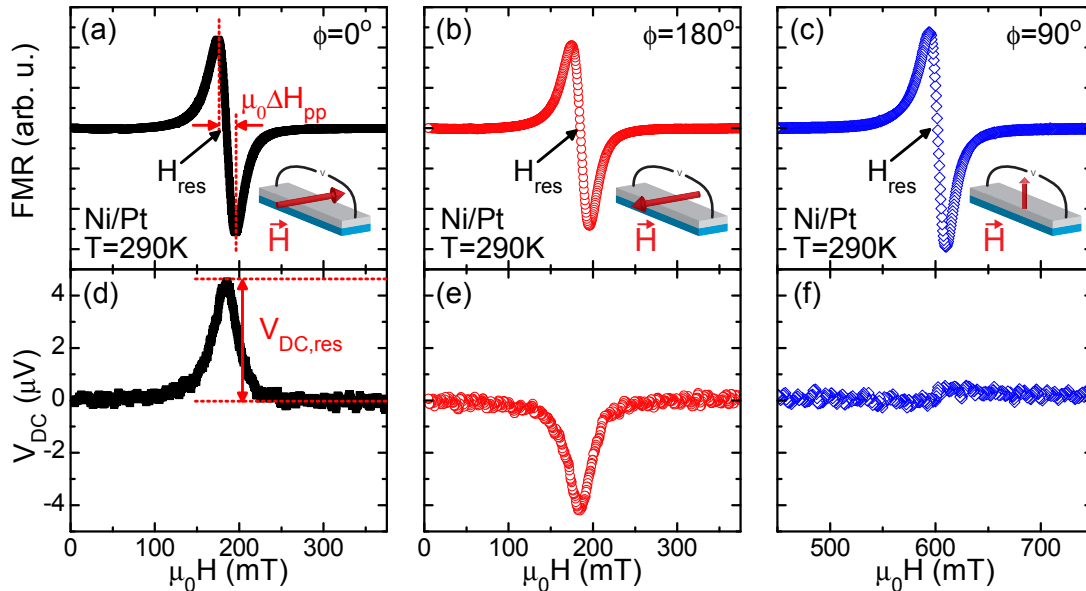
Figure 3.11: Simultaneously recorded FMR and V_{DC} traces for different orientations of the external magnetic field $\mu_0\mathbf{H}$. V_{DC} of both in-plane orientations (d,e) exhibits an extremum at H_{res}, the inflection point of the FMR. The sign of V_{DC}, however, changed from $\phi = 0°$ to 180°. For the out-of-plane orientation (c,f), no extremum in V_{DC} co-occurring with the FMR is observable. The peak-to-peak linewidth $\mu_0\Delta H_{pp}$ of the FMR and the DC voltage at resonance $V_{DC,res}$ used in the later analysis are exemplarily indicated in (a,d).

identical with a resonance field of $\mu_0 H_{res} = 185\,\text{mT}$ (Figs. 3.11(a,b)), whereas the resonance position for $\phi = 90°$ is shifted to a higher value ($\mu_0 H_{res} = 602\,\text{mT}$) due to the demagnetization field. The simultaneously recorded V_{DC} traces for the two in-plane orientations show one clear extremum with a magnitude of several μV at H_{res} (Figs. 3.11(d,e)) with the sign changing between $\phi = 0°$ and $180°$. The DC voltage recorded for $\phi = 90°$ does not exhibit an extremum.

We have not only investigated Ni/Pt bilayers but also several other F/Pt samples as shown in Fig. 3.12. A selection of FMR and V_{DC} spectra, recorded for two magnetic field orientations in the film plane is shown: $\phi = 0°$ corresponds to $\mathbf{H}$ parallel to $\hat{\mathbf{x}}$ (black full squares) while for $\phi = 180°$ $\mathbf{H}$ is antiparallel to $\hat{\mathbf{x}}$ (red open circles). For the epitaxially grown films, $\phi = 0°$ corresponds to $\mathbf{H}$ along [100] for (001)-oriented Fe_3O_4, along [1-10] for (111)-oriented Fe_3O_4 and along [110] for (Ga,Mn)As. All measurements in Fig. 3.12 were taken at $290\,\text{K}$ except for the (Ga,Mn)As data recorded
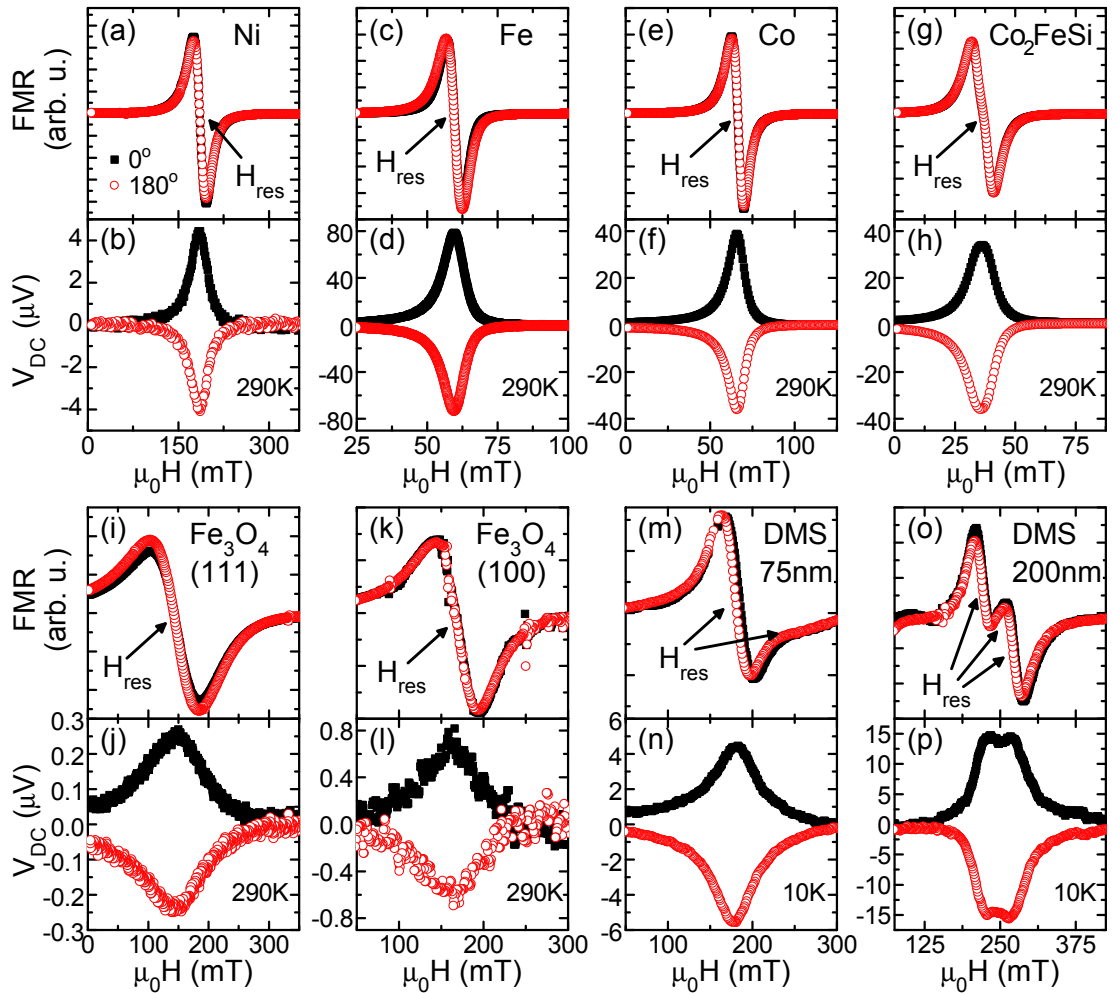
Figure 3.12: (a,c,e,g,i,k,m,o) FMR signal for different F/Pt bilayers recorded for $\mathbf{H}$ oriented in the film plane, parallel (full black squares) and antiparallel (open red circles) to $\hat{\mathbf{x}}$. The traces for both orientations superimpose in each case. (b,d,f,h,j,l,n,p) DC voltage measured simultaneously to the FMR. Upon magnetic field inversion, a sign change is observed.

at $T = 10\,\mathrm{K}$ (Figs. 3.12(m-p)). Since the FMR is invariant with respect to magnetic field inversion, the FMR traces for $\phi = 0°$ and $\phi = 180°$ should superimpose as is indeed observed in the experiment. The FMR signal of all samples in Fig. 3.12 consists of a single resonance line with the exception of (Ga,Mn)As in which several standing spin wave modes contribute to the FMR spectrum [136, 137]. All V_{DC} traces show one clear extremum at H_{res}; only in (Ga,Mn)As several V_{DC} extrema corresponding to the spin wave modes can be discerned. The magnitude of V_{DC} ranges from a few $100\,\mathrm{nV}$ in Fe_3O_4 to a few $10\,\mu\mathrm{V}$ in Co, Fe and Co_2FeSi. In contrast to the FMR, the extremum in V_{DC} changes sign when the magnetic field is reversed. It also is important to note that V_{DC} always has a maximum ($V_{\mathrm{DC}} > 0$) for $\phi = 0°$, whereas always a minimum ($V_{\mathrm{DC}} < 0$) is observed for $\phi = 180°$.

3.4.2 Interpretation of the DC voltage

As already discussed in the theory section (Sec. 3.2), microwave rectification and spin pumping in combination with the inverse spin Hall effect can generate a DC voltage co-occurring with FMR. In this section, we show that spin pumping is the origin of the DC voltage observed in our experiments.

3.4.2.1 Microwave rectification

As discussed in Sec. 3.2.6, the DC voltage generated by microwave rectification (Eq. (B.23)) obtained from the calculations detailed in Appendix B reads

$$V_{\mathrm{HD,y}} = \pm \frac{1}{2}\, E_1 L H_1 \left(\frac{\Delta\rho}{\rho} A_{\mathrm{yy}} \mathrm{L_{abs}} + \frac{\mu_0 R_{\mathrm{A}} M_{\mathrm{s}}}{\rho} A_{\mathrm{yz}} \mathrm{L_{dis}} \right) \qquad (3.31)$$

with a prefactor proportional to the length L of the sample and to the product $E_1 H_1$. Thus, as mentioned above, $V_{\mathrm{HD,y}} \equiv 0$ if the sample is positioned exactly at the center of the microwave cavity with $E_1 = 0$. When we consider the situation where the sample is positioned slightly off center with $E_1 \neq 0$, a DC voltage can be generated. The sum in Eq. (3.31) contains two terms, the first proportional to the anisotropic magnetoresistance (AMR) ratio $\Delta\rho/\rho$ which has the lineshape of a Lorentzian absorption function ($\mathrm{L_{abs}}$), and the second originating from the anomalous Hall effect, proportional to $\mu_0 R_{\mathrm{A}} M_{\mathrm{s}}/\rho$ with the lineshape of the derivative of a Lorentzian function, called dispersion ($\mathrm{L_{dis}}$). The exact descriptions of the parameters A_{yy}, $\mathrm{L_{abs}}$, A_{yz} and $\mathrm{L_{dis}}$ are given in Appendix B.

Figure 3.13(a) shows both terms of Eq. (3.31) (black dotted line: term proportional to the AMR and blue dotted line: term proportional to the AHE). As the DC voltages observed in our measurements (see Figs. 3.11 and 3.12) have the lineshape of a Lorentzian absorption function, only the part proportional to the AMR could be its origin. However, as discussed in Sec. 3.2.6.2, under inversion of the external static magnetic field **H**, only the part proportional to the AHE reverses sign. The AMR term remains unchanged (Figs. 3.13(a,b)). This excludes microwave rectification due to AMR or AHE as the origin of our signal. Moreover, if microwave rectification was the origin, our measurements should scale with the magnitude and
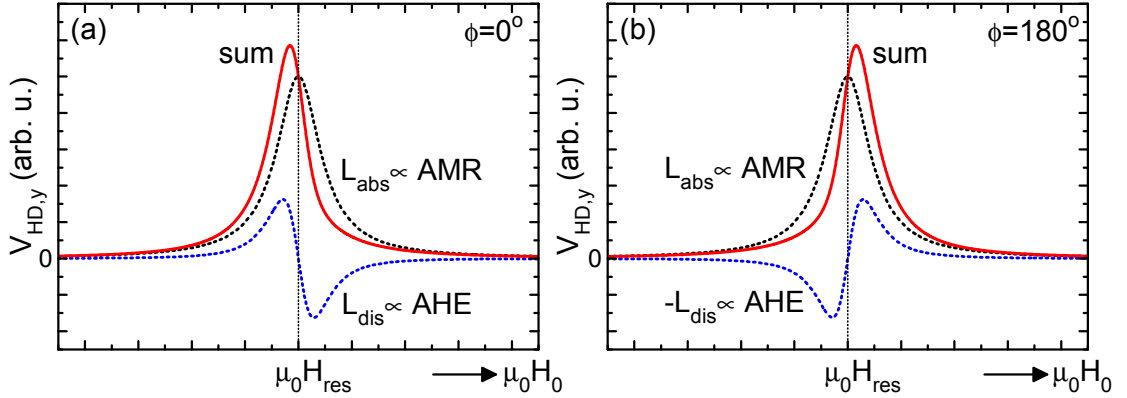
Figure 3.13: $V_{HD,y}$ split into the part proportional to the AMR (black) and to the AHE (blue) versus applied static field H. The two parts exhibit a different lineshape. The sum of both contributions is drawn as red line. (b) Situation after an inversion of **H** ($\phi = 180°$). The part proportional to the AMR remains unchanged, whereas the sign of the AHE part is changed.

sign of $\Delta\rho/\rho$ and $\mu_0 R_A M_s/\rho$. Table 3.1 lists these quantities for a selection of investigated ferromagnets. Their values vary by orders of magnitude and even the sign is different between the materials. This contradicts the experimental findings (see Fig. 3.12) that for $\phi = 0°$ a maximum in V_{DC} appears for all measured ferromagnet/Pt samples. Moreover, the scaling plot discussed in Sec. 3.4.7 cannot be explained with the values listed in Table 3.1.

   Another reason making microwave rectification extremely unprobable was given by Mosendz *et al.* [133]. They introduced a tunnel barrier between the F and the N layer. If microwave rectification was the origin of V_{DC}, no change should be observed. However, in their experiments, they found a suppression of V_{DC}. This can be explained in spin pumping theory. Due to the tunnel barrier, no spin current can enter the Pt layer, and thus, no charge current can be generated by the inverse spin Hall effect. We performed similar experiments (see Sec. 3.4.13), where a thin Al layer causing interface scattering was introduced between the F layer and Pt. In this case, also a drastic decrease of the signal was observed.

Table 3.1: Resistivity anisotropy ratio $\Delta\rho/\rho$ and $\mu_0 R_A M_s/\rho$ for different materials. *$T = 4\,K$, **$J \parallel [100]$, *** $J \parallel [100]$ and $T = 4.2\,K$.

	$\Delta\rho/\rho$ (10^{-2})	$\mu_0 R_A M_s/\rho$ (10^{-4})
Ni	2.5 [93]	-3.5 [93]
Co	3.0 [93]	10.7 [93]
Fe	0.8 [93]	40-100 [93]
Co_2FeAl	-0.13 [138]	113 [138]
Co_2FeSi	-0.8* [139]	58.3 [140]
Fe_3O_4 (001)	0.4** [141]	-31.5 [142]
(Ga,Mn)As	-5.0*** [143]	932*** [143]

In addition, Inoue *et al.* [98] observed that if the sample is positioned in a region of the microwave cavity where $E_1 \neq 0$, a DC voltage due to microwave rectification is measured. However, the lineshape is of the dispersion type and thus can't be the origin of V_{DC} observed in our experiments. It can be superimposed to the spin pumping signal which then leads to an asymmetry with respect to $\mu_0 H_{\mathrm{res}}$ in the DC voltage spectrum. We minimize this effect by carefully locating the sample in a node of the microwave electric field.

To summarize, the effect of microwave rectification can be excluded as the origin of the DC voltage observed in our experiments due to the reasons given above.

3.4.2.2 Spin pumping

In contrast, spin pumping in combination with the inverse spin Hall effect will account for the extrema in V_{DC} shown in Figs. 3.11 and 3.12 [7, 9, 71]. The spin pumping mechanism naturally explains that V_{DC} changes sign when the orientation of $\mathbf{H}$ is inverted from $\phi = 0°$ to $180°$. As $\mathbf{H}$ determines the spin orientation $\hat{\mathbf{s}}$ in Eq. (2.15) ($\mathbf{J}_c \propto (\hat{\mathbf{z}} \times \hat{\mathbf{s}})$), $\mathbf{J}_c$ and consequently also V_{DC} reverse if the magnetic field is inverted. For $\phi = 90°$ (Figs. 3.11(c,f)), $\hat{\mathbf{s}}$ is parallel to $\hat{\mathbf{z}}$ which results in zero for the cross product, and no DC voltage is expected. Furthermore, the experimental observation that V_{DC} invariably has the same polarity for a given field orientation ϕ irrespective of the ferromagnetic material used in the F/Pt bilayer is fully consistent with spin pumping theory. Not the polarization of the conduction electrons or the type of carriers is relevant but only the magnetization relaxation process [7, 8, 9, 10, 11, 144]. We thus attribute V_{DC} in our experiments to spin pumping.

3.4.3 Magnetization dynamics – Spin pumping

Magnetization dynamics was predicted as the origin of the spin pumping voltage (see Sec. 3.2.3). This implies that microwave absorption, a measure of the magnetization excitation, and the spin pumping voltage are closely related. Indeed, when integrating the FMR to recover the absorption line, and plotting this together with the measured DC voltage, a perfect agreement is obtained (Fig. 3.14). No shift with respect to the magnetic field can be observed and both lineshapes are identical within measurement uncertainty. This confirms that the origin of V_{DC} is magnetization dynamics.

3.4.4 Geometry dependence of the spin pumping signal

A further prediction of the spin pumping theory in combination with the inverse spin Hall effect can be seen from Eq. (3.21): the generated voltage should be independent of the sample width w but proportional to its length L. These correlations have technological relevance as they predict that a clever sample layout enables to drastically increase the obtained DC voltage without enlarging the sample. This can
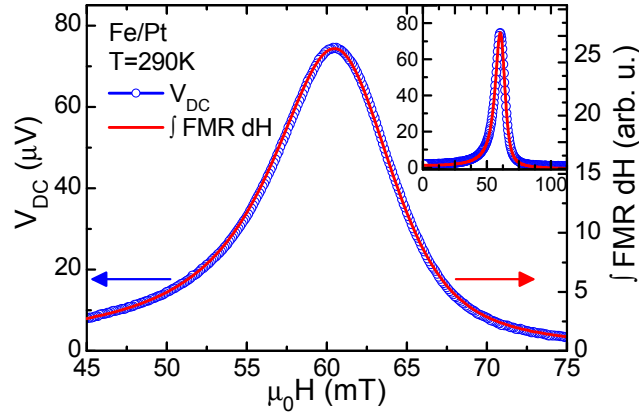
Figure 3.14: DC voltage and integrated FMR of a Fe/Pt bilayer versus the external
DC magnetic field H. Both traces match very well. The inset shows both signals
over a larger range.

be achieved by decreasing w and connecting multiple narrow stripes as discussed be-
low. Moreover, it enables to quantify even small spin Hall angles as demonstrated
in Ref. [9]. However, so far, these predictions have not been proven experimentally.

First, the voltage dependence on the width w of the sample is studied. We compare
FMR and V_{DC} measurements of two Fe/Pt bilayers with $w = 1\,\mathrm{mm}$ and $w = 100\,\mu\mathrm{m}$,
both having $L = 3\,\mathrm{mm}$ (Fig. 3.15). The intensities of the FMR signals (Fig. 3.15(a))
are normalized to compensate for the different sample volumes in the cavity. Clearly,
the two traces are identical as are the V_{DC} traces. The magnitude of V_{DC} at resonance
is identical for both samples although their width differs by a factor of ten. Thus,
V_{DC} is independent of the sample width w, confirming the theory (Eq. (3.21)).

To investigate the dependence of V_{DC} on the length L, a plain Fe/Pt film was
patterned via argon ion etching into four parallel stripes of width $w = 100\,\mu\mathrm{m}$
and length $L_0 = 3\,\mathrm{mm}$. The stripes are connected via aluminum bond wires as
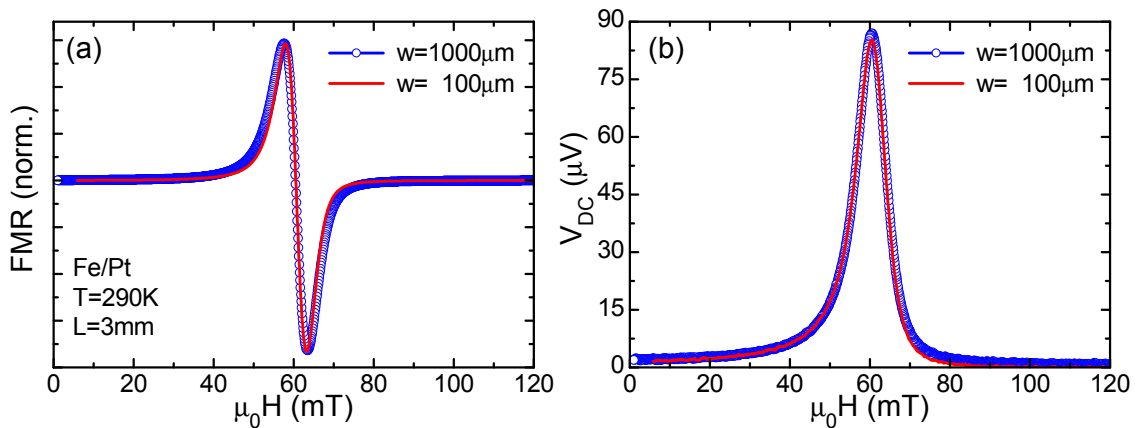
Figure 3.15: FMR and V_{DC} for two Fe/Pt samples of different width w. (a) The
normalized FMR of both samples are identical. (b) The magnitude of V_{DC} is
independent of the sample width.
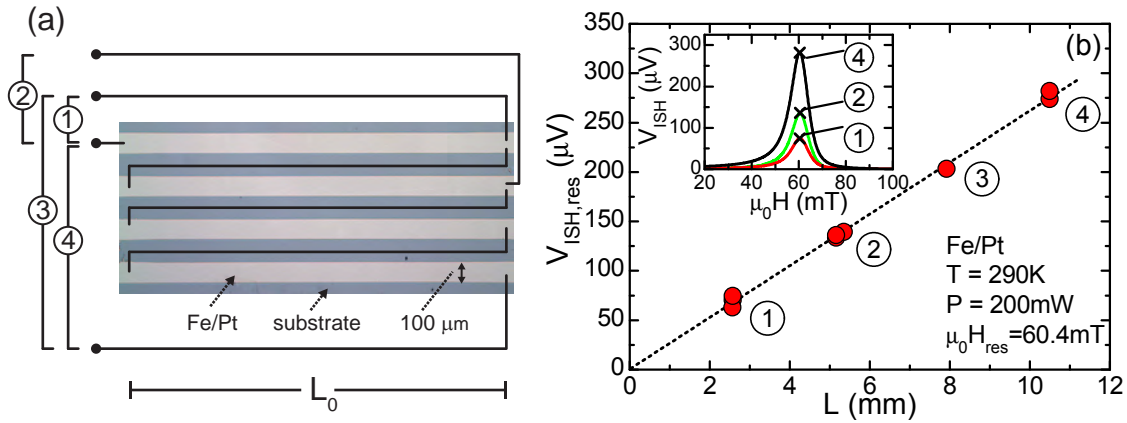
Figure 3.16: (a) Photograph of the four $100\,\mu$m wide Fe/Pt stripes patterned onto the Si/SiO$_x$ substrate with a sketch of the different contacting configurations labeled by the number of measured stripes. (b) $V_{\text{ISH,res}}$ extracted at the resonance field $\mu_0 H_{\text{res}} = 60.4\,$mT for different lengths L. The inset shows V_{DC} versus H between different contacts.

sketched in Fig. 3.16(a). The sensing leads are attached in a way that the voltages generated by a different amount of stripes (numbers in Fig. 3.16(a)) can be measured simultaneously. The results are presented in Fig. 3.16(b). The entire V_{DC} traces for one, two and four stripes are shown in the inset. More stripes ($L > L_0$) generate a larger DC voltage. For a quantitative analysis, the measured DC voltage at the resonance field $V_{\text{DC,res}} = V_{\text{ISH,res}}$ is plotted versus the effective length L of the Fe/Pt bilayer. Clearly, the measured points can be connected via a straight line through the origin. This proves the prediction of a linear dependence between V_{DC} and L (Eq. (3.21)).

These results open the door to new sample designs which allow to significantly increase the generated DC voltage. In many measurement setups, the homogeneity of the field distribution is the limiting factor for the sample size. Our results show that many parallel, narrow wires can be placed on a given sample dimension and that, if they are connected to each other as indicated in Fig. 3.16(a), the expected voltage is the voltage of one stripe multiplied by the number of stripes. This allows to quantify even very small spin Hall angles of various normal metals.

3.4.5 Power dependence

In this section, we investigate the dependence of the DC voltage on the microwave power P_{MW}. Figures 3.17 (a,b) show various simultaneously recorded FMR and V_{DC} traces of a Fe/Pt sample for microwave powers in the range of $0.2\,$mW $\leq P_{\text{MW}} \leq 200\,$mW. Assuming that the origin of V_{DC} is spin pumping in combination with the inverse spin Hall effect as suggested by theory (Sec. 3.2.3), Eq. (3.21) should describe the DC voltage. A variation of P_{MW} does not influence material properties, sample geometry or microwave frequency so that these parameters can be represented by
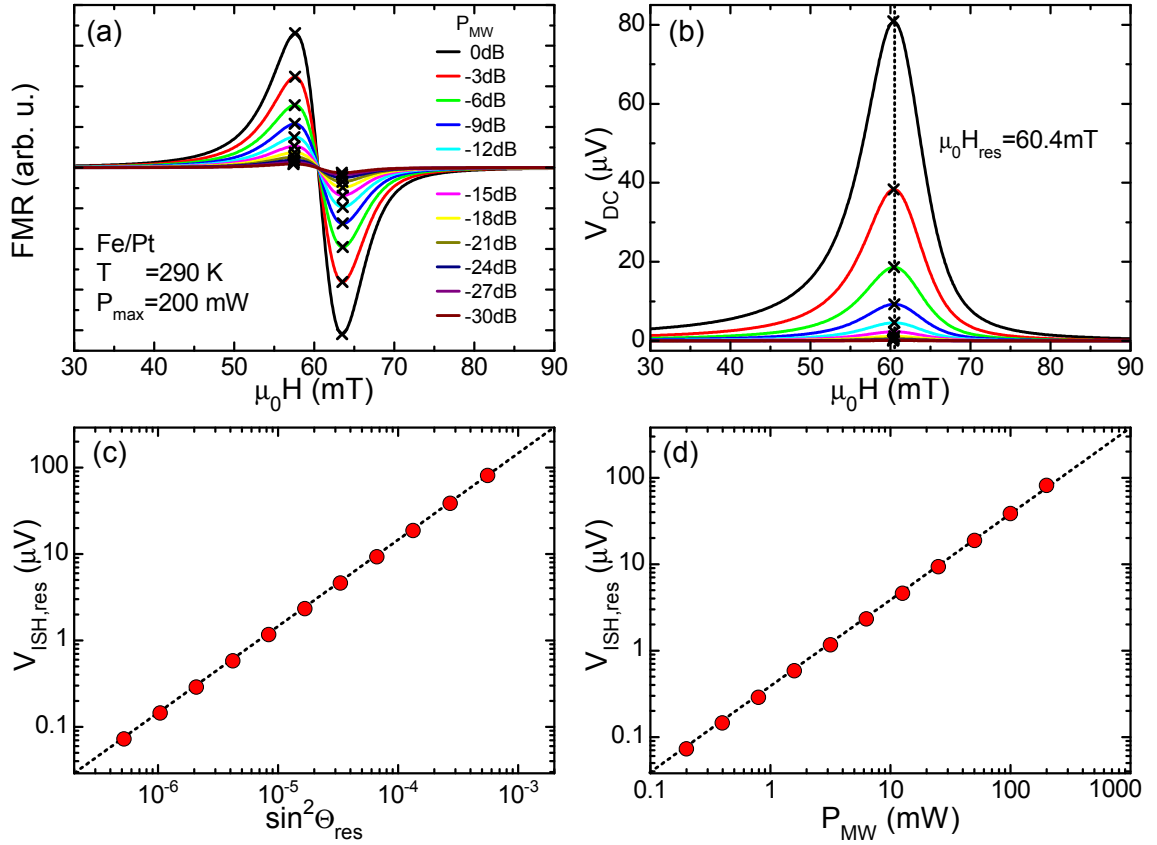
Figure 3.17: (a,b) Power dependence of FMR and V_{DC}. The microwave power is given in units of dB with respect to the maximum value of 200 mW. The crosses indicate the extracted values used in the further analysis. (c) The experimentally observed linear dependence of $V_{ISH,res}$ and $\sin^2 \Theta_{res}$ corroborates the present theory of spin pumping in combination with the inverse spin Hall effect as the origin of the DC voltage. (d) $V_{ISH,res}$ versus microwave power P_{MW}. The linear dependence is expected in the small angle approximation.

one single constant

$$A := \frac{e \left[\alpha_{SH} \lambda_{SD} \tanh \frac{t_N}{2\lambda_{SD}} \right]}{\sigma_F t_F + \sigma_N t_N} g^{\uparrow\downarrow} \nu_{MW} P L \tag{3.32}$$

which reduces Eq. (3.21) to

$$V_{ISH} = A \cdot \sin^2 \Theta. \tag{3.33}$$

Thus, disregarding saturation effects, $V_{ISH,res}$ should be directly proportional to $\sin^2 \Theta_{res}$. In Fig. 3.17(c), the DC voltage at ferromagnetic resonance $V_{DC,res} = V_{ISH,res}$, extracted from Fig. 3.17(b), is plotted versus $\sin^2 \Theta_{res}$. The magnetization precession cone angle at resonance $\sin^2 \Theta_{res}$ is given by Eq. (3.28) with the microwave magnetic field

$$H_1 = H_{1,\,200\,mW} \sqrt{\frac{P}{200\,mW}}, \tag{3.34}$$

where $H_{1,\,200\,\mathrm{mW}} = 0.12\,\mathrm{mT}$ as determined in paramagnetic resonance calibration experiments. All measured values lie on a straight line confirming the linear relation expected from Eq. (3.33). This confirms that, within measurement uncertainty, A is a constant, and, more importantly, it corroborates spin pumping theory. Furthermore, the linear dependence in Fig. 3.17(c) up to the maximum precession cone angle of $1.35\,°$, which is among the largest measured within this thesis, assures that all measurements performed here are in the linear regime and not limited by FMR saturation effects.

In previous publications (Refs. [10, 98]), a linear dependence between $V_{\mathrm{ISH,res}}$ and the microwave power P_{MW} was observed. We obtain the same result after further simplifications: Equation (3.28) shows that Θ_{res} is proportional to $1/\Delta H_{\mathrm{pp}}$ and to the microwave magnetic field H_1. ΔH_{pp} is virtually independent of P_{MW}, and H_1 is proportional to $\sqrt{P_{\mathrm{MW}}}$. This leads to $V_{\mathrm{ISH,res}} \propto \sin^2\left(\mathrm{const.}\cdot\sqrt{P_{\mathrm{MW}}}\right)$. Using the small angle approximation ($\sin\alpha \approx \alpha$) yields

$$V_{\mathrm{ISH,res}} \propto P_{\mathrm{MW}}. \tag{3.35}$$

Figure 3.17(d) shows the measured values of $V_{\mathrm{ISH,res}}$ versus P_{MW}. The straight line, representing Eq. (3.35), describes the experimental data quite well which confirms theory and justifies the small angle approximation for the range of P_{MW} used within this thesis.

3.4.6 Temperature dependence

To our knowledge, up to now, all spin pumping measurements in combination with the inverse spin Hall effect have been performed at room temperature. However, temperature might affect various parameters involved in our measurements, such as magnetic anisotropy, spin Hall angle, exchange interaction, or sample conductivity which makes such temperature dependent studies attractive. In this section, experimental FMR and V_{DC} spectra for several bilayer samples measured at different temperatures under an angle of $\phi = 0°$ are presented. The results are interpreted in Secs. 3.4.7 and 3.4.9. All temperature variations were performed at zero magnetic field, and all measurements were only started after the temperature had stabilized.

As representatives for $3d$-transition metals, Fig. 3.18 displays data of a Fe/Pt and a Co/Pt sample recorded for a series of temperatures $2\,\mathrm{K} \leq T \leq 290\,\mathrm{K}$. The original spectra for FMR and V_{DC} are shown in Figs. 3.18(a-d). For both samples, the resonance field of the FMR, H_{res}, and the field at which the maximum in V_{DC} occurs, $H_{\mathrm{DC,max}}$, shifts to lower H with decreasing T. Fig. 3.18(e) demonstrates for Fe/Pt and Fig. 3.18(f) for Co/Pt that $\mu_0 H_{\mathrm{res}}$ (full circles) and $\mu_0 H_{\mathrm{DC,max}}$ (open triangles) are indeed identical, for all T. With varying temperature, also the peak-to-peak linewidth $\mu_0\Delta H_{\mathrm{pp}}$ of the FMR (full circles) and the DC voltage at resonance $V_{\mathrm{ISH,res}}$ (open triangles) change as shown in Figs. 3.18(g,h). For the Fe/Pt sample, $\mu_0\Delta H_{\mathrm{pp}}$ increases from $5.9\,\mathrm{mT}$ at $290\,\mathrm{K}$ to $14.5\,\mathrm{mT}$ at $2\,\mathrm{K}$, whereas $V_{\mathrm{ISH,res}}$ decreases in magnitude from $72.3\,\mu\mathrm{V}$ at $290\,\mathrm{K}$ to $5.6\,\mu\mathrm{V}$ at $2\,\mathrm{K}$. For the Co/Pt bilayer sample, the evolution of $\mu_0\Delta H_{\mathrm{pp}}$ and $V_{\mathrm{ISH,res}}$ is qualitatively analogous to Fe/Pt with the
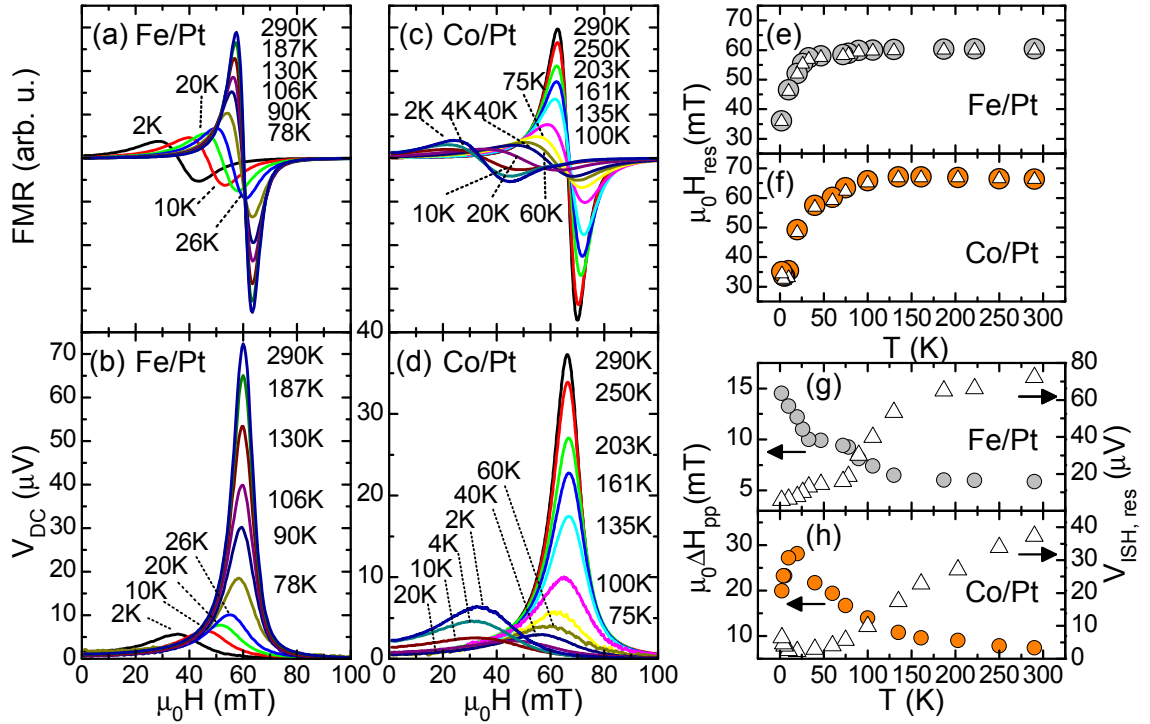
Figure 3.18: Temperature dependence of FMR and V_{DC} for (a,b) Fe/Pt and (c,d) Co/Pt samples. (e,f) With decreasing T, the resonance field $\mu_0 H_{res}$ (full circles) and $\mu_0 H_{DC,max}$ (open triangles) simultaneously shift to lower fields for both bilayers. (g,h) Temperature dependence of the extracted peak-to-peak linewidth $\mu_0 \Delta H_{pp}$ and the inverse spin Hall voltage at resonance $V_{ISH,res}$.

difference that an extremum occurs at around 20 K: the linewidth reaches a maximum (28.1 mT) and decreases for further decreasing T, and $V_{ISH,res}$ has a minimum (2.2 μV) before increasing slightly.

A shift and a broadening of the FMR-line with decreasing T were previously observed for Fe thin films [145, 146]. Both effects are attributed to temperature dependent inhomogeneous strain changing the magnetic anisotropy of the ferromagnetic film and the saturation magnetization. Further details can be found in Refs. [145, 146].

Additional measurements below room temperature were performed on three different epitaxially grown F/Pt bilayer samples, where (001)- and (111)-oriented Fe_3O_4 and (001)-oriented (Ga,Mn)As are used as F layers (Fig. 3.19). The FMR for (001)-Fe_3O_4/Pt exhibits a linewidth of around 50 mT and its intensity reduces with decreasing temperature until it entirely vanishes between 100 K and 93 K. This might be due to the Verwey transition and was previously observed in similar samples [147]. The additional sharp features around 150 mT originate from paramagnetic resonances of the MgO substrate. In analogy to the FMR, also the co-occurring peak in V_{DC} (Fig. 3.19(b)) vanishes between 100 K and 93 K. The FMR of the (111)-Fe_3O_4/Pt sample (Fig. 3.19(c)) with a linewidth of around 80 mT at 290 K changes only slightly between 290 K and 172 K. For lower temperatures, strong changes are observed. The FMR trace taken at 110 K has a decreased linewidth of 60 mT and
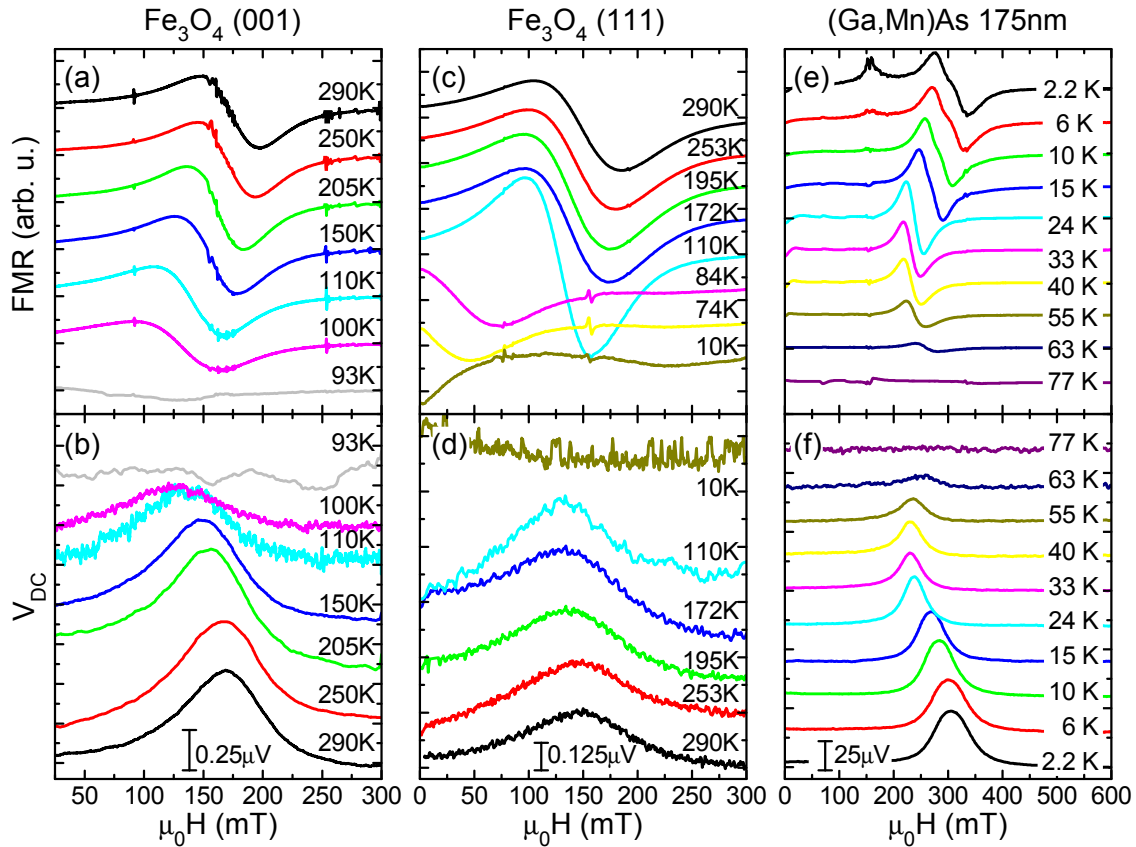
Figure 3.19: (a-d) FMR and V_{DC} of (001)- and (111)-oriented Fe_3O_4/Pt bilayers. For Fe_3O_4 (001) the FMR and thus also V_{DC} vanish below 100 K. (e,f) FMR and V_{DC} traces of a 175 nm thick (Ga,Mn)As film taken at different temperatures. The additional peak at 155 mT in (e) is caused by the sample holder and does not have a correspondence in V_{DC}. For $T \geq 77$ K, the FMR and the peak in V_{DC} vanish.

the resonance positions of the FMR traces taken below 110 K shift to very low values prohibiting an analysis. The corresponding DC voltages shown in Fig. 3.19(d) exhibit a maximum at the resonance position of the FMR down to 110 K. For lower temperatures (110 K > T > 10 K), a strongly increased noise prevented the analysis of V_{DC}.

FMR and V_{DC} of the (Ga,Mn)As/Pt sample with $t_F = 175$ nm are shown in Figs. 3.19(e,f). The most intense FMR-line is observed in the measurement at 2.2 K. With increasing temperature, the FMR intensity decreases, until it completely vanishes around the Curie temperature of ca. 77 K. Analogously to the FMR, also the maximum in V_{DC} decreases in magnitude with increasing T, until at 77 K no peak is observable anymore.

As the FMR of (Ga,Mn)As displays spin wave modes, a straightforward extraction of the peak-to-peak linewidth and of $V_{DC,res}$ is not possible. Therefore, both FMR and V_{DC} traces were fitted by Lorentzian lines as shown in Fig. 3.20. Hereby, the same resonance positions and linewidths were used both for FMR and V_{DC}. Two Lorentzian lines were required to reproduce the data taken at 2.2 K and 10 K, whereas one line was sufficient for higher temperatures.
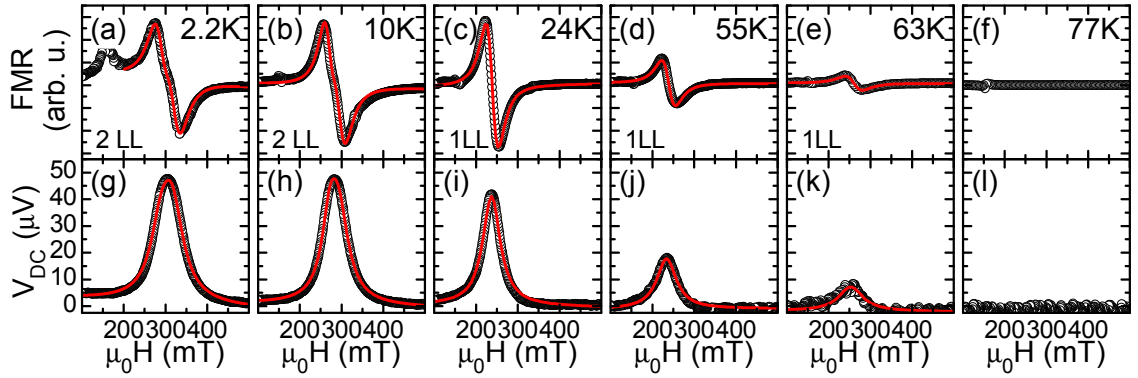
Figure 3.20: FMR and V_{DC} of a (Ga,Mn)As/Pt sample with $t_F = 175\,\text{nm}$ taken at different temperatures. The black circles represent the measurements and the red lines are the result of the fitting process with one (1LL) or two (2LL) Lorentzian lines. With increasing temperature, both FMR and V_{DC} decrease in magnitude. At 77 K neither FMR nor V_{DC} show structure. For the fit of FMR and V_{DC}, the same resonance position(s) and linewidth(s) were used.

3.4.7 Scaling behavior

In order to quantitatively compare our experimental data of the different F/Pt bilayers with spin pumping theory, we start from Eq. (3.21) for the inverse spin Hall voltage V_{ISH} arising due to spin pumping in F/N bilayers:

$$V_{ISH} = \frac{e\left[\alpha_{SH}\lambda_{SD}\tanh\frac{t_N}{2\lambda_{SD}}\right]g^{\uparrow\downarrow}}{\sigma_F t_F + \sigma_N t_N}\,\nu_{MW}PL\sin^2\Theta.$$

Since for all our bilayer samples, Pt with $t_N = 7\,\text{nm}$ is used as normal metal,

$$C := \alpha_{SH}\lambda_{SD}\tanh(t_N/2\lambda_{SD}) \tag{3.36}$$

is a constant at a given temperature. Moreover, the theoretical models for the spin mixing conductance [7, 79, 81] suggest that $g^{\uparrow\downarrow}$ of conductive ferromagnet/normal metal interfaces is determined mainly by the N layer, i.e., the Pt layer in our case. $g^{\uparrow\downarrow}$ thus should be of comparable magnitude in all our samples. Since the Pt conductivity dominates the F/N bilayer conductivity, in particular in samples with small σ_F such as Fe_3O_4 or (Ga,Mn)As, it also appears reasonable to assume that $\sigma_F t_F + \sigma_N t_N$ will be similar in all our samples. We thus expect a universal scaling behavior

$$\frac{V_{ISH}}{\nu_{MW}PL} = K\,\sin^2\Theta \tag{3.37}$$

in all F/Pt bilayers made from conductive ferromagnets. Hereby, Eq. (3.37) is universal in the sense that

$$K := \frac{e\,C g^{\uparrow\downarrow}}{\sigma_F t_F + \sigma_N t_N} \tag{3.38}$$

is virtually independent of the ferromagnetic material, its magnetic properties, or the details of the charge transport mechanism such as band conduction or charge carrier
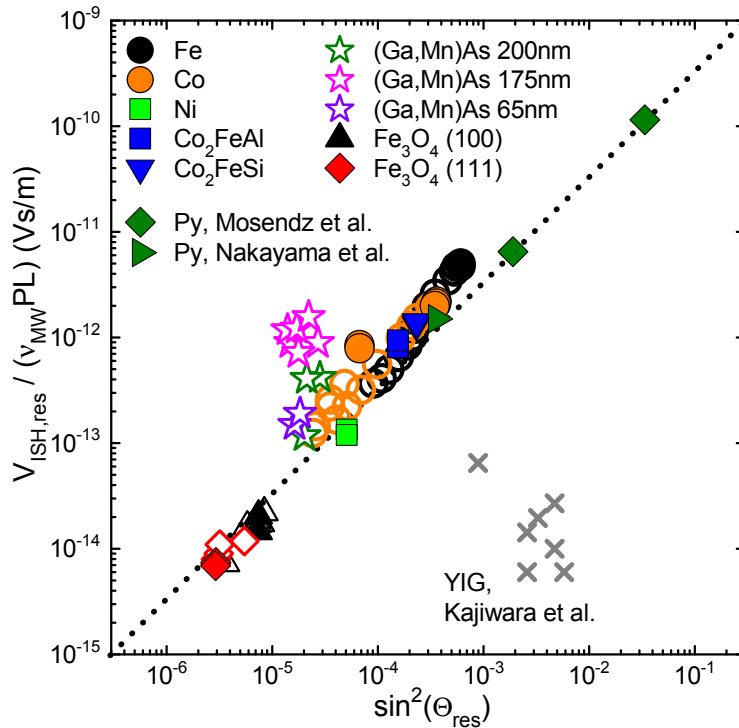
Figure 3.21: In all F/Pt bilayers made from conductive ferromagnets, $V_{\mathrm{ISH,res}}/(\nu_{\mathrm{MW}}PL)$ induced by a collective mode FMR scales with $\sin^2\Theta_{\mathrm{res}}$ with a universal prefactor. Full symbols represent data taken at $290\,\mathrm{K}$, open symbols correspond to data measured at lower T. The line is a guide to the eye. The permalloy (Py) and YIG data are taken from Refs. [9, 10, 42, 148].

hopping. Note that apart from the factor $\nu_{\mathrm{MW}}PL$, the constant K is identical to the constant A introduced during the analysis of the power dependence (Sec. 3.4.5). Here, however, K is assumed to be constant for different F/Pt samples, whereas A was identical for all power dependent measurements on a single sample.

Now, we test the scaling relation of Eq. (3.37) against our experimental data. At ferromagnetic resonance, the magnetization precession cone angle is given by Eq. (3.28) with the microwave magnetic field $H_1 = 0.12\,\mathrm{mT}$. We extract the FMR peak-to-peak line width ΔH_{pp} from the experimental data and use the measured DC voltage $V_{\mathrm{DC,res}}$ at H_{res} to determine $V_{\mathrm{ISH,res}} = V_{\mathrm{DC,res}}$ (see Fig. 3.11).

Figure 3.21 shows $V_{\mathrm{ISH,res}}/(\nu_{\mathrm{MW}}PL)$ versus $\sin^2\Theta_{\mathrm{res}}$ thus obtained. Full symbols indicate data measured at $290\,\mathrm{K}$, while measurements at lower temperatures are shown as open symbols and are discussed in Sec. 3.4.9. Data for permalloy/Pt extracted from Refs. [9, 10, 148] are also included in the figure. As evident from Fig. 3.21, $V_{\mathrm{ISH,res}}/(\nu_{\mathrm{MW}}PL)$ of all F/Pt bilayers made from conductive ferromagnets condense on a single, universal line when plotted against $\sin^2\Theta_{\mathrm{res}}$. This universal behavior is observed over more than four orders of magnitude in $V_{\mathrm{ISH,res}}/(\nu_{\mathrm{MW}}PL)$ and $\sin^2\Theta_{\mathrm{res}}$, for samples made from ferromagnetic films with qualitatively different exchange mechanisms, magnetic properties, crystalline quality, and crystalline structure as discussed in Sec. 3.3.2. Moreover, the scaling behavior applies to ferromagnets with band-like conduction as well as to materials dominated by hopping
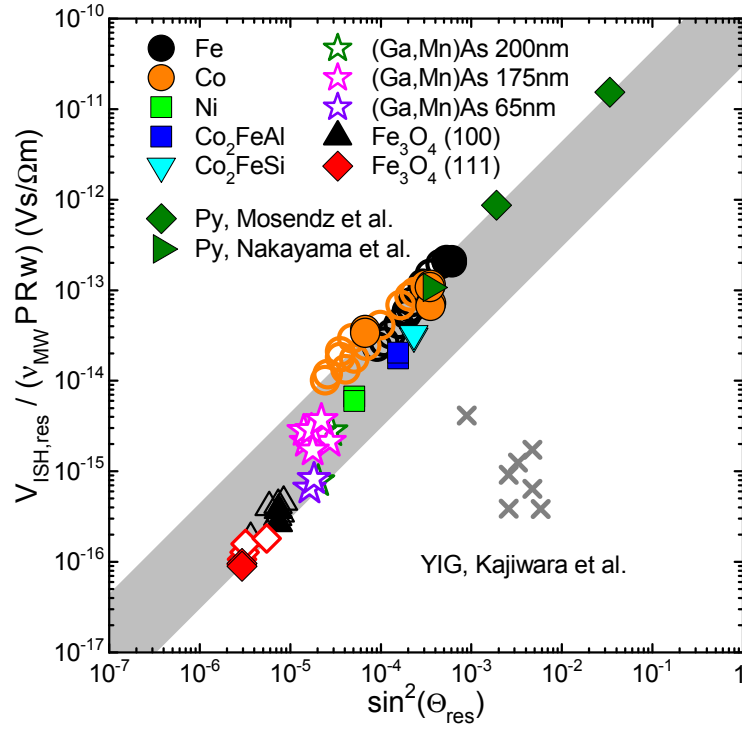
Figure 3.22: $V_{\mathrm{ISH,res}}/(\nu_{\mathrm{MW}} P R\, w)$ versus $\sin^2 \Theta_{\mathrm{res}}$. The grey bar indicates the scaling
relation for all F/Pt bilayers made from conductive ferromagnets. It is observed
over more than four orders of magnitude. Full symbols represent data taken at
$290\,\mathrm{K}$, open symbols correspond to data measured at lower T. The permalloy (Py)
and YIG data are taken from Refs. [9, 10, 42, 148].

conduction such as Fe_3O_4. Last but not least, F/N bilayer samples fabricated and
investigated by different groups are consistently described.

For the sake of completeness, data for $Y_3Fe_5O_{12}$/Pt (YIG/Pt) taken from
Ref. [42] are also shown. Since YIG is an insulator, $g^{\uparrow\downarrow}$ is predicted to be dominated
by its imaginary part in contrast to the mostly real $g^{\uparrow\downarrow}$ for conductive ferromag-
nets [7, 86, 88]. Moreover, spin wave modes govern the YIG FMR signal, impeding
a straightforward analysis [149]. Additionally, the $Y_3Fe_5O_{12}$ films were exposed to
the atmosphere before the Pt layer was deposited. This might create a "bad" inter-
face which reduces the spin current injection into the Pt. Due to these limitations,
we only focus on conductive ferromagnet/Pt bilayers here.

Deviations from the scaling behavior can in particular be observed for the
(Ga,Mn)As samples. To investigate these deviations, the experimental data are
analyzed in more detail by dropping the assumption of a "constant" K. Its con-
stituents $g^{\uparrow\downarrow}$ and $\sigma_{\mathrm{F}} t_{\mathrm{F}} + \sigma_{\mathrm{N}} t_{\mathrm{N}}$ are only at first sight identical for all bilayer samples.
$\sigma_{\mathrm{F}} t_{\mathrm{F}} + \sigma_{\mathrm{N}} t_{\mathrm{N}}$ can be experimentally determined via

$$\sigma_{\mathrm{F}} t_{\mathrm{F}} + \sigma_{\mathrm{N}} t_{\mathrm{N}} = \frac{L}{R\, w} \tag{3.39}$$

with the length L, the width w, and the four point resistance R of the bilayer. Using
this equation, we rewrite Eq. (3.21) as

$$\frac{V_{\mathrm{ISH}}}{\nu_{\mathrm{MW}}PR\,w} = e\,C g^{\uparrow\downarrow}\sin^2\Theta. \tag{3.40}$$

Figure 3.22 shows $V_{\mathrm{ISH,res}}/(\nu_{\mathrm{MW}}PR\,w)$ versus $\sin^2\Theta$ thus obtained for the data already presented in Fig. 3.21. For all samples containing a conductive ferromagnet (thus excluding YIG), $V_{\mathrm{ISH,res}}/(\nu_{\mathrm{MW}}PR\,w)$ indeed scales as suggested by Eq. (3.40) to within a factor of 10 (grey bar in Fig. 3.22). The deviations from perfect scaling are due to a slight material dependence of $g^{\uparrow\downarrow}$, as detailed in Sec. 3.4.9. The scaling behavior is again observed over more than four orders of magnitude in $V_{\mathrm{ISH,res}}/(\nu_{\mathrm{MW}}PR\,w)$ and $\sin^2\Theta$ for samples made from conductive ferromagnetic films with qualitatively different exchange mechanisms, transport properties, crystalline quality, and crystalline structure. Even the data for (Ga,Mn)As/Pt samples measured at different temperatures now fit into the scaling plot. These findings are discussed in detail in Sec. 3.4.9.

3.4.8 Ellipticity of the magnetization trajectory

The data shown in the scaling plots of Figs. 3.21 and 3.22 are corrected by P for the ellipticity of the magnetization precession trajectory due to the demagnetization fields. Potentially present magneto-crystalline anisotropies are not accounted for. In the following, important properties of P, given by Eq. (3.10), are discussed.

The frequency dependence of P for three representative materials (Ga,Mn)As (small saturation magnetization M_{s}), Ni (medium M_{s}) and Fe (high M_{s}) is shown in Fig. 3.23(a) with a magnetization orientation Φ_{M} in the film plane ($\Phi_{\mathrm{M}} = 0°$). For the calculations, values for g-factor and M_{s} of the respective materials were used as listed in Table 3.3. To understand the curve shape, one has to consider that microwave frequency ν_{MW} and resonance field $\mu_0 H_{\mathrm{res}}$ of the FMR are closely linked (see Eq. (3.1)): a small ν_{MW} requires only a small Zeeman split caused by $\mu_0 H$. This explains that for small ν_{MW}, the demagnetization fields dominate and force
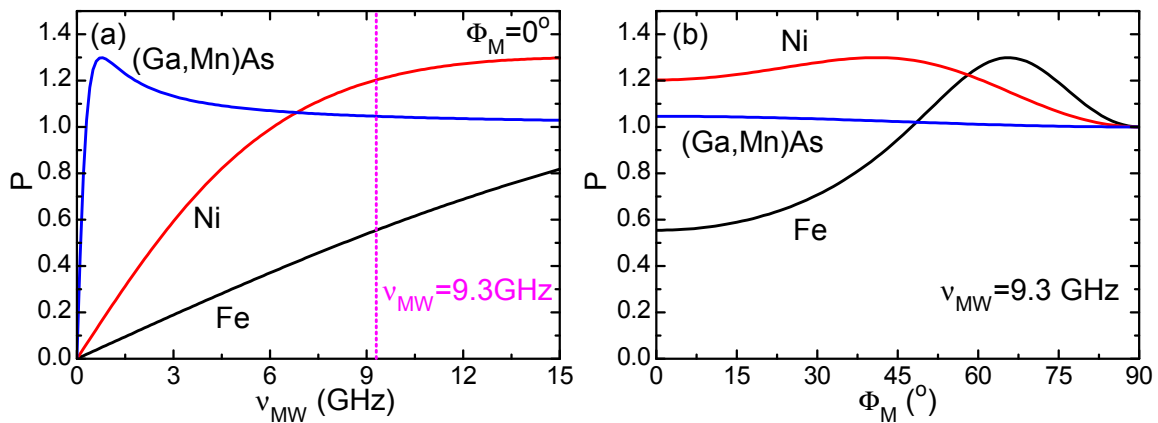
Figure 3.23: (a) Ellipticity correction factor P versus microwave frequency ν_{MW} for different ferromagnets. (b) Magnetization orientation dependence of P for different ferromagnets. Φ_{M} is the angle of the magnetization orientation in the x-z-plane as indicated, e.g., in Fig. 3.28.

Table 3.3: Saturation magnetization M_s, g-factor, microwave frequency ν_{MW} and ellipticity correction factor P of various studied samples. *measurements performed at the University of Bielefeld by I.-M. Imort.

	M_s(kA/m)	g-factor	ν_{MW} (GHz)	P
Ni	490 [19]	2.185 [150]	9.3	1.20
Co	1422 [19]	2.15 [151]	9.3	0.636
Fe	1717 [19]	2.088 [152]	9.3	0.554
Co_2FeSi	945*	2.0	9.3	0.914
Co_2FeAl	864*	2.0	9.3	0.967
Fe_3O_4 (001)	471 [153]	2.12 [154]	9.3	1.23
Fe_3O_4 (111)	394 [155]	2.41 [155]	9.3	1.24
(Ga,Mn)As	25 [99]	2.00 [156]	9.3	1.05
Py ($Ni_{80}Fe_{20}$) [9]	852 [9]	2.01 [157]	4	0.489
Py ($Ni_{81}Fe_{19}$) [148]	593 [158]	2.01 [157]	9.43	1.15
YIG ($Y_3Fe_5O_{12}$) [42]	155.7 [42]	0.633 [42]	9.4	1.09

the magnetization precession trajectory onto a strongly elliptical trajectory with small area and thus an inefficient generation of spin currents. With increasing ν_{MW}, the area of the ellipse and thus the generation efficiency increase. The optimum condition is reached when the trajectory describes an ellipse with a ratio of $\sqrt{3}$ between major and minor axis [90]. For the (Ga,Mn)As sample, this condition is already reached below 1 GHz due to the small M_s, whereas for Ni and Fe, it lies above 15 GHz and is not shown. All FMR measurements within this thesis are performed at $\nu_{MW} = 9.3$ GHz indicated as dashed vertical line.

The variation of P with the magnetization angle Φ_M in the x-z-plane (see e.g., Fig. 3.28) at $\nu_{MW} = 9.3$ GHz is displayed in Fig. 3.23(b). The three materials show a very different behavior. Whereas P for (Ga,Mn)As with a low saturation magnetization is essentially constant, P of the two other materials increases with increasing angle, reaches a maximum value of 1.3 and then decreases to a value of 1 at $\Phi_M = 90°$. For $\Phi_M = 90°$, the magnetization is perpendicular to the film plane, leading to a circular precession which makes a correction unnecessary. Again, the differences in lineshape for the different materials are due to the differences in saturation magnetization.

As obvious from the previous argumentation, the saturation magnetization is a crucial parameter. Therefore, Fig. 3.24 displays P versus M_s for $g = 2.1$, $\nu_{MW} = 9.3$ GHz and the magnetization oriented in the film plane ($\Phi_M = 0°$) as blue line. P begins at $M_s = 0$ kA/m with a value of 1, then it increases with increasing M_s, reaches its maximum of 1.3 at $M_s = 293$ kA/m and then decreases continuously. In this diagram, the calculated values of all studied samples are included as red symbols, taking M_s, g-factor, and ν_{MW} as indicated in Table 3.3. The deviations of the symbols from the blue line are due to different g-values for different materials or different microwave frequencies used in the references.
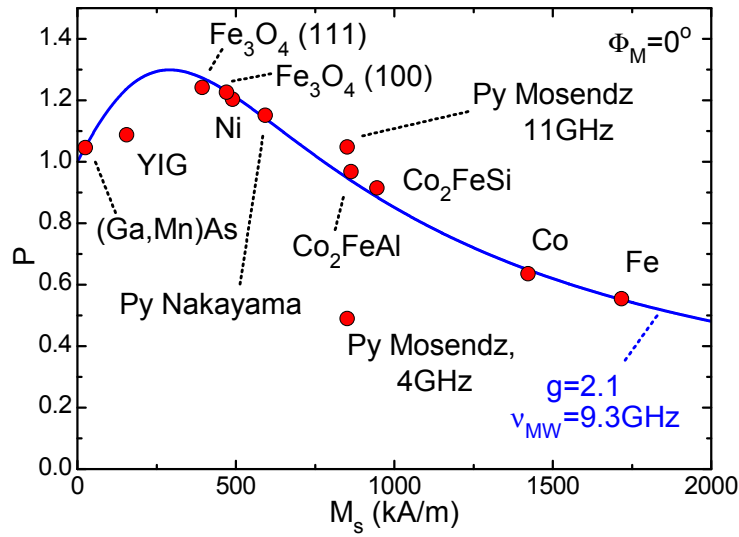
Figure 3.24: Dependence of the ellipticity correction factor P on the saturation
magnetization calculated for $g = 2.1$ and $\nu_{MW} = 9.3$ GHz (blue line). The values of
P used for the samples shown in Figs. 3.21 and 3.25(a) are indicated as red circles.

To visualize the effect of the ellipticity correction on the scaling plot, Fig. 3.25
compares scaling with correction (a) to scaling without inclusion of P (b). As
expected for factors close to one, no drastic change between the two situations can be
observed. However, the magnetite and Ni data are shifted to slightly smaller values,
whereas the Fe and Co data are slightly increased in magnitude when the data are
corrected for P. The strongest influence can be observed on the measurement with
the largest cone angle, extracted from [9]. This is caused by the microwave frequency
of $\nu_{MW} = 4$ GHz for that measurement, which drastically reduces P.
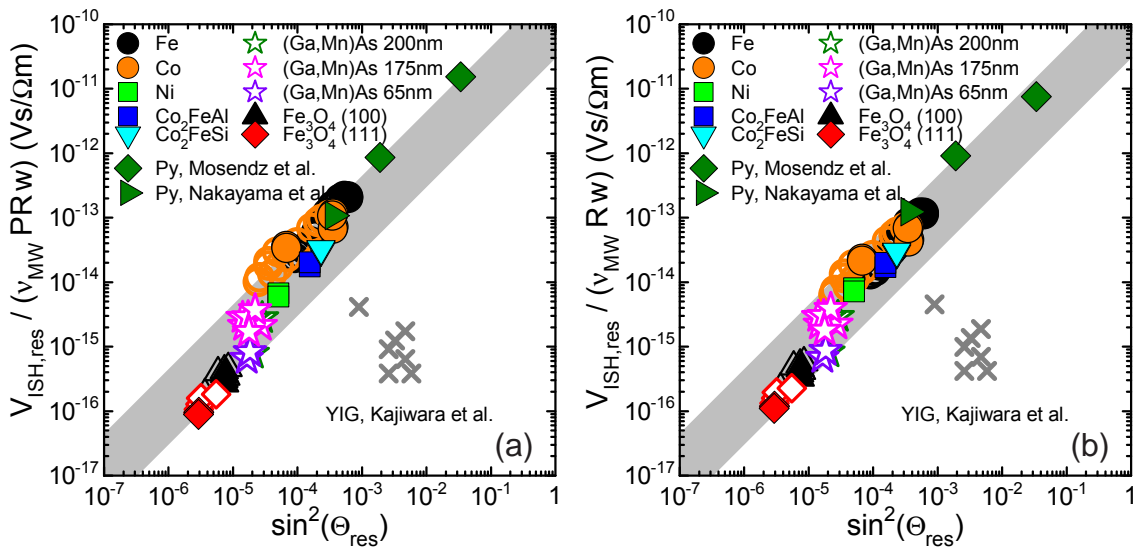
Figure 3.25: Comparison of the scaling plot with (a) and without (b) the ellipticity
correction factor P. No drastic change can be observed.

3.4.9 Quantification of the spin mixing conductance

A crucial parameter in spin transfer torque and spin pumping measurements is the spin mixing conductance $g^{\uparrow\downarrow}$ as discussed above in Secs. 3.2.2 and 3.2.3. So far, however, the magnitude of $g^{\uparrow\downarrow}$ is mainly discussed in terms of ab initio calculations [86, 88, 159], while little experimental data are available. Therefore, we have further analyzed our measurements to extract quantitative values for $g^{\uparrow\downarrow}$. The magnitude of $g^{\uparrow\downarrow}$ can be calculated from our data by writing Eq. (3.40) as

$$g^{\uparrow\downarrow} = \frac{V_{\text{ISH,res}}}{e\,C\,R\,w\,\nu_{\text{MW}}\,P\,\sin^2\Theta_{\text{res}}}, \tag{3.41}$$

using the room temperature values $\alpha_{\text{SH}} = 0.013$ and $\lambda_{\text{SD}} = 10\,\text{nm}$ for Pt [10, 160]. P is calculated as detailed in Sec. 3.4.8, and literature values for the conductivities of Py and Pt [9, 161] for the data points extracted from Refs. [9, 10, 148] are used. $g^{\uparrow\downarrow}$ obtained from these calculations is plotted in Fig. 3.26 versus temperature.

For highly conductive ("metallic") ferromagnets, such as the $3d$-transition metals, permalloy, or the Heusler compounds, the assumption that $g^{\uparrow\downarrow}$ is independent of the F layer properties (see Sec. 3.4.7) is well fulfilled, since values of $g^{\uparrow\downarrow} = (4 \pm 3) \times 10^{19}\,\text{m}^{-2}$ are obtained. In the low-conductivity ferromagnet Fe_3O_4, $g^{\uparrow\downarrow}$ is about a factor of six smaller and the values for (Ga,Mn)As, measured at low temperature, appear to be between these two regimes. However, in (Ga,Mn)As several spin wave modes contribute to the FMR (see Fig. 3.12(o) and Sec. 3.4.11), and a fit with multiple Lorentzian lines was required to reproduce the FMR and V_{DC} data. So, the assumption of a single, position-independent magnetization precession cone angle Θ_{res} is not warranted [136, 137]. Moreover, in systems with large spin-orbit coupling such as (Ga,Mn)As, magnetization precession can cause a charge pumping across the
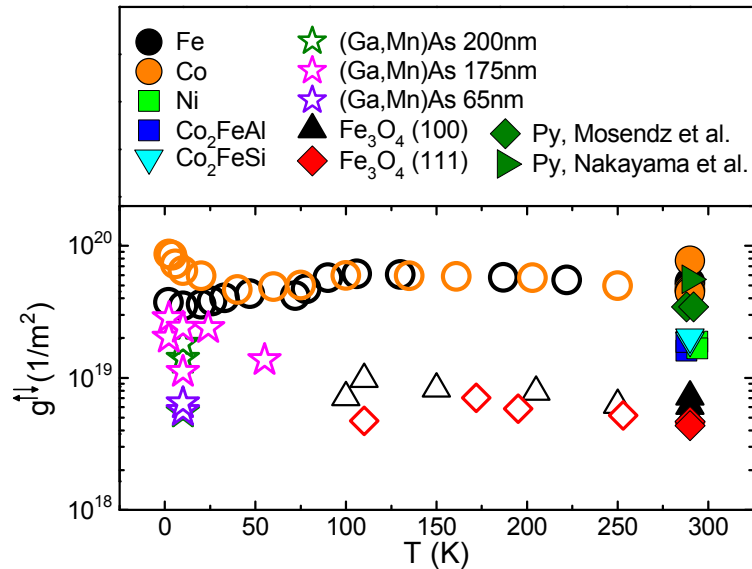
Figure 3.26: Taking into account the bilayer conductivity, the spin mixing conductance $g^{\uparrow\downarrow}$ can be quantified from the scaling analysis. Full symbols represent data taken at 290 K, open symbols correspond to data obtained at lower T.
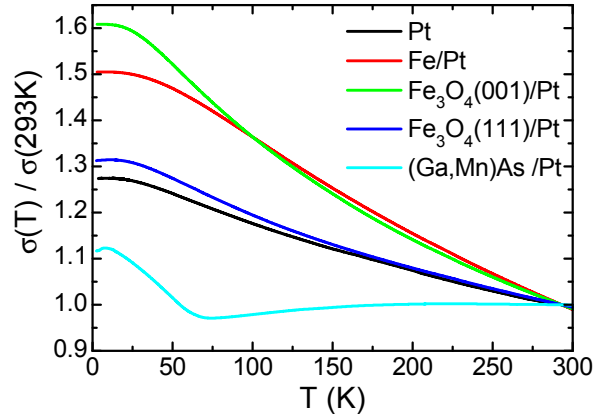
Figure 3.27: Temperature dependence of the conductivity for different F/Pt bi-
layers and a single Pt layer, normalized to the conductivity at 293 K. For the
(Ga,Mn)As/Pt layer with $t_F = 200$ nm, the non-monotonic temperature depen-
dence is due to the ferromagnetic transition. For the single Pt layer (black line),
the measured conductivity $\sigma(T)$ equals the normal metal conductivity $\sigma_N(T)$.

(Ga,Mn)As/Pt interface. In combination with the anisotropic magnetoresistance,
this can result in an additional contribution to the DC voltage [162].

In Fig. 3.26, also the temperature dependence of $g^{\uparrow\downarrow}$ for the Fe/Pt, Co/Pt and
Fe_3O_4/Pt samples is shown. As already mentioned in Sec. 3.4.6, the Fe_3O_4/Pt
samples could only be investigated above 100 K, since a vanishing FMR line and an
enhanced noise prevented measurements at lower T.

Interestingly, temperature has little influence on $g^{\uparrow\downarrow}$. According to the present
theoretical understanding, $g^{\uparrow\downarrow}$ in diffusive bilayers is governed by the conductivity
$\sigma_N(T)$ of the normal metal [7, 79, 81]. The weak temperature dependence of $g^{\uparrow\downarrow}$
(Fig. 3.26) thus suggests that $\sigma_N(T)$ of our Pt films also should not substantially
change with temperature. This is corroborated by 4-point resistance measurements
shown in Fig. 3.27. Indeed, $\sigma_N(T)$ for Pt increases by less than a factor of 1.3 from
290 K to 2 K.

Moreover, since $\alpha_{SH} \propto \sigma^x$ with $0.6 \leq x \leq 1$ [160, 163] is governed by $\sigma_N(T)$, and
since λ_{SD} in Pt increases from about 10 nm at 290 K to about 14 nm at 2 K [160, 164],
$C = \alpha_{SH}\lambda_{SD} \tanh(t_N/2\lambda_{SD})$ at most changes by a factor of three in the entire tem-
perature range investigated experimentally. (This warrants the use of $e\,C\,g^{\uparrow\downarrow}$ as an
essentially temperature-independent scaling constant in Eq. (3.40) and explains the
nice scaling in Figs. 3.21 and 3.22. Moreover, the resistance R of the bilayer sample
entering Eq. (3.41) also varies by less than a factor of two in the entire studied tem-
perature range (see the bilayer conductivity in Fig. 3.27). These estimates explain
why $g^{\uparrow\downarrow}$ is essentially temperature independent.

The results presented in this section are one main finding of this thesis. Our mea-
surements allow to quantify the spin mixing conductance $g^{\uparrow\downarrow}$, a parameter crucial
for spin transfer torque, spin Seebeck and spin pumping measurements. The values
were determined for various F/Pt interfaces, where on the one hand, we used for the
F layer conductive materials such as the $3d$-transition metals Ni, Co, Fe and Heusler
compounds. On the other hand, low conductive materials such as Fe_3O_4 and the

dilute magnetic semiconductor (Ga,Mn)As were used. From our studies, we could confirm that for conductive ferromagnets, $g^{\uparrow\downarrow}$ is indeed independent of the ferromagnetic layer properties as predicted by theory. For low-conductivity ferromagnets, we measure values by a factor of six smaller. Moreover, our measurements showed that temperature has little influence on $g^{\uparrow\downarrow}$. Taken together, our experimental results represent an incentive to theory to calculate $g^{\uparrow\downarrow}$ for ferromagnets with different conductivity magnitude, transport mechanisms, and inhomogeneous spin texture.

3.4.10 Magnetic field orientation dependence for a Ni/Pt bilayer

In addition to the spin pumping experiments with the static magnetic field applied in the film plane ($\phi = 0°$ or $180°$), measurements at various other field orientations were performed. Figures 3.28(a,b) present the FMR and V_{DC} measurements of a Ni/Pt sample wherein the resonance positions of the FMR and the extrema of V_{DC} are indicated as black squares, respectively. Due to the shape anisotropy, both FMR resonance position and the extremum in V_{DC} shift with ϕ. As evident from Fig. 3.28(c), $\mu_0 H_{res}$ for FMR and V_{DC} simultaneously move from $185\,\mathrm{mT}$ for $\phi = 0°$ to $602\,\mathrm{mT}$ for the out-of-plane orientation ($\phi = 90°$) and then back to $185\,\mathrm{mT}$ for $\phi = 180°$. At $\phi = 90°$, the spin pumping signal is suppressed, and no extremum can be observed. The FMR resonance position can be simulated by means of a free energy approach including one uniaxial anisotropy term along $\hat{z}$ with $K_{u,z} = 150\,\mathrm{mT}$ as detailed in Ref. [147]. As a consequence of the shape anisotropy, $\mathbf{M}$ is generally not aligned parallel to $\mathbf{H}$. The angle Φ_M of $\mathbf{M}$ with respect to the film plane (see sketch in Fig. 3.28(a)) can be extracted from the free energy simulations and is sketched in Fig. 3.28(d). For $\phi = 0°$, $90°$ and $180°$, $\Phi_M = \phi$, whereas for other ϕ, $\mathbf{M}$ is oriented further towards the film plane. This is crucial as the detected DC voltage depends on the cross product $\hat{z} \times \hat{s}$ (compare Eq. (2.15)), where the spin orientation $\hat{s}$ is determined by the magnetization orientation and thus Φ_M. To demonstrate the difference, Figs. 3.28(f,g) show $V_{ISH,res}$ versus ϕ and $V_{ISH,res}$ versus Φ_M. The cosine (red line) indicates the expected dependence due to the cross product. Clearly, $V_{ISH,res}$ versus Φ_M much better fits the cosine function. This shows that indeed the magnetization (respectively spin) orientation is the relevant quantity. For Py/Pt, this conclusion was drawn by Ando *et al.* [158]. Furthermore, the ellipticity correction factor $P(\Phi_M)$, as shown in Fig. 3.28(e) can be taken into account. The corrected data together with a cosine (red line) are shown in Fig. 3.28(h). No drastic change is observed. This is probably due to the relatively small variation of P for Ni in comparison to, e.g., Fe as shown in Fig. 3.23(b).
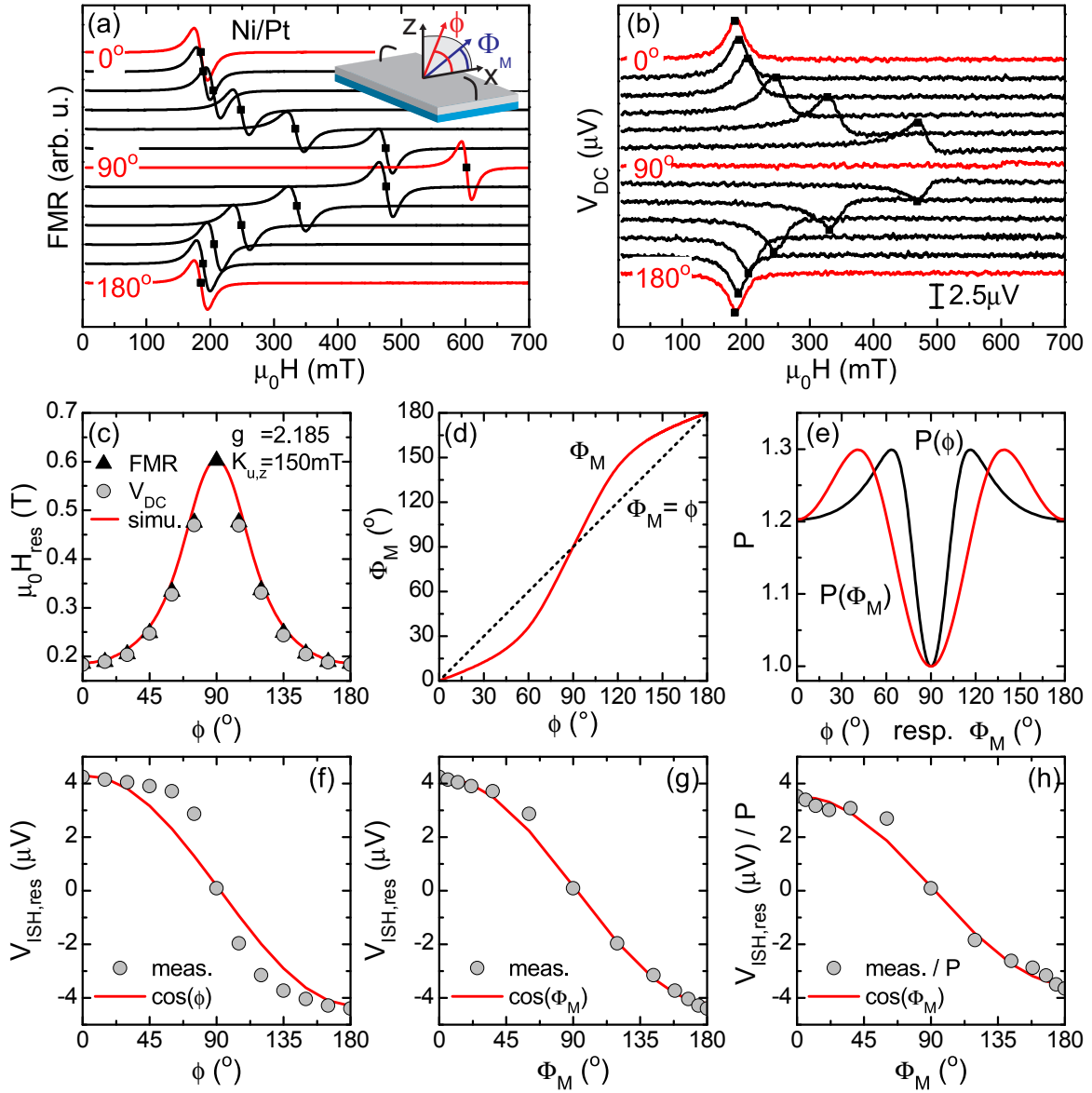
Figure 3.28: Magnetic field orientation dependent measurements of a Ni/Pt bilayer. ϕ is the angle between $\mathbf{H}$ and $\hat{\mathbf{x}}$, and Φ_M the angle between $\mathbf{M}$ and $\hat{\mathbf{x}}$, both vary in the $\hat{\mathbf{x}}$-$\hat{\mathbf{z}}$-plane. (a) FMR signal and (b) simultaneously detected DC voltage. The resonance position and the extremum of V_{DC} are indicated as black squares, respectively. (c) Resonance position versus field orientation ϕ. The solid line is the result of a free energy simulation (see, e.g., Ref. [147]). (d) Magnetization orientation Φ_M versus static field orientation ϕ. (e) Ellipticity correction factor versus Φ_M resp. ϕ. (f-h) Comparison of $V_{ISH,res}$ versus ϕ resp. Φ_M with and without ellipticity correction factor P.

3.4.11 Spin pumping from spin wave resonances
– (Ga,Mn)As/Pt

In contrast to the polycrystalline Ni discussed in the previous section, the (Ga,Mn)As films are epitaxially grown and thus exhibit in addition to the shape anisotropy a magneto-crystalline anisotropy. Here, we investigate the magnetic field orientation dependence of a (Ga,Mn)As/Pt bilayer sample with $t_F = 200\,\text{nm}$ at $10\,\text{K}$. In our measurements, $\mathbf{H}$ is varied in the $\hat{\mathbf{x}}$-$\hat{\mathbf{z}}$-plane. The in-plane $\hat{\mathbf{x}}$-direction ($\phi = 0°$) equals the crystallographic [110]-direction and the out-of-plane $\hat{\mathbf{z}}$-direction ($\phi = 90°$) corresponds to the crystallographic [001]-direction. After a presentation of the experimental data, simulations of both FMR and spin pumping signal are performed and discussed.

3.4.11.1 Experimental data

Figures 3.29(a,b) show FMR and V_{DC} measurements for different ϕ. As previously observed in Sec. 3.4.6, the FMR of the here studied (Ga,Mn)As film exhibits multiple resonances called spin wave resonances (SWRs). They are the result of a inhomogeneous magnetic film, where the magnetization precession amplitude M_1 varies as a function of the film thickness. This situation can be described via spin wave excitations (magnons) with non-zero wave vector. The multiple resonances originate from the selective amplification of spin wave excitations (magnons) fulfilling the boundary conditions of the film. Detailed information on spin waves can be found, e.g., in Ref. [165].

The SWRs in Fig. 3.29(a) prevent a straightforward analysis of FMR and V_{DC} spectra. Hence, both V_{DC} and FMR traces were fitted by Lorentzian lines, respectively their derivatives. To reproduce the FMR data, three derivatives of Lorentzian lines were required for the traces taken at angles $0° \leq \phi \leq 70°$, four for $\phi = 75°$, six for $80° \leq \phi \leq 85°$ and seven for $\phi = 90°$. To reproduce the V_{DC} traces, the same number of lines, the same resonance positions, and the same corresponding widths ($\Delta H_{pp} = 2/\sqrt{3}\Delta H$, see Eq. (3.29)) were used. The result of the fitting procedure is plotted in Figs. 3.29(c,d) and accurately reproduces the measured data in panels (a,b).

From the fitted lines, the resonance position $\mu_0 H_{res}$ and the peak-to-peak linewidth $\mu_0 \Delta H_{pp}$ can be extracted. They are shown in Figs. 3.29(e,f). Each point at a certain angle corresponds to the resonance position, respectively linewidth of a certain SWR, numbered from high to low resonance field. With increasing angle, the resonance positions of the different SWRs shift to higher values and for $\phi \geq 75°$ they split into up to seven distinguishable modes, spanning a range of $466\,\text{mT} \leq \mu_0 H_{res} \leq 765\,\text{mT}$.

Using a free energy approach (see Ref. [147]) including an uniaxial and a cubic anisotropy, the resonance positions of the most intense SWR can be reasonably reproduced (black line Fig. 3.29(e)). However, as discussed by Bihler [166] and Liu *et al.* [167], the maximum resonance position of the SWR ($765\,\text{mT}$ at $\phi = 90°$) might differ from the uniform resonance field which complicates the extraction of the anisotropy parameters. Thus, the given values of the anisotropy fields should
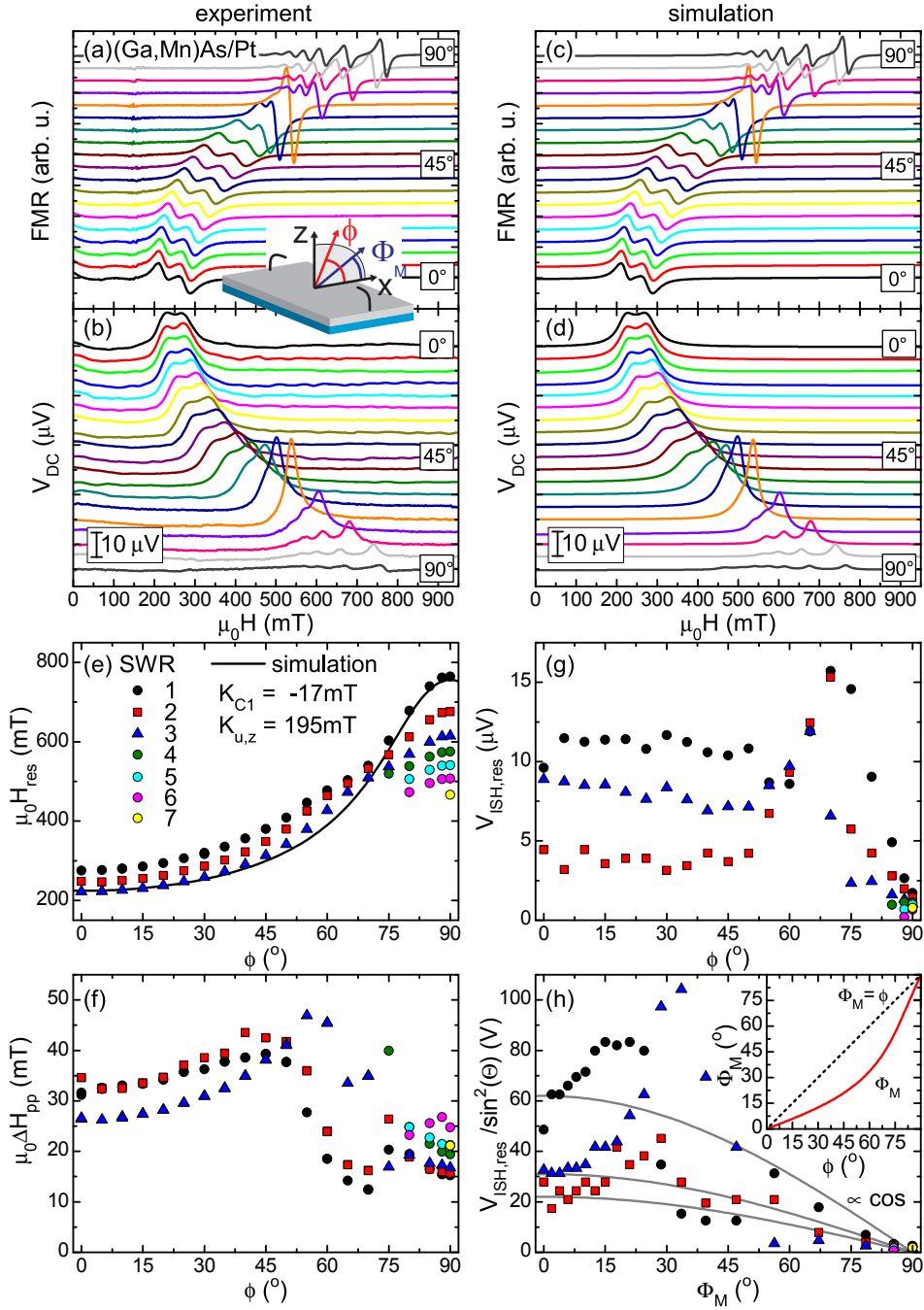
Figure 3.29: Measurements of a (Ga,Mn)As/Pt bilayer with $t_F = 200\,\text{nm}$ at $T = 10\,\text{K}$ for different orientations of the external magnetic field. (a) FMR signal and (b) simultaneously detected DC voltage. (c,d) Results of a fitting procedure of (a,b) with three to seven Lorentzian lines. From these curves, the resonance positions (e), the peak-to-peak linewidth (f) and $V_{\text{ISH,res}}$ of the different spin wave resonance (SWR) modes are extracted and shown in different colors. (h) $V_{\text{ISH,res}}/\sin^2\Theta$ versus the magnetization angle Φ_M. The solid lines represent a $\cos\Phi_M$-dependence with three different amplitudes. The inset depicts Φ_M versus ϕ.

be just taken as estimates. From the simulation, the magnetization orientation can be extracted. It rotates in the same plane as $\mathbf{H}$ but is oriented more towards the film plane (see inset in Fig. 3.29(h)), similar to the case of Ni/Pt discussed in the previous section.

The peak-to-peak linewidth (Fig. 3.29(f)) is different for the different spin wave modes and lies between $26\,\mathrm{mT} \leq \mu_0 \Delta H_{\mathrm{pp}} \leq 34\,\mathrm{mT}$ for $\phi = 0°$. With increasing angle, $\mu_0 \Delta H_{\mathrm{pp}}$ increases until a maximum value of $47\,\mathrm{mT}$ at $\phi = 55°$. For larger ϕ, the linewidth decreases to a value between $15\,\mathrm{mT} \leq \mu_0 \Delta H_{\mathrm{pp}} \leq 25\,\mathrm{mT}$ at $\phi = 90°$.

Figure 3.29(g) shows $V_{\mathrm{ISH,res}}$, the amplitude of the different Lorentzian functions extracted from the Lorentzian fits. The DC voltage varies between single SWRs but is relatively constant for each mode from $\phi = 0°$ to $50°$. For larger ϕ, the amplitudes of the SWRs increase up to $16\,\mu\mathrm{V}$ before the voltage reduces to zero at $\phi = 90°$.

To test to what extent spin pumping theory describes the experimental observations for a inhomogeneous magnetization, Fig. 3.29(h) shows $V_{\mathrm{ISH,res}}/\sin^2\Theta$ (see Eq. (3.21)) versus Φ_{M}. Taking into account the cross product of $\hat{\mathbf{z}}$ and the magnetization orientation (Eq. (2.15)), a cosine lineshape is expected as indicated by the three grey lines of arbitrary magnitude. Strong deviations between theory and experiment can be observed in the entire range. Due to the small saturation magnetization of (Ga,Mn)As, the ellipticity correction factor is close to 1 for all Φ_{M} (see Fig. 3.23(b)) and can be neglected.

This analysis shows that spin pumping measurements in (Ga,Mn)As/Pt bilayer samples exhibiting spin wave excitations cannot be fully described by the present theory which was developed for a homogeneous magnetization. The assumption of a single, position-independent magnetization precession cone angle Θ_{res} is not warranted in materials exhibiting spin wave resonance excitations as (Ga,Mn)As [136, 137, 156, 167]. Rather, the impact of the different magnetization precession cone angles as a function of depth into the film must be quantitatively taken into account. Here, further theory is needed which quantitatively describes spin pumping for a position dependent magnetization.

3.4.11.2 Comparison of FMR and spin pumping from SWRs

An intuitive approach to compare the generation efficiency of individual SWRs is presented in the following. We compare the intensities of the integrated FMR signal and the measured DC voltage V_{DC}, both normalized to the intensity of the SWR with index 1 (Figs. 3.30(a,b)).

Figure 3.30(a) shows the result for $\mathbf{H}$ applied in the film plane along $\hat{\mathbf{x}}$ ($\phi = 0°$). Both FMR and V_{DC} trace show a similar lineshape which might indicate that these spin waves equally contribute to the spin pumping signal. However, since the spin waves cannot be separated, a quantitative interpretation is difficult. More SWRs are observed for larger angles. Therefore, Fig. 3.30(b) shows the integrated FMR signal together with the V_{DC} trace for $\phi = 88°$. Again, the relative intensities of the SWRs are similar in FMR and V_{DC}. A closer look reveals that the magnitude of V_{DC} for the SWR modes 3-6 seems to be slightly decreased in comparison to the integrated FMR. This can either be due to a variation of the background or to the
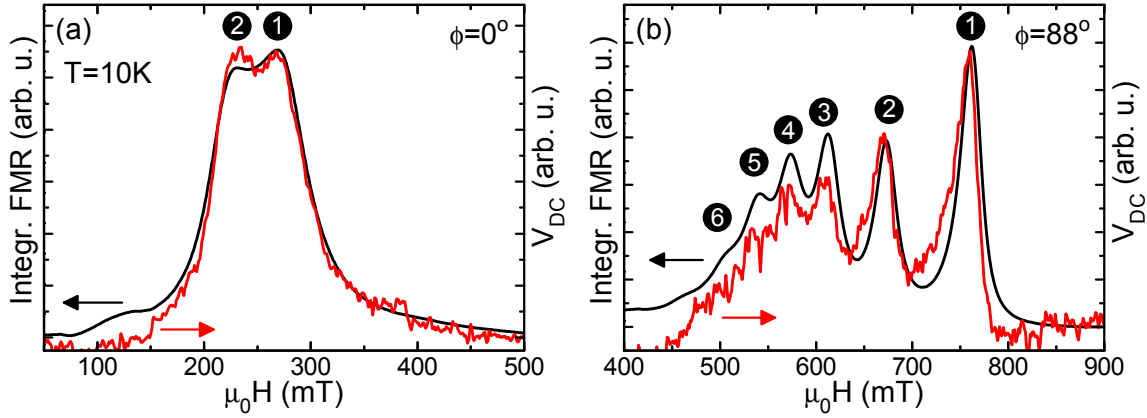
Figure 3.30: Comparison of integrated FMR and DC voltage for (a) $\phi = 0°$ and (b) $\phi = 88°$. The spin wave resonances are numbered from high to low field.

spin pumping generation efficiency of the individual SWR modes. To study the spin wave spectrum of the FMR and the spin pumping generation efficiency of individual SWRs in detail, a more elaborated theoretical model is presented in the following.

3.4.11.3 Simulation of the spin wave resonance spectrum

The here presented model describes the FMR spin wave spectrum and was developed by Hoekstra *et al.* [168] and adapted to (Ga,Mn)As by Bihler *et al.* [136]. The simulations emerged from a close cooperation with Lukas Dreher from the Walter Schottky Institut. We consider the case where $\mathbf{H}$ is oriented perpendicular to the film plane (along $\hat{\mathbf{z}}$ in Fig. 3.1) and is sufficiently large to align $\mathbf{M}_0 \parallel \mathbf{H}$. In the model, the anisotropy field in growth direction $\mu_0 H_{\mathrm{aniso}}^{001}$ consists of the demagnetization term and a magneto-crystalline term with an uniaxial and a cubic contribution (see Ref. [136]). Moreover, a variation of the magnetic properties is assumed only along the growth direction (here along $\hat{\mathbf{z}}$) which leads to an inhomogeneous anisotropy field $\mu_0 H_{\mathrm{aniso}}^{001} = \mu_0 H_{\mathrm{aniso}}^{001}(z)$. Hence, the excitation of the magnetic moments due to the microwave can be described by $\mathbf{M} = M_0 \hat{\mathbf{z}} + M_1(z) e^{-i\omega t} (\hat{\mathbf{x}} + i\hat{\mathbf{y}})$ with a z-dependent AC magnetization $M_1(z)$. Inserting this expression into the Landau-Lifshitz-Gilbert equation (Eq. (3.2)) (neglecting the damping term) with the exchange field [169, 170]

$$\mu_0 \mathbf{H}_{\mathrm{ex}} = \frac{D}{M_{\mathrm{s}}} \nabla^2 \mathbf{M} \tag{3.42}$$

and the z-dependent crystal anisotropy field $\mu_0 H_{\mathrm{aniso}}^{001}(z)$, one obtains the spin wave equation

$$D \frac{\partial^2 M_1(z)}{\partial z^2} + \left[-\mu_0 H_{\mathrm{aniso}}^{001}(z) + \frac{\omega}{\gamma} \right] M_1(z) = \mu_0 H \cdot M_1(z). \tag{3.43}$$

Here, $D = 2A_{\mathrm{s}}/M_{\mathrm{s}}$ is the exchange constant of the magnetic moments with the exchange stiffness A_{s}. Equation (3.43) is formally equivalent to a one-dimensional time-independent Schrödinger equation. Thus, the resonance fields $\mu_0 H_{\mathrm{res},n}$ (=eigenvalues) and the corresponding spin-wave profiles $M_{1,n}(z)$ (=eigenfunctions) for a given

uniaxial anisotropy profile $\mu_0 H_{\text{un}}^{001}(z) = \frac{\omega}{\gamma} - \mu_0 H_{\text{aniso}}^{001}(z)$ can be obtained by solving the spin wave equation (3.43). As boundary conditions for the Pt/(Ga,Mn)As and the (Ga,Mn)As/substrate interface, unpinned modes, i.e., $\partial M_1(z)/\partial z = 0$ are used [136]. The intensity I_n with which an individual spin wave is excited in SWR experiments depends on its net magnetic moment. For well separated modes (small damping), I_n for $\omega = \omega_n$ can be written as [168, 171]

$$I_n = \frac{\gamma M_s H_1^2}{\eta t_F} \frac{\left(\int_0^{-t_F} M_{1,n}(z)\,\mathrm{d}z\right)^2}{\int_0^{-t_F} (M_{1,n}(z))^2\,\mathrm{d}z} = \frac{\gamma M_s H_1^2}{\eta t_F} \left(\int_0^{-t_F} m_n(z)\,\mathrm{d}z\right)^2, \qquad (3.44)$$

where $z = 0$ corresponds to the Pt/(Ga,Mn)As and $z = -t_F$ to the (Ga,Mn)As/substrate interface. $m_n(z)$ are chosen real and form a complete set of orthonormal functions as discussed later in this section. The calculated spectrum is obtained by a superposition of derivatives of Lorentzian functions at $\mu_0 H_{\text{res},n}$ with a fixed linewidth of $\mu_0 \Delta H_{\text{pp}} = 17\,\text{mT}$ (determined by fitting) multiplied by the intensity I_n of Eq. (3.44).

We performed two simulations using different parameters to be able to compare the results. In simulation 1 (Sim. 1) the uniaxial anisotropy profile was modeled as $\mu_0 H_{\text{un}}^{001}(z) = \frac{\omega}{\gamma} - [O + G_1(z - t_F)]$ with the anisotropy field O at the surface and a linear gradient in the anisotropy field with slope G_1. In this simulation, the thickness t_F of the (Ga,Mn)As layer is used as a fitting parameter. In the second simulation (Sim. 2), the uniaxial anisotropy profile is modeled as $\mu_0 H_{\text{un}}^{001}(z) = \frac{\omega}{\gamma} - [O + G_i(z - t_F)]$ with two gradients: G_1 for $0 < z < 100\,\text{nm}$ and G_2 for $100\,\text{nm} < z < 200\,\text{nm}$. In this case, the geometric thickness of the (Ga,Mn)As layer $t_F = 200\,\text{nm}$ is used.

For the field configuration discussed above – $\mathbf{H}$ perpendicular to the film plane – the spin pumping signal is completely suppressed. To strike a balance, we consider spectra taken slightly off perpendicular orientation at an angle of $\phi = 88°$, where the above derivation is assumed to be still valid, and, in addition, a small spin pumping signal can be detected.

In Figs. 3.31(a,c), the results of both Sim. 1 and Sim. 2 are compared to the experimental data taken at $T = 10\,\text{K}$. The FMR displays at least six distinguishable spin wave resonances with decreasing intensity and decreasing spacing numbered 1 through 6. Both simulations quantitatively reproduce the experimentally observed resonance positions and the relative intensities of the spin waves. The parameters used are listed in Table 3.4. For Sim. 1, a (Ga,Mn)As layer thickness of $t_F = 165\,\text{nm}$ was used – 25 nm thinner than the geometric one. Nevertheless, this appears reasonable, since etching experiments on similar samples showed that the FMR vanished already before the entire geometric thickness of the (Ga,Mn)As layer was etched away. This was attributed to a smaller ferromagnetic film thickness compared to the geometric one [136], probably due to high defect densities in the initial stages of growth. The gradient in the magnetic properties used for both simulations is attributed to a gradient in hole concentration p [136]. By electrochemical capacitance voltage profiling and Raman spectroscopy, indeed a monotonical decrease of p from its maximum value near the sample surface to the (Ga,Mn)As/substrate interface
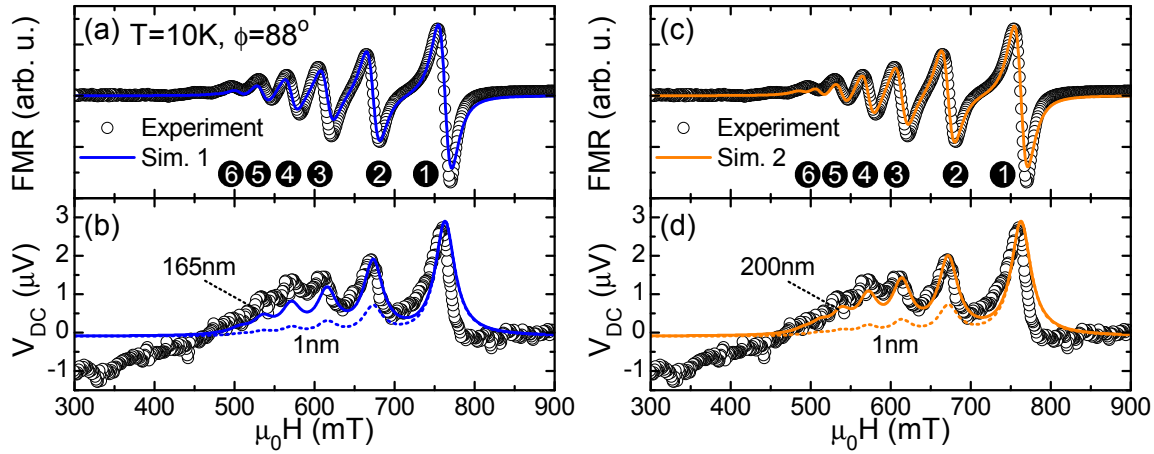
Figure 3.31: The identical experimental data of FMR and V_{DC} are shown as open symbols two times, in (a,b) and in (c,d). They are compared to different simulations (Sim. 1 and Sim. 2) using the parameters listed in Table 3.4. Both simulations describe the FMR signal very well. To obtain a good agreement between simulations and the DC voltage, not just the interface (1 nm) but a significant part of the ferromagnetic film thickness has to be taken into account (165 nm or 200 nm).

was found [172, 173]. The origin might be diffusion and/or rearrangement of Mn interstitials [174, 175]. In contrast to Bihler *et al.* [136], we use a linear gradient in D ranging from its maximum value to zero. This can be justified as the exchange field (Eq. (3.42)), mediated by the holes, should depend on the hole concentration.

Figure 3.32(a) shows the variation of the amplitude of $m_{1,n}$ with z for the different spin wave modes obtained from Sim. 2 with the same numbering as in Fig. 3.31(c). They are shifted by the calculated resonance fields $\mu_0 H_{\text{res},n}$, indicated as horizontal dotted black lines. In addition, the uniaxial anisotropy profile $\mu_0 H_{\text{un}}^{001}(z)$, used for Sim. 2 is plotted. The SWR modes $1 \leq n \leq 3$ are more localized at the Pt/(Ga,Mn)As interface and exponentially decrease towards the (Ga,Mn)As/substrate interface. In contrast, the higher modes $n > 3$ are rather equally distributed over the whole sample thickness which might influence the spin pumping efficiency. As the FMR can be simulated very well, we concentrate on the spin pumping signal in the following.

Table 3.4: Parameters of the two different spin wave spectrum simulations.

	Sim. 1	Sim. 2	
O (mT)	-477	-477	
$\mu_0 \Delta H_{\text{pp}}$ (mT)	17	17	
$D_{z=0} - D_{z=-t_F}$ (Tnm²)	24 – 0	29 – 0	
region	1	1	2
z (nm)	0 – -165	0 – -100	-100 – -200
G_i (mT/nm)	1.9	1.74	1.42

3.4.11.4 Simulation of the spin pumping signal from SWRs

So far, no theory dealing with spin pumping from a inhomogeneous magnetization exists. Here, we present the first approach to simulate the intensity of the spin pumping signal from spin wave resonances.

In the homogeneous case, the intensity of the spin pumping signal is proportional to the square of the AC component of the magnetization: $(M_1)^2$ (see Eq. (3.8)). Since M_1 changes as a function of z across the film thickness and is different for each SWR, we consider $|M_{1,n}(z)|^2$. Moreover, to investigate which part of the F layer contributes to the spin pumping signal (just the interface or a thicker region), we suggest for the spin pumping intensity of the n-th mode

$$I_{\text{SP},n} \propto \int_0^{-t_{\text{F}}} (M_{1,n}(z))^2 f(z)\, dz, \tag{3.45}$$

where $z = 0$ corresponds to the Pt/(Ga,Mn)As interface and $z = -t_{\text{F}}$ to the (Ga,Mn)As/substrate interface. The function $f(z)$ weights the contribution of different regions of the ferromagnet to the spin pumping signal. To obtain the quantity $M_{1,n}(z)$, one has to multiply the normalized AC magnetization mode $m_n(z)$ with its coupling F_n to the microwave: $M_{1,n}(z) = F_n \cdot m_n(z)$. We assume this coupling to be proportional to the net magnetic moment of the SWR mode, such that $F_n \propto \left|\int_0^{-t_{\text{F}}} m_n(z)\, dz\right| \propto \sqrt{I_n}$. Therefore, we obtain for the intensity of the spin pumping signal for the n-th SWR

$$I_{\text{SP},n} \propto I_n \cdot \int_0^{-t_{\text{F}}} (m_n(z))^2 f(z) dz. \tag{3.46}$$

The identical result can be obtained by a strict mathematical derivation presented in the following. A new coordinate system $\hat{\mathbf{e}}_{\parallel}$, $\hat{\mathbf{e}}_{\perp}$ is chosen which rotates around the $\hat{\mathbf{z}}$-axis with the angular frequency ω in the sames sense as $\mathbf{M}$ rotates around the effective magnetic field ($\hat{\mathbf{e}}_{\parallel} = \cos\omega t \cdot \hat{\mathbf{x}} + \sin\omega t \cdot \hat{\mathbf{y}}$, $\hat{\mathbf{e}}_{\perp} = -\sin\omega t \cdot \hat{\mathbf{x}} + \cos\omega t \cdot \hat{\mathbf{y}}$). In this system, the magnetization can be written as

$$\mathbf{M} = m_{\parallel}\hat{\mathbf{e}}_{\parallel} + m_{\perp}\hat{\mathbf{e}}_{\perp} + M_{\text{z}}\hat{\mathbf{e}}_{\text{z}} \tag{3.47}$$

with the modes $m_{\parallel}(z) = \sum_n a_n m_n(z)$ and $m_{\perp}(z) = \sum_n b_n m_n(z)$ excited by the stationary microwave field $\mathbf{H}_1 = H_1 \hat{\mathbf{e}}_{\parallel}$ [168]. Here, $m_n(z)$ are solutions of the spin wave equation in the case of zero driving field and zero damping. The normal modes $m_n(z)$ are chosen real and form a complete set of orthonormal functions: $\int_0^{-t_{\text{F}}} m_i(z) m_j(z)\, \mathrm{d}z = \delta_{ij}$ [168].

Under these prerequisites, one obtains as solution of the spin wave equation the components of the magnetization [168]

$$m_{\parallel}(z) = \sum_n -\frac{(\omega - \omega_n)\gamma M_{\text{s}} H_1}{(\omega - \omega_n)^2 + \eta^2\omega^2} \int_0^{-t_{\text{F}}} m_n(z)\, \mathrm{d}z \cdot m_n(z),$$

$$m_{\perp}(z) = \sum_n -\frac{\eta\omega\gamma M_{\text{s}} H_1}{(\omega - \omega_n)^2 + \eta^2\omega^2} \int_0^{-t_{\text{F}}} m_n(z)\, \mathrm{d}z \cdot m_n(z). \tag{3.48}$$

The spin pumping spin current given by Eq.(3.7) is proportional to the cross product $\hat{\mathbf{m}} \times \frac{\partial \hat{\mathbf{m}}}{\partial t}$. This can be evaluated for the coordinate system chosen here and gives $\omega(m_\parallel^2 + m_\perp^2)\hat{\mathbf{e}}_z$. The term in brackets can be calculated for the n-th SWR using Eqs. (3.48):

$$(m_{\parallel,n}^2 + m_{\perp,n}^2) = \gamma^2 M_{\mathrm{s}}^2 H_1^2 \left(\int_0^{-t_{\mathrm{F}}} m_n(z)\, dz \right)^2 (m_n(z))^2 \frac{(\omega - \omega_n)^2 + \eta^2\omega^2}{\left((\omega - \omega_n)^2 + \eta^2\omega^2\right)^2}.$$
(3.49)

For convenience, the fraction in Eq. (3.49) is abbreviated with $F(\omega)$. Now, the spin current generated by the n-th SWR mode in a depth z can be written as

$$
\begin{aligned}
J_{\mathrm{s},n}^{\mathrm{pump}}(z)\,\hat{\mathbf{s}} &= \frac{\hbar\omega}{4\pi}g^{\uparrow\downarrow} \cdot (m_{\parallel,n}^2(z) + m_{\perp,n}^2(z))\hat{\mathbf{e}}_z \\
&= \frac{\hbar\omega}{4\pi}g^{\uparrow\downarrow} \cdot \gamma^2 M_{\mathrm{s}}^2 H_1^2 \left(\int_0^{-t_{\mathrm{F}}} m_n(z)\, dz \right)^2 (m_n(z))^2 F(\omega)\,\hat{\mathbf{e}}_z.
\end{aligned}
$$
(3.50)

We now suggest that the spin pumping signal of the entire ferromagnet can be obtained by an integration over the entire ferromagnetic film thickness ($-t_{\mathrm{F}} \le z \le 0$), whereby the weighting function $f(z)$ is included:

$$J_{\mathrm{s},n}^{\mathrm{pump}}\hat{\mathbf{s}} = \frac{\hbar\omega}{4\pi}g^{\uparrow\downarrow} \cdot \gamma^2 M_{\mathrm{s}}^2 H_1^2 F(\omega) \left(\int_0^{-t_{\mathrm{F}}} m_n(z)\, dz \right)^2 \int_0^{-t_{\mathrm{F}}} (m_n(z))^2 f(z)\, \mathrm{d}z\, \hat{\mathbf{e}}_z.$$
(3.51)

We assumed that $g^{\uparrow\downarrow}$, γ^2 and H_1^2 are independent of z and can be put outside the integral.

It is important to note that the derivation of the spin pumping spin current is based on a pure interface effect [7, 8]. We chose the approach shown here to test whether really only the Pt/(Ga,Mn)As interface is relevant for the magnitude of the spin pumping signal, or a larger part of the ferromagnetic layer has to be taken into account. This can be achieved by properly choosing the weighting function $f(z)$.

From Eq. (3.51), we find that $J_{\mathrm{s},n}^{\mathrm{pump}} \propto \left(\int_0^{-t_{\mathrm{F}}} m_n(z)\, dz \right)^2 \int_0^{-t_{\mathrm{F}}} (m_n(z))^2 f(z)\, \mathrm{d}z$ which exactly equals the result obtained from the intuitive approach for the spin pumping intensity $I_{\mathrm{SP},n}$ generated by the n-th mode (see Eq. (3.46)). This shows that under the assumed conditions the exact mathematical and the much simpler intuitive approach yield the sample dependence.

The actual spin pumping spectrum is obtained by a superposition of Lorentzian functions at $\mu_0 H_{\mathrm{res},n}$ with a fixed linewidth of $\Delta H = (\sqrt{3}/2) \cdot 17\,\mathrm{mT}$ (corresponding to the one used to simulate the FMR) multiplied by the intensity $I_{\mathrm{SP},n}$ of the respective mode (see Eqs.(3.46) and (3.51)). The results of Sim. 1 and Sim. 2 are shown in Figs. 3.31(b,d). As a first approach, we chose for the weighting function $f(z)$ a unit step function $H(z + t_{\mathrm{d}})$ which is 0 for values smaller than $z + t_{\mathrm{d}}$ and 1 for larger values. Hence, just the part of the ferromagnet from the F/Pt interface to the depth t_{d} is included in the spin pumping signal. Two integration depths are exemplary shown: $t_{\mathrm{d}} = 1\,\mathrm{nm}$, where just the Pt/(Ga,Mn)As interface contributes, and $t_{\mathrm{d}} = t_{\mathrm{F}}$, where the entire ferromagnetic layer thickness is taken into account.
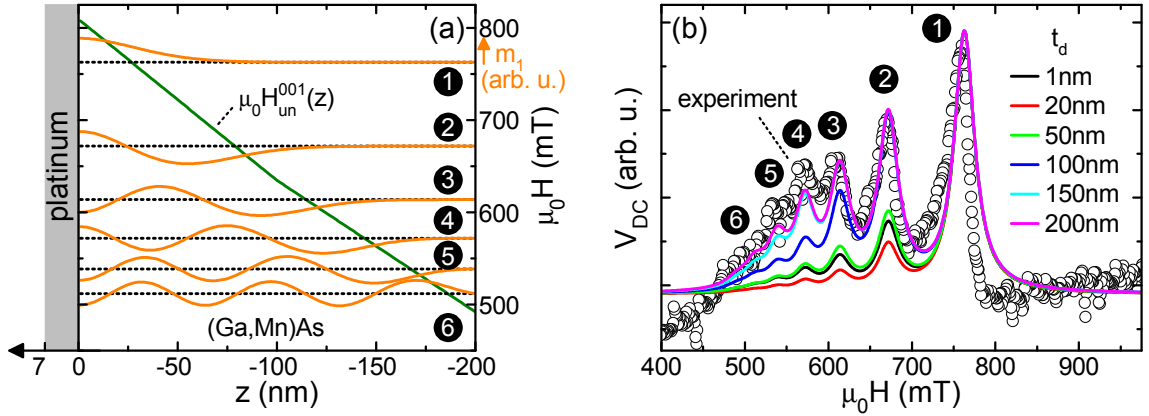
Figure 3.32: (a) $m_n(z)$ versus z for the different spin wave modes calculated by Sim. 2. The modes are offset by the calculated resonance fields $\mu_0 H_{\mathrm{res},n}$ indicated as dotted black lines. (b) Comparison of the calculated spin pumping signal (Sim. 2) for different integration depths t_{d}.

All spectra are normalized to the intensity of the first SWR. Both simulations taking just the interface into account ($t_{\mathrm{d}} = 1\,\mathrm{nm}$) underestimate the contribution of the higher indexed SWRs. In contrast, the two simulations considering a significant part of the ferromagnetic film thickness (165 nm or 200 nm) describe the whole spectrum reasonably well.

To investigate the influence of the integration depth in more detail, the calculated spin pumping signal obtained from Sim. 2 for various t_{d} is plotted in Fig. 3.32(b) together with the experimental data. Again, all traces are normalized to the intensity of SWR number 1. As already mentioned above, when taking just the interface into account ($t_{\mathrm{d}} = 1\,\mathrm{nm}$), the intensities of SWRs 2-6 are much smaller than observed in experiment. Upon increasing t_{d}, their intensities even further decrease up to an integration depth of $t_{\mathrm{d}} \approx 20\,\mathrm{nm}$. For larger values of t_{d}, their intensities increase and for calculations taking into account the major part of the ferromagnetic film thickness $150\,\mathrm{nm} \lesssim t_{\mathrm{d}} \lesssim 200\,\mathrm{nm}$, a reasonably good agreement between simulation and experiment is obtained. These results suggest that a large part of the ferromagnetic layer and not just the interface has to be taken into account to properly describe spin pumping in (Ga,Mn)As/Pt thin film samples.

The traces of Sim. 1 are very similar to the ones obtained from Sim. 2 and thus are not shown here. To decide which simulation better describes our experiments, one has to extend the theory to arbitrary orientations of the external magnetic field and use a single set of parameters to consistently describe experiments at all $\mathbf{H}$ orientations. Such experiments are rather involved, and represent a challenge for the future. However, it should be emphasized that as the two simulations gave very similar results, the approach presented here seems to be robust.

Our findings are not in contradiction to the results presented by Sandweg *et al.* [149] who found in $Y_3Fe_5O_{12}$/Pt samples with $t_{\mathrm{F}} = 2.1\,\mu\mathrm{m}$ that different SWRs contribute differently to the spin pumping signal: surface modes result in larger signals than volume modes. Due to the much smaller film thickness of our samples,

no clear distinction between surface and volume modes can be made. This can be seen from the different SWR profiles in Fig. (3.32)(a). Therefore, a similar contribution of the individual SWRs seems reasonable.
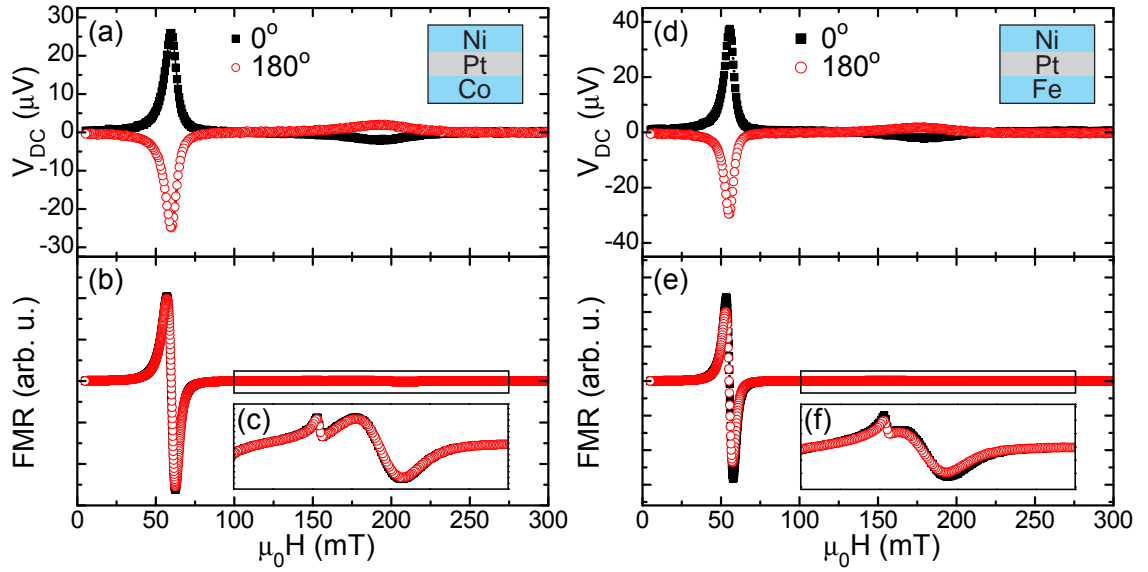
To sum up, we presented magnetic field orientation dependent measurements of FMR and spin pumping in a (Ga,Mn)As/Pt sample. Both FMR and spin pumping signal showed a rich spin wave spectrum. We presented a theoretical model which reproduces our FMR signal and extended it to also describe the intensity of the spin pumping signal of the individual spin wave resonance modes. We found that for our (Ga,Mn)As/Pt samples not only the F/N interface region, but a substantial part of the ferromagnetic layer has to be included into the calculation to describe our experimental data. Clearly, more elaborate theoretical descriptions are now required to further investigate the influence of a inhomogeneous magnetization on the spin pumping signal. Particularly interesting is the question, to which extend deeper regions in the ferromagnet "feel" the interface, and what the corresponding length scale is. For example, the unit step function $H(z + t_d)$ used so far might be replaced by a function reflecting an exponential decay inside the ferromagnet.

3.4.12 F1/N/F2 multilayer structures

This section shows first spin pumping measurements of F1/N/F2 multilayer structures consisting of a normal metal layer ($t_N = 7\,\text{nm}$) sandwiched between two different ferromagnetic layers (F1 and F2 with $t_{F1} = t_{F2} = 10\,\text{nm}$). Among other things, these measurements allow to unambiguously determine the relative spin orientation of the emitted spin current. Figure 3.33 shows a comparison of FMR and V_{DC} for two of such tri-layer structures, Co/Pt/Ni (panels (a-c)) and Fe/Pt/Ni (panels (d-f)) for two magnetic field orientations ($\phi = 0°$ and $180°$). The V_{DC} trace of the Co/Pt/Ni tri-layer in panel (a) for $\phi = 0°$ (black squares) clearly shows two separated peaks: a maximum at $60\,\text{mT}$ (corresponding to the Co-FMR) and a minimum at $193\,\text{mT}$ (corresponding to the Ni-FMR). An inversion of the magnetic field direction ($\phi = 180°$, red open circles) leads to a sign change of both extrema. On the first glance, in the corresponding FMR data (Fig. 3.33(b)), just a single resonance at $60\,\text{mT}$ (Co-FMR) can be observed. Only a zoom reveals a second resonance at the position of the minimum of V_{DC} at $193\,\text{mT}$ (Ni-FMR) (Fig. 3.33(c)). There is no change of the FMR signal upon field inversion ($\phi = 0°$; $\phi = 180°$). The small peak dip structure at $155\,\text{mT}$ is due to the sample holder, and consequently has no correspondence in V_{DC}. The data for the second tri-layer – Fe/Pt/Ni – exhibit an identical phenomenology but a different magnitude.

Our data can be interpreted as follows: the FMR of the first F layer generates a spin current which diffuses into the Pt, where it causes a detectable charge current via the inverse spin Hall effect. At another value of H, the second F layer is in resonance and emits a spin current which again diffuses into the Pt layer and generates a charge current. Here, it is assumed that the entire spin current is absorbed within the Pt layer and the two F layers do not interact.

From the different signs of the extrema in V_{DC} for $\phi = 0°$, the relative spin orientation of the emitted spin current can be deduced. Therefore, we consider

Figure 3.33: FMR and V_{DC} of a (a-c) Co/Pt/Ni ($10\,\text{nm}/7\,\text{nm}/10\,\text{nm}$) and a (d-f) Fe/Pt/Ni ($10\,\text{nm}/7\,\text{nm}/10\,\text{nm}$) tri-layer, where the layer thicknesses are given in brackets. (a,d) DC voltage for two oppositely oriented magnetic field orientations. Clearly, one maximum and one minimum for each field orientation can be discerned. Both reverse sign under field inversion. (b,e) On the first glance, the FMR exhibits only one peak-dip structure which does not change under field inversion. (c,f) Zoom in the region of the Ni FMR. Clearly, the second FMR can be observed.

$\mathbf{J}_c^{ISH} \propto [\hat{\mathbf{z}} \times \hat{\mathbf{s}}]$ (Eq. (2.15)) with the flow direction $\hat{\mathbf{z}}$ and the spin orientation $\hat{\mathbf{s}}$ of the spin current. For the tri-layer, the spin current flow direction is inverted between the two FMRs. At the Ni-FMR, $\mathbf{J}_s$ diffuses "downwards" from the Ni into the Pt layer, whereas at the Co/Fe-FMR, $\mathbf{J}_s$ diffuses "upwards" from the Co/Fe into the Pt layer (Figs. 3.33(a,d)). As V_{DC}^{ISH} ($\propto \mathbf{J}_c^{ISH}$) changes sign, and the flow directions is inverted, one finds that the spin orientation $\hat{\mathbf{s}}$ of the spin current entering the Pt layer has to be oriented in the same direction for both ferromagnetic layers. From band-structure calculations [23, 93], it is known that for Ni and Co the density of states at the Fermi energy is much higher for the minority spin band, whereas for Fe, the density of the majority spin band dominates. As $\hat{\mathbf{s}}$ is identical for all investigated ferromagnets, our findings prove that not the spin orientation of the dominating density of states at the Fermi energy defines the spin orientation of the generated spin current. It is rather defined by the relaxation process of the magnetization given by Eq. (3.5).

Our measurements confirm the applicability of the spin pumping principle to multilayer structures. They furthermore open the way for studies of the interaction of pure spin currents emitted from one F layer with another ferromagnetic thin film. This can be achieved by varying the ratio of spin diffusion length to normal metal interlayer thickness. In this case, a pure (possibly dissipationless) spin current acts on the magnetization of the second ferromagnet in contrast to conventional spin torque measurements, where the spin angular momentum is accompanied by a flow of charge.

3.4.13 Pure spin currents through normal metal interlayers

In the following, spin pumping experiments on tri-layer samples F/N1/N2 (Fig. 3.34) with one ferromagnetic layer F and two normal metal layers N1 and N2 are discussed. Hereby, the thicknesses $t_F = 10\,\text{nm}$ and $t_2 = 7\,\text{nm}$ are fixed, whereas the thickness t_1 of the interlayer is varied. For our experiments, Co was chosen as F layer, since
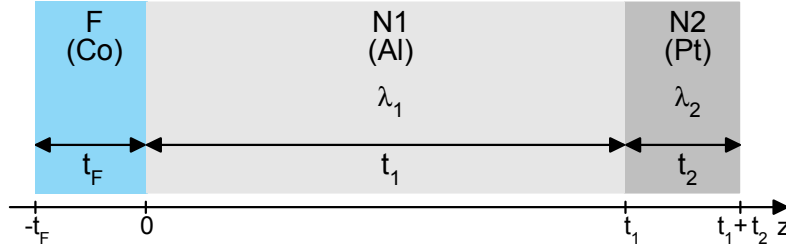
Figure 3.34: F/N1/N2 tri-layer geometry with thicknesses t_1, t_2 and spin diffusion lengths λ_1, λ_2 of the normal metals N1, N2, respectively.

it generates a large spin pumping signal (see Fig. 3.12). Pt, a material being a good spin sink with a large spin flip probability $\epsilon \gtrsim 10^{-2}$ [8] (see Sec. 3.3.2) was selected for N2, and Al, a material being a less good spin sink $\epsilon \lesssim 10^{-2}$ but with a long spin flip length [8, 132] for the interlayer N1.

Figure 3.35(a) shows normalized FMR traces obtained from FMR/spin pumping measurements for samples with Al layer thicknesses of $t_{Al} = 0\,\text{nm}$, $10\,\text{nm}$ and $30\,\text{nm}$. The extracted peak-to-peak linewidth ΔH_{pp} of all studied samples is plotted in Fig. 3.35(b). ΔH_{pp} slightly decreases with increasing Al layer thickness from about $7.3\,\text{mT}$ for $t_{Al} = 0\,\text{nm}$ to about $4.7\,\text{mT}$ for $t_{Al} = 30\,\text{nm}$. A clear decrease of ΔH_{pp} with increasing interlayer thickness was observed by Mizukami *et al.* [176] for Cu/Py/Cu 2/Pt films where the thickness of the Cu 2 layer (t_{Cu}) was varied. These results were interpreted as follows [7, 8, 176]: in the case of large damping ($t_{Cu} = 0\,\text{nm}$) the spin current, emitted from the F layer, is absorbed within the Pt
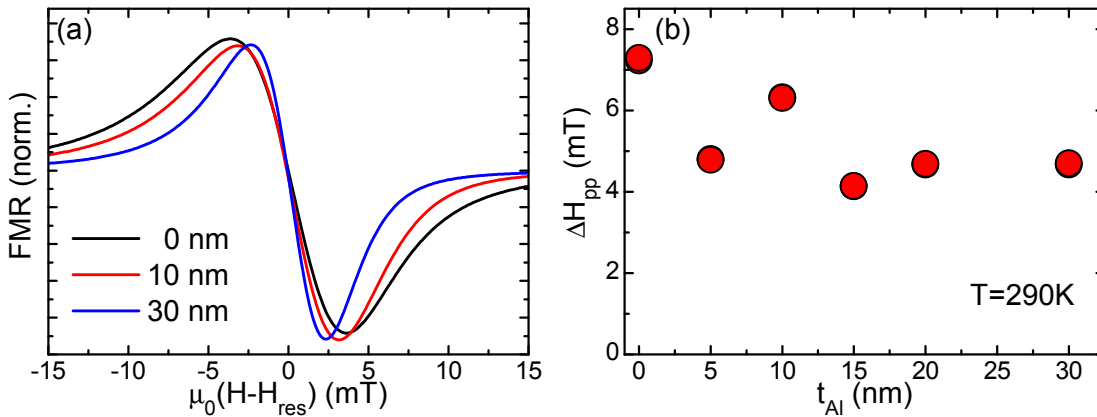
Figure 3.35: (a) FMR traces of Co/Al/Pt ($10\,\text{nm}/t_{Al}/7\,\text{nm}$) heterostructures for different Al layer thicknesses t_{Al}. (b) ΔH_{pp} versus t_{Al}. With increasing Al layer thickness, the linewidth and thus also the damping slightly decrease.
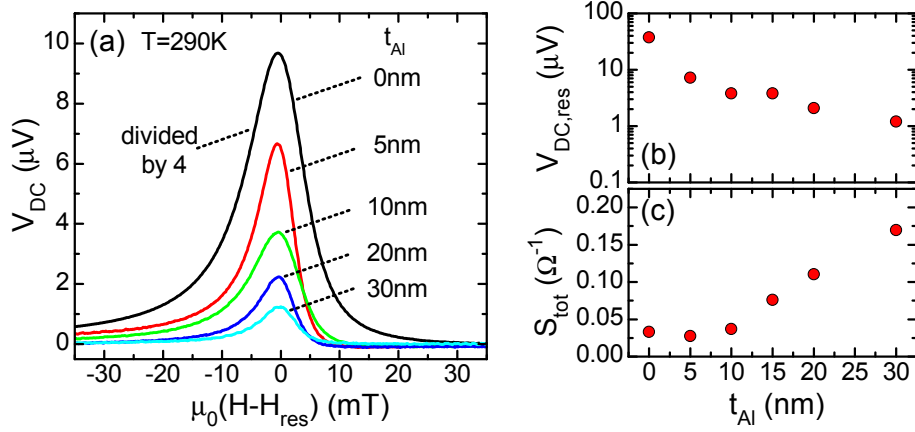
Figure 3.36: (a) V_{DC} co-occurring with the FMR for various Co/Al/Pt heterostructures with different thicknesses of the Al layer $0\,\text{nm} \leq t_{Al} \leq 30\,\text{nm}$. The signal for the sample without Al interlayer ($t_{Al} = 0\,\text{nm}$) is divided by 4. (b) $V_{ISH,res}$ versus t_{Al}. (c) "Weighted conductivity" $S_{tot} = \sigma_{Al}t_{Al} + \sigma_{Pt}t_{Pt} + \sigma_{Co}t_{Co} = L/(R_{tot}\,w)$ versus t_{Al} for sample dimensions $L = 3\,\text{mm}$ and $w = 1\,\text{mm}$.

layer due to the large spin flip probability in Pt. This leads to a loss of angular momentum of the magnetization precession and thus to additional damping of the FMR which results in an increased linewidth ΔH_{pp}. When introducing a Cu interlayer with small ϵ, the emitted spin current is partly reabsorbed by the Py layer. This reduces the loss of angular momentum of the precessing ferromagnet. With increasing t_{Cu}, more and more spin current is reabsorbed without spin relaxation which explains the decrease of damping and of ΔH_{pp} with increasing t_{Cu} or t_{Al}. However, Mizukami *et al.* only performed FMR measurements and were thus limited to the interpretation of the linewidth. Our additional measurements of the DC voltage allow for a direct electrical detection of the spin current as discussed in the following.

Figure 3.36(a) shows the DC voltage obtained during spin pumping measurements for samples with different Al interlayer thicknesses t_{Al}. For all studied samples, a spin pumping voltage co-occurring with the FMR could be observed. Thereby, $V_{DC,res}$ decreases with increasing t_{Al} from $37.4\,\mu\text{V}$ for $t_{Al} = 0\,\text{nm}$ to $1.2\,\mu\text{V}$ for $t_{Al} = 30\,\text{nm}$ as shown in Fig. 3.36(b). At the same time, the "weighted conductivity" of the trilayer samples $S_{tot} = \sigma_{Al}t_{Al} + \sigma_{Pt}t_{Pt} + \sigma_{Co}t_{Co}$ increases from $0.033\,\Omega^{-1}$ ($t_{Al} = 0\,\text{nm}$) to $0.169\,\Omega^{-1}$ ($t_{Al} = 30\,\text{nm}$) as presented in Fig. 3.36(c).

The fact that a peak in the DC voltage at H_{res} occurs for all studied samples demonstrates that spin current generated by the F layer can be injected into the Al layer, can diffuse through it, and can cross the Al/Pt interface. Only in the Pt layer, the spin current is converted into a charge current generating a DC voltage.

The large difference – a factor of five – between the V_{DC} signal for $t_{Al} = 0\,\text{nm}$ and $5\,\text{nm}$ contradicts microwave rectification as the origin of our observations. If the generated voltage was just due to microwave rectification in the ferromagnetic layer, the only difference between the two samples should be their conductivity. However,

the conductivity differs only by a factor of 1.2. In contrast, spin pumping theory can naturally explain our observations as discussed in the following.

To analyze the experimental data, we calculate the DC voltage predicted by spin pumping theory [7, 8]. In analogy to Eq. (3.19), the electric field along the measurement direction y for the tri-layer geometry is given by

$$E_{\text{comp}} = \frac{-\int_{t_1}^{t_1+t_2} J_{\text{c}}^{\text{ISH}}(z)\,dz}{S_{\text{tot}}} \tag{3.52}$$

with the "weighted conductivity"

$$S_{\text{tot}} := (t_1 + t_2 + t_{\text{F}})\,\sigma_{\text{tot}} = \sigma_1 t_1 + \sigma_2 t_2 + \sigma_{\text{F}} t_{\text{F}} = L/(R_{\text{tot}}\,w). \tag{3.53}$$

S_{tot} can thus be determined experimentally from the sample resistance R_{tot}, the sample length L and the width w. The integration limits in Eq. (3.52) take into account that the inverse spin Hall effect in the Al layer is negligible in comparison to the one in Pt [68, 33]. Therefore, $J_{\text{c}}^{\text{ISH}}$ is generated only inside the Pt. With $V_{\text{ISH}} = E_{\text{comp}} \cdot L$, Eq. (3.52) transforms into

$$V_{\text{ISH}}\,S_{\text{tot}} = -L \int_{t_1}^{t_1+t_2} J_{\text{c}}^{\text{ISH}}(z)\,dz. \tag{3.54}$$

Using Eq. (2.15) for $J_{\text{c}}^{\text{ISH}}(z)$ and carrying out the integration results in

$$V_{\text{ISH}}S_{\text{tot}} = \left[L\,\alpha_{\text{SH}}\frac{2e}{\hbar}\lambda_{\text{SD}}\tanh\frac{t_2}{2\lambda_{\text{SD}}}\right] J_{\text{s,N2}}^0 \tag{3.55}$$

with $J_{\text{s,N2}}^0$ being the spin current density in N2 at $z = t_1$ which crossed the N1/N2 interface.

Since the expression in brackets in Eq. (3.55) is independent of the N1 layer and thus identical for all investigated samples in this section, we set $[L\,\alpha_{\text{SH}}\frac{2e}{\hbar}\lambda_{\text{SD}}$ $\tanh\frac{t_2}{2\lambda_{\text{SD}}}] \equiv 1/D$. Equation (3.55) then reads

$$V_{\text{ISH}}S_{\text{tot}}D = J_{\text{s,N2}}^0 \tag{3.56}$$

which enables to experimentally determine the spin current density $J_{\text{s,N2}}^0$ in N2 at the N1/N2 interface and compare it between the different samples. Using the room temperature values $\alpha_{\text{SH}} = 0.013$ and $\lambda_{\text{SD}} = 10\,\text{nm}$ for Pt [10, 160], and $L = 3\,\text{mm}$, we calculated $D = 3.81 \times 10^{12}\,\frac{\hbar}{\text{e}\,\text{m}^2}$.

Figure 3.37 displays $J_{\text{s,N2,res}}^0 = V_{\text{ISH,res}}S_{\text{tot}}D$ versus the thickness of the Al layer t_{Al}. For the sample without Al layer ($t_{\text{Al}} = 0\,\text{nm}$), a value of $J_{\text{s,N2,res}}^0 = 4.7\,\text{A}\hbar/\text{m}^2\text{e}$ is observed. When introducing the Al interlayer, $J_{\text{s,N2,res}}^0$ drops by a factor of more than five and remains on a similar level ($0.54\,\text{A}\hbar/\text{m}^2\text{e} \leq J_{\text{s,N2,res}}^0 \leq 1.1\,\text{A}\hbar/\text{m}^2\text{e}$) up to the largest studied interlayer thickness of $t_{\text{Al}} = 30\,\text{nm}$. Thus, the presence of an Al interlayer drastically reduces the spin current density entering the Pt layer.

One reason might be that the spin mixing conductance $g^{\uparrow\downarrow}$ is strongly different for Co/Pt and Co/Al interfaces. To calculate these values exactly, first principle band-structure calculations as performed in Refs. [86, 87] are needed. As no values exist for
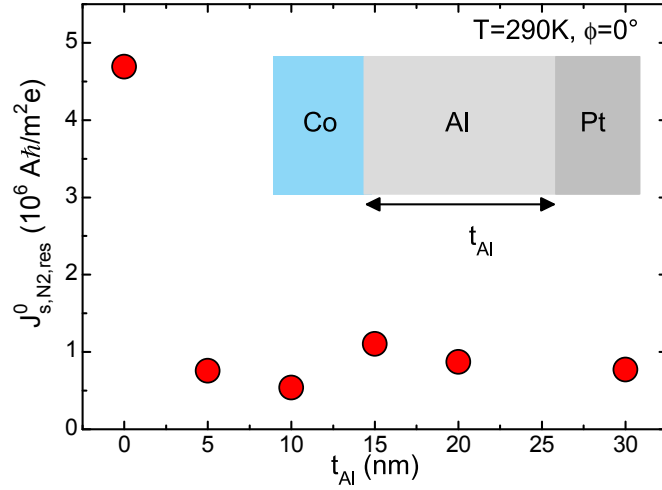
Figure 3.37: $J^0_{s,N2,res}$ versus thickness t_{Al} of the Al interlayer. For vanishing interlayer ($t_{Al} = 0\,\mathrm{nm}$), a value of $4.7\,\mathrm{A}\hbar/\mathrm{m}^2\mathrm{e}$ is observed. When an Al interlayer is present, $J^0_{s,N2,res}$ is significantly decreased. For all studied samples with $t_{Al} \neq 0\,\mathrm{nm}$, values around $0.85\,\mathrm{A}\hbar/\mathrm{m}^2\mathrm{e}$ were found.

these interfaces, we use the model of a free electron gas as given by Eq. (3.6). With the Fermi energies of Pt ($E_{F,Pt} = 8.77\,\mathrm{eV}$ [177]) and Al ($E_{F,Al} = 11.7\,\mathrm{eV}$ [178]), one obtains spin mixing conductances $g^{\uparrow\downarrow}_{Pt} = 1.84 \times 10^{19}\,\mathrm{m}^{-2}$ and $g^{\uparrow\downarrow}_{Al} = 2.44 \times 10^{19}\,\mathrm{m}^{-2}$. The values differ by a factor of around 1.3 and $g^{\uparrow\downarrow}_{Al}$ is larger than $g^{\uparrow\downarrow}_{Pt}$ which should result in a larger spin current for Co/Al than for Co/Pt. Thus, within the limits of this model, the difference in $g^{\uparrow\downarrow}$ cannot explain our observations.

Another reason for the strongly reduced spin current entering the Pt layer when an Al interlayer is present can originate from the spin diffusion and relaxation processes in the normal metal layers. To get an impression of the spin current profile over the sample thickness, we solve the spin diffusion equation (Eq. 3.11) for the two normal metal layers. As boundary conditions

$$J_{s,N1}(0)\,\hat{\mathbf{s}} = J^0_{s,N1}\,\hat{\mathbf{s}} = -\frac{\hbar}{2e}\frac{\sigma}{e}\frac{\partial\boldsymbol{\mu}_{s,N1}}{\partial z}\bigg|_{z=0} \quad \text{and}$$

$$J_{s,N2}(t_1 + t_2)\,\hat{\mathbf{s}} = 0 = -\frac{\hbar}{2e}\frac{\sigma}{e}\frac{\partial\boldsymbol{\mu}_{s,N2}}{\partial z}\bigg|_{z=t_1+t_2} \tag{3.57}$$

for the F/N1 ($z = 0$) and the N2/vacuum ($z = t_1+t_2$) interfaces are used. Moreover, we demand continuity of the spin accumulation and the spin current density at the N1/N2 ($z = t_1$) interface:

$$\boldsymbol{\mu}_{s,N1}\big|_{z=t_1} = \boldsymbol{\mu}_{s,N2}\big|_{z=t_1}, \quad J_{s,N1}(t_1)\,\hat{\mathbf{s}} = J_{s,N2}(t_1)\,\hat{\mathbf{s}}. \tag{3.58}$$

With these conditions, we obtain the spin current density $J_{s,N1}(z)$ in N1 and $J_{s,N2}(z)$ in N2:
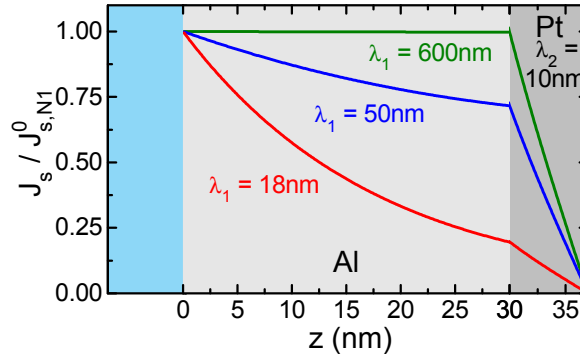
Figure 3.38: Spin current density versus z for a Co/Al/Pt heterostructure with $t_1 = t_{Al} = 30$ nm for different values of the spin diffusion length λ_1 in Al.

$$J_{s,N1}(z) = J_{s,N1}^0 \frac{e^{\frac{2(\lambda_1+\lambda_2)t_1}{\lambda_1\lambda_2}}(\lambda_1-\lambda_2)+e^{\frac{2t_1+t_2}{\lambda_2}+\frac{2z}{\lambda_1}}(\lambda_2-\lambda_1)-e^{\frac{2t_1}{\lambda_1}+\frac{2t_1+t_2}{\lambda_2}}(\lambda_1+\lambda_2)+e^{\frac{2t_1}{\lambda_2}+\frac{2z}{\lambda_1}}(\lambda_1+\lambda_2)}{e^{\frac{z}{\lambda_1}}\left(e^{\frac{2(\lambda_1+\lambda_2)t_1}{\lambda_1\lambda_2}}(\lambda_1-\lambda_2)+e^{\frac{2t_1+t_2}{\lambda_2}}(\lambda_2-\lambda_1)+e^{\frac{2t_1}{\lambda_2}}(\lambda_1+\lambda_2)-e^{\frac{2t_1}{\lambda_1}+\frac{2t_1+t_2}{\lambda_2}}(\lambda_1+\lambda_2)\right)},$$

$$J_{s,N2}(z) = J_{s,N1}^0 \frac{2e^{\frac{(\lambda_1+\lambda_2)t_1-\lambda_1 z}{\lambda_1\lambda_2}}\left(-e^{\frac{2t_1+t_2}{\lambda_2}}+e^{\frac{2z}{\lambda_2}}\right)\lambda_1}{e^{\frac{2(\lambda_1+\lambda_2)t_1}{\lambda_1\lambda_2}}(\lambda_1-\lambda_2)+e^{\frac{2t_1+t_2}{\lambda_2}}(\lambda_2-\lambda_1)+e^{\frac{2t_1}{\lambda_2}}(\lambda_1+\lambda_2)-e^{\frac{2t_1}{\lambda_1}+\frac{2t_1+t_2}{\lambda_2}}(\lambda_1+\lambda_2)}, \quad (3.59)$$

where λ_1 and λ_2 are the spin diffusion lengths in N1 and N2, respectively.

Figure 3.38 shows the calculated spin current density profile versus z for a Co/Al/ Pt sample with $t_1 = t_{Al} = 30$ nm, $t_2 = t_{Pt} = 7$ nm, $\lambda_2 = 10$ nm [10, 160] and different spin diffusion lengths λ_1 in Al. For $\lambda_1 = 600$ nm [33], the spin current density within the Al layer is next to unchanged (green line in Fig. 3.38). 99.7% of the injected spin current reach the Pt layer. Even for an assumed very short spin diffusion length in Al of $\lambda_1 = 50$ nm (blue line), still 71.6% reach the Pt film. To obtain a value of around 20% as observed in experiment, a spin diffusion length of $\lambda_1 = 18$ nm (red line) has to be assumed which is very small compared to other experimental findings ranging between 330 nm $< \lambda_1 < 600$ nm [70].

In this simulation, no spin relaxation at the N1/N2 interface was assumed although strong spin-flip scattering might be possible as Al and Pt intermix [179]. Even $Pt_x Al_y$ alloys can form at temperatures as low as 225°C [180, 181] which might have been present due to the radiation heat during the Pt evaporation. Such a disordered interface leads to additional scattering which causes spin relaxation. Therefore, the magnitude of the spin current entering the Pt layer might be strongly reduced. Here, further theoretical and experimental work is needed.

Similar to our results, also Mizukami *et al.* [176] observed in their Cu/Py/Cu(t_{Cu})/ Pt heterostructures a significant decrease in damping (decrease of around 50 % in ΔH_{pp} from $t_{Cu} = 0$ nm to 3 nm) when the additional Cu layer was introduced. They concluded that an "intimate" contact to the Pt layer is needed.

To summarize, we found that a pure spin current can be detected after traversing a normal metal interlayer with a thickness up to $t_1 = 30$ nm. However, its intensity is strongly reduced which might be either due to spin relaxation in the interlayer or at the interface between the two normal metals.

3.5 Summary

In this chapter, we presented the concept of spin pumping and our experimental results in this field. The term "spin pumping" refers to the emission of a pure spin current from a ferromagnet into an adjacent normal metal due to a time-dependent magnetization. For the generation of the spin current, we employed a magnetization precession driven by ferromagnetic resonance. The inverse spin Hall effect is used as detection mechanism. First, a detailed theoretical explanation of the spin pumping process in combination with the inverse spin Hall effect was given (Sec. 3.2). This was contrasted to our calculations of DC voltages generated by microwave rectification due to a nonlinear interaction of the dynamic components of current density and magnetization performed in the spirit of the pioneering work by Juretschke [94] (Sec. 3.2.6).

To study spin pumping in combination with the inverse spin Hall effect, we performed simultaneous FMR and DC voltage measurements on various ferromagnet/Pt bilayer samples. We could unambiguously prove that the origin of the peak in the DC voltage – co-occurring with FMR – originates from spin pumping in combination with the inverse spin Hall effect and is not caused by microwave rectification (Sec. 3.4.2). This is based on two arguments: first, the observed signal symmetry with respect to the resonance field and the transformation of the signal upon magnetic field inversion is only compatible with spin pumping. Second, the fact that the same sign of V_{DC} is observed for all investigated samples at a fixed orientation of $\mathbf{H}$ is only compatible with spin pumping. If the signal was due to microwave rectification, its magnitude and sign should depend on the values of the spontaneous resistivity anisotropy or the anomalous Hall coefficient. This was not observed experimentally.

Moreover, fundamental properties as the geometry and power dependence of the spin pumping signal were investigated (Secs. 3.4.4 and 3.4.5). We experimentally demonstrated that V_{DC} is indeed independent of the sample width and proportional to its length and the microwave power as predicted by theory.

Furthermore, we experimentally proved that the present theories for spin pumping (Sec. 3.2) are not limited to transition metal-based bilayers but also apply to the ferromagnetic Heusler compounds Co_2FeAl and Co_2FeSi, the ferrimagnetic oxide spinel Fe_3O_4, and the dilute magnetic semiconductor (Ga,Mn)As (Sec. 3.4.7). This could be shown by scaling plots of V_{DC} (normalized to the relevant parameters) versus $\sin^2 \Theta$, where Θ is the precession cone angle of the magnetization. A linear scaling was observed over more than four orders of magnitude, in full agreement with the theoretical predictions. Additionally, the spin mixing conductance $g^{\uparrow\downarrow}$, a crucial parameter for spin transfer torque, spin Seebeck [17] and spin pumping measurements, was experimentally quantified (Sec. 3.4.9). We found that $g^{\uparrow\downarrow}$ is essentially independent of the ferromagnetic layer properties for conductive ferromagnets as predicted by theory with $g^{\uparrow\downarrow} = (4 \pm 3) \times 10^{19}\,\mathrm{m}^{-2}$. For the low-conductivity ferromagnet Fe_3O_4, a value by a factor of six smaller was obtained, and $g^{\uparrow\downarrow}$ for the dilute magnetic semiconductor (Ga,Mn)As/Pt interface lies between these values. In this context, we also performed (to our knowledge the first) temperature dependent ($2\,\mathrm{K} < T < 290\,\mathrm{K}$) spin pumping measurements in combination with the

inverse spin Hall effect. We found that $g^{\uparrow\downarrow}$ is essentially temperature independent which can be understood considering the temperature dependencies of the different parameters.

Subsequently, the influence of the magnetic field orientation on the spin pumping signal was investigated for two samples, one polycrystalline F/Pt (Ni/Pt) and one epitaxial F/Pt ((Ga,Mn)As/Pt) sample (Secs. 3.4.10 and 3.4.11). The measurement of the Ni/Pt bilayer enabled to confirm that indeed the magnetization orientation determines the spin orientation $\hat{\mathbf{s}}$ of the spin current. The measurement of the (Ga,Mn)As/Pt sample allowed to investigate the (Ga,Mn)As spin wave spectrum and its influence on the spin pumping signal. In this context, the theoretical model by Hoekstra *et al.* [168] and Bihler *et al.* [136] for the FMR spectrum was extended to include the DC voltage generated by spin pumping. From these simulations, we concluded that the entire (Ga,Mn)As layer thickness contributes to the observed V_{DC} signal and not only the interface region.

Finally, the first spin pumping measurements on multilayer structures with more than two layers have been performed. From experiments on F1/N/F2 tri-layers with two different ferromagnets (Sec. 3.4.12), it was possible to unambiguously determine the relative spin orientation $\hat{\mathbf{s}}$ of the spin currents emitted by the F layers. It could be confirmed that the spin orientation is not determined by the majority spin band but by the relaxation process of the magnetization. Finally, we studied F/N1/N2 tri-layer structures with an interlayer N1 of variable thickness t_{N1} separating spin current generation (F) and detection (N2) (Sec. 3.4.13). Aluminum, a material with a long spin diffusion length was chosen for N1 and Pt with a short one for N2. We could show that it is possible to inject a pure spin current from F into N1 and subsequently detect it in N2 up to an interlayer thickness of $t_{\mathrm{N1}} = 30\,\mathrm{nm}$. The magnitude of the spin current entering the Pt layer decreased by a factor of about five if an interlayer is present, but it is independent of t_{N1} in the investigated region ($5\,\mathrm{nm} < t_{\mathrm{N1}} < 30\,\mathrm{nm}$). This can be explained by spin relaxation in N1 or by spin flip scattering at the N1/N2 interface.

To summarize, we successfully performed extensive spin pumping experiments, where the spin currents are detected utilizing the inverse spin Hall effect. Our experiments on more than 80 different N/F multilayer systems considerably extended the present spin pumping data and allowed to confirm several important predictions from spin pumping theory.

An outlook on the effects discussed here is given in Chapter 5.

Chapter 4

Non-local spin current sources

Hankiewicz *et al.* [14] and Abanin *et al.* [15] put forward an idea to generate and detect spin currents which impresses by its simplicity. It frees spin current generation of certain constraints associated with the spin current source concept presented in the previous chapter. Drawbacks are, for instance, the need of heterostructures to separate generation and detection of the spin current and the thus comprised interfaces causing spin-flip scattering. Moreover, a complex measurement setup providing microwaves and static magnetic fields is required. The idea presented here requires just an H-shaped structure from a single non-magnetic electrical conductor, a conventional current source, and a multimeter.
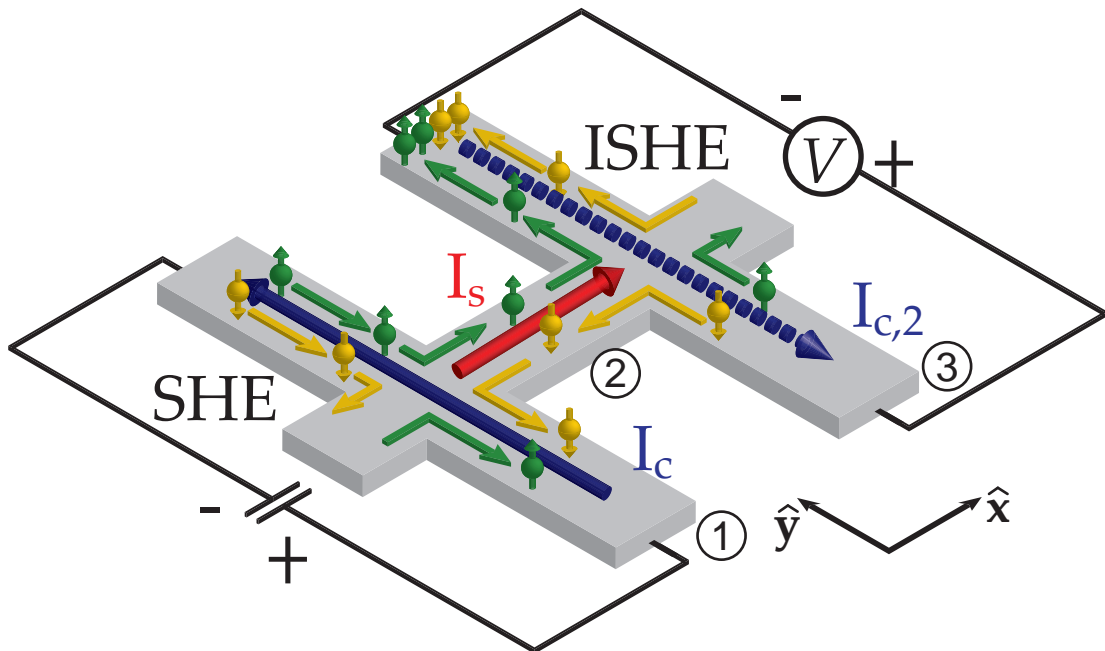
Figure 4.1: Generation and detection principle of a pure spin current via an H-shaped structure made of a single electrical conductor. An applied charge current I_c in wire (1) generates a pure spin current I_s in a bridging wire (2) via the spin Hall effect. This spin current, in turn, causes a pure charge current $I_{c,2}$ in wire (3) via the inverse spin Hall effect. Under open circuit conditions, $I_{c,2}$ is compensated for by an electric field causing a non-local voltage which can be detected by conventional electronics. Illustration in analogy to [31].

The concept is illustrated in Fig. 4.1: in wire (1), a charge current I_c from a conventional charge current source is applied. Due to the spin Hall effect (see Sec. 2.3), spin-up (green) and spin-down (yellow) charge carriers are deflected to opposite sides of the wire. This creates a pure spin current I_s (red arrow) which diffuses along the bridging wire (2). This pure spin current now generates a pure charge current $I_{c,2}$ via the inverse spin Hall effect in wire (3). Under open circuit conditions, this charge current causes a charge accumulation and thus a non-local potential difference along wire (3) which can be detected via a conventional multimeter.

Recently, the concept presented here was reported to be experimentally confirmed in high-mobility semiconductor structures made of HgTe/(Hg, Cd)Te quantum wells [182]. However, for metallic structures, there is only one publication by Mihajlović *et al.* [183], where surprising experimental data of one single sample are presented which are not fully understood so far. Therefore, we performed calculations (see Sec. 4.1.3) which show that for Au nanowires with wire widths below 100 nm, a demonstration of this spin-mediated effect should be possible. For the calculations, we assumed that the largest spin Hall angles α_{SH} published in the literature [68] indeed are correct. Subsequently, we conducted extensive studies on various metallic devices to investigate this effect in detail.

This chapter is organized as follows: first, a theoretical introduction to non-local voltages including spin-mediated and diffusive effects is given. Then, the sample fabrication involving metallic nanowires with widths well below 100 nm and the low-level, low-noise measurement technique developed within this thesis are explained. After that, our measurements on various metallic nanostructures of different materials are presented. This is followed by a discussion of the results and the presentation of a theory framework which allows to consistently explain all our observations. Finally, an interesting discovery, closely related to the non-local measurement configuration is discussed: the non-local anisotropic magnetoresistance, which does not exponentially decrease with distance from the main current flow but even *increases* in magnitude.

A significant part of the experiments presented in this chapter was performed together with my diploma student Daniel Rüffer. A more detailed description of the sample fabrication and the development of the low-level measurement techniques can be found in his diploma thesis [31]. In this chapter, the emphasis lies on the analysis of the various data sets and their theoretical interpretation.

4.1 Theory of non-local voltages

Non-local voltages are potential differences arising in regions outside of the nominal current path[1]. When looking at Fig. 4.1, the intuitively expected current path of I_c is limited to wire (1), whereas the voltage is measured along wire (3). Thus, the voltage is non-local. In this section, two origins of such non-local voltages are presented. First, the concept developed by Hankiewicz *et al.* [14] and Abanin *et al.* [15], where the non-local voltage is spin current-mediated. Second, a non-local voltage due to diffusive transport is discussed. Finally, the magnitudes of the two effects are calculated for different materials and compared to each other.

4.1.1 Spin-mediated non-local resistance

As mentioned in the introduction of this chapter, a spin-mediated non-local voltage can be generated via a combination of spin Hall and inverse spin Hall effect. The situation is illustrated more schematically in Fig. 4.2, where the vertical wires (wire (1) and (3)) of the H-shaped structure are replaced by the point-like contacts of the current and voltage leads. An applied charge current I_c generates a transverse spin current I_s. This spin current diffuses through the material and creates a non-local charge current $I_{c,2}$. The range of non-locality L is given by the material specific spin diffusion length λ_{sd} (see Sec. 2.4).
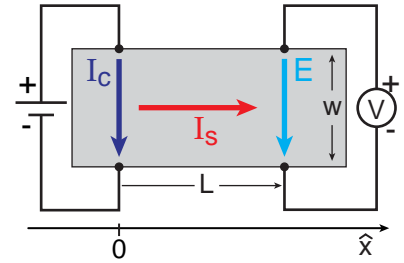
Fig. 4.2: Sketch of a spin-mediated non-local voltage at a distance L in a device of width w.

Under open circuit conditions, the non-local charge current causes a charge accumulation which results in a non-local compensating electric field E and thus a non-local voltage. The expected value of the non-local voltage is "positive" for a measurement configuration as shown in Fig. 4.2: "high" of the non-local voltage is at the same side of the wire (here at the top) as "high" of the current source. This can be understood when looking for example at a spin-up electron being injected into the structure from the current source (see Fig. 4.1). In the sketched case, it is deflected to its left and enters the bridging part (wire (2)). At the next intersection, it is again deflected to the left, as the same mechanism causes both the spin Hall effect and its inverse. Thus, at the left side of the wire (3) the charge carriers (here electrons) accumulate resulting in a low potential. For the contact configuration sketched in Figs. 4.1 and 4.2, which is used throughout this chapter, a positive non-local voltage is expected.

The magnitude of this non-local voltage $R_{NL}^{SH}(L)$ was calculated by Abanin *et al.* [15]. They started to determine the spin current by solving the one-dimensional spin diffusion equation (Eq. (3.11)). The results are restricted to the case, where the width w of the wire is much larger than the electron mean free path λ_t and much smaller than the spin diffusion length λ_{sd}, i.e., $\lambda_t \ll w \ll \lambda_{sd}$. In this diffusive case, the

---

[1]Actually, the transport related effects measured in the "non-local" measurement configuration (see Sec. 4.3.1) discussed in this chapter are "local" effects as (in the diffusive case) the current density at a position $\mathbf{r}$ solely depends on the electric field at the position $\mathbf{r}$: $\mathbf{J}(\mathbf{r}) = \sigma(\mathbf{r})\mathbf{E}(\mathbf{r})$. However, we adapt the terminology used by the community for this measurement configuration and also call the transport related effects measured in this configuration "non-local".

spin current at a distance L from the current leads is given by [15]

$$I_{\rm s}(L) = \frac{1}{2}\alpha_{\rm SH}I_{\rm c}\frac{\hbar}{2q}\frac{w}{\lambda_{\rm sd}}\exp\left(-\frac{|L|}{\lambda_{\rm sd}}\right) \tag{4.1}$$

with the spin Hall angle $\alpha_{\rm SH}$, the applied charge current $I_{\rm c}$, and carriers with charge q and spin angular momentum $\hbar/2$.

This spin current generates a transverse charge current via the inverse spin Hall effect according to Eq. (2.15). Under open circuit conditions, this charge current creates a non-local voltage

$$V_{\rm NL}^{\rm SH}(L) = wE(L) = \frac{\rho}{t}I_{\rm c,2}(L) = \alpha_{\rm SH}\left(\frac{2q}{\hbar}\right)\frac{\rho}{t}I_{\rm s}(L), \tag{4.2}$$

where t is the thickness and ρ the resistivity of the device. With Eq. (4.1), one obtains the spin-mediated non-local resistance $R_{\rm NL}^{\rm SH}(L) = V_{\rm NL}^{\rm SH}(L)/I_{\rm c}$ at the distance L [15]:

$$R_{\rm NL}^{\rm SH}(L) = \frac{1}{2}\alpha_{\rm SH}^2\frac{\rho}{t}\cdot\frac{w}{\lambda_{\rm sd}}\exp\left(-\frac{L}{\lambda_{\rm sd}}\right). \tag{4.3}$$

It decays as $\lambda_{\rm sd}^{-1}\cdot\exp(-|L|/\lambda_{\rm sd})$ and is independent of the charge q. Note that $R_{\rm NL}^{\rm SH}(L)$ is a normalized voltage signal and thus can also be negative. However, as the same conversion process enters twice, the magnitude of $R_{\rm NL}^{\rm SH}(L)$ quadratically depends on the spin Hall angle and therefore is *strictly positive*.

4.1.2 Transport related non-local phenomena: current spreading
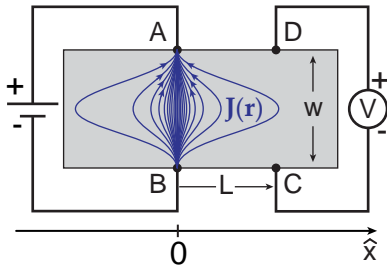
Fig. 4.3: Sketch of the current paths in a diffusive conductor of width w with point-like current and voltage leads.

Not only spin-related non-local effects but also classic transport phenomena generate non-local voltages[1]. In this case, the mean free path $\lambda_{\rm t}$ sets the relevant length scale. Two situations can be discerned:

In the diffusive transport regime, $\lambda_{\rm t}$ is much smaller than the relevant sample dimensions, whereas in the ballistic regime, it is much larger [184]. As we expect the mean free path to be smaller than the device dimensions in our polycrystalline, metallic samples, this section concentrates on the diffusive regime.

A current injected at point A into a diffusive material $(L, w \gg \lambda_{\rm t})$ does not exclusively flow via the shortest path to the extraction point B, but it spreads into the material as sketched in Fig. 4.3. Again, the vertical wires are replaced by the point-like current and voltage leads. A simple analytical solution to the problem can be obtained by employing the van-der-Pauw theorem [185]

$$\exp\left(-\frac{\pi t}{\rho}R_{\rm AB,CD}\right) + \exp\left(-\frac{\pi t}{\rho}R_{\rm BC,DA}\right) = 1. \tag{4.4}$$

It applies for homogeneous, isotropic, hole-free samples with thickness t, resistivity ρ and four point-like contacts A, B, C and D. $R_{\mathrm{AB,CD}}$ is defined as the voltage difference $V_{\mathrm{D}} - V_{\mathrm{C}}$ of point D and C divided by the current I between A and B, and $R_{\mathrm{BC,DA}}$ as the respective permutation. In the situation shown above, $R_{\mathrm{AB,CD}}$ corresponds to the non-local resistance $R_{\mathrm{NL}}^{\mathrm{CS}}$, and $R_{\mathrm{BC,DA}}$ to a local resistance for $L \gg w$ which is then given by $R_{\mathrm{BC,DA}} = \rho L/(wt)$. When expanding the first exponential function of Eq. (4.4)[2], the non-local resistance due to current spreading is obtained:

$$R_{\mathrm{NL}}^{\mathrm{CS}}\left(L\right) = \frac{\rho}{\pi t} \exp\left(-\frac{\pi L}{w}\right). \tag{4.5}$$

It decays on a length scale w/π which is solely determined by the device geometry.

A numerically calculated voltage profile taking into account the finite width of the contacts is discussed in Sec. 4.4.3.

4.1.3 Comparison of non-local resistance magnitudes

In the previous sections, two mechanisms generating non-local signals were presented. Now, the magnitudes of the non-local resistances are compared. This comparison is essential, as it shows whether a device layout can be designed which enables the spin-mediated effect to dominate over the current spreading.

Figure 4.4 displays calculations of the spin-mediated non-local resistance R^{SH} and the non-local resistance due to current spreading R^{CS} for different materials using Eqs. (4.3) and (4.5).

The results for Au devices are presented in Fig. 4.4(a) using the recently published large spin Hall angle $\alpha_{\mathrm{SH}} = 0.113$ [68], a spin diffusion length of $\lambda_{\mathrm{sd}} = 168\,\mathrm{nm}$ [186], a resistivity of $\rho = 2.271\,\Omega\mathrm{cm}$ [187] at $T = 300\,\mathrm{K}$, and a sample thickness of $t = 50\,\mathrm{nm}$. R^{SH} is shown as solid lines for three different ranges of non-locality: $L = 150\,\mathrm{nm}$, $200\,\mathrm{nm}$ and $225\,\mathrm{nm}$. It increases linearly with the wire width w, and for larger L, smaller values of R^{SH} are obtained. The non-local resistance due to diffusive current spreading R^{CS} is shown as dotted lines for the same three distances L. For very narrow wires ($w \ll 75\,\mathrm{nm}$), R^{CS} is negligible but starts to increase rapidly at $w \approx 75\,\mathrm{nm}$ and quickly exceeds the spin-mediated contribution R^{SH}. At a fixed value of w, R^{CS} decreases with increasing L.

In Fig. 4.4(a), the intersection of solid and dotted line of one color gives the wire width, where spin-mediated and diffusive contribution have the same size: $R^{\mathrm{SH}} = R^{\mathrm{CS}}$. When connecting these points for various L, one obtains the red bold line. For the parameters used, a maximum of $0.61\,\mathrm{m\Omega}$ at $w = 97\,\mathrm{nm}$ is obtained.

To detect the spin-mediated effect, R^{SH} has to dominate over R^{CS} which can be achieved by decreasing the wire width for a given L as explained in the following. When taking $L = 200\,\mathrm{nm}$ as an example, the intersection of the solid and dotted blue line occurs at $w = 115\,\mathrm{nm}$ and gives a value of $R_{\mathrm{NL}} = 0.6\,\mathrm{m\Omega}$ which is very close to the maximum. With decreasing w (while leaving L constant at $200\,\mathrm{nm}$), $R_{\mathrm{NL}}^{\mathrm{CS}}$ decreases exponentially, whereas the spin-mediated resistance decreases only linearly. This reveals a region where R^{SH} dominates the non-local resistance and measurements are promising.

---

[2]As the absolute magnitude of the argument of the first exponential function is small, it can be expanded as $\exp(x) \approx 1 + x$. For the second exponential function, this is not possible.
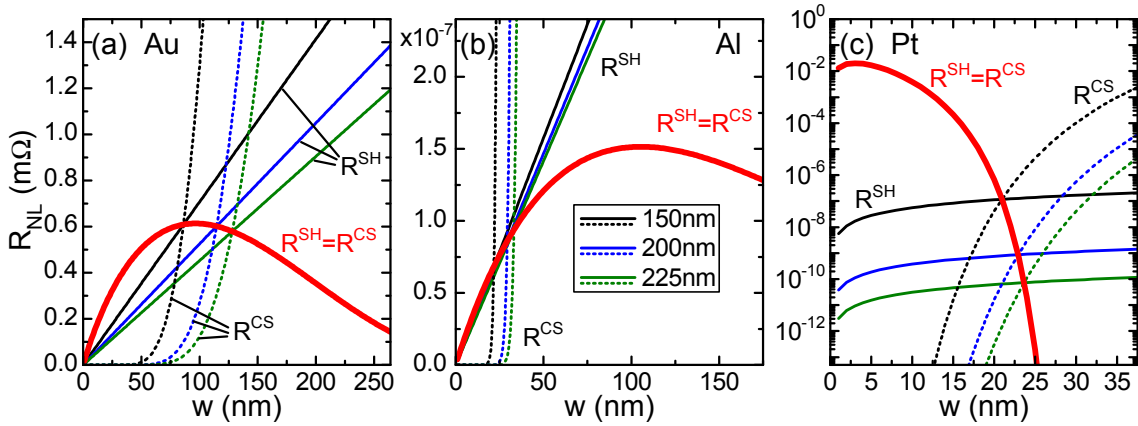
Figure 4.4: Comparison of non-local resistance magnitudes originating from diffusive current spreading R^{CS} (thin dotted lines) and from a combination of spin Hall and inverse spin Hall effect R^{SH} (thin solid lines). Both resistances are plotted for $L = 150\,\text{nm}$ (black), $200\,\text{nm}$ (blue), and $225\,\text{nm}$ (green) versus width w in (a) Au, (b) Al and (c) Pt. The thick red lines represent the value of R_{NL} for $R^{SH} = R^{CS}$.

Moreover, we performed calculations for two other metals with a very small spin Hall angle (Al, $\alpha_{SHE} = 1 \times 10^{-4}$ [188]) and a very large spin Hall angle (Pt, $\alpha_{SHE} = 0.013$ [10]). For Al, $\lambda_{sd} = 0.7\,\mu\text{m}$ [188, 189], $\rho = 2.733\,\Omega\text{cm}$ [187], and $t = 50\,\text{nm}$ were used, while for Pt, $\lambda_{sd} = 10\,\text{nm}$ [10, 160], $\rho = 10.8\,\Omega\text{cm}$ [187], and $t = 50\,\text{nm}$ were utilized.

The results for the same values of L as used in the case of Au are shown in Figs. 4.4(b,c). For Al, the maximum of the red curve ($R^{SH} = R^{CS}$) occurs for $w = 105\,\text{nm}$, but its magnitude of $1.5 \times 10^{-7}\,\text{m}\Omega$ is far below the achievable measurement resolution of about $4 - 7\,\text{nV}$ which corresponds to $40 - 70\,\mu\Omega$ for a maximum current of $100\,\mu\text{A}$ (see Sec. 4.3.1 and 4.3.3). For Pt (Fig. 4.4(c)), the maximum of the red curve is shifted to a width $w < 5\,\text{nm}$ due to the short spin diffusion length. For the values of L discussed previously, the non-local resistance is already smaller than $1 \times 10^{-7}\,\text{m}\Omega$ and thus far below the measurement resolution limit. Furthermore, the required wire width for measurements in the region of the maximum, $w < 10\,\text{nm}$, is much smaller than the minimum wire width of about $65\,\text{nm}$ achievable with the available equipment (see Sec. 4.2.1).

From our calculations, we conclude that the most promising material to observe the spin-mediated non-local resistance is Au. However, sample dimensions of L smaller than a few $100\,\text{nm}$ and wire widths smaller than $100\,\text{nm}$ are essential. This requires a highly optimized fabrication process. Moreover, the small magnitude of the non-local resistances requires advanced low-level measurement techniques with a resolution well below $0.5\,\text{m}\Omega$. For the two other materials Al and Pt, the extremely small values of the non-local resistance impede a detection of the spin-induced signal.

In the following section, we show that both sample fabrication and measurement technique can be optimized to an extent which should allow to detect the spin-mediated non-local resistance.

4.2 Experimental methods

First, the optimized sample fabrication process for nanostructures with dimensions below 100 nm is explained. Subsequently, the measurement setup and in particular the low-level measurement technique developed within this thesis are discussed which allow to resolve voltage signals in the nV-range.

4.2.1 Sample fabrication

For metallic nanostructures with dimensions below 100 nm, we chose a combination of optical and electron beam lithography, where each lithography step is followed by metal deposition and lift-off. Undoped (100)-oriented Si/SiO_x-wafers with a resistivity larger than $3000\,\Omega$cm and an oxide thickness of 50 nm were used as substrates. Due to the thick oxide, the substrate is insulating for the metal nanostructures, and at the same time, the thick Si wafer minimizes charging effects during electron-beam writing.
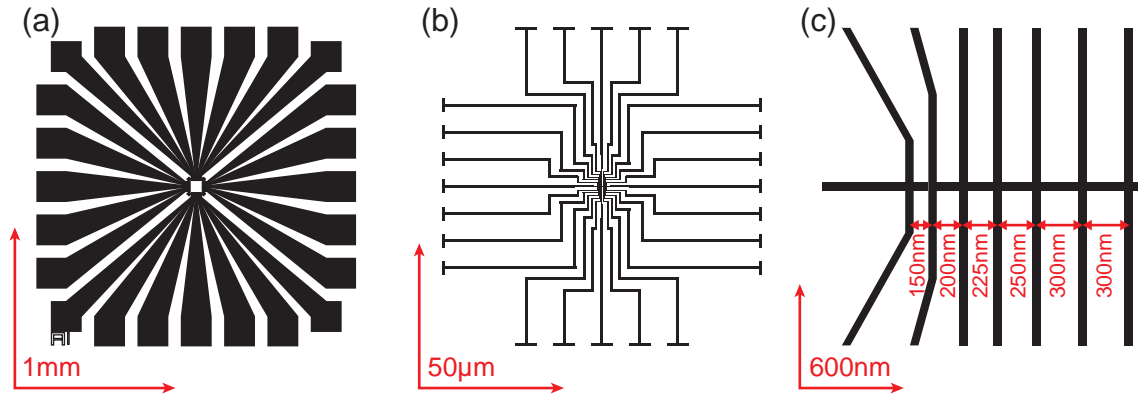
Figure 4.5: (a) Optically defined outer contact structures making the connection between inner nanostructures and bond wires. (b) Inner structures defined by electron beam lithography. (c) Actual design of the H-shaped nanowire device consisting of multiple parallel nanowires with different separations connected by one orthogonal bridging wire.

The outer contact structures (Fig. 4.5(a)) are defined by optical lithography. Using a MJB 3 HP/350W UV400 mask aligner from SÜSS MicroTec AG, the patterns from a chromium coated quartz glass mask are transferred to a photoresist (AZ® 5214E from MicroChemicals GmbH). After the development (AZ® Developer), a 25 nm thick layer of Au is deposited in an argon atmosphere of $p = 5 \times 10^{-2}$ mbar in a BAL-TEC MED 020 HR DC sputtering machine with a base pressure of 3×10^{-5} mbar.

The inner structures (Fig. 4.5(b)) are fabricated via electron beam lithography at 30 kV with a Philips XL30 SFEG scanning electron microscope equipped with the lithography software ELPHY Plus from Raith. The difficulty in the fabrication consists in the fact that multiple very narrow but very long nanowires have to be put very close together. This places high demands on resist and layout design. After an elaborate optimization process, a double layer of electron beam resist (both from MicroChem Corp.) was chosen with the highly sensitive PMMA 495K A6 (thickness
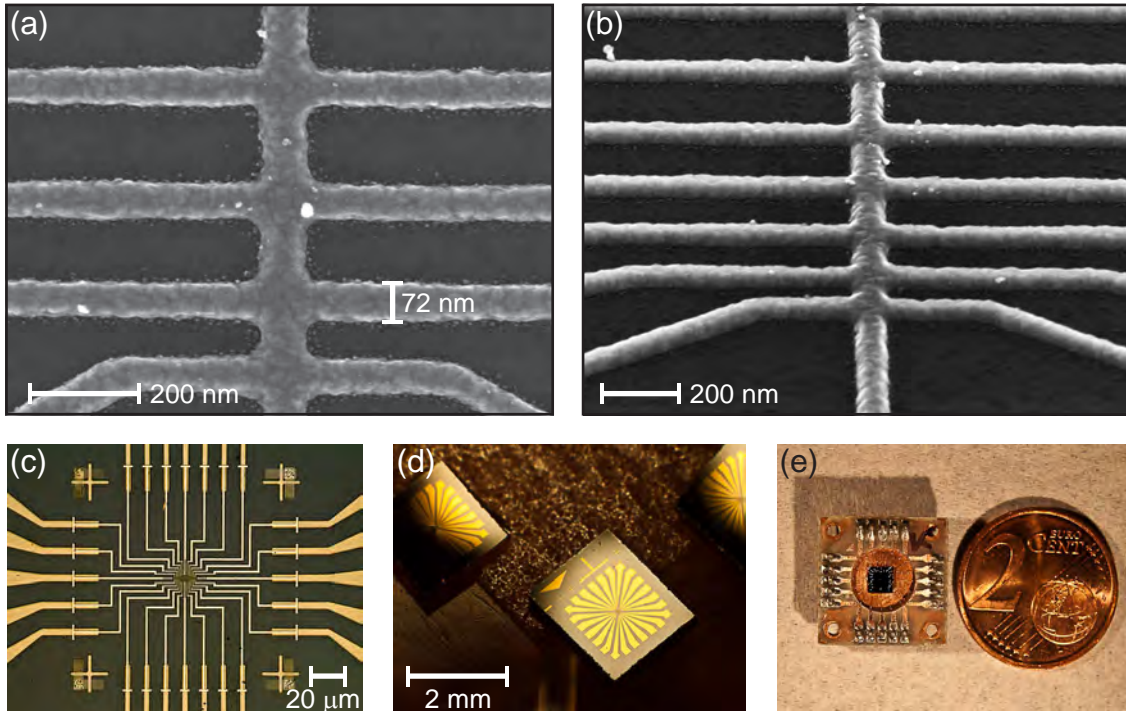
Figure 4.6: (a) Scanning electron microscope (SEM) image of 50 nm thick Au nano-
structures. Single grains can be resolved. (b) Tilted SEM image of Au nano-
structures. (c) Connecting region of inner and outer contact structures. (d) Photo-
graph of a chip after lithography and metal deposition. (e) Chip mounted on a chip
carrier and contacted via aluminum bond wires, ready to be measured. The orien-
tation of images (a) and (b) is rotated by 90° compared to the sketch in Fig. 4.5.

ca. 300 nm) as first layer and the less sensitive PMMA 950K A4 (thickness ca.
100 nm) as second layer. The double layer results in an undercut which simplifies the
lift-off process. The optimized layout design is shown in Fig. 4.5(c): multiple parallel,
vertical wires separated by $150\,\text{nm} \leq L \leq 300\,\text{nm}$ are orthogonally connected by one
horizontal bridging wire. This enables to investigate multiple wire-wire separations
in a single device. Note that the distances given are always measured from wire
center to wire center. After development (AR 600-56 from Allresist), a metallic thin
film is deposited. We fabricated nanostructures made from Au, Al, Pt, Fe, Ni and
Co with thicknesses between $26\,\text{nm} \leq t \leq 200\,\text{nm}$.

The metal layer is deposited either via electron beam evaporation or via an ef-
fusion cell. During electron beam evaporation, the target material is heated by an
electron beam and evaporates. Rates between $1.2\,\text{Å/s}$ and $12\,\text{Å/s}$, depending on the
respective material, were used. The base pressure of the system was $2 \times 10^{-8}\,\text{mbar}$.
Some of the Au samples were fabricated via a high temperature effusion cell, where
a cell temperature of 1530°C corresponds to a deposition rate of $0.2\,\text{Å/s}$. A very
smooth lift-off in hot acetone is used to reveal the nanostructures.

Typical samples obtained with the optimized parameters are presented in Fig. 4.6.
Uniform nanowires with dimensions down to ca. 65 nm and separations down to
70 nm can be fabricated for wire lengths of many micrometers.

4.2.2 Measurement Setup

The experimental study of nanostructures puts high demands on the electrical measurement setup. On the one hand, it has to protect the samples from electrostatic discharge, while at the same time, it has to provide a sufficiently small noise level. After a short description of the measurement environment, several sources of spurious signals are discussed. Finally, the optimized low-level measurement technique is presented.

4.2.2.1 Measurement environment

All measurements were performed in liquid helium magnet cryostats from Oxford Instruments with magnetic fields up to $14\,\mathrm{T}$ and temperatures ranging between $1.4\,\mathrm{K} \leq T \leq 350\,\mathrm{K}$. Via a stepper motor, the sample stage (dip stick) could be rotated with respect to the magnetic field.

All samples were mounted onto 20-pin chip carriers (Fig. 4.6(e)) and were contacted via aluminum bond wires. From the chip carrier, twisted copper wires lead to a so-called matrix module, where the measurement instrumentation is connected to the sample. The matrix module enables three states for each sample contact: grounded, floating, or connected to the instrument. This is essential for protecting the sensitive samples from electrostatic discharges (ESDs).

4.2.2.2 Spurious signals

Non-local voltage measurements in our devices require the detection of very small voltages (nV). Several spurious effects can distort the actual signal and impede an analysis. In the following, the most important effects are discussed briefly.

Thermal noise, also called *Johnson-Nyquist noise* or *white noise* is caused by the thermal fluctuations of the charge carriers inside an electrical conductor regardless of any applied bias [190, 191, 192]. For a resistor with resistance R at temperature T and the Boltzmann constant k_B, the power spectral density is given by $S_\mathrm{V,th} = 4k_\mathrm{B}TR$ in units of V^2/Hz. $S_\mathrm{V,th}$ is temperature dependent and constant over the whole frequency spectrum.

1/f noise, also called *pink noise, colored noise,* or *flicker noise* is present in almost all electronic devices [192]. Its possible origins are manifold, for example, impurities in a conductive channel. Its spectral power density scales as $1/f$ and therefore is most prominent for low-frequencies.

Shot noise originates from the quantized amount of electric charge per particle [192]. This results in statistical fluctuations of the device's electrical current I which results in a spectral power density of $S_\mathrm{I,sn} = 2eI$ given in units of A^2/Hz.

Thermoelectric effects can also generate spurious voltages [193]. The presence of a temperature gradient in a material results in a voltage difference and vice versa. This so-called Seebeck effect can be explained as follows: at the hot end of a material with temperature T_2, the charge carriers have a higher average velocity compared to the ones at the cold end with T_1. Thus, "hotter" carriers diffuse towards

the cold end which leads to a potential difference $V_{\text{Seebeck}} = \int_{T_1}^{T_2} S(T)\,\mathrm{d}T$. The Seebeck coefficient $S(T)$ is a temperature dependent material parameter. If just a single material is used, no thermoelectric voltage is measured, as the thermal gradients and thus the thermoelectric voltages cancel each other (Fig. 4.7(a)). In conventional measurements, different materials with different Seebeck coefficients are combined, for instance, Cu or Al wires and Au nanostructures. The simple case of two materials with S_A and S_B (called thermocouple) is

**Fig. 4.7:** (a) Despite a thermal gradient, no thermoelectric voltage is detected if just a single material is used. (b) For two different materials with the connecting regions at different temperatures (T_1 and T_2), a thermoelectric voltage can be measured. [31]

sketched in Fig. 4.7(b). There, the two different temperatures at the two contact regions (T_1 and T_2) lead to a Seebeck voltage $V_{\text{Seebeck}} = \int_{T_1}^{T_2} (S_A(T) - S_B(T))\,\mathrm{d}T$. For metals, V_{Seebeck} is in the range of μV/K [187]. Temperature gradients during measurements can be created, for example, via Joule heating ($P = RI^2$) of an applied current varying across the wire or by different thermal contacts of wire regions to a thermal bath. Typically, thermal voltages are independent of the current direction. This is exploited in the measurement analysis as discussed in Sec. 4.2.2.3.

Common-mode offset and noise are a source of spurious voltages during high-precision measurements which are caused by the amplifiers themselves. An important parameter called common-mode rejection ratio (CMRR) describes the ability of a measurement device (or amplifier) to reject fluctuations common to both input leads [192, 194, 195]. It is defined as CMRR$=A_D/A_{\text{CM}}$ with the amplifier's differential and common-mode gain A_D and A_{CM}.
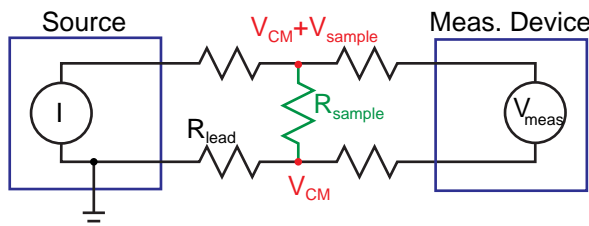
Fig. 4.8: Conventional 4-point measurement setup. Sample and lead resistances are important factors for common-mode offsets and noise. [31]

When considering a typical 4-point measurement configuration as sketched in Fig. 4.8, the measured sample resistance $V_{\text{sample}} = R_{\text{sample}} \cdot I$ is independent of the resistances of the connecting wires. However, when taking into account the common-mode effect, an additional common mode voltage $V_{\text{CM}} = R_{\text{lead}} \cdot I$ occurs. Therefore, the output of the measurement device is $V_{\text{meas}} = A_D^{-1}(A_D V_{\text{sample}} + A_{\text{CM}} V_{\text{CM}}) = V_{\text{sample}} + V_{\text{CM}}/\text{CMRR}$.

Thus, the ratio of spurious voltage $V_{\text{spu}} = V_{\text{CM}}/\text{CMRR}$ to sample voltage V_{sample} is given by

$$\frac{V_{\text{spu}}}{V_{\text{sample}}} = \frac{R_{\text{lead}}}{R_{\text{sample}}} \cdot \text{CMRR}^{-1}. \tag{4.6}$$

Note that not only the offset but also the noise of the lead resistances are weighted by the factor given in Eq. (4.6) and contribute to the spurious signal.

For most measurements, the common-mode contribution to the signal is negligible. However, for small R_sample and large R_lead, common-mode offsets and noise can be significant. For example, for a sample resistance $R_\mathrm{sample} = 1\,\mathrm{m\Omega}$ connected via leads with $R_\mathrm{lead} = 100\,\Omega$ and an instrument CMRR of $100\,\mathrm{dB}$, the spurious voltage V_spu is equal to V_sample. For our measurements, common-mode effects are important and high CMRR values are essential, since the lead resistances are in the range of several hundred Ω and the sample resistance is in the range of a couple of $\mathrm{m\Omega}$.

4.2.2.3 Low-level voltage measurements

To minimize the above mentioned spurious contributions to the measured signal, we implemented and tested two types of measurement setups. The first consisted of a Stanford Research Systems SR-830 lock-in amplifier with a CMRR of $100\,\mathrm{dB}$, operating at frequencies up to $100\,\mathrm{kHz}$[3]. The second setup was a combination of a SourceMeter 2400 and a Nanovoltmeter 2182A from Keithley Instruments Inc. with a CMRR of $140\,\mathrm{dB}$[4]. Both setups were remote controlled using home-made software based on Labview from National Instruments. For the Keithley instruments, a software which enables to use current source and nanovoltmeter in a hardware synchronization mode was programmed. In this mode, the instruments supply an alternating (switched) DC current and read the corresponding voltage.

The AC currents we used in both setups are advantageous, as constant and slowly varying offsets such as, for example, thermovoltages cancel [194], since these voltages generally do not invert sign upon current polarity inversion[5].

Comparing both setups, we found that for our devices, the alternating DC current measurements exhibit a peak-to-peak noise level which is about an order of magnitude smaller than that found for the setup with the lock-in amplifier. A peak-to-peak noise level as low as $12\,\mathrm{nV}$ was achieved for a current of $\pm100\,\mathrm{\mu A}$, an integration time of $20\,\mathrm{ms}$, and a digital filter averaging 15 subsequent voltage readings. These parameters resulted in a total settling time of $1.95\,\mathrm{s}$. For the non-local measurement configuration (see Sec. 4.3.1), about ten of these acquisitions were averaged which resulted in a resolution limit of $40 - 70\,\mathrm{\mu\Omega}$ $(4 - 7\,\mathrm{nV})$ given by the CMRR of the used instruments in combination with typical lead resistances of $400 - 700\,\Omega$. For ideal conditions, hence small sample resistances, we obtained a resolution limit of about $1\,\mathrm{nV}$.

The superior sensitivity of the DC current reversal technique compared to the lock-in measurements can be explained by the larger CMRR of the Keithley instruments

---

[3]See data sheet SR-830 DSP lock-in amplifier, Stanford Research Systems.

[4]See data sheet Nanovoltmeter 2182A, Keithley Instruments Inc.

[5]It is conceivable, however, that there are situations, where an inversion could take place, e.g., when two different regions exhibit a diode like behavior with opposite pass direction. Then, the heated region (reverse-biased diode) changes with current polarity which is accompanied by an inversion of the temperature gradient and hence with an inversion of an eventually present thermovoltage.

and our limitation to rather low frequencies ($\approx 17\,\text{Hz}$) which was due to the high inductances and capacitances of the devices.

To summarize, we established an electron-beam lithography fabrication process for a complex pattern of nanostructures with wire widths below $100\,\text{nm}$. Moreover, a low-level low-noise voltage measurement setup including software control and hardware triggering was developed. It enables high resolution voltage measurements of the fabricated nanostructures with a noise level as low as $4 - 7\,\text{nV}$.

4.3 Experimental results

After introducing the local and the non-local measurement configuration, characteristic results are illustrated taking a typical Au device as an example. Control measurements show that the findings are reliable and independent of the specific contacting scheme or the applied current density. Subsequently, measurements on samples of different Au layer thickness and on devices made of various metals are compared and discussed.

4.3.1 Local and non-local measurement configuration

To investigate the electric properties of the fabricated nanostructures, two measurement configurations are used. The first one is a conventional 4-point measurement technique, shown in Fig. 4.9(a). A current I is applied along the "horizontal" wire, and the local voltage V_{local} is detected via two different "vertical" wires separated by a distance L[6]. The local resistance is given by $R_{\text{local}} = V_{\text{local}}/I$. From these data, one obtains the resistivity $\rho = R_{\text{local}} \cdot w \cdot t/L$. In our experiments, local measurements were mainly used to characterize the devices and determine the metal nanowire quality.
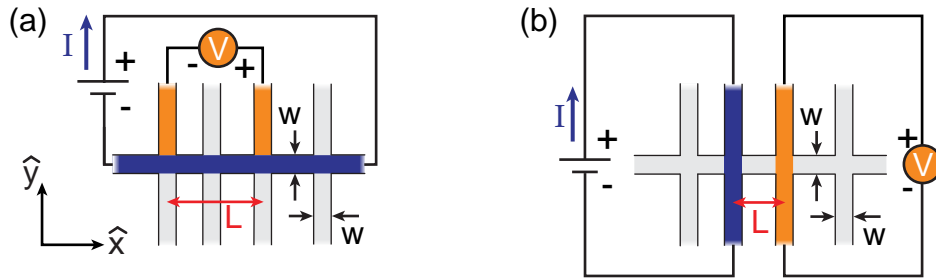
Figure 4.9: (a) Conventional 4-point measurement configuration. (b) Non-local measurement configuration. The voltage is measured in a region spatially separated by a distance L from the main current path.

The second measurement configuration is sketched in Fig. 4.9(b). A current is applied along one "vertical" wire, and the voltage is measured between top and bottom of another "vertical" wire at a distance L, where L is always measured from wire center to wire center. Since we are measuring a potential difference in a region spatially separated from the main current flow, the contacting scheme is called *non-local configuration.* The only connection between current carrying wire and voltage leads is the horizontal bridging nanowire. In all measurements, "high" (+) of the current source is connected at the same side of the horizontal wire (here at the top) as "high" (+) of the nanovoltmeters. The measured non-local voltage V_{NL} is normalized to the applied current I, so that a non-local resistance $R_{\text{NL}} = V_{\text{NL}}/I$ is obtained. As R_{NL} is not a true resistance but a normalized voltage signal, it can be positive as well as negative depending on the sign of V_{NL}.

---

[6]horizontal $\widehat{=}$ parallel to $\hat{\mathbf{x}}$, vertical $\widehat{=}$ parallel to $\hat{\mathbf{y}}$

All data presented in the following were acquired via the DC current reversal method established within this thesis. For setups as presented in Sec. 4.2.2.3 and for our devices, the DC current reversal method outperformed lock-in measurements as the noise level is smaller by about an order of magnitude. For our devices and a current of $100\,\mu$A, we obtain a resolution limit of $40 - 70\,\mu\Omega$ ($4 - 7\,$nV) as discussed in Sec. 4.2.2.3.

In the following, the experimental results are presented.

4.3.2 A typical multi-terminal gold nanostructure

Au has a large spin diffusion length of up to $\lambda_\text{s} = 168\,$nm [186], and Seki *et al.* [68] also reported a very large spin Hall angle of $\alpha_\text{SH} = 0.113$. Thus, Au should be an ideal material to demonstrate and study the spin-mediated non-local resistance introduced in Sec. 4.1.3. Within this chapter, many different samples are presented. We start by discussing the typical measurement procedure and generic results taking the sample "Au/50 nm" as an example. The Au nanowires of this sample were fabricated via the effusion cell and "50 nm" in the device name denotes the nanowire's thickness t.

First, every sample is characterized through local measurements, where the 4-point resistance R_local between a variety of different vertical wires is determined. This enables to identify possible local defects or irregularities in certain wires. In Fig 4.10(a), the thereby determined values of R_local for Au/50 nm are plotted against the voltage probe separation L for $T = 300\,$K (red symbols) and $T = 3\,$K (blue symbols). Fitting all measurements at a given temperature with a straight line, representing the relation $R_\text{local} = \rho(T) \cdot (t \cdot w)^{-1}(L + L_\text{offset})$, yields two parameters: first, the intersection of the fitted line with the x-coordinate, L_offset, and second, the wire resistivity $\rho(T)$.

The values of L_offset, 3.39 nm at 300 K and 1.29 nm at 3 K, are within the error bar of the fitting process and are negligibly small compared to the wire width. For all studied samples, comparably small values of L_offset were obtained, which shows that Ohm's law is also well fulfilled at these short length scales, i.e., that our nanowires are homogeneous on this scale. This is in contrast to the observations of Mihajlović *et al.* [183] who found $L_\text{offset} = (72 \pm 17)\,$nm for Au wires of 110 nm width and attributed this to a spreading of the current density into the voltage leads. This indicates that the metal properties in our samples, such as grain size or microstructure, are different from those of Mihajlović *et al.*

For the resistivity, values of $\rho(300\,\text{K}) = 5.74\,\mu\Omega$cm and $\rho(3\,\text{K}) = 3.35\,\mu\Omega$cm are extracted (Fig 4.10). Note that all symbols in Fig 4.10(a) are in close proximity to the fitted line expected from Ohm's law which proves the high quality of all nanowires. Figure 4.10(b) shows the temperature dependence of $\rho(T)$, measured for a local voltage probe distance of $L = 425\,$nm. With decreasing T, $\rho(T)$ decreases approximately linearly as expected from electron phonon scattering [196], until its value saturates for temperatures below 30 K due to impurity scattering.

The room temperature resistivity $\rho(300\,\text{K}) = 5.74\,\mu\Omega$cm is roughly by a factor of three higher than in the bulk ($\rho(300\,\text{K})_\text{bulk} = 2.271\,\mu\Omega$cm [187]), whereas the residual resistance ratio RRR $= \rho(300\,\text{K})/\rho(3\,\text{K}) = 1.7$ is significantly smaller than
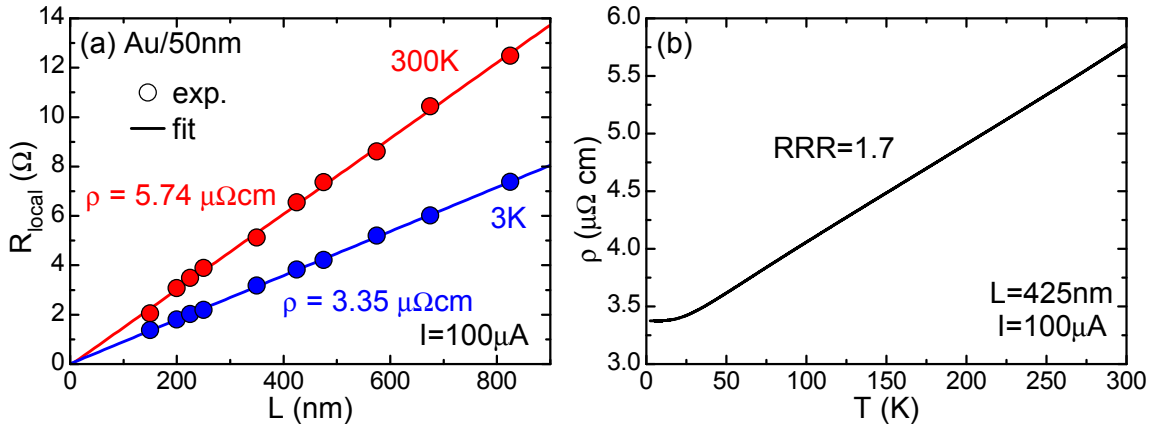
Figure 4.10: Typical local characterization data shown for the Au/50 nm sample.
(a) 4-point resistance R_{local} probed for different voltage lead separations L. All
experimentally determined values (symbols) closely follow the line predicted by
Ohm's law which demonstrates the high quality of our nanowires. (b) Temperature
dependence of the local resistivity ρ. A residual resistance ratio (RRR) of 1.7 is
extracted.

bulk values of $\text{RRR}_{\text{bulk}} \approx 100$ [187]. This can be explained by enhanced carrier
scattering at the rough surfaces of the nanowires [197, 198, 199, 200]. The values
obtained in our experiments compare well to literature data of similar nanowires
$3.7\,\mu\Omega\text{cm} < \rho(300\,\text{K}) < 12\,\mu\Omega\text{cm}$ [201, 202, 203, 204]. In our measurements, the
uncertainty of ρ is dominated by the precision of the nanowire width measurement
which is limited by the resolution of the scanning electron microscope ($\approx 5\,\text{nm}$).
This gives an error of less than $8\,\%$.

Having established that the sample is of high structural quality, the rather time-
consuming non-local measurements were performed. Figure 4.11(a) shows the non-
local resistance R_{NL} versus temperature for different degrees of non-locality L taking
Au/50 nm as example. For the shortest separation between current and voltage
leads ($L = 150\,\text{nm}$), a positive non-local resistance of $R_{\text{NL}} = 3.4\,\text{m}\Omega$ is observed
at $T = 300\,\text{K}$. For larger L, values below $0.2\,\text{m}\Omega$ are measured. With decreasing
temperature, R_{NL} decreases for all L, becomes negative, and decreases further until
about $30\,\text{K}$, where a saturation is reached. The non-local resistance for $L = 425\,\text{nm}$
is zero to within our measurement resolution in the entire investigated temperature
range.

The decay of the non-local signal with distance L is plotted for $T = 300\,\text{K}$ (red
symbols, Fig. 4.11(b)) and $T = 3\,\text{K}$ (blue symbols, Fig. 4.11(c)). All measurements
obtained at $300\,\text{K}$ show a positive value, whereas those taken at $3\,\text{K}$ are all negative.
The magnitude $|R_{\text{NL}}|$ exponentially decays with L as indicated by the straight line
in the logarithmic representation of Figs. 4.11(b,c). An exponential fit with $|R_{\text{NL}}| =
|R_0|\exp(-L/\lambda)$ leads to a decay length of $\lambda = 16.6\,\text{nm}$ for $T = 300\,\text{K}$ and to about
twice the value, $\lambda = 35.6\,\text{nm}$, for $T = 3\,\text{K}$. The resolution limit of $40 - 70\,\mu\Omega$
($4 - 7\,\text{nV}$) given by the CMRR and a lead resistance of about $400 - 700\,\Omega$ in these
samples is indicated as grey bars in Figs. 4.11(b,c).
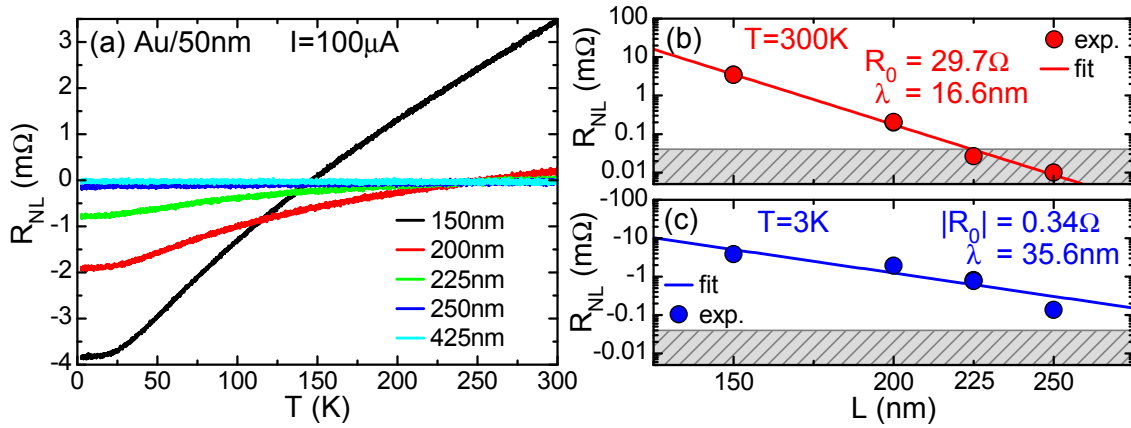
Figure 4.11: Non-local resistance of sample Au/50 nm. (a) R_{NL} versus T for different distances L between current leads and non-local voltage probes. An unexpected sign change of R_{NL} from $R_{\mathrm{NL}} > 0$ at high T to $R_{\mathrm{NL}} < 0$ at low T is observed. (b,c) The non-local signal exponentially decays with L both at $T = 300\,\mathrm{K}$ and $3\,\mathrm{K}$. The decay length λ at $T = 3\,\mathrm{K}$ is about twice the value determined at $T = 300\,\mathrm{K}$. The grey shaded areas indicate the error bounds due to the measurement resolution.

To investigate whether the measured non-local signal is determined by the classical local sheet resistance ρ/t, Fig. 4.12 shows the ratio $R_{\mathrm{NL}}(T)/(\rho(T)/t)$ versus T. Clearly, the ratio is not constant. Instead, a strong, non-linear temperature dependence is observed. This is in contrast to the calculations of Sec. 4.1 which predict that both spin-mediated non-local resistance and the non-local resistance due to diffusive current spreading are proportional to the sheet resistance ρ/t. Thus, apart from the classical sheet resistance, also other effects contribute to the non-local signal.

The observed sign change and the negative non-local resistance at low temperatures are further unexpected features, as both spin-mediated and diffusive non-local
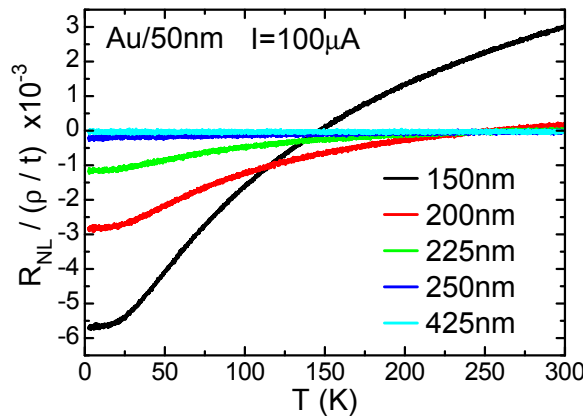
Figure 4.12: $R_{\mathrm{NL}}(T)/(\rho(T)/t)$ versus T for sample Au/50 nm. Clearly, a strong temperature dependence can be observed which indicates that the non-local signal is not determined by the sheet resistance. In that case, a temperature-independent R_{NL}/ρ would be expected.

resistance should result in positive non-local signals. Moreover, the measured decay length of 16.6 nm $< \lambda <$ 35.6 nm is significantly smaller than the literature values of the spin diffusion length 60 nm $< \lambda_{\text{sd}} <$ 168 nm [70, 186, 205] in lateral Au devices. To exclude measurement artifacts as the source for the R_{NL} signal, we performed a couple of control experiments presented in the next section.

4.3.3 Control measurements

The large current densities in the current carrying nanowires lead to large dissipated power densities $P/A = R \cdot I^2/A$ of about 500 W/cm^2. Such large values[7] create thermal gradients and eventually related thermovoltages. Therefore, we performed a couple of control experiments to ensure that thermal voltages are not the origin of the observed non-local signal.

To ensure that our results are not distorted or even caused by the magnitude of the applied current, differential resistance measurements were performed. Figure 4.13 shows both the local (red, orange) and the non-local (blue, cyan; $L = 150$ nm) differential resistances (taken at $T = 3$ K) versus the bias current I_{bias} for the Au/50 nm sample.
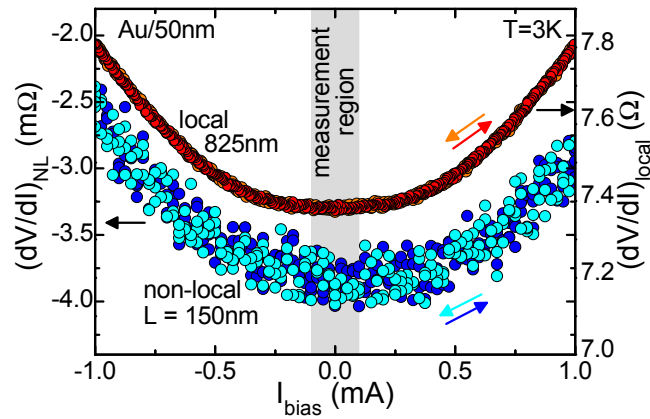
Figure 4.13: Differential local and non-local resistance signal of sample Au/50 nm. The arrows indicate the sweep direction of the bias current. dV/dI is constant for $|I_{\text{bias}}| \lesssim 0.3$ mA. At larger bias currents, the local signal increases in magnitude, and the non-local signal comes closer to zero. This excludes a high current density as origin of the negative non-local signal. All measurements in the remainder of this chapter were performed in the dV/dI=const. region with a maximum current of $I = 100$ μA (grey shaded area).

The local resistance is independent of the bias current for $|I_{\text{bias}}| \lesssim 0.3$ mA[8]. For higher values, it increases due to Joule heating in combination with the positive

---

[7]The value of 500 W/cm^2 is obtained when using an applied current of 100 μA and assuming a nanowire width of 100 nm, a length of 10 μm, and a nanowire resistance of $R \approx 500\,\Omega$. Note that 500 W/cm^2 is a very large value compared to a conventional hotplate used in the kitchen. (For a typical power of $P = 1500$ W and a diameter of $d = 19$ cm, one obtains a maximum hotplate power density of about 5 W/cm^2.)

[8]As $\partial R/\partial T \approx$ const. for $T \lesssim 20$ K, this does not mean that there is no temperature change of the sample for this current. However, the experiments clearly show that local and non-local resistance do not vary with I_{bias} for $|I_{\text{bias}}| \lesssim 0.3$ mA.
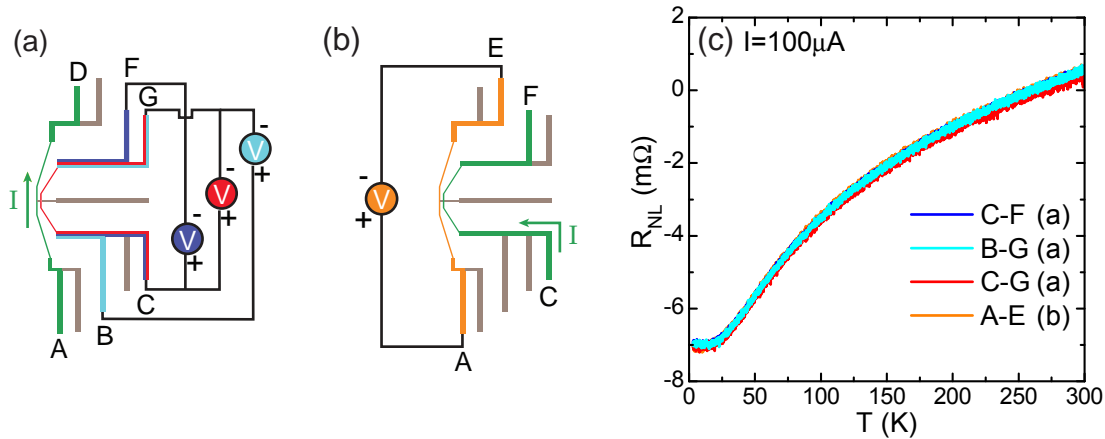
Figure 4.14: (a,b) Different contact configurations for current leads and non-local voltage probes are shown. (c) Independent of the used lead configuration, always the same temperature dependence of R_{NL} is observed. This excludes thermoelectric voltages as the origin of our non-local signal.

$\partial\rho/\partial T$ for Au (see Fig. 4.10). The non-local resistance shows a very similar behavior: for $|I_{bias}| \lesssim 0.3\,\mathrm{mA}$, no changes are observed[8], whereas for larger I_{bias}, the differential resistance increases (decreases in absolute magnitude). This is again consistent with the observed positive $\partial\rho/\partial T$ of R_{NL} (see Fig. 4.11(a)). These observations rule out large current densities as origin of the negative non-local signal, since an increasing current *reduces* the absolute magnitude of the non-local signal. All measurements shown in the remainder of this chapter were performed at a maximum current of $|I| = 100\,\mu\mathrm{A}$ (indicated by a grey bar in Fig. 4.13) which is in the constant region of $\partial V/\partial I$. All in all, we exclude large current densities as the origin of the negative non-local resistance at low T.

Thermoelectric effects as discussed in Sec. 4.2.2.2 generally depend on the power ($P \propto I^2$) and hence are independent of the current direction. Consequently, they cancel in AC or DC current reversal measurements as used here. However, certain diode like contacts might lead to temperature gradients which reverse with the current and thus lead to spurious signals. To exclude these effects as well, we modified our device geometry such that a particular nanowire can be measured via multiple contacts. Therefore, the inner contact structures were split into multiple parts which allows to vary all subsequent contacts on the way to the measurement equipment (inner contact structure/outer contact structure, outer contact structure/bond wire, bond wire/contact pad, etc.). A sketch of the asymmetric layout and the contacting scheme is shown in Fig. 4.14(a). The current flows between A-D, and the voltage can be measured via three different contact geometries: C-F, C-G, and B-G. Figure 4.14(c) depicts the non-local signal plotted against T we obtained. All curves superimpose perfectly in the whole temperature range from 300 K to 3 K. Another configuration, where current and voltage leads are exchanged is presented in Fig. 4.14(b). In this case, the current flows between C-F and the voltage is measured between A-E. The obtained data are also included in Fig. 4.14(c). Again, the curves superimpose perfectly.

In summary, our measurements demonstrate that the temperature dependence of the non-local signal and in particular the negative non-local resistance are not caused by the magnitude of the applied current density used in our experiments and are independent of the contact configuration. We thus conclude that thermoelectric voltages or effects related to "bad" contacts are not the origin of the observed non-local signal and its temperature dependence.

4.3.4 Magnetic field dependence

In addition, we studied the influence of external magnetic fields on the non-local signal. The field was applied in different directions, parallel and perpendicular to the current in the film plane, as well as perpendicular to the film plane. For all field orientations very similar observations were made. Here, we will focus on data taken with **H** oriented perpendicular to the film plane. Figure 4.15(a) shows the measurements of the non local resistance of Au/50 nm for $L = 200$ nm and $T = 3$ K. Clearly, the negative value of R_{NL} observed for vanishing magnetic field persists throughout the entire studied field range $|\mu_0 H| \leq \pm 14$ T. Only a slight reduction in the absolute magnitude of R_{NL} (about 5 %) is observed. These observations are in stark contrast to the magnetic field dependence of the spin-mediated R_{NL} predicted by Abanin $et\,al.$ [15]. The authors calculated an oscillation and finally a suppression of the non-local resistance on a field scale $\mu_0 H_* = \hbar/(g\mu_{\mathrm{B}}\tau_{\mathrm{sf}})$, where g is the g-factor, μ_{B} the Bohr magneton, and τ_{sf} the spin flip time. With the bulk values $g = 2.11$ and $\tau_{\mathrm{sf}} = 5 \times 10^{-10}$ s [206], a field scale of $\mu_0 H_* \approx 11$ mT is calculated. Thus, at fields as high as ± 14 T, the spin-mediated non-local resistance should be suppressed. We would like to stress that similar experimental results were obtained for the other investigated Au samples.

Let us briefly mention another observation which is actually not related to the subject of this chapter. Figure 4.15(b) shows a similar measurement as Fig. 4.15(a)
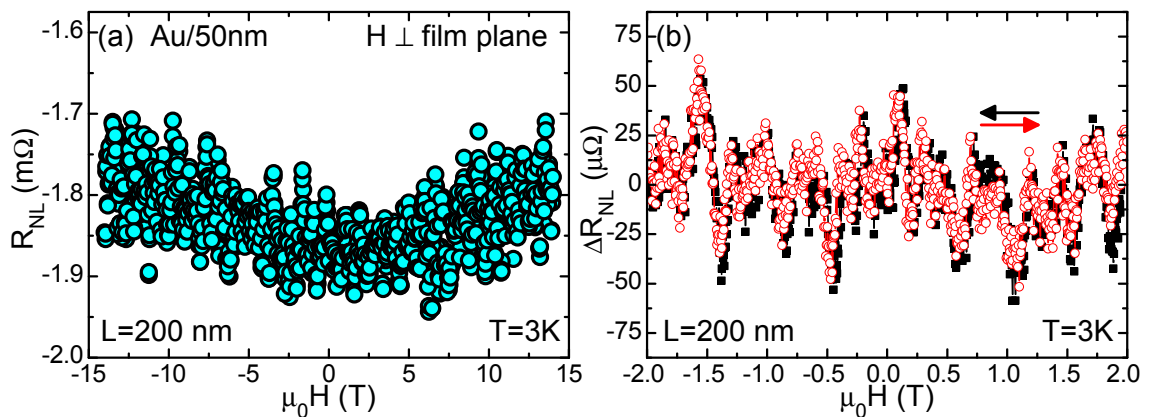
Figure 4.15: R_{NL} versus magnetic field for $L = 200$ nm of sample Au/50 nm. (a) No substantial change in R_{NL} could be observed for fields up to ± 14 T. In particular, $R_{\mathrm{NL}} < 0$ is found for the entire studied field range. (b) Non-local resistance fluctuations measured at a distance $L = 200$ nm. The arrows indicate the direction of the magnetic field sweep.

but with a higher field resolution (5 mT field steps) in a field range $|\mu_0 H| \leq 2$ T. A constant offset is subtracted to shift the signal to 0. At first glance, an enhanced noise is observed, but when comparing up-sweep (-2 T $\rightarrow 2$ T, red symbols) and down-sweep (2 T $\rightarrow -2$ T, black symbols), identical fluctuations with an average amplitude of about $\Delta R = 75 \, \mu\Omega$ are observed. These are non-local resistance fluctuations as previously reported, e.g., in Refs. [207, 208, 209, 210] and investigated theoretically, e.g., in Ref. [211]. The reason for these fluctuations is that the sample dimensions are in the same range as the phase coherence length $L_\varphi = \sqrt{D\tau_\varphi}$ of the charge carriers, where τ_φ is the phase relaxation time. In this case, interferences of different electron paths enclosing magnetic flux lead to Aharonov-Bohm fluctuations in the conductance [212]. Resistance fluctuations are observed in both the local and the non-local measurement configuration given that $L \lesssim L_\varphi$. Thereby, it is not crucial whether or not the classic current path spans any of the voltage probes [207, 213, 214].

It is thanks to the improvements of the measurement technique during this thesis (see Sec. 4.2.2.3) that it has become possible to resolve these oscillations in the $\mu\Omega$ range.

4.3.5 Comparison of various multi-terminal gold nanostructures

To further investigate the non-local resistance, we fabricated and investigated a series of different Au nanostructures. A selection of samples made from films with different thicknesses ($t = 20$ nm, 26 nm, 50 nm, 100 nm, 200 nm) and fabricated via different methods (effusion cell, electron beam evaporation and line scan[9]) are presented in Fig. 4.16. The top line indicates the nanowire thickness and the fabrication technique (evap. = electron beam evaporation and area scan, line = effusion cell and line scan, nothing = effusion cell and area scan). R_{NL} for $L = 150$ nm, 200 nm, 225 nm and 250 nm versus temperature is shown. The insets display the temperature dependence of the respective sample's local resistivity ρ.

Let us now discuss the experimental findings. All samples qualitatively show a very similar behavior with slight differences in the magnitudes of both the local and the non-local resistance. The local measurements reveal that the resistivity decreases with increasing layer thickness as expected from the reduction of surface scattering. An exception is the sample with $t = 100$ nm which exhibits a slightly smaller resistivity than that with $t = 200$ nm. The different fabrication methods (line scan vs. area scan, electron-beam evaporation vs. effusion cell) can be compared when looking at the samples Au/50 nm/line, Au/50 nm/evap. and Au/50 nm (Figs. 4.16(c-e)). No substantial differences are found; the slightly enhanced resistivity for Au/50 nm/line might be due to the less uniform wire width resulting from the line scans. Moreover, Au deposition via the effusion cell (Au/50 nm) leads to

---

[9]Line scan describes an exposure technique, where the electron beam is scanned just once per nanowire. During the conventionally used area scan, the beam is scanned multiple times with a lower dose. The line scan generally results in a slightly smaller but less uniform wire width which was verified by SEM measurements.
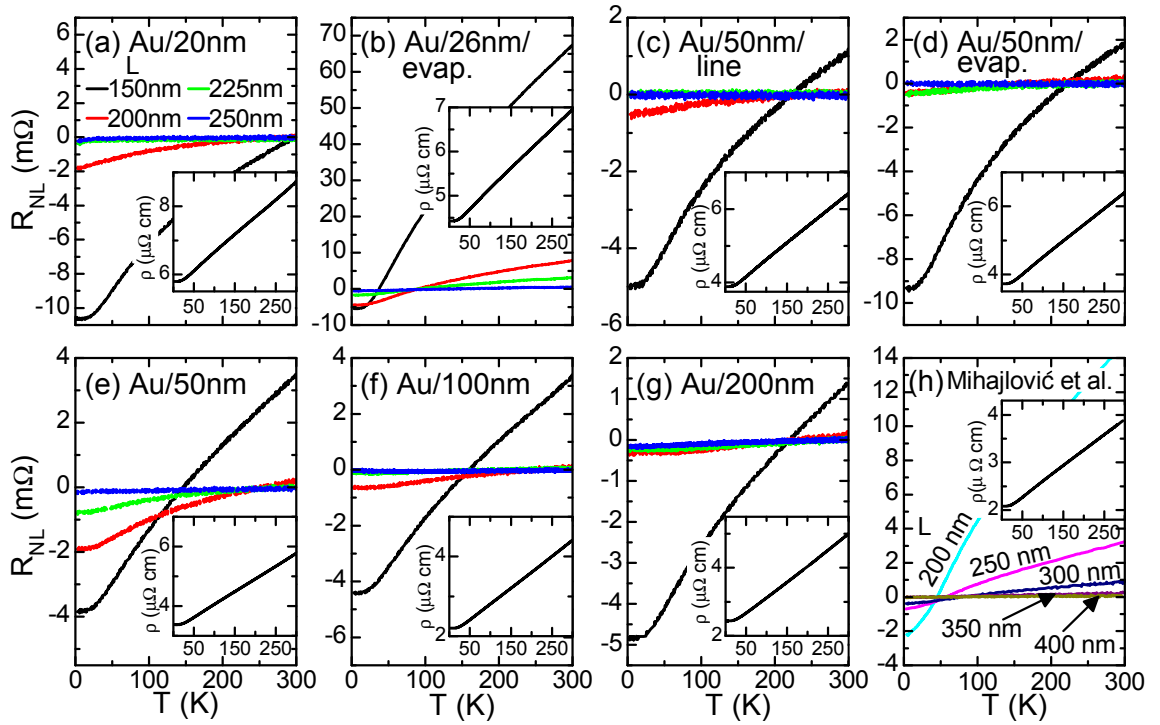
Figure 4.16: Non-local resistance versus temperature for various Au nanostructures varying in nanowire thicknesses and fabrication method. For all samples, a qualitatively very similar behavior is observed. With decreasing T, R_{NL} decreases and becomes negative for low T. The largest negative values are observed for the smallest separations L. The inset of each panel shows the resistivity of the respective sample. In panel (h), literature data from Mihajlović *et al.* [183] of similar Au nanostructures are included into this overview for comparison.

a somewhat lower resistivity compared to that of the electron beam evaporation process (Au/50 nm/evap.). This can have multiple reasons: first, the larger growth rate during the evaporation process results in a smaller grain size and thus in an increased grain boundary scattering which might lead to a higher resistivity. Second, a different impurity concentration in the target material or the higher base pressure in the electron-beam evaporation chamber leading to more impurities could be responsible for the different resistivities.

The non-local resistance differs in magnitude between the samples, but several features are generic: for all samples, R_{NL} is positive at $T = 300\,\mathrm{K}$ and decreases with decreasing temperature. Moreover, all samples show a considerable negative non-local resistance at low temperatures independent of thickness or fabrication method. R_{NL} for $L = 150\,\mathrm{nm}$ at $T = 3\,\mathrm{K}$ is in the range $-10.6\,\mathrm{m\Omega} < R_{NL} < -3.8\,\mathrm{m\Omega}$. Furthermore, with increasing L, the absolute magnitude of the non-local signal decreases for all samples as discussed in detail in Sec. 4.4.1. These findings are robust even for a moderate variation of the wire width w. Although w was designed to be 70 nm for all samples presented in Fig. 4.16, values between $65\,\mathrm{nm} < w < 105\,\mathrm{nm}$ were obtained (see Table 4.1 in Sec. 4.4.4.2). Nevertheless, R_{NL} of all samples shows a very similar behavior.

The difference in magnitude of R_{NL} between the individual samples is probably caused by the different sample thicknesses, fabrication methods, grain configurations, and by slight variations in the device geometry.

For comparison, experimental data of similar Au structures with $t = 60\,\text{nm}$ and $w = 110\,\text{nm}$ extracted from Mihajlović *et al.* [183] are plotted in Fig. 4.16(h). Compared to our samples, the resistivity measured by these authors is smaller by a factor of about two. This might be related to the larger width of their nanowires making grain boundary and surface scattering effects less important. Also the distances L at which they detected the non-local signal are different from ours. Despite these differences, the non-local data of Mihajlović *et al.* exhibit exactly the same behavior as ours: the positive value of R_{NL} at high temperatures decreases with decreasing T and becomes negative for low T.

Thus, the temperature dependence of the non-local resistance, including the negative values at low T, is a generic feature of all studied Au samples and is independent of sample thickness ($20\,\text{nm} < t < 200\,\text{nm}$), wire width ($65\,\text{nm} < w < 105\,\text{nm}$), and fabrication method.

4.3.6 Multi-terminal nanostructures made from other metals

To further study the behavior of the non-local resistance, samples made from different materials were fabricated and measured. Figure 4.17 gives an overview of the experimental results of resistivities (insets) and non-local resistances versus temperature.

The non-local resistance of the Al sample Al/50 nm with a thickness of $t = 50\,\text{nm}$ (Fig. 4.17(a)) exhibits a very similar phenomenology as the Au samples. At $T = 300\,\text{K}$, a positive value of R_{NL} is observed which decreases with decreasing T and becomes negative for low T. The absolute magnitude of $R_{\text{NL}} = -2.2\,\text{m}\Omega$ at $T = 3\,\text{K}$ and $L = 150\,\text{nm}$ is slightly smaller than the values obtained for the Au samples.

For Pt and the transition metal ferromagnets Ni, Co and Fe with $t = 25\,\text{nm}$, we found positive values of R_{NL} at $T = 300\,\text{K}$ much larger than those measured for the Au and Al samples. This is accompanied by much larger values of ρ. With decreasing temperature, R_{NL} decreases for all samples but stays positive well above zero.

This concludes the presentation of our experimental data. In summary, the non-local resistance for all Au samples and the Al sample exhibits a very similar behavior. It is positive for high temperatures, decreases with decreasing T and becomes negative for low T. In contrast to that, samples made of Pt, Ni, Co or Fe exhibit a positive non-local resistance in the entire investigated temperature region ($3\,\text{K} \le T \le 300\,\text{K}$), much larger than those of Au and Al.

In the following, we discuss our experimental findings.
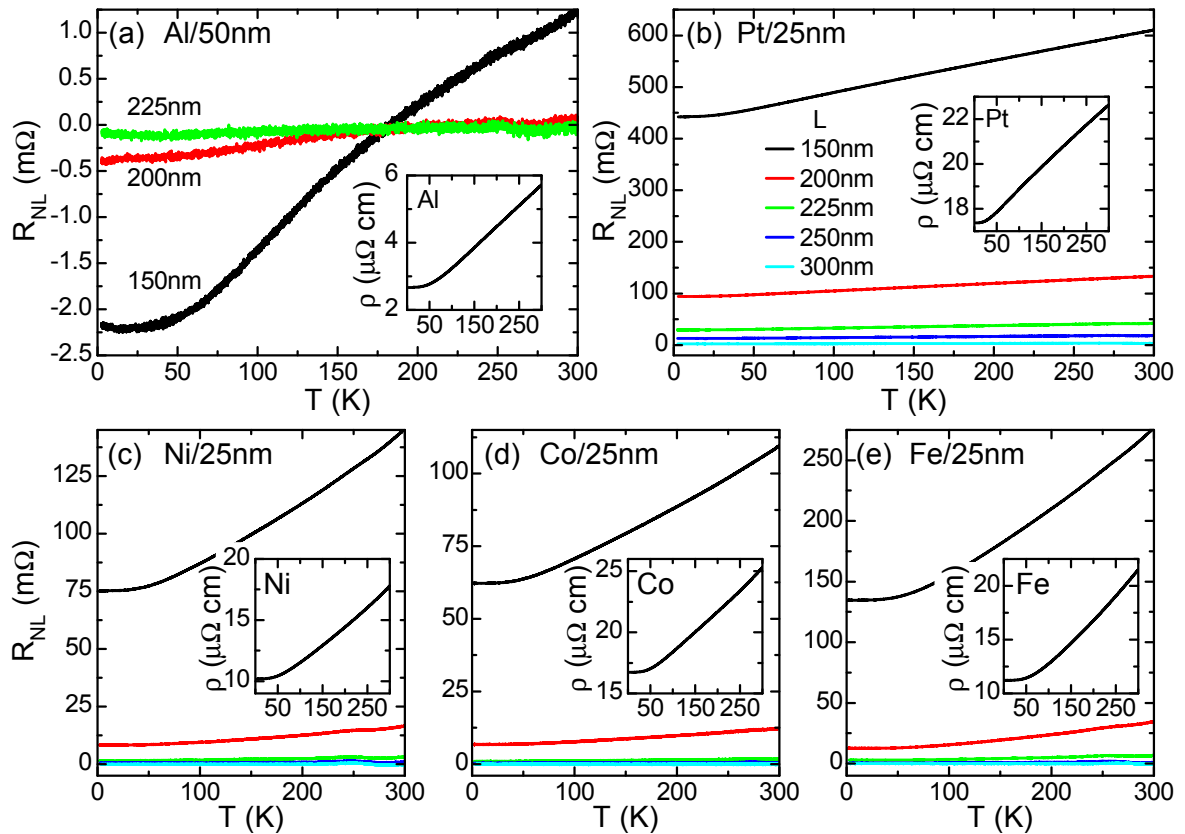
Figure 4.17: Non-local resistance of nanostructures made from various materials versus temperature for different L, color coded as shown in panel (b). (a) The Al sample exhibits a qualitatively very similar temperature dependence as the previously presented Au samples: at high T, $R_{NL} > 0$. It decreases with decreasing T and becomes negative for low T. (b-e) In contrast, Pt and the $3d$-transition metal ferromagnets Ni, Co, and Fe show positive values of R_{NL} in the entire studied temperature region with a much larger magnitude. The insets display the conventional, local resistivity of the respective sample.

4.4 Discussion

We start the analysis of the experimental data presented in the previous sections by determining the decay lengths of the non-local signal for the different samples. Subsequently, we present a spin dependent mechanism leading to a negative non-local resistance, and afterwards, we discuss classical (spin-independent) transport effects. In this context, a theoretical model including the transition from diffusive to ballistic transport is developed which is able to consistently explain all our experimental observations. Finally, we determine an upper limit of α_{SH} for our Au structures and list material requirements for the detection of a spin-mediated non-local signal.

4.4.1 Decay length

The samples presented in Sec. 4.3 can be divided into two groups: group 1 contains all Au samples and the Al device. For this group, the non-local resistance is positive at high T, crosses zero and is negative at low T. Group 2 consists of the samples made from Pt, Ni, Co and Fe and features a positive non-local resistance in the entire studied temperature region.

   To explore the origin of the non-local resistance, we first determine the decay length of the non-local signal for the different samples. To this end, the magnitude of the non-local resistance at $T = 300\,\mathrm{K}$ and at $T = 3\,\mathrm{K}$ is extracted and plotted versus L (cf. discussion in the context of Fig. 4.11). A fit with $|R_{\mathrm{NL}}| = |R_0|\exp(-L/\lambda)$ yields the decay length λ shown in Fig. 4.18 (300 K: red symbols, 3 K: blue symbols). Multiple dots of one color for one material and one thickness originate from different devices and reflect the scattering between samples. The error bars represent the uncertainty in the fitting procedure. Samples showing a small non-local signal (e.g., Al) generally exhibit larger error bars than samples with a large non-local signal as e.g., Pt.

   From Fig. 4.18, one can deduce that the decay lengths for all studied samples are comparable and approximately range between 15 nm and 42 nm (orange horizontal bar). The shortest decay lengths ($15\,\mathrm{nm} \lesssim \lambda \lesssim 20\,\mathrm{nm}$) are observed for the transition metal ferromagnets, whereas for the Al sample the largest values ($32\,\mathrm{nm} \lesssim \lambda \lesssim 42\,\mathrm{nm}$) are extracted. With the exception of Au/20 nm, λ at low temperature is larger by a factor of up to two than λ at high temperature. The differently fabricated Au samples with $t = 50\,\mathrm{nm}$ discussed in Sec. 4.3.5 are all plotted under Au 50 nm and show a similar decay length. This demonstrates that the fabrication method has only little influence on λ.

   Subsequently, we use the decay length λ to critically test the applicability of different theoretical models.
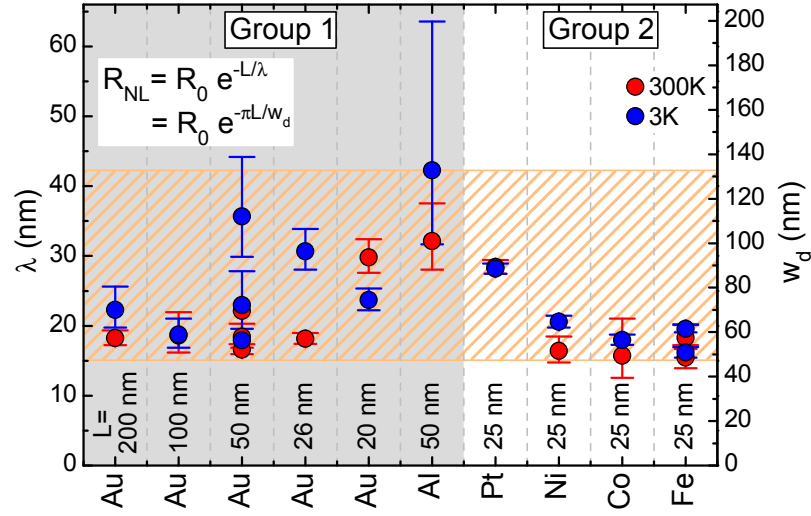
Figure 4.18: Decay length of the non-local resistance R_{NL} for various samples at $T = 300\,\text{K}$ (red symbols) and $T = 3\,\text{K}$ (blue symbols). The values are obtained from a fit with the function $|R_{NL}| = |R_0| \exp(-L/\lambda)$ (cf. Fig. 4.11). The grey shaded area denotes the samples of group 1 which show a negative non-local resistance at low T. The orange horizontal bar highlights the distribution of λ between the different samples. As right y-axis, $w_d = \lambda \cdot \pi$ is added which can be determined for diffusive transport. The resulting values range between $47\,\text{nm} \lesssim w_d \lesssim 133\,\text{nm}$ and are close to the actual wire widths w measured by the scanning electron microscope.

4.4.2 Negative spin-mediated resistance

The spin-mediated non-local resistance as derived by Abanin *et al.* [15] (Sec. 4.1.1) always results in positive R_{NL} values even for negative spin Hall angles, since R_{NL} quadratically depends on α_{SH}. This is visualized in Fig. 4.19(a): a spin-up electron coming from the current source enters junction A and is deflected to its left (for $\alpha_{SH} > 0$). The generated spin current I_s entering junction B also contains spin-up electrons which are again deflected to the same side (here to the left due to the same sign of α_{SH}). For $\alpha_{SH} < 0$, spin-down electrons would be deflected to the left twice resulting in an identical charge accumulation. Thus, in any case, one obtains a positive non-local voltage.

However, there is a situation which can generate a negative spin-mediated non-local voltage: it requires a broken symmetry between spin Hall effect and inverse spin Hall effect sketched in Fig. 4.19(b). Junction A still exhibits a positive α_{SH} (blue), whereas junction B now has a negative α_{SH} (red). This leads to the situation, where a spin-up electron is deflected to its left in junction A and to the right in junction B. Thus, the spin current generated in A causes a charge accumulation at the opposite side compared to the situation of Fig. 4.19(a). This results in a negative non-local voltage.
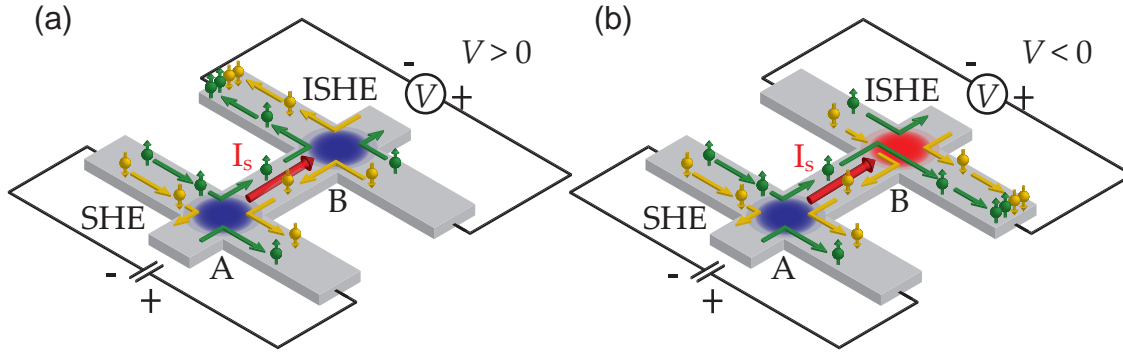
Figure 4.19: (a) Identical spin-orbit coupling in regions A and B leads to a positive value of the non-local voltage. (b) A different spin-orbit coupling (indicated as blue and red) in junction A and B can lead to different signs of α_{SH} and thus to a negative non-local voltage.

Different spin Hall angles can for example originate from different impurities at junction A and B. Gradhand *et al.* [66] calculated the spin Hall angle due to the extrinsic spin Hall effect for a Au host with impurities of different elements. They found positive values for Li, C, N, Ag, Pt and Bi impurities, whereas Mg and Cu yield negative values. The calculated magnitudes are in the same range as the intrinsic contribution [215]. Thus, in the case of Mg or Cu impurities in one of the junctions, a negative non-local resistance can be explained. Cu impurities in our samples can, e.g., originate from the used Cu liners in the electron-beam evaporation process. However, it is rather unlikely to have different impurities in simultaneously fabricated regions separated only by $\backsim 100\,$nm, and that these different impurities are invariably and reproducibly present in all measured Au and Al devices.

Another suggestion by M. Gradhand [216] does not require different types of impurities but just the presence of impurities and different conductivities in the two junction regions. The spin Hall conductivity in metals mainly consists of two contributions: the extrinsic skew scattering and the intrinsic effect (see Sec. 2.2). The extrinsic spin Hall effect depends on the impurity type and on the longitudinal conductivity σ_{xx}, whereas the intrinsic spin Hall effect is independent of these factors. Thus, the overall spin Hall conductivity σ_{yx} can be written as

$$\sigma_{yx} = \alpha_{SH,ss}\,\sigma_{xx} + \sigma_{int} \tag{4.7}$$

with $\alpha_{SH,ss}$ being the spin Hall angle due to skew scattering and σ_{int} the intrinsic spin Hall conductivity. Now, the only requirements for a negative non-local resistance are a different sign for intrinsic and extrinsic effect and different conductivities between junction A and B. Then, depending on the conductivity, either the first or the second term in Eq. (4.7) dominates and determines the sign of σ_{yx}. A negative spin Hall angle of the extrinsic contribution can be achieved, e.g., by Mg or Cu impurities in the Au host as mentioned above [66] and a different conductivity, e.g., by a variation of the impurity concentration or by any other scattering mechanism.

Again, it appears highly unlikely that such a combination of impurities and con-ductivity differences should be present in all studied Au samples. Moreover, also the studied Al samples showed a negative non-local resistance. For this material, the spin Hall angle determined in experiment [188] is orders of magnitude smaller than in Au which should prohibit an observation in our experimental geometry[10].

Another reason making spin-related effects rather unlikely as the explanation for our data are the experimentally observed decay lengths of $15\,\mathrm{nm} < \lambda < 35\,\mathrm{nm}$ in Au and $32\,\mathrm{nm} < \lambda < 42\,\mathrm{nm}$ in Al (see Sec. 4.4.1). These values are rather small compared to literature data of the spin diffusion length in Au of $60\,\mathrm{nm} < \lambda_{\mathrm{sd}} < 168\,\mathrm{nm}$ [70, 186, 205] and in Al of several hundred nanometers [188, 189]. A significantly reduced spin-flip length in our devices due to an additional strong spin-flip scattering process seems rather unlikely, as the measured resistivities are comparable to literature values for similar structures.

Last but not least, the magnetic field dependence of the non-local signal, discussed in Sec. 4.3.4, is strong evidence against a spin-related effect: the negative non-local resistance remains negative for applied external magnetic fields up to several Tesla, although fields of a couple of mT are predicted to suppress the spin-mediated non-local resistance [15].

From these arguments, we conclude that the experimentally observed non-local resistance is most likely unrelated to the spin. Therefore, we concentrate on spin-independent transport effects in the following.

4.4.3 Diffusive transport effects

To motivate the use of a diffusive transport model (although it cannot explain a neg-ative non-local resistance, as we will see later), we analyze the decay lengths shown in Fig. 4.18 in more detail. In the diffusive transport regime as discussed in Sec. 4.1.2, the decay of the non-local signal is determined by $\exp{(-\pi L/w)}$ (Eq. (4.5)) and thus solely depends on the wire width w. Assuming that purely diffusive transport is the origin of the non-local signal, we can calculate the wire width $w_{\mathrm{d}} = \lambda \cdot \pi$ from Fig. 4.18 as shown on the right-hand y-axis. We obtain wire widths ranging between $47\,\mathrm{nm} < w_{\mathrm{d}} < 133\,\mathrm{nm}$. These values are very close to the widths determined via the scanning electron microscope (SEM) ranging between $65\,\mathrm{nm} < w < 105\,\mathrm{nm}$ (see Table 4.1 in Sec. 4.4.4.2). We interpret this accordance as strong evidence that diffu-sive transport is the dominant mechanism for the positive non-local signal obtained at high temperatures. Therefore, we calculate numerically the potential landscape $\Phi(x, y)$ of the actually used device layout, taking into account the finite width of the current and voltage leads.

In the diffusive regime, the current density is proportional to the gradient of the electrochemical potential as derived in Eq. (2.8): $\mathbf{J} = -(\sigma/e)\nabla\mu$. To calculate the voltage profile of the entire structure, the diffusion equation for the electrochemi-cal potential $\nabla^2\mu = 0$ (see Eq. (2.10)) is solved. Due to charge neutrality in the structure, the electrochemical potential can be identified with the electric potential: $\mu = -e\Phi$.

---

[10]Although, in principle, α_{SH} could again be significantly enhanced by impurities.
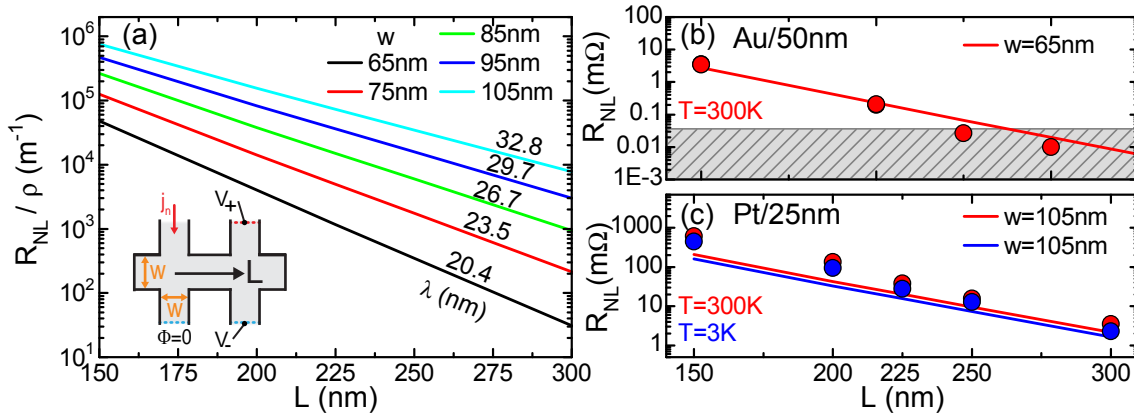
Figure 4.20: (a) Simulation of the non-local resistance for different wire widths w. (b,c) Comparison of simulation (lines) and experimental data (symbols) for the Au sample Au/50 nm and for the Pt sample Pt/25 nm. The grey shaded area in (b) shows the error bound. The good agreement between theory and experiment indicates diffusive transport as the dominating mechanism for the non-local data shown.

These types of calculation were performed with the finite element method (FEM) software COMSOL Multiphysics 3.2 for an H-shaped device layout sketched in the inset of Fig. 4.20(a). A constant and isotropic resistivity ρ and a wire width w, identical for horizontal and vertical wires were chosen. The potential of one end of the current carrying wire was set to zero ($\Phi = 0$), and for the other, an inward current flow of $-\mathbf{n} \cdot \mathbf{j} = j_n$ was defined, where $\mathbf{n}$ is the normal vector of the boundary. All other boundaries were set as electrical insulating ($\mathbf{n} \cdot \mathbf{j} = 0$). From the simulations, the electric field distribution in the structure was obtained. The non-local voltage is the difference between the two voltage probes V_+ and V_-.

Figure 4.20(a) shows the calculated results of the non-local resistance divided by the sample resistivity against the distance L for different wire widths $65\,\text{nm} < w < 105\,\text{nm}$. R_{NL}/ρ exponentially decreases with L on slightly different decay lengths ranging between $20\,\text{nm} \lesssim \lambda \lesssim 33\,\text{nm}$ for the different w. These calculated values of λ are very close to the experimentally obtained values shown in Fig. 4.18 (and later presented in Fig. 4.27).

Figure 4.20(b) depicts a direct comparison between theory (line) and non-local experimental data of Au/50 nm (symbols). The simulation for $w = 65\,\text{nm}$ using the previously determined sample resistivity $\rho(300\,\text{K}) = 5.74\,\mu\Omega\text{cm}$ matches the measured non-local signal very well. Experimentally, a wire width of $w = 75\,\text{nm} \pm 5\,\text{nm}$ was determined which is quite close to the value obtained from the simulation. Note that the only free parameter in these simulations is the wire width w. A comparison of the low temperature data for samples of group 1 and the simulation apparently does not make sense, since the negative R_{NL} observed in experiment is not reproduced by the simulation.

A second comparison between experiment and theory is shown in Fig. 4.20(c). R_{NL} of the sample Pt/25 nm measured at 300 K (red circles) and 3 K (blue circles) is plotted together with the simulation performed for $w = 105\,\text{nm}$ using the resistivities

$\rho(300\,\text{K}) = 27.6\,\mu\Omega\text{cm}$ and $\rho(3\,\text{K}) = 21.2\,\mu\Omega\text{cm}$ determined from local experiments. Here, also the low T data show $R_{\text{NL}} > 0$, such that a comparison is possible. The calculated results reasonably reproduce the experimental data. Again, the width used in the simulation is close to the value of $w = 95\,\text{nm} \pm 5\,\text{nm}$ determined by the SEM.

To summarize, the numerical simulations using a diffusive transport model describe the measured decay lengths and the magnitude of the non-local resistance at 300 K quite well. However, they cannot explain the observed temperature dependence and in particular the negative values of R_{NL} of the Au and Al samples at low temperatures. So, which mechanism can create a negative non-local signal?

4.4.4 Ballistic transport effects

When reducing the sample dimensions below the transport mean free path λ_{t}, one enters the ballistic transport regime [184]. For such systems, Takagaki *et al.* [217] calculated that negative non-local resistances can occur due to direct ballistic transmission of charge carriers into the voltage leads. This was indeed experimentally confirmed in high mobility GaAs/Al$_\text{x}$Ga$_{1-\text{x}}$As heterostructures [218, 219]. However, such effects are expected to be relevant only in high purity semiconductor devices, where the mean free path exceeds the characteristic device dimensions. In this section, we show that the crossover from diffusive to ballistic transport can explain our experimental observations in polycrystalline, metallic samples, and that negative non-local voltages already occur for device dimensions larger than the mean free path. We will use the term *ballistic* not in the strict sense, where all sample dimensions are much smaller than λ_{t} but as soon as deviations from the classic diffusive regime occur.

4.4.4.1 First approach

A first approach to explain the negative non-local resistance in Au nanostructures was made by Mihajlović *et al.* [183]. The authors suggested a sequence of diffusive and ballistic transport: "the negative R_{NL} comes from electrons that reach the region between the voltage probes diffusively and then ballistically scatter into the [...] [upper] voltage lead, generating a negative voltage". They fitted their data with $R_{\text{NL}} = \rho t^{-1} a\,[1 - b\exp\left(-w/\lambda_{\text{t}}\right)]$ containing two dimensionless fit parameters a and b, where $a = \exp\left(-\pi L/w\right)$ represents the diffusive part and decays exponentially with L. Although Mihajlović *et al.* could reasonably describe their data with that model, it fails to describe our measurements as discussed in Ref. [31]. Moreover, it seems arbitrary that the transport in the bridging wire is diffusive, but ballistic scattering occurs just in the contact region of the voltage leads.

In Sec. 4.4.4.3, we present a model which resolves these discrepancies. In preparation for this model, we start with an analysis of the mean free path for the different samples.
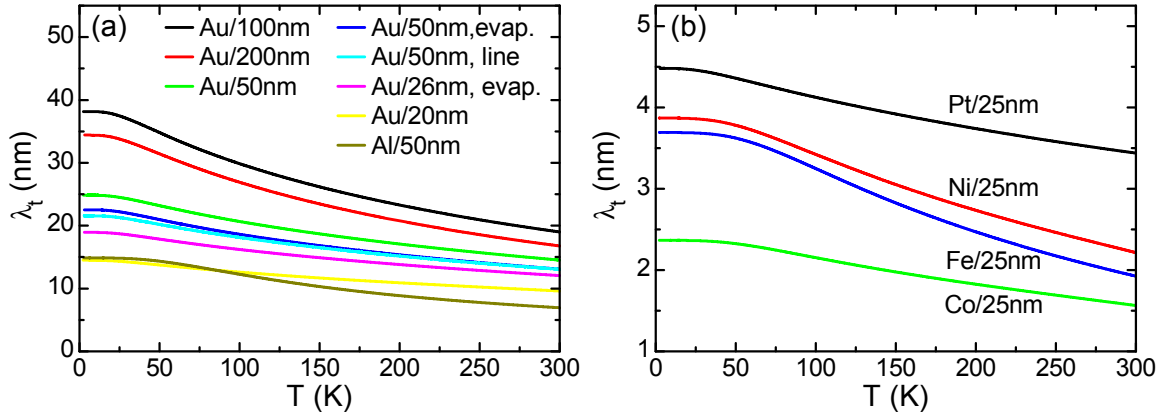
Figure 4.21: (a) Electron mean free path λ_t versus T of all studied samples exhibiting a negative non-local resistance R_{NL} at low T. (b) λ_t versus T of all samples showing a positive R_{NL} in the entire studied temperature region. Significantly smaller values of λ_t compared to (a) are obtained.

4.4.4.2 Mean free path

In our devices the length scale to distinguish between diffusive and ballistic transport is determined by the ratio λ_t/w of mean free path λ_t and wire width w. In the Drude model, λ_t can be calculated by [178]

$$\lambda_t = \frac{\hbar}{e^2 \rho} \left(\frac{3\pi^2}{n^2} \right)^{1/3} \tag{4.8}$$

with Planck's constant $\hbar$, the elementary charge e, the resistivity ρ, and the electron density n. In this model, a constant electron mean free path is assumed over the entire Fermi surface. The electron density can be extracted from the literature or calculated by $n = Y \cdot \xi/m_{atom}$, where Y is the number of electrons that an atom with mass m_{atom} supplies, and ξ is the density of the respective material [178]. We performed the calculations to obtain a consistent set of values for all studied materials. The results for n are listed in Table 4.1 and are assumed to be temperature independent. Note that Eq. (4.8) is valid only for cubic, non-magnetic metals. Thus, the values given for the transition metal ferromagnets Ni, Fe and Co can only be roughly estimated.

The electron mean free path depends on ρ and thus varies with temperature. Figure 4.21 shows its temperature dependence for the different materials, split into the first group exhibiting a negative non-local resistance at low T (Fig. 4.21(a)), and the second group showing a positive non-local signal in the entire studied temperature region (Fig. 4.21(b)). In the first group, mean free paths ranging between $7.0\,\text{nm} < \lambda_t < 38.2\,\text{nm}$ are obtained, whereas for group 2, much smaller values $1.6\,\text{nm} < \lambda_t < 4.5\,\text{nm}$ are found.

Moreover, as the experimentally determined sample resistivity is thickness dependent, an influence of the Au layer thickness on the mean free path is observed. The thinner nanowires exhibit a smaller λ_t compared to the thicker ones. Nevertheless, the smallest λ_t for the Au devices is still a factor of about two larger than λ_t for Pt

Table 4.1: Overview of all investigated samples. Here, Gr. refers to the group the samples are attributed to, w to the wire width, RRR to the residual resistance ratio, n to the calculated electron density, max. λ_t/w and min. λ_t/w to the maximum and minimum value of λ_t/w, and λ_t/w at $R_{NL} = 0$ for $L = 150\,\text{nm}$ to the value of λ_t/w at which the non-local resistance for $L = 150\,\text{nm}$ changes sign.

	Gr.	w (nm)	RRR	n ($10^{28}\,\text{m}^{-3}$)	max. λ_t/w	min. λ_t/w	λ_t/w at $R_{NL} = 0$ for $L = 150\,\text{nm}$
Au/20 nm	1	65	1.51	5.9	0.22	0.15	0.15
Au/26 nm/evap.	1	105	1.57	5.9	0.18	0.12	0.17
Au/50 nm/line	1	65	1.65	5.9	0.33	0.20	0.23
Au/50 nm/evap.	1	75	1.72	5.9	0.30	0.17	0.20
Au/50 nm	1	75	1.70	5.9	0.33	0.19	0.25
Au/100 nm	1	66	2.01	5.9	0.58	0.29	0.39
Au/200 nm	1	65	2.05	5.9	0.53	0.26	0.31
Au/60 nm, [183]	1	110	1.86	5.9	0.37	0.19	0.34
Al/50 nm	1	65	2.14	18.1	0.23	0.11	0.14
Pt/25 nm	2	95	1.30	6.6	0.064	0.049	-
Ni/25 nm	2	75	1.75	18.3	0.055	0.031	-
Co/25 nm	2	75	1.51	18.2	0.034	0.022	-
Fe/25 nm	2	75	1.92	17	0.053	0.027	-

which is the material with the largest value in group 2. A further decrease of the Au nanowire thickness to obtain equal values of λ_t as in Pt was not possible as no uniform Au wires could be fabricated below $t = 20\,\text{nm}$.

As it is the ratio λ_t/w that determines the transport mechanism, and the wire widths of our samples vary by a factor of up to two, Fig. 4.22 shows the non-local resistance of various studied samples versus λ_t/w. Figures 4.22(a-h) display samples of group 1 with a negative non-local resistance at low T. For these devices, $0.11 \leq \lambda_t/w \leq 0.58$ holds. The change of sign at $L = 150\,\text{nm}$ occurs for values in the range $0.14 \leq \lambda_t/w \leq 0.39$. In Figs. 4.22(i-l), samples of group 2 are shown, where R_{NL} is positive in the entire investigated temperature region. Here, λ_t/w ranges between $0.027 \leq \lambda_t/w \leq 0.064$ which is significantly smaller than the values observed for Au and Al in the first two rows. For all presented samples, a detailed list of the minimum and maximum value of λ_t/w together with the value of λ_t/w where the non-local resistance at $L = 150\,\text{nm}$ changes sign is given in Table 4.1.

From the calculation of the mean free path, the two groups 1 and 2 can be distinguished: λ_t/w of group 1 (Au and Al samples with a negative R_{NL} at low T) is about one order of magnitude larger than the values found for group 2 (Pt, Ni, Co and Fe with an always positive R_{NL}). Moreover, for all studied devices, λ_t/w increases with decreasing temperature. This drives the systems towards $\lambda_t/w = 1$ upon temperature decrease, i.e., towards the ballistic transport regime. This might explain the sign change of R_{NL} for certain devices as discussed in the next section.

Note that the numbers presented here should be considered as estimates, since they are subject to certain limitations (e.g., the analysis is based on a simple model which completely neglects the structure of the Fermi surface).
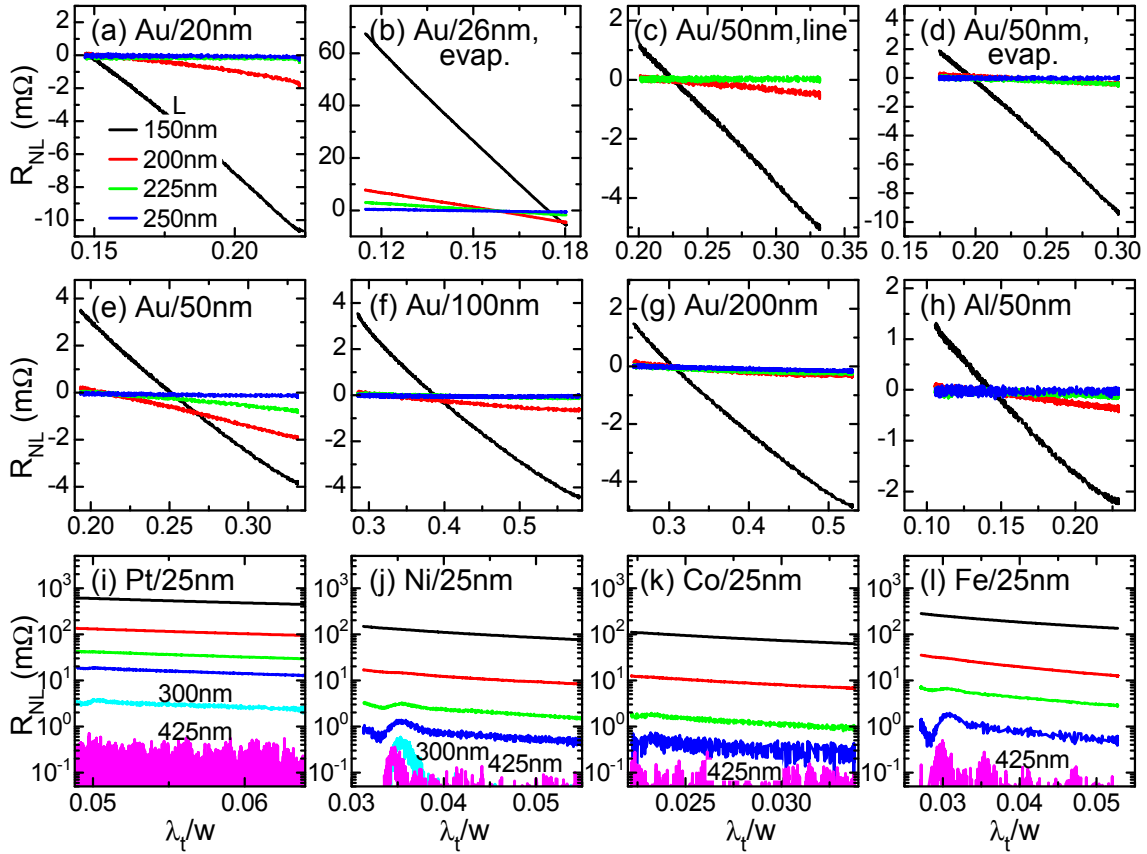
Figure 4.22: R_{NL} versus λ_{t}/w plotted for different values of L, color coded in (a) and for different samples as indicated in the first line of each panel. The value of w varies from sample to sample as listed in Table 4.1. For panels (a-h), a sign change of the non-local resistance is observed and λ_{t}/w is in the range $0.11 \leq \lambda_{\mathrm{t}}/w \leq 0.58$. The always positive values of R_{NL} for the samples presented in panels (i-l) come together with much smaller values of λ_{t}/w: $0.027 \leq \lambda_{\mathrm{t}}/w \leq 0.064$.

4.4.4.3 "Augsburg" model for a negative non-local resistance

The model presented here naturally explains the temperature dependence of the non-local resistance including negative values at low temperatures for certain samples. It was proposed by our collaborators Peter Schwab and Michael Dzierzawa from the University of Augsburg.
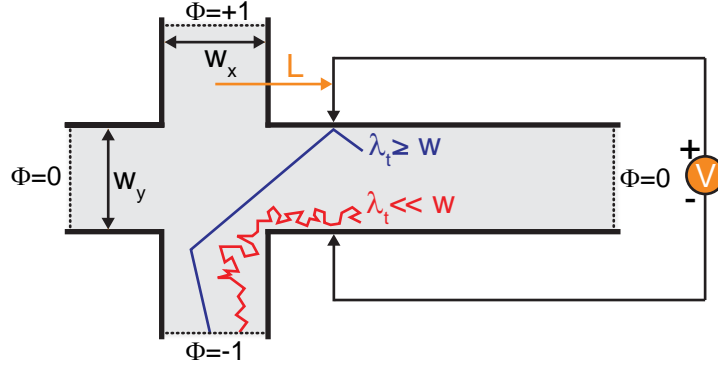
Figure 4.23: Sketch of the device layout used in the model calculations. Along the vertical wire, a potential difference ($\Phi = +1$ at the top and $\Phi = -1$ at the bottom) is applied. Depending on the transport regime – diffusive or ballistic – a positive or a negative non-local voltage is measured in the horizontal wire at a distance L. In the calculations $w_x = w_y = w$ is used.

The main idea is illustrated in Fig. 4.23 which schematically shows the intersection of a vertical and a horizontal wire. A potential difference between the two ends of the vertical wire ($\Phi = +1$ at the top and $\Phi = -1$ at the bottom) creates a potential landscape $\Phi(x, y)$ in the entire structure. The voltage is measured betweeen upper and lower edge of the horizontal wire at a distance L by two voltage probes ("high" at the top and "low" at the bottom), indicated as vertical arrows. The sign of the detected voltage depends on the dominating transport mechanism. On the one hand, for diffusive transport ($\lambda_t \ll w$, red line), the electrons coming from the lower part of the vertical wire are scattered many times and hence first reach the lower part of the horizontal wire and afterwards the upper part. This results in a lower potential at the lower side with respect to the upper side of the horizontal wire. For the used measurement configuration, this corresponds to a positive non-local voltage. On the other hand, in the ballistic transport regime ($\lambda_t \gg w$, blue line), the electrons are only rarely scattered when crossing the device. Thus, the electrons coming from the lower part of the vertical wire first hit the upper side of the horizontal wire which therefore has a lower potential than the later reached lower side. For the depicted measurement configuration, a negative voltage is detected. Hence, the crossover from positive to negative non-local voltage can be explained by a transition from diffusive to ballistic transport which is caused by a variation of the electron mean free path with temperature.

To quantify this idea, Peter Schwab and Michael Dzierzawa performed calculations which are briefly discussed in the following [220]. A detailed explanation of the calculation method can be found in Ref. [221].

In the ballistic transport regime, it is not possible to rely on the diffusion equation

anymore. Instead, one starts from the static Boltzmann transport equation [222]

$$\mathbf{v} \cdot \nabla_{\mathbf{r}} f(\mathbf{k}, \mathbf{r}) + \mathbf{F} \cdot \nabla_{\hbar, \mathbf{r}} f(\mathbf{k}, \mathbf{r}) = I[f] \qquad (4.9)$$

with velocity $\mathbf{v}$, position $\mathbf{r}$, wave vector $\mathbf{k}$, force $\mathbf{F} = -e\mathbf{E}$ and collision integral $I[f]$. For the sake of simplicity, only elastic scattering is assumed. From the distribution function $f(\mathbf{k}, \mathbf{r})$, observables like the charge density

$$\rho_{\mathrm{c}}(\mathbf{r}) = -2e \int f(\mathbf{k}, \mathbf{r}) \frac{d\mathbf{k}}{(2\pi)^3} \qquad (4.10)$$

can be determined [223]. Assuming deviations from equilibrium of the distribution function only close to the Fermi surface, the variation in the charge density can be expressed as

$$\delta\rho_{\mathrm{c}}(\mathbf{r}) = -2e\mathscr{N} \left\langle \int d\epsilon_p \delta f(\mathbf{k}, \mathbf{r}) \right\rangle_{\mathrm{FS}}, \qquad (4.11)$$

where $\mathscr{N}$ is the density of states per spin at the Fermi energy, ϵ_p is the energy variable, $\delta f = f - f_0$ is the deviation from the equilibrium distribution function f_0, and $\langle ... \rangle_{\mathrm{FS}}$ denotes an average over the Fermi surface.

The electrochemical potential for particles moving in $\hat{\mathbf{k}}$ direction $\mu(\hat{\mathbf{k}}, \mathbf{r})$ can be defined as

$$\mu(\hat{\mathbf{k}}, \mathbf{r}) = \int d\epsilon_p \delta f(\hat{\mathbf{k}}, \mathbf{r}) - e\Phi \qquad (4.12)$$

which is convenient, as the integration of the Boltzmann equation (Eq. (4.9)) over the energy ϵ_p yields an equation for $\mu(\hat{\mathbf{k}}, \mathbf{r})$:

$$\mathbf{v}_{\mathrm{F}} \cdot \nabla_{\mathbf{r}} \mu(\hat{\mathbf{k}}, \mathbf{r}) = -\frac{1}{\tau_{\mathrm{t}}} \left(\mu(\hat{\mathbf{k}}, \mathbf{r}) - \langle \mu(\hat{\mathbf{k}}, \mathbf{r}) \rangle_{\mathrm{FS}} \right). \qquad (4.13)$$

In this equation, the only inherent length scale is the mean free path $\lambda_{\mathrm{t}} = v_{\mathrm{F}} \tau_{\mathrm{t}}$. Equation (4.13) is identical to the equation of motion of a quasiclassical Green's function. It has a similar form as the Boltzmann equation but does not contain a force term and can also be derived without making use of the Boltzmann equation [221].

To determine the voltage profile of a real device in the ballistic regime, Eq. (4.13) has to be solved for the geometry under consideration. For interfaces connected to reservoirs, a fixed value of $\mu(\hat{\mathbf{k}}, \mathbf{r})$ for the incoming directions is assumed, whereas $\mu(\hat{\mathbf{k}}, \mathbf{r})$ for the outgoing directions is calculated from Eq. (4.13). All other surfaces are set as reflecting. In analogy to the diffusive case, charge neutrality is assumed, and the voltage is identified with the electrochemical potential: $e\Phi = \langle \mu(\hat{\mathbf{k}}, \mathbf{r}) \rangle_{\mathrm{FS}}$. The results of these calculations are presented in the following.

4.4.4.4 Comparison of the "Augsburg" model and our experimental data

We start with the voltage profile obtained for purely diffusive transport. The calculated potential distribution in the diffusive regime (Sec. 4.4.3) for a device layout as sketched in Fig. 4.23 is illustrated in Fig. 4.24(a). The potential is color coded
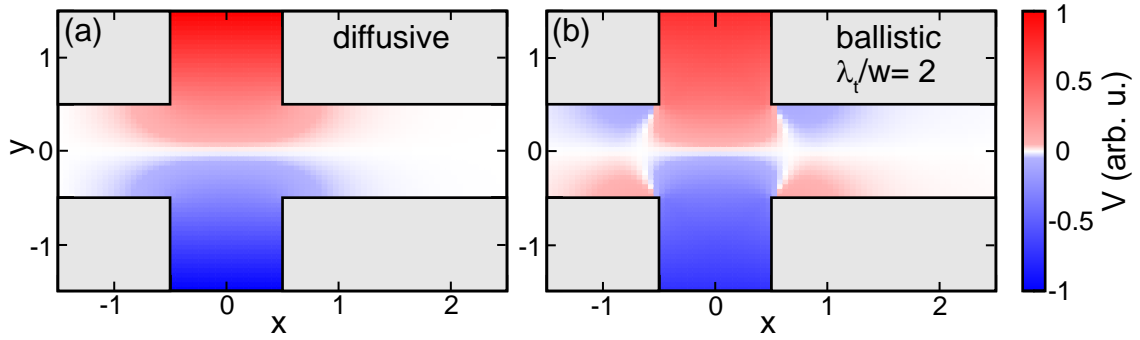
Figure 4.24: Potential distribution calculated for (a) the diffusive case and (b) in the ballistic regime for $\lambda_t/w = 2$ in the "Augsburg" model (see Sec. 4.4.4.3). An inversion of the potential gradient in the horizontal wire is obtained for ballistic transport which results in a negative non-local resistance [220].

where red corresponds to "high" and blue to "low". It decreases from top to bottom of the vertical wire. This gradient simply spreads into the horizontal wire generating "high" at the top and "low" at the bottom which leads to a positive non-local voltage for our contact configuration (Fig. 4.23).

On the other hand, the results of the ballistic calculations in the "Augsburg" model (see Sec. 4.4.4.3) are shown in Fig. 4.24(b) taking an exemplary mean free path of twice the wire width. Analogous to the diffusive case, a potential gradient in the vertical wire from top ("high", red) to bottom ("low", blue) is seen. However, in the horizontal wire outside the crossing region, this gradient is inverted: "low" is obtained at the top and "high" at the bottom. In our contact configuration, this leads to a negative non-local voltage.

As already stated in Sec. 4.4.4, the appearance of a negative non-local voltage in the ballistic regime is not a new phenomenon but expected only in high mobility semiconductor devices with $\lambda_t \gg w$. The "Augsburg" model enables us to investigate the dependence of the non-local signal on the ratio λ_t/w and thus depicts the transition from diffusive to ballistic transport. This transition of R_{NL} is shown in Fig. 4.25(a) for different distances L/w. The chosen values of L/w correspond to the distances L used in our devices for a typical average wire width of 70 nm: $L/w = 2.1 \,\widehat{=}\, L = 150$ nm; $L/w = 2.9 \,\widehat{=}\, L = 200$ nm; $L/w = 3.2 \,\widehat{=}\, L = 225$ nm and $L/w = 3.6 \,\widehat{=}\, L = 250$ nm. R_{NL} calculated in the "Augsburg" model shows a similar behavior for all L/w: in the case of $\lambda_t/w \gg 1$, a negative non-local resistance is obtained. With decreasing λ_t/w, the R_{NL} signal increases until it reaches zero. A further decrease of λ_t/w leads to a positive non-local resistance which matches the values calculated for the diffusive transport in the limit $\lambda_t \to 0$. A negative non-local resistance is not only obtained far in the ballistic regime ($\lambda_t/w \gg 1$) but already for values of $\lambda_t/w \gtrsim 0.45$ (inset of Fig. 4.25(a)), where the mean free path is clearly smaller than the wire width.

To further investigate the applicability of this theory to our measurements, the decay length of the calculated non-local signal was determined for different values of λ_t/w (0.46, 0.5, 0.6 and 1) indicated as dotted vertical lines in the inset of Fig. 4.25(a). Figure 4.25(b) shows the extracted values of R_{NL} (symbols) for a
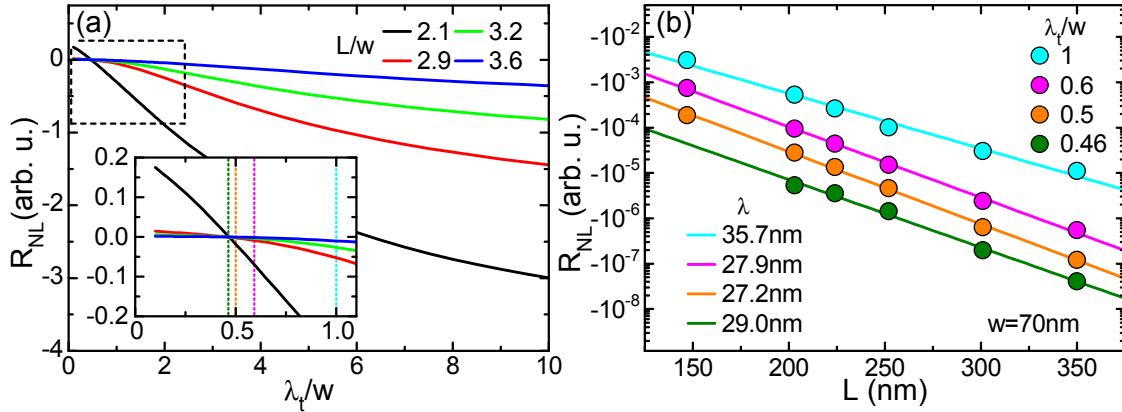
Figure 4.25: (a) R_{NL} calculated in the "Augsburg" model versus λ_{t}/w for different L/w. The inset shows a magnification of the framed area. The sign change of R_{NL} occurs already for mean free paths clearly smaller than the wire width, i.e., $\lambda_{\mathrm{t}}/w < 1$. (b) Calculated decay of R_{NL} with L for different values of λ_{t}/w indicated by vertical dotted lines in the inset of (a). From the Augsburg model, decay lengths between $27.2\,\mathrm{nm} < \lambda < 35.7\,\mathrm{nm}$ are obtained for a typical wire width of $w = 70\,\mathrm{nm}$.

typical wire width $w = 70\,\mathrm{nm}$. From a fit with $|R_{\mathrm{NL}}| = |R_0|\exp(-L/\lambda)$ (lines in Fig. 4.25(b)), decay lengths ranging between $27.2\,\mathrm{nm} < \lambda < 35.7\,\mathrm{nm}$ are obtained. Equivalent calculations performed for wire widths between $50\,\mathrm{nm} < w < 90\,\mathrm{nm}$ result in decay lengths ranging between $20.4\,\mathrm{nm} < \lambda < 46.0\,\mathrm{nm}$. These values of λ are in good agreement with the experimentally determined decay lengths $15\,\mathrm{nm} < \lambda < 42\,\mathrm{nm}$ (see also Fig. 4.27).

Finally, we compare the "Augsburg" model calculations to the experimental data taking Au/50 nm as example. Figure 4.26(a) shows the calculated non-local resistance for different L/w versus λ_{t}/w in the region of the R_{NL} sign change. The experimental data are displayed in Fig. 4.26(b) with the color code corresponding to that of panel (a). A striking qualitative agreement between theory and experiment is obvious. Even the fact that the R_{NL} sign change for the shortest L value occurs at slightly higher λ_{t}/w is reproduced by the calculations (inset of Fig. 4.26(a)).

Quantitatively, the R_{NL} sign change differs by a factor of less than two in λ_{t}/w. This is a good agreement, considering the uncertainties both in theory and experiment. For instance, the non-local resistance is calculated for one given value of L/w, whereas in experiment, the voltage leads exhibit a finite width w and thus average over a certain distance. Moreover, the calculations are performed for a two-dimensional system with an idealized structure and reflecting surfaces, whereas the measured devices have rough edges, rounded corners, and rough surfaces (see SEM images of Fig. 4.6). In addition, the determination of λ_{t} as discussed in Sec. 4.4.4.2 is inaccurate as the simple Drude model is used, and the device dimensions necessary to determine ρ further contain a significant uncertainty due to the inaccuracy of the lateral and vertical dimension measurement. Thus, the similarities of λ_{t}/w between experiment and theory is convincing. To sum up, the "Augsburg" model describes the experimental observations for Au/50 nm very well, in particular the temperature dependence and the negative non-local resistance at low T.
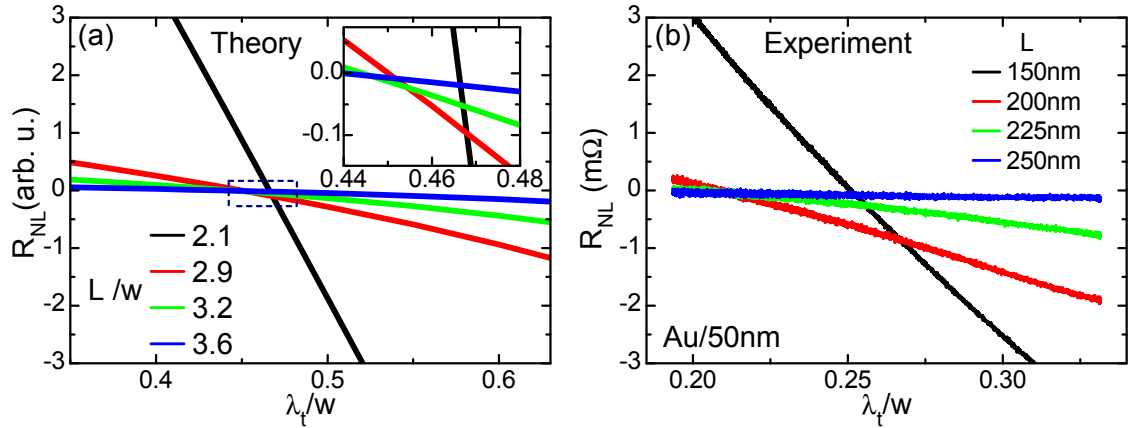
Figure 4.26: Comparison of (a) the calculated non-local resistance and (b) the experimentally determined data of the sample Au/50 nm. The same color code is chosen in (a) and (b). The qualitative agreement between theory and experiment is excellent. Even the experimental finding that the zero crossing for $L = 150\,\text{nm}$ occurs at larger values of λ_t/w is reproduced by the calculations as shown in the inset of (a). The values of λ_t/w of the zero crossing differ by less than a factor of two between theory and experiment which is reasonably good when taking into account the uncertainties both in experiment and theory.

The data obtained from the other Au and Al samples can also be explained quite well. For all these samples, the calculated mean free path ranging between $0.11 < \lambda_t/w < 0.58$ (see Table 4.1) is in the same region as for the Au/50 nm sample, discussed above. Thus, the "Augsburg" model is able to analogously explain the experimental observations for all these samples. However, the sign change of R_{NL} does not occur at a fixed value of λ_t/w for all samples, and no strict correlation between the maximum value of λ_t/w and the maximum value of the negative non-local resistance can be found. This implies that imperfections in the device geometry and/or the particular grain structure at the junctions strongly influence the actually measured magnitude of the non-local signal.

The "Augsburg" model also straightforwardly explains why the samples of group 2 (Pt, Ni, Co, Fe) do not show a negative non-local resistance at low T. When looking at λ_t/w of that group, $0.027 \leq \lambda_t/w \leq 0.064$ is significantly smaller than the values obtained for the Au and Al samples. From the inset of Fig. 4.25(a), it can be seen that for these values of λ_t/w, positive non-local resistances are expected. In fact, in that range, the transport is dominated by diffusive effects resulting in positive non-local signals in the entire temperature range.

In summary, all our experimental findings can be consistently and "semi-quantitatively" explained by the "Augsburg" model. The temperature dependence of the non-local signal and the fact that for certain materials a negative non-local resistance occurs at low temperatures is explained by the electron mean free path. Depending on λ_t/w, the system either is in a purely diffusive regime which results in $R_{NL} > 0$ (Pt, Ni, Co, Fe), or the system approaches the ballistic regime which results in a sign change of R_{NL} for low T (Au, Al).

4.4.5 Conclusions

As detailed in the previous section, all our experimental findings in the metallic nanostructures can be consistently explained by charge transport effects when taking into account diffusive and ballistic transport. To further illustrate this, Fig. 4.27 compares the experimentally obtained decay lengths (symbols) with the ones resulting from diffusive transport theory (see Sec. 4.4.3) (magenta hatched bar) and those from the "Augsburg" model (see Sec. 4.4.4.4) (green hatched bar). A good agreement between the theories and the values resulting from experiment is obtained which confirms that transport effects are indeed the origin of our findings. We thus conclude that spin-related phenomena, exhibiting a longer decay length, do not significantly contribute to the overall non-local signal. This might either be due to a very short spin diffusion length or to a much smaller spin Hall angle in our Au devices compared to the value $\alpha_{\mathrm{SH}} = 0.13$ reported by Seki *et al.* [68]. To quantify this last point, we now estimate an upper limit of α_{SH} for our typical Au sample Au/50 nm.
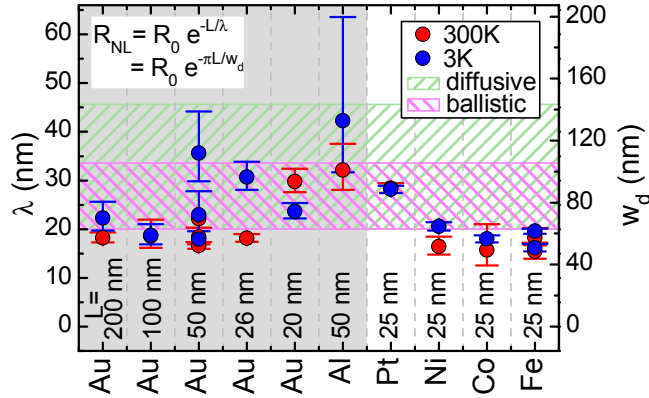
Figure 4.27: Experimentally determined decay lengths λ (symbols) of R_{NL} for various samples as presented in Fig. 4.18. The right axis is given by $w_{\mathrm{d}} = \lambda \cdot \pi$. The calculated decay lengths deduced from diffusive and ballistic theory are indicated as green and magenta hatched areas. They are very similar to the experimental results and make a pure transport related effect very likely as the origin of our observations.

Upper limit of α_{SH} from our experiments

Assuming purely diffusive transport at $T = 300\,\mathrm{K}$, a quantitative comparison between calculated and actually measured non-local resistance can be undertaken. From the measurements at $L = 150\,\mathrm{nm}$ in sample Au/50 nm, a value of $R_{\mathrm{NL}} = 3.49\,\mathrm{m\Omega}$ is obtained, whereas from the simulations for a wire width of 65 nm, a value of $R_{\mathrm{NL,sim}} = 2.75\,\mathrm{m\Omega}$ is extracted (see Fig. 4.20(b)). We assume that the difference of $74\,\mu\Omega$ is due to the spin-mediated effect. By means of Eq. (4.3) and using a wire width of 65 nm and a conservative value for the spin diffusion length of $\lambda_{\mathrm{sd}} = 60\,\mathrm{nm}$ [205], an upper limit of the spin Hall angle of $\alpha_{\mathrm{SH}} = 0.04$ is calculated. This value is smaller by a factor of more than three compared to $\alpha_{\mathrm{SH}} = 0.13$ reported

by Seki *et al.* [68]. Note that a larger spin diffusion length in our calculation would lead to a smaller upper limit for α_{SH}. However, a quantitative analysis is tricky as the simulation results depend strongly on the used wire width. For a slightly increased width of $w = 75\,\text{nm}$, the calculated non-local resistance is larger than the measured one. This would require an additional negative contribution to the non-local signal which is not compatible with the conventional spin-mediated resistance. Therefore, the calculation just presented is only a rough estimate. Nevertheless, our measurements demonstrate that in our structures, the spin Hall angle must be substantially smaller than the value suggested by Seki *et al.* This is in accordance with the findings of Mihajlović *et al.* [183] who estimated an upper limit of $\alpha_{SH} = 0.027$ in their measurements on Au nanostructures at $T = 295\,\text{K}$.

## Spin-mediated non-local resistance in Au

To put the significance of the experimentally obtained values into perspective, the spin-mediated non-local resistance and the non-local signal due to current spreading are calculated using parameters determined in our experiments on Au nanostructures. The results are shown in Fig. 4.28(a) which is inspired by Fig. 4.4(a) of the introductory theory section (Sec. 4.1.3). All calculations are performed for two values of L: the upper solid line of a pair always represents $L = 150\,\text{nm}$ and the lower dashed line $L = 200\,\text{nm}$.

The non-local resistances due to current spreading R^{CS} are shown as open symbols (circles for $L = 150\,\text{nm}$ and triangles for $L = 200\,\text{nm}$) and were calculated using the experimentally determined resistivity $\rho = 5.74\,\mu\Omega\text{cm}$ from Au/50 nm at 300 K.

The spin-mediated non-local resistance R^{SH} is calculated for different parameters of λ_{sd} and α_{SH} indicated as thin lines of different colors. The black thin lines are obtained for the spin Hall angle of $\alpha_{SH} = 0.13$ reported by Seki *et al.* [68] and a spin diffusion length of $\lambda_{sd} = 168\,\text{nm}$ [186]. In this case, as argued in Sec. 4.1.3, R^{SH} should be detectable and dominate over R^{CS}, e.g., when measured at a distance $L = 200\,\text{nm}$ and a wire width of $w = 70\,\text{nm}$. For these values, $R^{SH} = 0.92\,\Omega$ is much larger than $R^{CS} = 0.046\,\Omega$. This difference is indicated as magenta arrow in Fig. 4.28(a).

For clarity, the regions where experimental limitations prevent measurements are indicated as grey and blue shaded areas. One restriction is given by the fabrication process which does not allow wire widths smaller than $w \approx 65\,\text{nm}$. The second constraint is given by the previously discussed maximum voltage resolution which renders measurements below $50\,\mu\Omega$ impossible. Thus, our measurements are limited to the white region in Fig. 4.28(a). From this, it becomes clear that as already argued in Sec. 4.1.3 a detection of the spin-mediated non-local resistance should be possible if the values of λ_{sd} and α_{SH} used in the calculations are correct.

The bold black line in Fig. 4.28(a) represents the value of R_{NL}, where the magnitude of spin-mediated non-local resistance and non-local resistance due to current spreading are equal ($R^{SH} = R^{CS}$). Hence, a detection of the spin-mediated non-local resistance is restricted to the area below that line. While Fig. 4.28 is rather complex, it clearly shows, whether certain parameters enable a detection of R^{SH} or not.
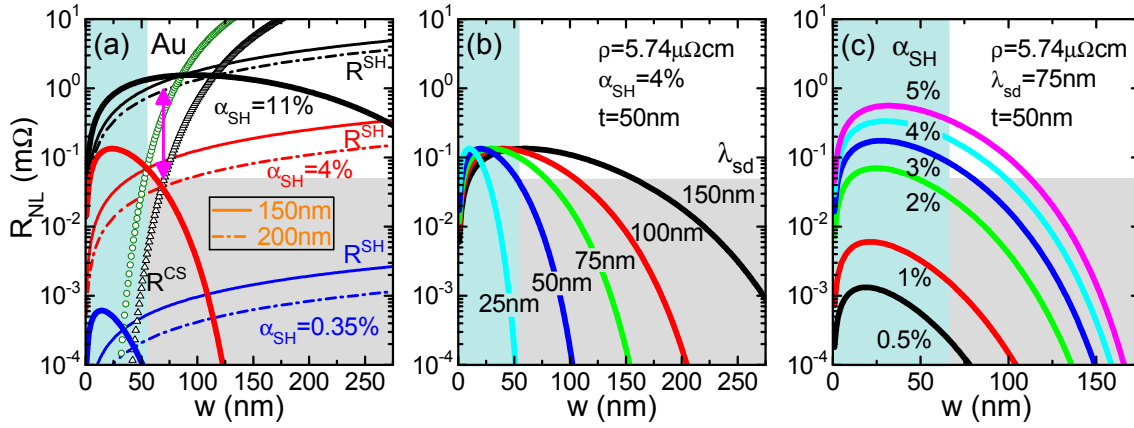
Figure 4.28: (a) Comparison of the magnitude of non-local resistances originating from diffusive current spreading R^{CS} (open green circles for $L = 150\,\text{nm}$ and open black triangles for $L = 200\,\text{nm}$) and from a combination of spin Hall and inverse spin Hall effect R^{SH} (thin lines of different color). R^{SH} is calculated for different values of λ_{sd} and α_{SH}. The thick lines represent the relation $R^{SH} = R^{CS}$ which is a measure for the maximum magnitude of the expected non-local signal. (b) $R^{SH} = R^{CS}$ calculated for different spin diffusion lengths λ_{sd}. (c) $R^{SH} = R^{CS}$ calculated for different spin Hall angles α_{SH}. (a-c) The shaded areas represent regions, where measurements are impossible due to the measurement resolution (grey shaded areas) or due to limitations in the sample fabrication process (blue shaded areas).

At the beginning of this section, we determined an upper limit of the spin Hall angle in our Au devices of $\alpha_{SH} = 0.04$. When using this value together with a more conservative spin diffusion length of $\lambda_{sd} = 60\,\text{nm}$ [205], the red lines in Fig. 4.28(a) are obtained. The values of the red bold line ($R^{SH} = R^{CS}$) correspond to much smaller values of R_{NL} than the black bold line almost exclusively in shaded regions. As this line represents the upper limit of α_{SH} for our Au devices, a detection of the spin-mediated non-local resistance is not possible with the available equipment.

When using a recently reported spin Hall angle in Au of $\alpha_{SH} = 0.0035$ [10] and $\lambda_{sd} = 60\,\text{nm}$, the blue lines in Fig. 4.28(a) are obtained. The calculated magnitudes of the spin-mediated non-local resistance are clearly much too small to be detected with the available equipment (note the logarithmic scaling of the y-axis).

Requirements for the detection of a spin-mediated non-local resistance

Considering that in our experiments, it was not possible to demonstrate a spin-mediated non-local resistance in metallic nanostructures, we discuss essential requirements which enable to decide a priori whether a detection of R^{SH} is possible or not. The two significant parameters determining magnitude and decay of the spin-mediated non-local resistance are α_{SH} and λ_{sd}. The influence of these parameters is analyzed with the help of the equality $R^{SH} = R^{CS}$. Only below these lines, R^{SH} is larger than R^{CS}, and a detection of the spin-mediated non-local resistance is possible. The bold lines in Fig. 4.28(b) represent $R^{SH} = R^{CS}$ calculated for different values of λ_{sd} using $\rho = 5.74\,\mu\Omega\text{cm}$, $\alpha_{SH} = 0.04$ and a typical layer thickness of

$t = 50$ nm. Again, the shaded areas represent regions not accessible in our measurements. As obvious from Fig. 4.28(b), the spin diffusion length λ_{sd} strongly influences the wire width necessary for an observation of the spin-mediated effect. For large λ_{sd} (e.g., $\lambda_{sd} = 150$ nm, black line), the value of $R^{SH} = R^{CS}$ slowly decreases with increasing wire width, whereas for short λ_{sd} (e.g., $\lambda_{sd} = 25$ nm, cyan line), a drastic decay is observed. This elucidates that the smallest realizable wire width determines the required minimum of λ_{sd} for which a spin-mediated non-local signal still can be detected at a given measurement resolution. For our fabrication process allowing a minimal wire width of $w = 65$ nm, the spin diffusion length should be larger than 75 nm to enable a detection.

Obviously, the value of the spin Hall angle also determines whether a detection is possible or not. The influence of α_{SH} on $R^{SH} = R^{CS}$ is shown in Fig. 4.28(c) calculated with $\lambda_{sd} = 75$ nm, $\rho = 5.74\,\mu\Omega$cm, and $t = 50$ nm. As expected from Eq. (4.3), the maximum of $R^{SH} = R^{CS}$ increases in magnitude with α_{SH}, actually proportional to α_{SH}^2. For $\alpha_{SH} < 0.03$ and the parameters used in these calculations, a detection is not possible due to the resolution limit of the measurement equipment. Note that in the calculations presented here, ρ and t of the sample Au/50 nm were used. As the absolute magnitudes are proportional to ρ/t, the values for other samples are different and increase with increasing resistivity and decreasing layer thickness (see Eq. (4.3)).

To summarize, for the used fabrication process and the available low-level measurement techniques, a spin diffusion length larger than $\lambda_{sd} \approx 75$ nm and a spin Hall angle larger than $\alpha_{SH} \approx 0.04$ are essential prerequisites to detect the spin-mediated non-local resistance and to distinguish it from the non-local resistance due to current spreading.

This points towards a fundamental problem of the scheme for generation and detection of spin currents (via spin Hall and inverse spin Hall effect) in H-shaped structures made from one single material: the mechanism causing the spin current, namely the spin-orbit coupling (see Sec. 2.2 and 2.3) is at the same time the main reason for spin relaxation. Thus, it is difficult to simultaneously obtain a large spin diffusion length and a large spin Hall angle, since a large λ_{sd} requires small spin-orbit coupling, while for a large α_{SH} strong spin-orbit coupling is required.

This correlation was recently demonstrated for Cu doped to different extents with Ir [69]. For pure Cu, large spin diffusion lengths of several 100 nm [224] are observed. Upon doping with Ir atoms, λ_{sd} monotonically decreases to $\lambda_{sd} = 5$ nm for an Ir doping level of 12 %. At the same time, the spin Hall angle, very small for pure copper, rose to a value above $\alpha_{SH} = 0.02$. This demonstrates that a large spin Hall angle is generally accompanied by a short spin diffusion length which complicates generation and detection of pure spin currents via spin Hall and inverse spin Hall effect in H-shaped devices made from a single material.

4.5 Non-local anisotropic magnetoresistance

In this section, we discuss a non-local effect related to the magnetic field orientation. This effect does not decay exponentially with distance from the current path but in contrast *increases* in magnitude. First, the experimental data are presented. Subsequently, a theory is developed and compared to our observations.

4.5.1 Experimental data

Some of the nanostructures investigated in the previous sections are made of ferromagnetic materials. For these materials, the resistance depends on the angle between magnetization $\mathbf{M}$ and current direction $\mathbf{J}$ [93]. Here, we investigate the local and non-local resistance dependence of H-shaped devices made of Ni, Co and Fe upon rotating an external magnetic field $\mu_0\mathbf{H}$ in the sample plane ($\hat{\mathbf{x}}$-$\hat{\mathbf{y}}$-plane, see Fig. 4.9). A value of $\mu_0 H = 2\,\mathrm{T}$ was used for all studies, as previous measurements showed that for such fields, all anisotropy fields are overcome and that $\mathbf{M}$ is parallel to $\mathbf{H}$ in good approximation [31].
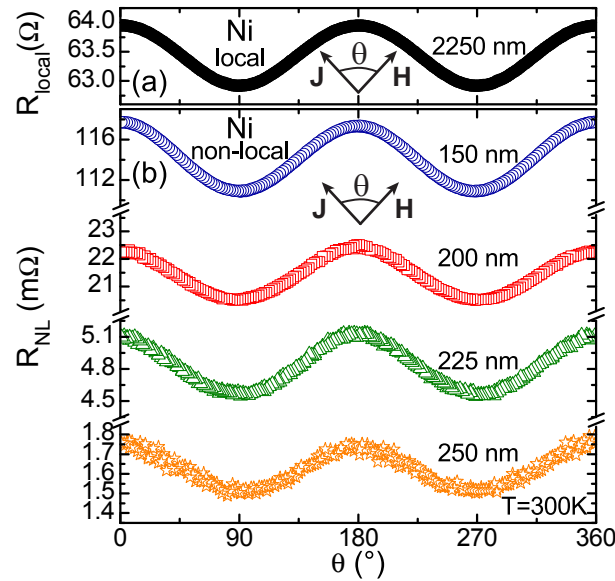
Figure 4.29: Magnetic field orientation dependence of (a) local and (b) non-local resistance in Ni nanostructures for an external field of $\mu_0 H = 2\,\mathrm{T}$ and different L. θ indicates the angle between $\mathbf{J}$ and $\mathbf{H}$, where $\mathbf{H}$ is rotated in the sample plane. A $\cos^2\theta$-type dependence is observed both in the local and the non-local resistance.

As typical example for our measurements on ferromagnetic nanostructure devices, we show the experimental data of a Ni sample with $t = 50\,\mathrm{nm}$ and $w = 110\,\mathrm{nm}$. In Fig. 4.29(a), the local resistance R_{local} (for the measurement configuration see Sec. 4.3.1) measured for a distance $L = 2250\,\mathrm{nm}$ is plotted versus the angle θ between current direction $\mathbf{J}$ and orientation of the external magnetic field $\mathbf{H}$. A 180° periodicity is observed with maxima for $\mathbf{H} \parallel \mathbf{J}$ ($\theta = 0°$, 180° and 360°) and minima for $\mathbf{H} \perp \mathbf{J}$ ($\theta = 90°$ and 270°). This effect is the well known anisotropic magnetoresistance (AMR) [30, 93, 225].
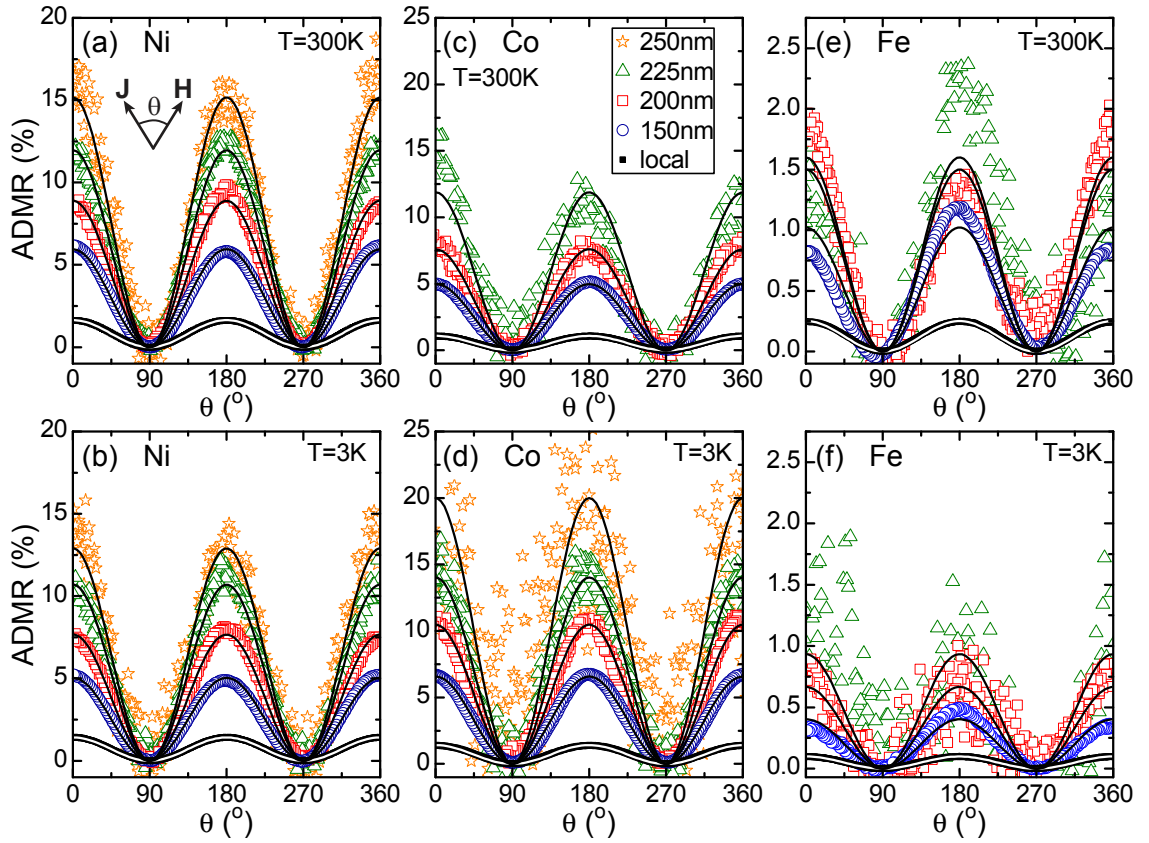
Figure 4.30: Local and non-local angle dependent magnetoresistance (ADMR) of Ni,
Co and Fe devices at $T = 300\,\mathrm{K}$ and $3\,\mathrm{K}$ for a constant magnetic field value of
$\mu_0 H = 2\,\mathrm{T}$. The color code for the different configurations and distances is given
in (c). Common to all samples is that the non-local ADMR is much larger than the
local ADMR, and that it increases in magnitude with the degree of non-locality L.
The solid lines are fits according to $A \cdot \cos^2 \theta$.

The non-local resistance R_{NL} (again, for the measurement configuration see
Sec. 4.3.1) measured at the same sample is shown in Fig. 4.29(b) for different degrees
of non-locality L, i.e., for different distances between the main current flow and the
voltage probes. For all L, oscillations in R_{NL} with the same periodicity and phase
as in the local case are observed. It is important to note that also in the non-local
configuration, θ is defined as angle between $\mathbf{J}$ and $\mathbf{H}$ while the current is now applied
along a "vertical" wire. This definition is chosen since for the AMR effect, only the
angle between $\mathbf{M}$ and $\mathbf{J}$ is significant.

To compare the magnitude of the oscillations in the local and the different non-
local resistances, we define the angle-dependent magnetoresistance (ADMR) and the
anisotropic magnetoresistance (AMR) as

$$\mathrm{ADMR}\,(\theta) \equiv \frac{R\,(\theta) - R_\perp}{R_\perp} \qquad \text{and} \qquad \mathrm{AMR} \equiv \frac{R_\parallel - R_\perp}{R_\perp}, \qquad (4.14)$$

where $R_\parallel$ and $R_\perp$ are the resistances for $\mathbf{H} \parallel \mathbf{J}$ and $\mathbf{H} \perp \mathbf{J}$ at $\mu_0 H = 2\,\mathrm{T}$, respectively.
The ADMR describes the full angle dependence, whereas the AMR – which simply
is $\mathrm{ADMR}\,(\theta = 0°)$ – is a measure for the magnitude of the effect.

Table 4.2: AMR(%) for different 3*d*-transition metal ferromagnet nanostructures at $300\,\mathrm{K}$ and $3\,\mathrm{K}$ for $\mu_0 H = 2\,\mathrm{T}$. The first row shows the values for the local configuration, whereas the following rows indicate the values measured in the non-local configuration at a distance L.

AMR (%)	Ni 300 K	Ni 3 K	Co 300 K	Co 3 K	Fe 300 K	Fe 3 K
local	1.6	1.4	1.1	1.4	0.25	0.1
150 nm	5.9	5.0	5.0	6.6	1.0	0.4
200 nm	8.9	7.7	7.6	10.5	1.5	0.7
225 nm	12.0	10.7	11.9	14.0	1.6	0.9
250 nm	15.2	12.9	–	20.0	3.0	–

Figure 4.30(a) shows the calculated ADMR for $T = 300\,\mathrm{K}$ for the raw data shown in Fig. 4.29. Astonishingly, the magnitude of the ADMR is significantly different for the local and non-local measurement geometries. The AMR in the local configuration ($\mathrm{AMR_{local}}$) amounts to $1.6\,\%$, whereas the values for the non-local AMR ($\mathrm{AMR_{NL}}$) are much larger. Particularly striking is that the magnitude of $\mathrm{AMR_{NL}}$ *increases* with the degree of non-locality L. All values of $\mathrm{AMR_{local}}$ and $\mathrm{AMR_{NL}}$ extracted from a fit with a $\cos^2 \theta$-function are listed in Table 4.2. At low temperature ($T = 3\,\mathrm{K}$, Fig. 4.30(b)), the behavior is identical: a small $\mathrm{AMR_{local}}$ and a $\mathrm{AMR_{NL}}$ which increases in magnitude with L is observed. The absolute values are slightly smaller compared to $300\,\mathrm{K}$ (see Table 4.2).

As mentioned before, we did not only investigate Ni samples but also devices made of Co and Fe with $w = 75\,\mathrm{nm}$ and $t = 25\,\mathrm{nm}$. Figures 4.30(c-f) show the corresponding ADMR for $T = 300\,\mathrm{K}$ and $3\,\mathrm{K}$, and Table 4.2 lists the extracted values for $\mathrm{AMR_{local}}$ and $\mathrm{AMR_{NL}}$. For all studied samples – both at high and at low temperature – the same qualitative results are obtained: the $\mathrm{AMR_{NL}}$ is much larger than the $\mathrm{AMR_{local}}$ and increases with the degree of non-locality L.

Note that although the $\mathrm{AMR_{NL}}$ increases with L and is up to an order of magnitude larger than the $\mathrm{AMR_{local}}$, one has to take into account that the magnitude of $R_{\parallel}$ and $R_{\perp}$ exponentially decrease with the degree of non-locality. Therefore, the measurement resolution sets a limit to the maximal observable magnitude of $\mathrm{AMR_{NL}}$.

The absolute magnitude of $\mathrm{AMR_{local}}$ observed in our experiments is comparable to the values reported in literature for similar nanowires [226, 227, 228].

To our knowledge, we are the first to report the observation of a non-local anisotropic magnetoresistance and its unexpected increase with L. In the following, we develop a theory which is able to explain our observations.

4.5.2 Theory

In a ferromagnetic material, the resistivity depends on the angle between current density $\mathbf{J}$ and magnetization $\mathbf{M}$ which is called anisotropic magnetoresistance (AMR) [30, 93, 225]. As discussed in the following, also the extent of current spreading depends on the field orientation. Schematically, the current paths in a horizontal wire of width w are shown in Fig. 4.31(a) for two magnetic field orientations: $\mathbf{H} \parallel \hat{\mathbf{x}}$ (blue) and $\mathbf{H} \parallel \hat{\mathbf{y}}$ (orange). Here, we illustrate the situation of the typical $3d$-transition metal ferromagnets, where the resistivity for $\mathbf{J} \parallel \mathbf{M}$ is larger than for $\mathbf{J} \perp \mathbf{M}$. In this case, the current spreads further away from the current leads for $\mathbf{H} \parallel \hat{\mathbf{y}}$ ($\rho_y > \rho_x$, orange) than for $\mathbf{H} \parallel \hat{\mathbf{x}}$ ($\rho_x > \rho_y$, blue).
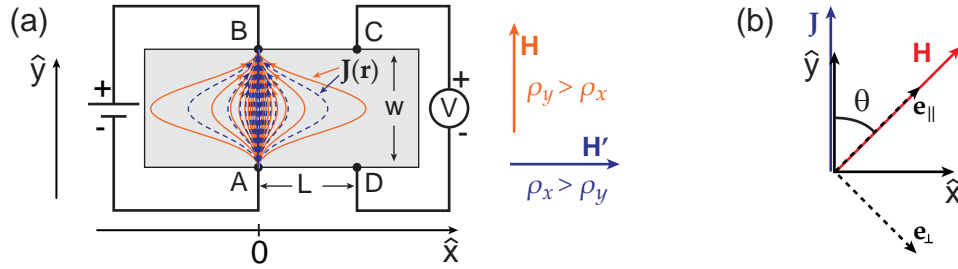
Figure 4.31: (a) Sketch of the current paths for two orientations of the external magnetic field ($\mathbf{H} \parallel \hat{\mathbf{x}}$ (blue) and $\mathbf{H} \parallel \hat{\mathbf{y}}$ (orange)). The extent of spreading critically depends on the field orientation. Here, the situation $\rho_\parallel > \rho_\perp$ is sketched. (b) Coordinate system in the sample frame. θ is the angle between $\mathbf{J}$ and $\mathbf{H}$.

To qualitatively study this approach, we employ the van-der-Pauw theorem (see Eq. (4.4)) generalized to anisotropic media. For point like contacts, it takes the form [229, 230]

$$\exp\left(-\frac{\pi t}{\left(\rho_\parallel \rho_\perp\right)^{1/2}} R_{\mathrm{AB,CD}}\right) + \exp\left(-\frac{\pi t}{\left(\rho_\parallel \rho_\perp\right)^{1/2}} R_{\mathrm{BC,DA}}\right) = 1, \qquad (4.15)$$

where $\rho_\parallel$ and $\rho_\perp$ are the diagonal components of the resistivity tensor for the two principal directions of the current density $\mathbf{J}$, parallel and perpendicular to $\mathbf{M}$. In Eq. (4.15), the resistivity ρ used in the isotropic case (see Eq. (4.4)) is replaced by $(\rho_\parallel \rho_\perp)^{1/2} = 1/\sqrt{\det\hat{\sigma}}$, where $\hat{\sigma} = \hat{\rho}^{-1}$ is the conductivity tensor. $R_{\mathrm{AB,CD}}$ is defined as the voltage difference between point D and C divided by the current flowing from A to B (Fig. 4.31(a)), and is just the non-local resistance R_{NL} of the previous sections. $R_{\mathrm{BC,DA}}$, defined as the respective permutation, is the classical local resistance $R_{\mathrm{local,x}}$ along the $\hat{\mathbf{x}}$-direction. In analogy to Sec. 4.1.2, R_{NL} is obtained by expanding the first exponential function in Eq. (4.15):

$$R_{\mathrm{NL}} = \frac{\left(\rho_\parallel \rho_\perp\right)^{1/2}}{\pi t} \exp\left(-\frac{\pi t}{\left(\rho_\parallel \rho_\perp\right)^{1/2}} R_{\mathrm{local,x}}\right). \qquad (4.16)$$

From this equation, it can be seen that the decay of the non-local signal depends on the resistance in $\hat{\mathbf{x}}$-direction which, in turn, is determined by the orientation of the
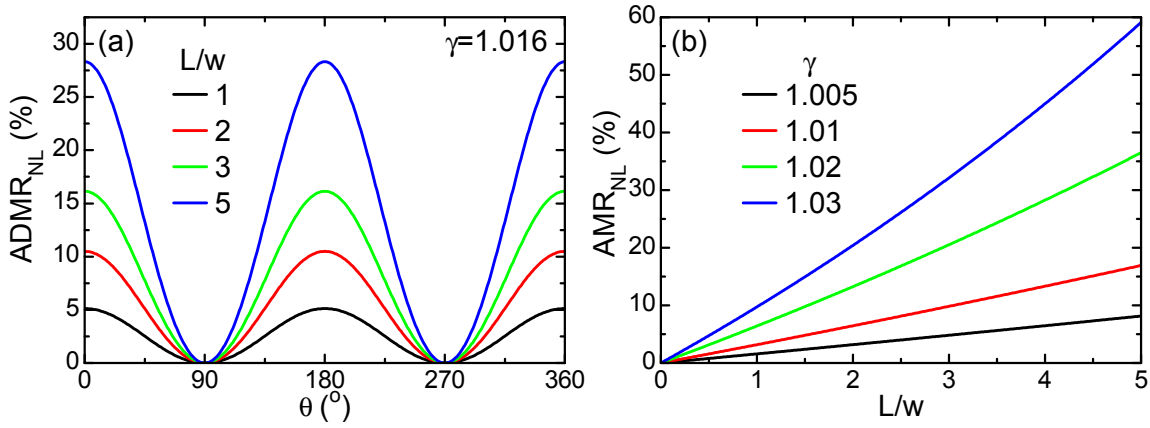
Figure 4.32: (a) Non-local ADMR versus magnetic field orientation θ for different L/w. Clearly, ADMR_{NL} increases with the degree of non-locality L. (b) AMR_{NL} versus L/w for different values of $\gamma = \rho_\parallel / \rho_\perp$. In first approximation, a linear increase of the ADMR_{NL} with L/w is observed.

external magnetic field. The magnetic field dependence of $R_{\text{local,x}}$ is extracted from the resistivity tensor $\hat{\rho}$ in the coordinate system of the sample defined by $\hat{\mathbf{x}}$ and $\hat{\mathbf{y}}$ (Fig. 4.31(b)):

$$\hat{\rho} = \begin{pmatrix} \rho_{xx} & \rho_{xy} \\ \rho_{yx} & \rho_{yy} \end{pmatrix} = \begin{pmatrix} \rho_\parallel - \Delta\rho \cos^2\theta & \Delta\rho \sin\theta \cos\theta \\ \Delta\rho \sin\theta \cos\theta & \rho_\perp + \Delta\rho \cos^2\theta \end{pmatrix} \tag{4.17}$$

with $\Delta\rho = \rho_\parallel - \rho_\perp$. In the limit $L \gg w$, $R_{\text{local,x}}$ is given by $R_{\text{local,x}} = \rho_{xx} L/(wt) = (\rho_\parallel - \Delta\rho \cos^2\theta) L/(wt)$. When inserting this into Eq. (4.16), we get the angle-dependent non-local resistance at a distance L from the main current flow

$$\begin{aligned} R_{\text{NL}}(L,\theta) &= \frac{(\rho_\parallel \rho_\perp)^{1/2}}{\pi t} \exp\left(-\frac{\pi L}{w} \cdot \frac{1}{(\rho_\parallel \rho_\perp)^{1/2}} \left[\rho_\parallel - \Delta\rho \cos^2\theta\right]\right) = \\ &= \frac{(\rho_\parallel \rho_\perp)^{1/2}}{\pi t} \exp\left(-\frac{\pi L}{w} \cdot \left[\gamma^{1/2} - \left(\gamma^{1/2} - \gamma^{-1/2}\right)\cos^2\theta\right]\right) \end{aligned} \tag{4.18}$$

with the resistivity ratio $\gamma = \rho_\parallel/\rho_\perp = 1 + \text{AMR}_{\text{local}}$. With Eq. (4.18), the non-local ADMR reads

$$\text{ADMR}_{\text{NL}}(L,\theta) = \frac{R_{\text{NL}}(L,\theta) - R_{\text{NL},\perp}(L)}{R_{\text{NL},\perp}(L)} = \exp\left(\frac{\pi L}{w} \cdot \left[\gamma^{1/2} - \gamma^{-1/2}\right]\cos^2\theta\right) - 1. \tag{4.19}$$

Figure 4.32(a) shows this function for different degrees of non-locality L/w. A value of $\gamma = 1.016$ extracted from the measurements in the Ni sample at $T = 300\,\text{K}$ is used. Clearly, the magnitude of the ADMR_{NL} *increases* with L/w and shows a qualitatively very similar behavior to the experimental data presented in Fig. 4.30.

The non-local anisotropic magnetoresistance AMR_{NL} is obtained by setting $\theta = 0°$ in Eq. (4.19):

$$\text{AMR}_{\text{NL}}(L) = \exp\left(\frac{\pi L}{w} \cdot \left[\gamma^{1/2} - \gamma^{-1/2}\right]\right) - 1. \tag{4.20}$$

Just as the $\mathrm{ADMR_{NL}}$, also the $\mathrm{AMR_{NL}}$ increases with increasing L. Figure 4.32(b) shows the $\mathrm{AMR_{NL}}$ for different values of γ. $\mathrm{AMR_{NL}}$ increases with L/w for all γ. To first order, the increase with L/w is linear as can be seen when approximating Eq. (4.20). For $\mathrm{AMR_{local}} \ll 1$, $\gamma^{1/2} \approx 1 + {}^1\!/{}_2\,\mathrm{AMR_{local}}$ and $\gamma^{-1/2} \approx 1 - {}^1\!/{}_2\,\mathrm{AMR_{local}}$ which results in $\mathrm{AMR_{NL}} \approx \exp\left(\frac{\pi L}{w} \cdot \mathrm{AMR_{local}}\right) - 1$. For our device dimensions, the exponential function can be expanded resulting in

$$\mathrm{AMR_{NL}} \approx \frac{\pi L}{w} \cdot \mathrm{AMR_{local}} \qquad (4.21)$$

which clearly shows the linear increase of $\mathrm{AMR_{NL}}$ with the degree of non-locality L.

To sum up, our analytical calculations making use of the van-der-Pauw theorem for anisotropic media correctly describe the qualitative behavior of the non-local anisotropic magnetoresistance discovered in our experiments. In particular, we found that $\mathrm{AMR_{NL}}$ *increases* in magnitude with the degree of non-locality L, i.e., the separation of main current flow and non-local voltage probes.

4.5.3 Comparison of experiment and theory

We now quantitatively compare the measured $\mathrm{AMR_{NL}}$ to theory. Figure 4.33(b) shows the experimentally determined values for Ni, Co and Fe at $T = 300\,\mathrm{K}$ (red symbols) and $3\,\mathrm{K}$ (blue symbols) together with the calculations (solid lines) for $T = 300\,\mathrm{K}$ using Eq. (4.20). Note that there are no free parameters in the calculations: L and w are determined by scanning electron microscope measurements, and $\gamma = 1 + \mathrm{AMR_{local}}$ is extracted from the local measurements[11] as shown in Fig. 4.33(a) and listed in Table 4.2. Figure 4.33(b) elucidates that the analytical model describes the experimental data for all three materials very well. The absolute magnitude is accurately reproduced, and an increase with the degree of non-locality L is obtained. However, slight deviations between theory and experiments concerning the absolute magnitude for the larger distances $L = 225\,\mathrm{nm}$ and $250\,\mathrm{nm}$ are observed, whose origin is not clear up to now.

To explore the influence of the finite width of the current and voltage leads, also finite element method (FEM) calculations with COMSOL Multiphysics 3.2 as discussed in Sec. 4.4.3 were performed. An anisotropic resistivity tensor was implemented to include the AMR. As an example, the simulation for Ni at $T = 300\,\mathrm{K}$ is plotted as dotted line in Fig. 4.33(b). The numerical calculations perfectly describe the non-local AMR for distances of $L = 150\,\mathrm{nm}$ and $200\,\mathrm{nm}$ and also reproduce the main result of the analytical calculations: the magnitude of $\mathrm{AMR_{NL}}$ increases with L. The marginal difference between the FEM simulation and the analytical calculations indicate that the finite width of the current and voltage leads only slightly influences the results. The good accordance between these two approaches confirms the validity of our analytical model.

---

[11]Note that here, we use $\mathrm{AMR_{local}} = (\rho_\parallel/\rho_\perp) - 1 \approx (R_\parallel(2\,\mathrm{T})/R_\perp(2\,\mathrm{T})) - 1$.
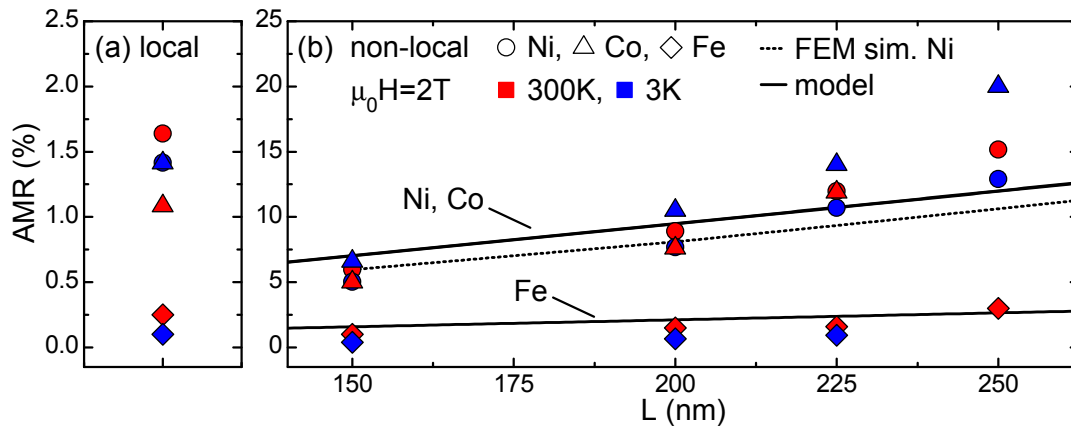
Figure 4.33: (a) Local and (b) non-local AMR of Ni, Co and Fe nanostructures for $T = 300\,\mathrm{K}$ (red symbols) and $3\,\mathrm{K}$ (blue symbols). The magnitude of the non-local AMR is much larger than in the local case and increases with L. The solid lines represent analytical calculations as detailed in the text. The dotted line is obtained from finite element method calculations for Ni at $300\,\mathrm{K}$. Both approaches describe our experimental data very well.

4.5.4 Summary

In this section, we reported a new effect, the non-local anisotropic magnetoresistance which does not exponentially decrease in magnitude with the distance L between the main current flow and the non-local voltage probes but in contrast *increases*. Values up to an order of magnitude larger than the local AMR were observed. Inspired by this discovery, we developed an analytical model based on the van-der-Pauw theorem for anisotropic conductors which correctly describes our experimental observations in Ni, Co and Fe nanostructures. This analytical model accurately reproduces both the absolute magnitude of the non-local AMR and its increase with L. Moreover, finite element method simulations taking into account the actual device geometry and the anisotropic resistivity gave very similar results compared to the analytical calculations and thus confirm our model.

4.6 Summary

In this chapter, we investigated a generation and detection principle of pure spin currents in metallic, normal metal nanostructures. Following the prediction of Hankiewicz *et al.* [14] and Abanin *et al.* [15], only an H-shaped structure of one given electric conductor is required. The spin current caused by a charge current flow in one leg of the H-structure generates a non-local voltage in the other.

From our calculations in the theory section (Sec. 4.1) using a recently reported large spin Hall angle [68], we found that for Au nanostructures and wire widths below $100\,\mathrm{nm}$, this non-local spin-mediated voltage dominates over another non-local effect, diffusive current spreading. The expected non-local resistance $R_{\mathrm{NL}} = V_{\mathrm{NL}}/I$ is quite small in the range of several $100\,\mu\Omega$.

Therefore, an experimental study of such effects requires advanced sample fabrication techniques and measurement setups with exquisite sensitivity. We thus developed a highly optimized sample fabrication process and a low-level, low-noise measurement technique.

The samples were fabricated via two lithography steps: the outer, larger structures were defined by optical lithography, whereas for the inner nanostructures, electron-beam lithography was used. After the optimization of the electron beam process, nanostructures with thicknesses of $50\,\mathrm{nm}$, widths of down to $65\,\mathrm{nm}$ and distances of less than $85\,\mathrm{nm}$ could be fabricated.

To measure these nanostructures, two measurement setups were developed and their performance compared. The first setup consisted of a lock-in amplifier (Stanford Research Systems SR-830) and used an AC current, whereas the second consisted of a hardware triggered combination of current supply (Keithley SourceMeter 2400) and voltage reading (Keithley Nanovoltmeter 2182A) which used an alternating DC current. For both setups, software was programmed which allowed remote control, real time data analysis, and an integration into the already present cryostat control software. We found that due to the higher common-mode rejection ratio, the hardware triggered SourceMeter and Nanovoltmeter outperformed the lock-in technique by about an order of magnitude in peak-to-peak noise level. For the measurement of our devices with the present setup, a peak-to-peak noise level of only $4-7\,\mathrm{nV}$ could be achieved which reduced to about $1\,\mathrm{nV}$ under ideal conditions.

To investigate the spin current generation and detection, we fabricated and measured various devices made from different materials (Au, Al, Pt, Ni, Co, Fe) and sample thicknesses ($20\,\mathrm{nm}$ – $200\,\mathrm{nm}$).

First, local resistance measurements were performed, where the 4-point resistance between nanowires of different separations is determined. These measurements showed a high quality of the fabricated samples with nanowires devoid of defects or irregularities.

Subsequently, the rather time consuming non-local measurements were carried out. Based on their results, the samples could be divided into two groups: group 1 (Au and Al samples) showed a positive non-local resistance at $300\,\mathrm{K}$ which decreased with temperature and became negative for low T. The thickness of the nanowires had no crucial influence. In contrast, the non-local resistance of samples from group 2

(Pt, Ni, Co and Fe samples) was positive in the entire studied temperature region ($3\,\mathrm{K} < T < 300\,\mathrm{K}$). The observation of negative resistances is astonishing, since for both the spin-mediated non-local resistance and the non-local resistance due to diffusive current spreading, positive values are expected. Careful checks, varying the contact configuration and the current density, demonstrated the robustness of the negative signal and excluded thermoelectric or other spurious effects as origin of the observed R_{NL}.

In the following, we critically discussed possible mechanisms which would result in negative R_{NL} values. One mechanism demands different signs of the spin Hall angle in the two junctions of the H-shaped structure (Sec. 4.4.2). This could for example be realized via different impurities in the junction areas or via one type of impurity and a difference in conductivity between the junctions. However, such differences in areas as close together as 150 nm and reproducibly present for all studied samples of group 1 seems highly unlikely. Moreover, the determined decay lengths of the non-local signal ($15\,\mathrm{nm} < \lambda < 42\,\mathrm{nm}$) which were similar for all studied samples and in particular independent of the nanowire thickness, are very small compared to the reported spin diffusion lengths for Au and Al. Furthermore, a magnetic field of several Tesla did not suppress the effect.

Current spreading is another mechanism leading to finite R_{NL}. And indeed, simulations of the non-local resistance using the Laplace equation and Ohm's law reproduced the measured R_{NL} values at high temperature (Sec. 4.4.3) very well. However, negative values could not be explained.

Negative non-local signals were predicted in the ballistic transport regime, thus for a mean free path much larger than the device dimensions. Such a situation is generally only realized in high mobility semiconductor devices. Here, we presented a theoretical model developed by Peter Schwab and Michael Dzierzawa which describes the non-local signal for a system which evolves from diffusive to ballistic transport (Sec. 4.4.4.3). Indeed, a sign change in R_{NL} was found, and it already occured for mean free paths smaller than the wire width. A comparison of experimental data and calculations revealed a convincing degree of agreement (Sec. 4.4.4.4). The value of λ_{t}/w for which R_{NL} changes sign is very similar, and the decay lengths are predicted correctly. From this, we concluded that a transition from diffusive to ballistic transport is the origin of the temperature dependence and the negative sign of the non-local resistance. The fact that for samples of group 2 only positive non-local values were obtained can be explained by the much smaller mean free paths of these samples. Therefore, in the entire temperature range studied, ballistic effects do not play a role. In any case, spin-mediated effects can only be a minor contribution to the observed non-local signal.

From a comparison of non-local measurements and simulation, we estimated an upper limit of the spin Hall angle in our Au devices (Sec. 4.4.5). We chose the measurements at room-temperature and assumed a purely diffusive transport in the simulation. Under these prerequisites, we obtained an upper limit of $\alpha_{\mathrm{SH}} = 0.04$, much smaller than the value $\alpha_{\mathrm{SH}} = 0.13$ reported by Seki *et al.* [68].

To decide a priori, whether or not a detection of the spin-mediated non-local resistance is possible, we calculated R_{NL} due to current spreading and R_{NL} due

to spin-related effects for different values of the spin diffusion length and the spin Hall angle. These calculations show that for a maximum resolution of $50\,\mu\Omega$ and a minimum nanowire width of $65\,\mathrm{nm}$, a spin diffusion length larger than $\lambda_{\mathrm{sd}} \approx 75\,\mathrm{nm}$ and a spin Hall angle larger than $\alpha_{\mathrm{SH}} \approx 0.04$ are essential for the detection of a spin-related R_{NL}.

Finally, we reported and discussed the discovery of a new effect, the non-local anisotropic magnetoresistance (Sec. 4.5). Astonishingly, this effect does not decay with the degree of non-locality, i.e., the distance between the current leads and the non-local voltage probes but increases in magnitude. Calculations based on current spreading in an anisotropic conductor reproduced our experimental findings and additionally quantitatively described the observed magnitude of the non-local AMR effect.

In summary, we performed extensive studies of nanostructures made of various materials with various thicknesses. Our measurements of more than 100 samples set a broad basis for a theoretical investigation of spin and transport related effects in metallic nanostructures and allowed to interpret our observations in terms of diffusive and ballistic transport.

An outlook on the effects discussed here is given in Chapter 5.

Chapter 5

Summary & Outlook

In this chapter, the main results of the present thesis are summarized. We experimentally investigated two different concepts for an essential component in spintronic devices: a pure spin current source. Such a device solely emits spin angular momentum without an accompanying charge current flow. The first concept relies on a pure spin current from a resonantly precessing magnetization, injected into an adjacent non-magnetic normal metal. The second one is based on an H-shaped nanoscale device, where a charge current generates a perpendicular pure spin current. Below, we summarize only the key facts, whereas more detailed summaries are given after the two main experimental chapters (Chapters 3 and 4) and the Appendix A.

Spin pumping as spin current source

The first extensively studied spin current source is based on spin pumping, where a time-dependent magnetization emits a pure spin current into an adjacent normal metal (Chapter 3). In order to detect the spin current, we used the inverse spin Hall effect which converts the spin current back into a conventional charge current. Under open circuit conditions, this results in a DC voltage detectable using conventional electronics. For these experiments, we fabricated a series of ferromagnet/platinum (F/Pt) bilayer samples. The magnetization precession was stimulated by a microwave field during ferromagnetic resonance (FMR) spectroscopy. In our studies, we could unambiguously show that the observed peak in the DC voltage, co-occurring with the FMR signal, is caused by spin pumping and not by a microwave rectification effect. This was concluded from the observed symmetry of the signal with respect to the external magnetic field and its behavior upon field inversion. In addition, it was concluded from a fixed orientation of the external magnetic field – all investigated F/Pt samples showed the same DC voltage sign independent of the sign of the spontaneous resistivity anisotropy or the Hall coefficient (Sec. 3.4.2). These results in particular firmly establish for the first time that the theoretical model for spin pumping [7, 8, 12] in combination with the inverse spin Hall effect indeed is quantitatively correct. Spin pumping thus is a new powerful way to generate pure spin currents.

Moreover, we could experimentally prove that, as predicted by theory, the magnitude of the spin pumping signal is proportional to the sample length but independent of its width. This sets the basis for advanced sample designs allowing to increase the generated DC voltage which should enable to also quantify very small spin Hall angles in various normal metals (Sec. 3.4.4).

A main result of our experiments was the finding that the present theories for spin pumping are not limited to transition metal-based bilayers but also apply to the ferromagnetic Heusler compounds Co_2FeAl and Co_2FeSi, the ferrimagnetic spinel oxide Fe_3O_4, and the dilute magnetic semiconductor (Ga,Mn)As (Sec. 3.4.7). For all these materials, despite the magnetic exchange mechanism, the spin polarization, the saturation magnetization, the charge carrier transport mechanism and the charge carrier polarity being qualitatively different, spin pumping could be observed. The validity of the spin pumping theories in combination with the inverse spin Hall effect could be demonstrated via the observation of a scaling behavior over more than four orders of magnitude of the generated DC voltage versus the precession cone angle of the magnetization.

The second main result was the determination of quantitative values for the spin mixing conductance $g^{\uparrow\downarrow}$ for various ferromagnet/Pt interfaces, a parameter crucial in spin transfer torque, spin Seebeck and spin pumping measurements (Sec. 3.4.9). We found that $g^{\uparrow\downarrow}$ is essentially independent ($g^{\uparrow\downarrow} = (4 \pm 3) \times 10^{19}\,\mathrm{m}^{-2}$) of the ferromagnetic layer properties for high-conductive ferromagnets (Ni, Co, Fe, Co_2FeAl and Co_2FeSi) as predicted by theory, whereas for the low-conductivity ferromagnet Fe_3O_4 and the dilute magnetic semiconductor (Ga,Mn)As, values smaller by about one order of magnitude were obtained. We furthermore found that $g^{\uparrow\downarrow}$ is essentially temperature independent in the entire studied temperature range of $2\,\mathrm{K} < T < 290\,\mathrm{K}$.

Additionally, spin pumping from standing spin wave excitations was investigated using (Ga,Mn)As/Pt samples (Sec. 3.4.11). We extended a simulation of the FMR signal to also describe spin pumping from inhomogeneous ferromagnets and found from a comparison with our experiments that not only the F/N interface but the major part of the (Ga,Mn)As film thickness (200 nm) contributes to the spin pumping signal.

Finally, we investigated several tri-layer structures. From F1/Pt/F2 devices, where F1 and F2 are two different ferromagnets, we concluded that the spin orientation of the spin current is not determined by the majority spin band of the ferromagnet but by the magnetization relaxation process (Sec. 3.4.12). From the measurements of various F/N1/N2 heterostructures, where N1 and N2 are two different normal metals, we were able to show that a pure spin current can be injected into N1 and subsequently detected in N2 for interlayer thicknesses of up to 30 nm (Sec. 3.4.13).

In summary, our extensive spin pumping measurements considerably extended the present knowledge about spin pumping, and in particular quantitatively corroborated important predictions from theory.

Non-local spin current source

The second device predicted to be a spin current source that we extensively studied consists of an H-shaped normal metal nanostructure: an applied current in one wire generates a pure spin current in a perpendicularly connected bridging wire via the spin Hall effect. By the inverse spin Hall effect, this spin current causes a charge current in a third wire perpendicularly connected to the second one. Under open circuit conditions, this charge current evokes a non-local voltage difference which can be measured with conventional electronics. The appealing feature of this approach is its simplicity and the fact that no ferromagnetic materials and no interfaces are needed. The entire device can be fabricated in one piece from a single material.

We performed calculations for different materials (Au, Al, Pt) using literature values for the spin diffusion length and the spin Hall angle and found that for Au devices, the expected non-local voltage should be detectable and dominate over non-local voltages originating from diffusive current spreading (Sec. 4.1). Moreover, we learned from these calculations that for a detection of the spin-mediated non-local resistance, nanostructures with widths below 100 nm and a measurement resolution of better than 0.5 mΩ are required which demands sophisticated fabrication and measurement techniques.

Therefore, we established an electron beam lithography process which enables to fabricate intersecting nanowires with widths down to 65 nm and distances of less than 85 nm (Sec. 4.2.1). In addition, two independent measurement setups were implemented and their noise level compared. We found that the best results were achieved when using an AC current reversal setup consisting of a hardware triggered combination of current source and voltage reading. With that setup, a final resolution limit under ideal conditions in the order of 1 nV was achieved (Sec. 4.2.2).

Conventional 4-point measurements confirmed the uniformity of the nanowires and thus demonstrated the sample quality. The non-local measurements on various Au and Al samples, made from films of different thickness, showed an unexpected temperature dependence: a positive non-local voltage at high temperature and negative values at low temperatures. We carefully checked that these results were not related to thermoelectric effects. From the independence of the non-local signal on an applied external magnetic field, the "wrong" sign at low temperatures, and the short decay length, a spin-related effect as the origin of our measured signal could be excluded.

From the difference between finite element method simulations for diffusive transport and our measurement data at high temperature, we could estimate an upper limit for the spin Hall angle in our Au devices of $\alpha_{SH} = 0.04$ which is significantly smaller than $\alpha_{SH} = 0.113$ reported by Seki $et\,al.$ [68]. However, our α_{SH} value is well within the range of values reported more recently, e.g., $\alpha_{SH} = 0.027$ [183].

To further investigate the origin of the non-local signal and its temperature dependence, we studied Au samples of different thickness as well as devices made of various materials: Au, Al, Pt, Ni, Co and Fe. We found that the Au and Al samples showed negative non-local signals at low temperatures, whereas the signal was positive in the entire studied temperature range for Pt, Ni, Co and Fe.

Following our experimental observations, P. Schwab and M. Dzierzawa (University of Augsburg) developed a Boltzmann transport theory which takes into account the transition from diffusive to ballistic transport. The negative non-local signal for certain samples at low temperatures originates from a direct transmission of electrons from "high" of the current injection lead to the "low" voltage probe. For this situation, the Boltzmann calculations revealed that the electron mean free path is of the same magnitude as the nanowire width. We found a very good qualitative agreement between this theory and experiment.

Based on our experimental findings, we also presented calculations which a priori allow to judge whether the spin-mediated non-local voltage is detectable or not. For an assumed measurement resolution of $50\,\mu\Omega$ and a nanowire width of about $65\,\mathrm{nm}$, we obtained values for the spin diffusion length larger than $\lambda_{\mathrm{sd}} \approx 75\,\mathrm{nm}$ and for the spin Hall angle larger than $\alpha_{\mathrm{SH}} \approx 0.04$.

Finally, we discovered another effect related to non-local voltages: the non-local anisotropic magnetoresistance. We found that this effect does not exponentially decay as a function of the separation L between the current leads and the non-local voltage probes as non-local effects conventionally do. In contrast, the non-local anisotropic magnetoresistance increases with L. These observations made for Ni, Co and Fe can be explained by differently pronounced current spreading depending on the orientation of the external magnetic field. We developed an analytical model based on the van-der-Pauw theorem for anisotropic media which allows for calculation of this effect. Finite element method simulations including an anisotropic resistivity tensor even quantitatively reproduce our measurement data and confirm the validity of our model.

In summary, we thoroughly investigated a predicted H-shaped spin current source concept in metallic nanostructures and found that the requirements for the generation and detection are so severe that an experimental detection is very difficult, if not impossible. The implementation of advanced fabrication and measurement techniques made it possible to exclude this spin-related effect as the origin of the measured non-local voltage in all our devices and allowed to discover a new non-local phenomenon, the non-local anisotropic magnetoresistance.

Spin-polarized supercurrents

For the investigation of spin-polarized triplet supercurrents, superconductor/CrO_2/ superconductor hybrids were fabricated and investigated (Appendix A). Crucial for these devices are transparent superconductor/CrO_2 interfaces. We performed extensive studies of surface cleaning via Ar-ion bombardment and found that even cleaning times up to $20\,\mathrm{min}$ did not result in small and reproducible interface resistances. One possible solution is the insertion of a thin RuO_2 interlayer resistant against oxidation and reduction or alternatively a very rapid processing of the different layers.

Outlook

Spintronics is a vital research field which aims to exploit the spin degree of freedom in electronic devices. Therefore, a major step forward would be the availability of a spin current source supplying a pure spin current without accompanying net charge current since this would allow to exclusively study spin-related effects. In this thesis, we experimentally investigated fundamental properties of different spin current sources. Our results show that spin pumping indeed is a robust and versatile spin current source, paving the way for further studies. In the following, several ideas for future research are presented.

On the one hand, further properties of spin pumping-based spin current sources should be investigated. For instance, our spin pumping measurements showed that the spin mixing conductance is about one order of magnitude different between high and low conductive ferromagnets. In particular, for ferromagnetic insulators distinctly lower values were found [42]. Therefore, it is important to investigate and clarify the evolution of the spin mixing conductance with the ferromagnets conductivity on one and the same sample. This could be achieved by temperature dependent measurements using Fe_3O_4 as the ferromagnet with a dirty metal conductivity at room temperature and a strongly increasing resistivity below $100\,K$.

Moreover, the influence of the magnetic layer thickness and in particular the significance of the homogeneity of the magnetization on the spin pumping signal is still unclear, as theory so far just considered an interface effect, whereas our measurements on (Ga,Mn)As/Pt indicate that the entire ferromagnetic layer thickness (at least in "thin" films) contributes to the spin pumping signal. Therefore, measurements on other ferromagnets exhibiting spin wave excitations or on ferromagnetic multilayer stacks covered with platinum, where the different layers can be separately excited, appears very promising to clarify this point.

Furthermore, it would be highly enlightening to investigate other methods causing magnetization motion. The advantage could be a much simpler setup without microwave radiation and DC magnetic field. First experiments in that direction were performed via thermal gradients and are referred to as spin Seebeck effect measurements. During these experiments, a thermal gradient applied along a ferromagnetic layer stripe causes an electrical potential difference between the ends of a platinum bar attached perpendicular to the gradient [17, 231, 232]. First theories explain this observation with different temperature profiles between the phonon and the magnon subsystems due to different boundary conditions at the F/N interface. The adjacent platinum acts as an additional relaxation channel for the magnon-system which results in the emission of a pure spin current. This spin current then generates a charge current via the inverse spin Hall effect which is the origin of the potential difference [233, 234]. In this context, for example waste heat could be used for a spin current source.

On the other hand, not the spin current source itself can be further explored but also its applications. The spin current source can, e.g., be used to study the spin Hall angle of different materials and its temperature dependence. First experiments are reported in Ref. [9].

Additionally, our experiments on multilayer structures, in which we could show that the generated spin current can be sent through an interlayer, open the doors for the direct usage of the spin current in various experiments, e.g., in spin torque devices. This calls for spin injection/spin transport experiments, e.g., in various metal or semiconductor devices, not with spin-polarized but with pure spin currents.

For the second investigated spin current source, the H structures, we showed that a spin Hall angle larger than $\alpha_{SH} \approx 0.04$ and a spin diffusion length exceeding $\lambda_{sd} \approx 75 \, \mathrm{nm}$ are essential for a detection. Therefore, further experiments should focus on the search for materials having these properties. In particular, impurity doping studies with various materials and concentrations might be helpful.

Another approach would be to separate the conversion processes (charge current $\longleftrightarrow$ spin current) from the spin transport process in the bridging wire. Thereby, the vertical wires could be made of a material with a large spin Hall angle (e.g., Pt) and the bridging horizontal wire of a material with a long spin diffusion length (e.g., Cu).

Finally, for the spin-polarized supercurrents in the superconductor/ferromagnet/ superconductor devices, the prerequisites for the observation of spin triplet supercurrents are known and first experiments successfully accomplished [235]. Therefore, now the influence of the magnetization orientation on the supercurrent can be investigated. Moreover, the proof of a non-monotonic temperature dependence of the critical Josephson current in the mK range could unequivocally confirm the presence of a spin-triplet supercurrent in such devices.

To sum up, the results presented in this thesis significantly contribute to the foundations for many more experiments and theoretical studies dealing with pure spin currents and related phenomena.

Appendix A

Spin-polarized supercurrents

Spin-polarized currents play an important role in the field of superconductivity. They are predicted for particular superconductor/ferromagnet/superconductor (S/F/S) Josephson junctions. In this context, we extensively studied the interface resistances of superconductor/ferromagnet hybrids.

The results presented here originate from a close cooperation with the group of Teun Klapwijk at the Technische Universiteit Delft, the group of Jan Aarts at the Universiteit Leiden, and the group of Arunava Gupta at the University of Alabama.

We start with a brief introduction to theory and subsequently give a short overview of sample fabrication, the measurement technique and our results.

A.1 S/F contacts – Long-range proximity effect

In a conventional s-wave superconductor, the supercurrent is carried by spin-singlet Cooper pairs, i.e., by pairs of electrons with opposite spin orientation. In contrast, in ferromagnets, a diametrically opposed coupling mechanism between the electron spins is present, since the exchange interaction energy E_{ex} makes a parallel alignment of the electron spins favorable. The spin configuration at the interface of a superconductor brought into contact with a ferromagnet thus is an interesting and complex question. To give some insight into this problem, we start with the case of a superconductor/normal metal (S/N) interface. Due to the so-called proximity effect [236, 237, 238], the superconducting correlations "leak" into the adjacent conductor. The decay length of singlet Cooper pair correlations inside a diffusive normal metal is given by $\xi_N = \sqrt{\hbar D / k_B T}$, where $\hbar$ is Planck's constant divided by 2π, D is the diffusion constant, k_B the Boltzmann constant and T the temperature. ξ_N is typically in the range of $100\,\text{nm} \leq \xi_N \leq 1\,\mu\text{m}$ at low T [239]. In the case of a superconductor/ferromagnet (S/F) interface, the singlet Cooper pair correlation decay length is given by $\xi_F = \sqrt{\hbar D / E_{ex}}$, where the thermal energy $k_B T$ in ξ_N for the S/N contact is replaced by the exchange energy E_{ex} of the ferromagnet. As the exchange energy is typically much larger than the thermal energy, ξ_F is extremely short, ranging from ca. $5\,\text{nm}$ for weak (PdNi[1]) to ca. $0.5\,\text{nm}$ for strong (Ni, CrO_2, Fe) ferromagnets [240, 241, 242]. One way to determine such decay lengths is via

---

[1]In general, the Ni concentration is in the range of 10-20 %.

studying S/X/S Josephson junctions [243], where X stands for N or F[2]. By such measurements, the here given equations for ξ_N and ξ_F and the related theory could indeed be confirmed (for further details see, e.g., Refs. [239, 241, 242, 244, 245]).

However, several experiments (see, e.g., Refs. [246, 247, 248]) did not fit into that picture but suggest a much larger value of ξ_F. Moreover, in 2006, Keizer *et al.* [249] demonstrated that a Josephson supercurrent can traverse a strong ferromagnet on a length scale of several hundred nanometers. We discuss this experiment in more detail, as it is the basis for our measurements presented later. Keizer *et al.* used NbTiN as the superconductor – a material resistant against oxidation. CrO_2, a strong ferromagnet with a predicted spin polarization of almost 100 % [250, 251, 252, 253, 254] was used for the magnetic part. Such ferromagnets are called half-metallic ferromagnets (HMF), since at the Fermi energy E_F, only one spin band is populated [255]. This implies that in HMFs, singlet Cooper pairs cannot propagate, since electrons with both spin orientations are required. Hence, supercurrents in CrO_2 should decay rapidly for two reasons: (i) the strong exchange interaction of CrO_2 and (ii) the half-metallicity of CrO_2 which already prohibits the formation of singlet Cooper pairs.

Shortly before the experiments by Keizer *et al.*, theories [240, 256] were developed predicting a s-wave triplet supercurrent for which a decay length equal to that of a normal metal is expected. Such a triplet supercurrent consists of Cooper pairs with both spins parallel[3]. This results in "magnetic Cooper pairs" with a total spin $S = \hbar$ (instead of 0 for a singlet Cooper pair) and thus in a spin-polarized supercurrent. A mechanism for the conversion from the singlet supercurrent in S into the triplet supercurrent in F was proposed by Bergeret *et al.* [256] and Eschrig *et al.* [258, 259]. It is a combination of two effects: spin mixing and spin-flip scattering which require a short-scale inhomogeneous magnetization orientation close to the S/F interface. As mentioned above, Keizer *et al.* observed supercurrents propagating in CrO_2 over length scales of several hundred nanometers. They suggested such a spin-triplet supercurrent as explanation for their observations. On the one hand, such long coherence lengths were predicted by theory, and on the other hand, only one spin species is required for the triplet correlations which is compatible with a half-metal.

However, the results of Keizer *et al.* [249] showed large differences in the critical current I_c between different devices and some devices even did not show the effect. Therefore, the results were controversially discussed. One key parameter in these experiments is the quality of the S/F interface. For an efficient transmission of superconducting correlations across the S/F boundary, a transparent interface is crucial as discussed by Blonder *et al.* [260]. This is in particular challenging, since the ferromagnetic CrO_2 is a metastable phase which reduces to the antiferromagnetic insulator Cr_2O_3 accompanied with a loss of oxygen [261, 262, 263]. Therefore, even after covering CrO_2 with another material, an oxidation of the interface might

---

[2]Sometimes, there are also tunnel barriers introduced at one or both interfaces to simplify measurements.

[3]A s-wave triplet wave function does not violate the Pauli principle if the generalized coordinates of the particles include time, and the states are odd in time. A detailed discussion is given in Refs. [240, 256, 257].

occur [261] and also the storage in vacuum does not prevent that transformation. The result is a CrO_2 film covered with a several nanometers thick, insulating Cr_2O_3 capping layer acting as barrier in transport experiments. Keizer *et al.* worked around this problem by an Ar-ion "cleaning" step which removes the Cr_2O_3 and a subsequent deposition of the superconductor NbTiN which is resistant against oxidation [249]. However, no systematic transport studies concerning the interface properties were performed. Therefore, the aim of this part of the thesis was to reproduce the measurements of Keizer *et al.* and to systematically investigate the electrical properties of various interfaces to CrO_2.

A.2 Sample fabrication and measurement technique

A typical sample in our experiments is sketched in Figure A.1(a). It consists of a substrate onto which a CrO_2 layer was grown, and pads for electrical contacting made of Au, Al, Nb or NbTiN were deposited. The CrO_2 film with a thickness of ca. 100 nm was grown on TiO_2 or Al_2O_3 substrates via chemical vapor deposition in the group of Arunava Gupta at the University of Alabama [264] and in the group of Jan Aarts at the Universiteit Leiden by Muhammad Shahbaz Anwar [265]. The samples were then sent to Munich or Delft, where we further processed and studied them. The contact pads (Au, Al, Nb or NbTiN) with length and width of 200 μm, a thickness of 50 nm and a distance of 100 μm were fabricated via optical or electron-beam lithography, Ar-ion sputtering and lift-off technique. However, due to the time delay between the CrO_2 fabrication and the contact pad deposition, Cr_2O_3 already formed at the CrO_2 surface. Therefore, we "cleaned" the CrO_2 surface via Ar-ion etching immediately prior to the metal deposition. However, one has to take into account that the Ar-ion bombardment can also cause structural defects at the surface which might result in high resistance interfaces. To thoroughly investigate the electrical interface properties, we varied the pad material and in particular the Ar-ion etching time for various CrO_2 layers obtained from the two different groups.
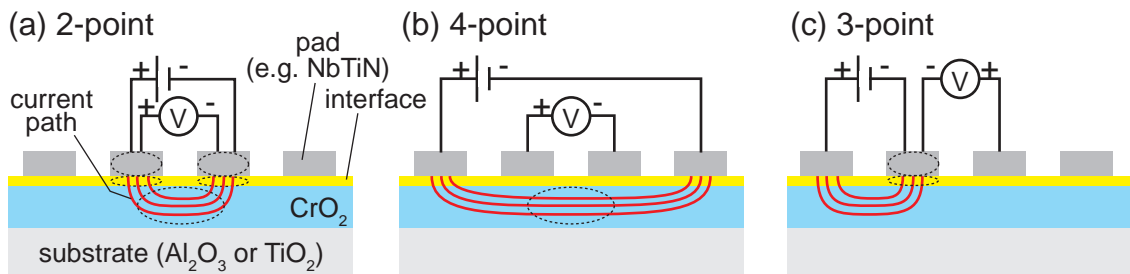
Figure A.1: Measurement configurations. The red lines sketch the current path and the dashed circles the regions contributing to the voltage reading. (a) 2-point configuration: both pads, both interfaces, and a region of the CrO_2 are probed. (b) 4-point configuration: just the region of CrO_2 between the center pads contributes. (c) 3-point configuration: one interface and one pad are probed.

The measurements were performed in liquid helium magnet cryostats described in Sec. 4.2.2. For the electrical measurements, a DC current and an AC current were applied causing a DC voltage measured by a multimeter and an AC voltage detected via a lock-in amplifier.

Different measurement configurations probing different regions of the sample are illustrated in Fig. A.1. We labeled the configuration depicted in Fig. A.1(a) *2-point* measurement configuration[4]. "High" of both the current source and the multimeter are connected to one pad and "low" of both instruments to a second pad. The current path is sketched as red lines. The sample regions contributing to the voltage reading are indicated by dashed circles. These are from "high" to "low": pad 1, interface 1, CrO_2, interface 2 and pad 2. Thus, this configuration includes both interface regions, but it might be impossible to determine their contribution due to the superimposed resistance of the film (here CrO_2). The often used *4-point* measurement configuration is depicted in Fig. A.1(b). Here, four different pads are used for the connections to the instruments. In this case, just the film between the voltage leads contributes to the measured signal. In particular, the interfaces do not contribute. The *3-point* configuration sketched in Fig. A.1(c) uses three pads, where the center one is contacted by two wires. In this configuration, the interface resistance and the resistance of the center pad contribute to the voltage reading. Therefore, we chose the *3-point* measurement configuration to investigate the interface resistances between contact pad and CrO_2.

A.3 Results and discussion

As the aim was to fabricate devices suitable for the observation of the long-range proximity effect, we first investigated the contact resistance of pads made of NbTiN, a conventional s-wave superconductor with a critical temperature of ca. 14 K [266]. Figure A.2(a) shows the temperature dependence of dV/dI obtained from the lock-in amplifier for three different superimposed DC currents ($I_{DC} = 0, 10, 100\,\mu A$). The CrO_2 surface was Ar-ion etched for 1 min prior to the deposition of the NbTiN pads. With decreasing temperature, dV/dI drastically increases, whereby the magnitude depends on the applied DC current. This is an indication of a thermally activated transport resulting in a barrier at low T. Indeed, a strongly non-linear $I - V$ curve was measured as displayed in the inset of Fig. A.2(a). Multiple experiments on nanoscale devices with such interfaces were performed, but no supercurrent traversing the CrO_2 could be observed. Therefore, we conclude that more transparent interfaces are required for the observation of the long-range proximity effect.

The observed increase in resistance with decreasing temperature in Fig. A.2(a) might be due to a leftover of the insulating Cr_2O_3. Therefore, we systematically varied the Ar-ion etching time t_{Ar}. To be able to rapidly compare the different measurements, we detected $R_n := dV/dI$ resulting from an AC current of $I_{AC} = 1\,\mu A$ in the absence of a DC current. The measurements were performed at liquid N_2

---

[4]Note that in the conventionally known "2-point" measurement configuration just one wire is used to contact each pad.

temperature, where the increase of dV/dI is already clearly visible, and where T is well above the critical temperature of NbTiN. In Fig. A.3(a), the resistance area product R_nA is plotted for the different Ar-ion etching times with A being the pad area ($200\,\mu\mathrm{m} \times 200\,\mu\mathrm{m}$). We assumed the pads to be equipotential regions. Two series of samples are shown: for the first series, we used CrO_2 films grown in Alabama (black squares) and for the second series CrO_2 films grown in Leiden (blue circles). The values obtained for R_nA scatter strongly and are mainly in the range $10^{-7}\,\Omega\mathrm{cm}^2 - 10^{-3}\,\Omega\mathrm{cm}^2$. No clear distinction between the samples made with CrO_2 from Alabama or from Leiden is possible. Considering the Ar-ion etching time, it seems that the smallest values of R_nA are obtained for $t_{Ar} = 2.5\,\mathrm{min}$. For longer times, R_nA scatters less but has very high values. Even for very long etching times of $10\,\mathrm{min}$, no decrease is observed.

To exclude any effects directly related to NbTiN as the origin of the high resistance interfaces, we additionally performed measurements on a series of samples with Au pads which are surely resistant against interface oxidation. The results (Fig. A.3(b)) are quite similar to the ones obtained for NbTiN pads: a large scattering of the measured R_nA is observed and also for very long etching times no decrease occurs. For the Au pads, the smallest R_nA values are obtained for $t_{Ar} = 5\,\mathrm{min}$.

In order to interpret the magnitude of R_nA, we estimate the minimum reachable value which is given by $R_{min}A = \rho\lambda_t$ with the resistivity ρ and the mean free path λ_t [178, 267]. Using $\rho = mv_F/(ne^2\lambda_t)$, $mv_F = \hbar k_F$ and $n = k_F^3/(3\pi^2)$, we find $R_{min}A = (h/e^2)(3\pi/2k_F^2)$, where m is the electron mass, n is the electron density, and v_F and k_F are the Fermi velocity and the Fermi wave vector. With the inverse of the universal conductance $h/e^2 = 25.8\,\mathrm{k\Omega}$ and a value of $k_F \approx 10^8\,\mathrm{cm}^{-1}$ for a typical metal [178], one estimates $R_{min}A \approx 1 \times 10^{-15}\,\Omega\mathrm{m}^2$.

The calculated value of R_nA is many orders of magnitude smaller than all measured values both for short and long Ar-ion etching times. We interpret this result
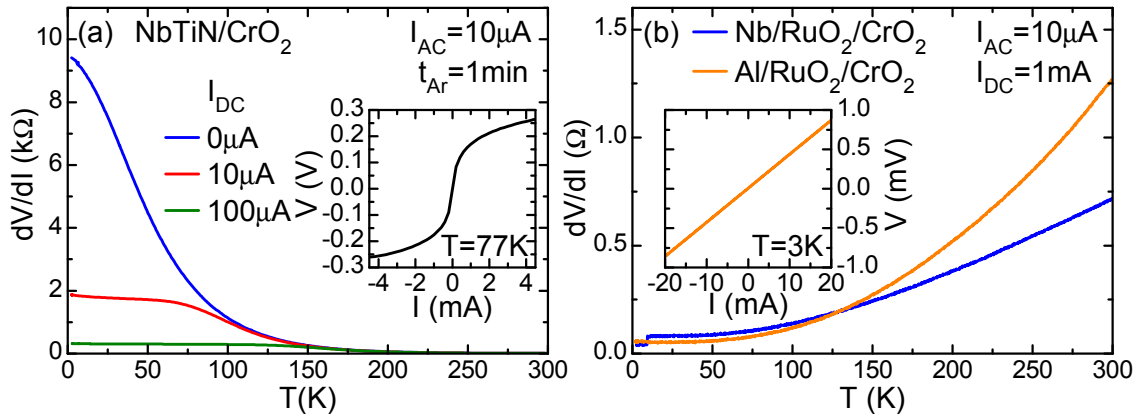
Figure A.2: (a) dV/dI versus T for a NbTiN/CrO_2 interface measured for different DC currents. With decreasing T, dV/dI increases. The inset shows a strongly non-linear $I-V$ curve indicating a non-transparent interface. (b) A thin RuO_2 interlayer significantly changes the temperature dependence of dV/dI. The resistances for the Nb/RuO_2/CrO_2 and the Al/RuO_2/CrO_2 interface now decrease with decreasing T. Also the $I-V$ curve with Al-pad, shown in the inset, is linear.
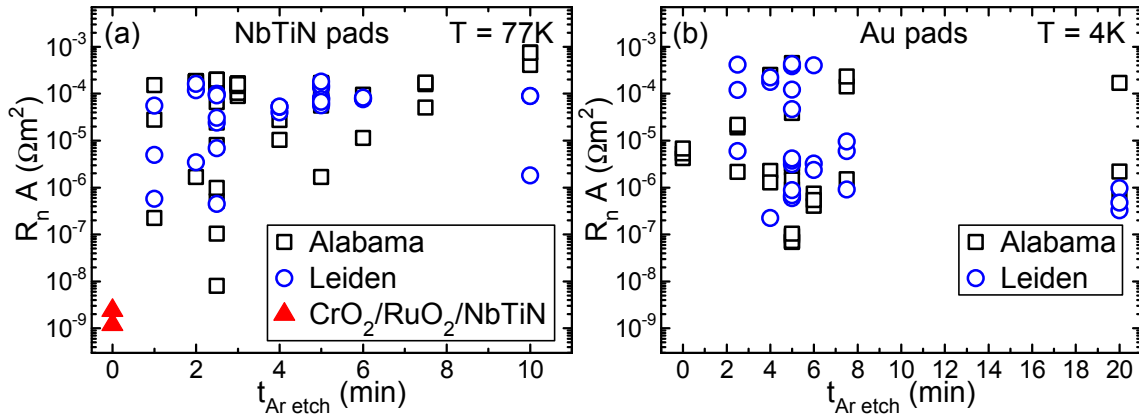
Figure A.3: $R_n A$ for (a) NbTiN pads and (b) Au pads plotted for different Ar-ion etching times. Also long etching times did not result in small $R_n A$ values.

as follows: for short/no Ar-ion etching, there are still insulating remnants of Cr_2O_3 leading to a high resistance interface, and a longer Ar-ion bombardment results in strong structural defects at the CrO_2/metal interface which again lead to high interface resistances. It was not possible to identify an intermediate Ar-ion etching time at which all Cr_2O_3 is removed and still negligible structural defects are created. We therefore conclude that the here chosen approach, where the CrO_2 films from Alabama and Leiden are shipped to another place and then are cleaned via Ar-ion etching does not yield transparent interfaces and is not suitable for the investigation of the long-range proximity effect.

Another approach proposed by A. Gupta is to in situ cover the CrO_2 with a thin RuO_2 layer which already proved to make low resistance contacts [268]. We obtained a sample from Alabama with a 100 nm thick CrO_2 layer covered with 2 nm RuO_2. On this sample, we deposited Al, Nb and NbTiN pads without any Ar-ion etching step. The measured values of $R_n A$ are also shown in Fig. A.3(a) (red triangles). Astonishingly, much smaller values than previously measured – in the range of $10^{-9}\,\Omega m^2$ – are obtained. The resolution limit of our measurement setup is in the same range which might account for the value being still clearly larger than the calculated resistance. Additionally, we measured the temperature dependence of dV/dI. The data for Nb and Al pads are shown in Fig. A.2(b). In contrast to Fig. A.2(a), dV/dI decreases with decreasing temperature. This indicates a much less pronounced if not vanishing barrier. Indeed, the inset of Fig. A.2(a) shows a linear $I - V$ curve. These results open the doors for a future investigation of the long-range proximity effect based on the ferromagnet CrO_2.

As a consequence of the studies presented above, an alternative approach was used by M. S. Anwar, F. D. Czeschka *et al.* [235]. Here, no RuO_2 interlayer but a very short delay between CrO_2 growth and superconductor deposition in combination with Ar-ion etching was used. This resulted in a larger yield of low resistance interfaces and made the observation of a long-range triplet supercurrent through the CrO_2 possible, as detailed in Refs. [235, 265].

A.4 Summary

The aim of this part of the thesis was to study spin-triplet supercurrents in CrO_2 based devices. It turned out that the superconductor/CrO_2 interfaces are crucial for these studies, since CrO_2 is a metastable phase and builds an insulating Cr_2O_3 surface. Therefore, we extensively studied the electrical interface properties of Nb, Al, NbTiN and Au contacts on CrO_2, whereby the CrO_2 surface was cleaned via Ar-ion etching prior to deposition. We found that independent of the Ar-ion etching time ($0\,min \leq t_{Ar} \leq 20\,min$) and for both series of CrO_2 films (grown in Alabama or in Leiden) the interface resistances were by many orders of magnitude larger than the calculated resistance for a transparent interface. Thus, such devices are not suitable for the investigation of the long-range proximity effect. However, a thin RuO_2 interlayer ($2\,nm$) covering the CrO_2 resulted in low resistance interfaces which makes the study of spin-polarized spin triplet supercurrents on such multilayers promising. Finally, we briefly noted that also a short delay between CrO_2 growth and superconductor deposition in combination with Ar-ion etching leads to low resistance interfaces. In such devices, it was possible to observe a long-range spin-triplet supercurrent.

An outlook on the effects discussed here is given in Chapter 5.

Appendix B

Calculation of homodyne DC voltage

Field configuration of the measurement setup

With the field configuration shown in Fig. 3.8, one obtains for the magnetization and current density components in vectorial description

$$
\mathbf{M}_0 = \begin{pmatrix} M_{\mathrm{s}} \\ 0 \\ 0 \end{pmatrix}, \qquad
\mathbf{M}_1 = \begin{pmatrix} 0 \\ m_{\mathrm{y}} \\ m_{\mathrm{z}} \end{pmatrix}, \qquad
\mathbf{J}_0 = \begin{pmatrix} 0 \\ 0 \\ 0 \end{pmatrix}, \qquad
\mathbf{J}_1 = \begin{pmatrix} j \\ 0 \\ 0 \end{pmatrix}.
\tag{B.1}
$$

The applied microwave magnetic field in complex phasor notation is given as

$$
\mathbf{H}_1 = H_1 \begin{pmatrix} 0 \\ 1 \\ 0 \end{pmatrix} e^{-i\omega t}
\tag{B.2}
$$

with the amplitude H_1, the microwave frequency $\omega = 2\pi\nu_{\mathrm{MW}}$ and its phase defined with respect to $\mathbf{E}_1$ so that $\mathrm{Re}\left(\mathbf{H}_1\right)$ is in phase with $\mathrm{Re}\left(\mathbf{E}_1 e^{-i(\omega t \pm \pi/2)}\right)$. The sign depends on the displacement direction in the cavity.

AC current density generated by microwave electric field

In the case of a single mode excitation, we assume that the high frequency current density $\mathbf{J}_1$ is linked to the microwave electric field via

$$
\mathbf{J}_1 = \frac{1}{\rho} \mathbf{E}_1
\tag{B.3}
$$

neglecting the tensor character of the resistivity tensor $\hat{\rho}$ ($\hat{\rho} \rightarrow \rho = 1/\sigma$) [94]. Moreover, we assume that the flow of $\mathbf{J}_1$ is restricted to the film plane, parallel to and in phase with $\mathbf{E}_1$ [94]. Thus, the microwave generated AC current density with the field configuration as shown in Fig. 3.8 is given as

$$
\mathbf{J}_1 = \begin{pmatrix} j \\ 0 \\ 0 \end{pmatrix} = \frac{1}{\rho} E_1 e^{-i(\omega t \pm \pi/2)} \begin{pmatrix} 1 \\ 0 \\ 0 \end{pmatrix}.
\tag{B.4}
$$

Adaption of Eq. (3.26) to our measurement geometry

To calculate the generated electric fields for our measurement geometry, the vectors defined in Sec. B are inserted into Eq. (3.26):

$$
\mathbf{E}_{\mathrm{HD}} = \frac{\Delta\rho}{M^2}\left[\underbrace{\left\langle\begin{pmatrix}j\\0\\0\end{pmatrix}\begin{pmatrix}0\\m_{\mathrm{y}}\\m_{\mathrm{z}}\end{pmatrix}\right\rangle\begin{pmatrix}M_{\mathrm{s}}\\0\\0\end{pmatrix}}_{=0} + \left\langle\begin{pmatrix}j\\0\\0\end{pmatrix}\times\begin{pmatrix}0\\m_{\mathrm{y}}\\m_{\mathrm{z}}\end{pmatrix}\right\rangle\times\begin{pmatrix}M_{\mathrm{s}}\\0\\0\end{pmatrix}\right] +
$$

$$
+ \mu_0 R_{\mathrm{A}}\left\langle\begin{pmatrix}j\\0\\0\end{pmatrix}\times\begin{pmatrix}0\\m_{\mathrm{y}}\\m_{\mathrm{z}}\end{pmatrix}\right\rangle . \quad\text{(B.5)}
$$

With the products

$$
\begin{pmatrix}j\\0\\0\end{pmatrix}\times\begin{pmatrix}0\\m_{\mathrm{y}}\\m_{\mathrm{z}}\end{pmatrix} = \begin{pmatrix}0\\-jm_{\mathrm{z}}\\jm_{\mathrm{y}}\end{pmatrix}\ \text{and}\ \begin{pmatrix}0\\-jm_{\mathrm{z}}\\jm_{\mathrm{y}}\end{pmatrix}\times\begin{pmatrix}M_{\mathrm{s}}\\0\\0\end{pmatrix} = \begin{pmatrix}0\\M_{\mathrm{s}}jm_{\mathrm{y}}\\M_{\mathrm{s}}jm_{\mathrm{z}}\end{pmatrix}
$$
$$\text{(B.6)}$$

it follows that the homodyne electric field in vector description reads

$$
\mathbf{E}_{\mathrm{HD}} = \frac{\Delta\rho}{M_{\mathrm{s}}}\begin{pmatrix}0\\\langle jm_{\mathrm{y}}\rangle\\\langle jm_{\mathrm{z}}\rangle\end{pmatrix} + \mu_0 R_{\mathrm{A}}\begin{pmatrix}0\\-\langle jm_{\mathrm{z}}\rangle\\\langle jm_{\mathrm{y}}\rangle\end{pmatrix} . \quad\text{(B.7)}
$$

The sensing wires attached along $\hat{\mathbf{y}}$ as shown in Fig. 3.8 allow to measure the $\hat{\mathbf{y}}$-component of the electric field:

$$
\mathbf{E}_{\mathrm{HD,y}} = \frac{\Delta\rho}{M_{\mathrm{s}}}\langle jm_{\mathrm{y}}\rangle - \mu_0 R_{\mathrm{A}}\langle jm_{\mathrm{z}}\rangle . \quad\text{(B.8)}
$$

Thus, an evaluation requires the calculation of the two time averages $\langle jm_{\mathrm{y}}\rangle$ and $\langle jm_{\mathrm{z}}\rangle$ as shown in the following section.

Calculation of the time averages $\langle jm_{\mathrm{y}}\rangle$ and $\langle jm_{\mathrm{z}}\rangle$

The relation between the dynamic components of the magnetization $\mathbf{M}_1$ and the dynamic components of the magnetic field $\mathbf{H}_1$ is described by the high-frequency magnetic susceptibility tensor $\hat{\chi}$:

$$
\mathbf{M}_1 = \hat{\chi}\mathbf{H}_1 \quad\text{(B.9)}
$$

with the complex vector quantities $\mathbf{M}_1$ and $\mathbf{H}_1$ [152]. $\hat{\chi}$ can be obtained by solving the Landau-Lifshitz-Gilbert equation (Eq. (3.2)). Adapting the calculation of Mecking *et al.* [97] to our coordinate system with the magnetization rotation in the y-z-plane and the static magnetic field applied in the film plane along $\hat{\mathbf{x}}$, $\hat{\chi}$ inside the sample is found to be

$$\hat{\chi} = \begin{pmatrix} 0 & 0 & 0 \\ 0 & \widetilde{\chi}_{yy} & i\widetilde{\kappa} \\ 0 & -i\widetilde{\kappa} & \widetilde{\chi}_{zz} \end{pmatrix}. \tag{B.10}$$

It contains the complex elements $\widetilde{\chi}_{yy} = \chi'_{yy} + i\chi''_{yy}$, $\widetilde{\chi}_{zz} = \chi'_{zz} + i\chi''_{zz}$ and $\widetilde{\kappa} = \kappa' + i\kappa''$ whose constituents are

$$\begin{aligned} \chi'_{yy} &= M_s A_{yy} L_{dis} & \chi''_{yy} &= M_s A_{yy} L_{abs} \\ \chi'_{zz} &= M_s A_{zz} L_{dis} & \chi''_{zz} &= M_s A_{zz} L_{abs} \\ \kappa' &= M_s A_{yz} L_{dis} & \kappa'' &= M_s A_{yz} L_{abs} \end{aligned} \tag{B.11}$$

with the scalar amplitudes [97]

$$M_s A_{yy} \approx \frac{\mu_0 \gamma M_s (H_{res} + M_s)}{\eta\omega (2H_{res} + M_s)}, \; M_s A_{zz} \approx \frac{\mu_0 \gamma H_{res} M_s}{\eta\omega (2H_{res} + M_s)}, \; M_s A_{yz} \approx \frac{M_s}{\eta (2H_{res} + M_s)}. \tag{B.12}$$

Here, $\widetilde{\chi}_{yy}$ and $\widetilde{\chi}_{zz}$ are different as the demagnetization of the thin ferromagnetic film is included. The resonance condition is defined by the Kittel formula [269] and the lineshape is given by the Lorentzian functions

$$L_{dis} \equiv \frac{\Delta H (H - H_{res})}{(H - H_{res})^2 + \Delta H^2} \quad \text{and} \quad L_{abs} \equiv \frac{\Delta H^2}{(H - H_{res})^2 + \Delta H^2}, \tag{B.13}$$

where L_{dis} exhibits a dispersion and L_{abs} an absorption lineshape. In the limit $|H - H_{res}| \ll H_{res}$, the width of the Lorentzian can be calculated as [97]

$$\mu_0 \Delta H \approx \frac{\eta\omega}{\gamma}. \tag{B.14}$$

Inserting the microwave magnetic field defined by Eq. (B.2) into Eq. (B.9) gives the magnetization components:

$$\begin{aligned} m_y &= \widetilde{\chi}_{yy} H_1 e^{-i\omega t} & m_z &= -i\widetilde{\kappa} H_1 e^{-i\omega t} \\ &= (\chi'_{yy} + i\chi''_{yy}) H_1 e^{-i\omega t} & &= -i(\kappa' + i\kappa'') H_1 e^{-i\omega t}. \end{aligned} \tag{B.15}$$

With the complex conjugate j^* of j obtained from Eq. (B.4), the two products $j^* m_y$ and $j^* m_z$ are given by

$$j^* m_y = \pm i \frac{1}{\rho} E_1 H_1 (\chi'_{yy} + i\chi''_{yy}),$$

$$j^* m_z = \pm \frac{1}{\rho} E_1 H_1 (\kappa' + i\kappa''). \tag{B.16}$$

Executing the time averages given by $\langle A\,B \rangle = \frac{1}{2}\mathrm{Re}(A^*B)$ [165] yields the expressions

$$\langle jm_y \rangle = \mp \frac{E_1 H_1}{2\rho} \chi''_{yy}, \tag{B.17}$$

$$\langle jm_z \rangle = \pm \frac{E_1 H_1}{2\rho} \kappa'. \tag{B.18}$$

Calculation of the homodyne electric field

The homodyne electric field is calculated by inserting the expressions for $\langle jm_\mathrm{y} \rangle$ and $\langle jm_z \rangle$ obtained in the previous section into Eq. (B.8). It follows

$$E_{\mathrm{HD,y}} = \mp \frac{1}{2} E_1 H_1 \left(\frac{\Delta \rho}{\rho} \frac{1}{M_\mathrm{s}} \chi_\mathrm{yy}'' + \frac{\mu_0 R_\mathrm{A}}{\rho} \kappa' \right) \tag{B.19}$$

and with χ_yy'' and κ' from Eq. (B.11):

$$E_{\mathrm{HD,y}} = \mp \frac{1}{2} E_1 H_1 \left(\frac{\Delta \rho}{\rho} A_\mathrm{yy} L_\mathrm{abs} + \frac{\mu_0 R_\mathrm{A} M_\mathrm{s}}{\rho} A_\mathrm{yz} L_\mathrm{dis} \right). \tag{B.20}$$

Calculation of the homodyne voltage

The potential difference between the wires contacting the sample (see Fig. 3.8) can be calculated by integrating the electric field $E_{\mathrm{HD,y}}$ along $\hat{\mathbf{y}}$ over the sample length L:

$$V_{\mathrm{HD,y}} = -\int_{-L/2}^{L/2} E_{\mathrm{HD,y}} \mathrm{d}y. \tag{B.21}$$

Assuming that $\mathbf{E}_1$ is constant over the whole sample (which is reasonable as the wavelength of the microwave ($L_{\mathrm{MW}} = 32\,\mathrm{mm}$) is much longer than the sample length $L \approx 3\,\mathrm{mm}$) the integration leads to

$$V_{\mathrm{HD,y}} = -E_{\mathrm{HD,y}} \cdot L. \tag{B.22}$$

Thus, the DC voltage generated by homodyning is given by

$$V_{\mathrm{HD,y}} = \pm \frac{1}{2} E_1 L H_1 \left(\frac{\Delta \rho}{\rho} A_\mathrm{yy} L_\mathrm{abs} + \frac{\mu_0 R_\mathrm{A} M_\mathrm{s}}{\rho} A_\mathrm{yz} L_\mathrm{dis} \right). \tag{B.23}$$

List of Publications

- S. Geprägs, F. D. Czeschka, M. Opel, S. T. B. Goennenwein, W. Yu, W. Mader, and R. Gross, *Epitaxial growth and magnetic properties of Sr_2CrReO_6 thin films*, Journal of Magnetism and Magnetic Materials **321**, 2001 (2009).

- F. D. Czeschka, S. Geprägs, M. Opel, S. T. B. Goennenwein, and R. Gross, *Giant magnetic anisotropy changes in Sr_2CrReO_6 thin films on $BaTiO_3$*, Applied Physics Letters **95**, 062508 (2009).

- M. S. Anwar, F. D. Czeschka, M. Hesselberth, M. Porcu, and J. Aarts, *Long-range supercurrents through half-metallic ferromagnetic CrO_2*, Physical Review B **82**, 100501 (2010).

- M. Opel, S. Geprägs, E. P. Menzel, A. Nielsen, D. Reisinger, K. Nielsen, A. Brandlmaier, F. D. Czeschka, M. Althammer, M. Weiler, S. T. B. Goennenwein, J. Simon, M. Svete, W. Yu, S. Hühne, W. Mader, and R. Gross, *Novel multifunctional materials based on oxide thin films and artificial heteroepitaxial multilayers*, Physica Status Solidi (a) **208**, 232 (2011).

- M. Weiler, F. D. Czeschka, A. Brandlmaier, I.-M. Imort, G. Reiss, A. Thomas, G. Woltersdorf, R. Gross, and S. T. B. Goennenwein, *Magnetic microstructure and magnetotransport in Co_2FeAl Heusler compound thin films*, Applied Physics Letters **98**, 042501 (2011).

- F. D. Czeschka, L. Dreher, M. S. Brandt, M. Weiler, M. Althammer, I.-M. Imort, G. Reiss, A. Thomas, W. Schoch, W. Limmer, H. Huebl, R. Gross, and S. T. B. Goennenwein, *Scaling behavior of the spin pumping effect in ferromagnet/platinum bilayers*, Physical Review Letters **107**, 046601 (2011).

- D. Rüffer, F. D. Czeschka, R. Gross, and S. T. B. Goennenwein, *Experimental observation of an enhanced anisotropic magnetoresistance in non-local configuration*, accepted by Applied Physics Letters.

Bibliography

[1] A. Volta, Phil. Trans. R. Soc. London **90**, 403 (1800).

[2] P. F. Mottelay, *Bibliographical History of Electricity and Magnetism* (Charles Griffin & Company Limited, London, 1922).

[3] J. J. Thomson, Phil. Mag. **44**, 293 (1897).

[4] J. A. Katine, F. J. Albert, R. A. Buhrman, E. B. Myers, and D. C. Ralph, Phys. Rev. Lett. **84**, 3149 (2000).

[5] E. B. Myers, D. C. Ralph, J. A. Katine, R. N. Louie, and R. A. Buhrman, Science **285**, 867 (1999).

[6] S. I. Kiselev, J. C. Sankey, I. N. Krivorotov, N. C. Emley, R. J. Schoelkopf, R. A. Buhrman, and D. C. Ralph, Nature **425**, 380 (2003).

[7] Y. Tserkovnyak, A. Brataas, and G. E. W. Bauer, Phys. Rev. Lett. **88**, 117601 (2002).

[8] Y. Tserkovnyak, A. Brataas, and G. E. W. Bauer, Phys. Rev. B **66**, 224403 (2002).

[9] O. Mosendz, J. E. Pearson, F. Y. Fradin, G. E. W. Bauer, S. D. Bader, and A. Hoffmann, Phys. Rev. Lett. **104**, 046601 (2010).

[10] O. Mosendz, V. Vlaminck, J. E. Pearson, F. Y. Fradin, G. E. W. Bauer, S. D. Bader, and A. Hoffmann, Phys. Rev. B **82**, 214403 (2010).

[11] X. Wang, G. Bauer, B. van Wees, A. Brataas, and Y. Tserkovnyak, Phys. Rev. Lett. **97**, 216602 (2006).

[12] A. Brataas, Y. Tserkovnyak, G. Bauer, and B. Halperin, Phys. Rev. B **66**, 060404(R) (2002).

[13] J. E. Hirsch, Phys. Rev. Lett. **83**, 1834 (1999).

[14] E. Hankiewicz, L. Molenkamp, T. Jungwirth, and J. Sinova, Phys. Rev. B **70**, 241301(R) (2004).

[15] D. Abanin, A. Shytov, L. Levitov, and B. Halperin, Phys. Rev. B **79**, 035304 (2009).

[16] P. Grünberg and A. Fert, Nobel Lectures, Nobelprize.org, 25.5.2011, http://nobelprize.org/nobel_prizes/physics/laureates/2007/grunberg-lecture.html and http://nobelprize.org/nobel_prizes/physics/laureates/2007/fert-lecture.html (2007).

[17] K. Uchida, S. Takahashi, K. Harii, J. Ieda, W. Koshibae, K. Ando, S. Maekawa, and E. Saitoh, Nature **455**, 778 (2008).

[18] C. Cohen-Tannoudji, B. Diu, and F. Laloe, *Quantum Mechanics* (Hermann and John Wiley & Sons, Paris, 1977).

[19] S. Chikazumi, *Physics of Ferromagnetism*, 2nd ed. (Oxford Science Publications, New York, 1997).

[20] B. T. Jonker, A. T. Hanbicki, D. T. Pierce, and M. D. Stiles, J. Magn. Magn. Mater. **277**, 24 (2004).

[21] W. Pauli, *Pauli Lectures on Physics: Volume 5. Wave Mechanics* (MIT Press, Massachusetts, 1973).

[22] X. Zhou, Z. Zhang, and C. Hu, arXiv:0904.3796 (2009).

[23] M. Ziese and M. J. Thornton, *Spin Electronics* (Springer, Berlin, 2001).

[24] J. Shi, P. Zhang, D. Xiao, and Q. Niu, Phys. Rev. Lett. **96**, 076604 (2006).

[25] S. Murakami, N. Nagosa, and S. Zhang, Phys. Rev. B **69**, 235206 (2004).

[26] P. Jin, Y. Li, and F. Zhang, J. Phys. A: Math. Gen. **39**, 7115 (2006).

[27] A. Vernes, B. L. Györffy, and P. Weinberger, Phys. Rev. B **76**, 012408 (2007).

[28] S. Lowitzer, D. Ködderitzsch, and H. Ebert, Phys. Rev. B **82**, 140402 (2010).

[29] N. F. Mott, Proc. R. Soc. Lond. A **153**, 699 (1936).

[30] I. A. Campbell and A. Fert, *Ferromagnetic Materials, Vol. 3* (North-Holland Publishing Co., Amsterdam, 1982).

[31] D. Rüffer, *Non-local Phenomena in Metallic Nanostructures*, Diploma thesis, Technische Universität München (2009).

[32] S. Datta, *Electronic Transport in Mesoscopic Systems* (Cambridge University Press, Cambridge, 1995).

[33] F. J. Jedema, M. S. Nijboer, Filip, and B. J. van Wees, Phys. Rev. B **67**, 085319 (2003).

[34] S. Takahashi and S. Maekawa, Sci. Technol. Adv. Mat. **9**, 014105 (2008).

[35] P. C. van Son, H. van Kempen, and P. Wyder, Phys. Rev. Lett. **58**, 2271 (1987).

[36] T. Valet and A. Fert, Phys. Rev. B **48**, 7099 (1993).

[37] C. Heide, Phys. Rev. B **65**, 054401 (2001).

[38] S. Takahashi and S. Maekawa, Phys. Rev. B **67**, 052409 (2003).

[39] M. Johnson and J. Byers, Phys. Rev. B **67**, 125112 (2003).

[40] S. Murakami, N. Nagaosa, and S. Zhang, Science **301**, 1348 (2003).

[41] M. I. Dyakonov, Conference on the Spin Hall Effect, Bad Honnef (2008).

[42] Y. Kajiwara, K. Harii, S. Takahashi, J. Ohe, K. Uchida, M. Mizuguchi, H. Umezawa, H. Kawai, K. Ando, K. Takanashi, S. Maekawa, and E. Saitoh, Nature **464**, 262 (2010).

[43] B. A. Bernevig and S. Zhang, IBM J. Res. & Dev. **50**, 141 (2006).

[44] H. Engel, E. I. Rashba, and B. I. Halperin, arXiv:0603306v3 (2006).

[45] M. I. Dyakonov, *Spin Physics in Semiconductors* (Springer, Berlin, 2008).

[46] T. Dietl, D. D. Awschalom, M. Kaminska, and H. Ohno, *Spintronics* (Academic Press, Amsterdam, 2008).

[47] S. Maekawa, *Concepts in Spin Electronics* (Oxford University Press, New York, 2006).

[48] R. Winkler, *Spin-orbit Coupling Effects in Two-Dimensional Electron and Hole Systems*, 1st ed. (Springer, Berlin, 2003).

[49] N. A. Sinitsyn, J. Phys.: Cond. Matter **20**, 023201 (2008).

[50] N. F. Mott, Proc. R. Soc. Lond. A **124**, 425 (1929).

[51] L. Berger, Phys. Rev. B **2**, 4559 (1970).

[52] G. Vignale, J. Supercond. Nov. Magn. **23**, 3 (2010).

[53] R. Karplus and J. M. Luttinger, Phys. Rev. **95**, 1154 (1954).

[54] J. Smit, Physica **21**, 877 (1955).

[55] J. Smit, Physica **24**, 39 (1958).

[56] J. M. Luttinger, Phys. Rev. **112**, 739 (1958).

[57] G. Sundaram and Q. Niu, Phys. Rev. B **59**, 14915 (1999).

[58] M. Gradhand, *The Extrinsic Spin Hall Effect*, Ph.D. thesis, Martin-Luther-Universität Halle-Wittenberg (2010).

[59] M. V. Berry, Proc. R. Soc. Lond. A **392**, 45 (1984).

[60] G. Y. Guo, S. Murakami, T. Chen, and N. Nagaosa, Phys. Rev. Lett. **100**, 096401 (2008).

[61] M. Dyakonov and V. Perel, JETP Lett. **13**, 467 (1971).

[62] Y. K. Kato, R. C. Myers, A. C. Gossard, and D. D. Awschalom, Science **306**, 1910 (2004).

[63] W. Tse and S. D. Sarma, Phys. Rev. B **74**, 245309 (2006).

[64] E. M. Hankiewicz and G. Vignale, Phys. Rev. Lett. **100**, 026602 (2008).

[65] J. L. Cheng and M. W. Wu, J. Phys.: Cond. Matter **20**, 085209 (2008).

[66] M. Gradhand, D. V. Fedorov, P. Zahn, and I. Mertig, Phys. Rev. B **81**, 245109 (2010).

[67] O. Mosendz, G. Woltersdorf, B. Kardasz, B. Heinrich, and C. H. Back, Phys. Rev. B **79**, 224412 (2009).

[68] T. Seki, Y. Hasegawa, S. Mitani, S. Takahashi, H. Imamura, S. Maekawa, J. Nitta, and K. Takanashi, Nat. Mater. **7**, 125 (2008).

[69] Y. Niimi, M. Morota, D. H. Wei, C. Deranlot, M. Basletic, A. Hamzic, A. Fert, and Y. Otani, Phys. Rev. Lett. **106**, 126601 (2011).

[70] J. Bass and W. P. Pratt, J. Phys.: Cond. Matter **19**, 183201 (2007).

[71] E. Saitoh, M. Ueda, H. Miyajima, and G. Tatara, Appl. Phys. Lett. **88**, 182509 (2006).

[72] L. Landau and E. Lifshitz, Phys. Z. Sowjetunion **8**, 153 (1935).

[73] T. Gilbert, Phys. Rev. **100**, 1243 (1955).

[74] T. Gilbert, IEEE Trans. Magn. **40**, 3443 (2004).

[75] C. P. Poole, *Electron Spin Resonance*, 2nd ed. (Dover Publications, New York, 1996).

[76] R. Meckenstock, *Untersuchung der magnetischen Eigenschaften von Fe/Ag-Schichtsystemen mit der konventionellen und der ortsaufgelösten ferromagnetischen Resonanz*, Ph.D. thesis, Ruhr-Universität Bochum (1997).

[77] J. C. Slonczewski, J. Magn. Magn. Mater. **159**, L1 (1996).

[78] L. Berger, Phys. Rev. B **54**, 9353 (1996).

[79] A. Brataas, Y. V. Nazarov, and G. E. W. Bauer, Phys. Rev. Lett. **84**, 2481 (2000).

[80] C. W. J. Beenakker, Rev. Mod. Phys. **69**, 731 (1997).

[81] A. Brataas, G. E. Bauer, and P. J. Kelly, Phys. Rep. **427**, 157 (2006).

[82] M. Büttiker, H. Thomas, and A. Pretre, Z. Phys. B **94**, 133 (1994).

[83] P. W. Brouwer, Phys. Rev. B **58**, R10135 (1998).

[84] A. Brataas, International Conference on Nanoelectronics, Lancaster University (2003).

[85] S. Mizukami, Y. Ando, and T. Miyazaki, J. Magn. Magn. Mater. **226-230**, 1640 (2001).

[86] K. Xia, P. J. Kelly, G. E. W. Bauer, A. Brataas, and I. Turek, Phys. Rev. B **65**, 220401 (2002).

[87] M. Zwierzycki, Y. Tserkovnyak, P. J. Kelly, A. Brataas, and G. E. W. Bauer, Phys. Rev. B **71**, 064420 (2005).

[88] K. Carva and I. Turek, Phys. Rev. B **76**, 104409 (2007).

[89] D. Huertas-Hernando, Y. V. Nazarov, and W. Belzig, Phys. Rev. Lett. **88**, 047003 (2002).

[90] K. Ando, T. Yoshino, and E. Saitoh, Appl. Phys. Lett. **94**, 152509 (2009).

[91] G. Schmidt, D. Ferrand, L. W. Molenkamp, A. T. Filip, and B. J. V. Wees, Phys. Rev. B **62**, 4790 (2000).

[92] M. Johnson and R. H. Silsbee, Phys. Rev. B **37**, 5312 (1988).

[93] R. C. O'Handley, *Modern Magnetic Materials: Principles and Applications* (John Wiley, New York, 2000).

[94] H. J. Juretschke, J. Appl. Phys. **31**, 1401 (1960).

[95] W. G. Egan and H. J. Juretschke, J. Appl. Phys. **34**, 1477 (1963).

[96] Y. S. Gui, N. Mecking, and C. M. Hu, Phys. Rev. Lett. **98**, 217603 (2007).

[97] N. Mecking, Y. S. Gui, and C. M. Hu, Phys. Rev. B **76**, 224430 (2007).

[98] H. Y. Inoue, K. Harii, K. Ando, K. Sasage, and E. Saitoh, J. Appl. Phys. **102**, 083915 (2007).

[99] S. Goennenwein, *Two-Dimensional Electron Gases and Ferromagnetic Semi- conductors: Materials for Spintronics*, Ph.D. thesis, Technische Universität München (2003).

[100] T. Graf, *Spin-spin interactions of localized electronic states in semiconductors*, Ph.D. thesis, Technische Universität München (2003).

[101] Y. Guan, W. Bailey, E. Vescovo, C. Kao, and D. Arena, J. Magn. Magn. Mater. **312**, 374 (2007).

[102] F. Heusler, Dtsch. Phys. Ges. **5**, 219 (1903).

[103] P. J. Webster, Contemp. Phys. **10**, 559 (1969).

[104] S. Trudel, O. Gaier, J. Hamrle, and B. Hillebrands, J. Phys. D: Appl. Phys. **43**, 193001 (2010).

[105] R. A. de Groot, F. M. Mueller, P. G. van Engen, and K. H. J. Buschow, Phys. Rev. Lett. **50**, 2024 (1983).

[106] I. Galanakis, P. H. Dederichs, and N. Papanikolaou, Phys. Rev. B **66**, 174429 (2002).

[107] H. C. Kandpal, G. H. Fecher, C. Felser, and G. Schönhense, Phys. Rev. B **73**, 094422 (2006).

[108] S. Wurmehl, G. H. Fecher, H. C. Kandpal, V. Ksenofontov, C. Felser, H. Lin, and J. Morais, Phys. Rev. B **72**, 184434 (2005).

[109] Y. Miura, K. Nagao, and M. Shirai, Phys. Rev. B **69**, 144413 (2004).

[110] E. Sasioglu, L. M. Sandratskii, P. Bruno, and I. Galanakis, Phys. Rev. B **72**, 184415 (2005).

[111] Y. Kurtulus, R. Dronskowski, G. D. Samolyuk, and V. P. Antropov, Phys. Rev. B **71**, 014425 (2005).

[112] J. Kübler, A. R. William, and C. B. Sommers, Phys. Rev. B **28**, 1745 (1983).

[113] B. Balke, S. Wurmehl, G. H. Fecher, C. Felser, and J. Kübler, Sci. Technol. Adv. Mat. **9**, 014102 (2008).

[114] D. Ebke, P. Thomas, O. Schebaum, M. Schäfers, D. Nissen, V. Drewello, A. Hütten, and A. Thomas, J. Magn. Magn. Mater. **322**, 996 (2010).

[115] E. J. W. Verwey and E. L. Heilmann, J. Chem. Phys. **15**, 174 (1947).

[116] H. Jeng and G. Y. Guo, Phys. Rev. B **65**, 094429 (2002).

[117] E. J. W. Verwey, Nature **144**, 327 (1939).

[118] K. Abe, Y. Miyamoto, and S. Chikazumi, J. Phys. Soc. Jpn. **41**, 1894 (1976).

[119] F. Walz, J. Phys.: Cond. Matter **14**, R285 (2002).

[120] S. Todo, K. Siratori, and S. Kimura, J. Phys. Soc. Jpn. **64**, 2118 (1995).

[121] S. Nakamura, L. Li, M. Tanaka, S. Todo, and K. Siratori, J. Phys. Soc. Jpn. **66**, 472 (1997).

[122] C. Boekema, R. L. Lichti, K. C. B. Chan, V. A. M. Brabers, A. B. Denison, D. W. Cooke, R. H. Heffner, R. L. Hutson, and M. E. Schillaci, Phys. Rev. B **33**, 210 (1986).

[123] D. Ihle and B. Lorenz, J. Phys. C **19**, 5239 (1986).

[124] D. Venkateshvaran, M. Althammer, A. Nielsen, S. Geprägs, M. S. R. Rao, S. T. B. Goennenwein, M. Opel, and R. Gross, Phys. Rev. B **79**, 134405 (2009).

[125] T. Dietl, Nat. Mater. **9**, 965 (2010).

[126] T. Jungwirth, J. Sinova, J. Mascaronek, J. Kuccaronera, and A. H. MacDonald, Rev. Mod. Phys. **78**, 809 (2006).

[127] M. Wang, R. P. Campion, A. W. Rushforth, K. W. Edmonds, C. T. Foxon, and B. L. Gallagher, Appl. Phys. Lett. **93**, 132103 (2008).

[128] R. Shioda, K. Ando, T. Hayashi, and M. Tanaka, Phys. Rev. B **58**, 1100 (1998).

[129] T. Dietl, H. Ohno, and F. Matsukura, Phys. Rev. B **63**, 195205 (2001).

[130] C. Zener, Phys. Rev. **81**, 440 (1951).

[131] W. Limmer, M. Glunk, J. Daeubler, T. Hummel, W. Schoch, R. Sauer, C. Bihler, H. Huebl, M. Brandt, and S. Goennenwein, Phys. Rev. B **74**, 205205 (2006).

[132] R. Meservey and P. M. Tedrow, Phys. Rev. Lett. **41**, 805 (1978).

[133] O. Mosendz, J. E. Pearson, F. Y. Fradin, S. D. Bader, and A. Hoffmann, Appl. Phys. Lett. **96**, 022502 (2010).

[134] F. D. Czeschka, L. Dreher, M. S. Brandt, M. Weiler, M. Althammer, I. M. Imort, G. Reiss, A. Thomas, W. Schoch, W. Limmer, H. Huebl, R. Gross, and S. T. B. Goennenwein, arXiv:1012.3017 (2010).

[135] F. D. Czeschka, L. Dreher, M. S. Brandt, M. Weiler, M. Althammer, I. Imort, G. Reiss, A. Thomas, W. Schoch, W. Limmer, H. Huebl, R. Gross, and S. T. B. Goennenwein, Phys. Rev. Lett. **107**, 046601 (2011).

[136] C. Bihler, W. Schoch, W. Limmer, S. T. B. Goennenwein, and M. S. Brandt, Phys. Rev. B **79**, 045205 (2009).

[137] S. T. B. Goennenwein, T. Graf, T. Wassner, M. S. Brandt, M. Stutzmann, J. B. Philipp, R. Gross, M. Krieger, K. Zürn, P. Ziemann, A. Koeder, S. Frank, W. Schoch, and A. Waag, Appl. Phys. Lett. **82**, 730 (2003).

[138] A. Krupp, *Growth and Characteriszation of Ferromagnetic Heusler Compound Thin Films*, Diploma thesis, Technische Universität München (2010).

[139] H. Schneider, G. Jakob, M. Kallmayer, H. Elmers, M. Cinchetti, B. Balke, S. Wurmehl, C. Felser, M. Aeschlimann, and H. Adrian, Phys. Rev. B **74**, 174426 (2006).

[140] H. Schneider, E. Vilanova, B. Balke, C. Felser, and G. Jakob, J. Phys. D: Appl. Phys. **42**, 084012 (2009).

[141] R. Ramos, S. Arora, and I. Shvets, Phys. Rev. B **78**, 214402 (2008).

[142] D. Reisinger, P. Majewski, M. Opel, L. Alff, and R. Gross, Appl. Phys. Lett. **85**, 4980 (2004).

[143] W. Limmer, J. Daeubler, L. Dreher, M. Glunk, W. Schoch, S. Schwaiger, and R. Sauer, Phys. Rev. B **77**, 205210 (2008).

[144] Y. Tserkovnyak, A. Brataas, G. E. W. Bauer, and B. I. Halperin, Rev. Mod. Phys. **77**, 1375 (2005).

[145] R. Meckenstock, K. Harms, O. von Geisau, and J. Pelzl, J. Magn. Magn. Mater. **148**, 139 (1995).

[146] B. K. Kuanr, V. Veerakumar, A. V. Kuanr, R. E. Camley, and Z. Celinski, IEEE Trans. Magn. **45**, 4015 (2009).

[147] A. Brandlmaier, *Magnetische Anisotropie in dünnen Schichten aus Magnetit*, Diploma thesis, Technische Universität München (2006).

[148] H. Nakayama, K. Ando, K. Harii, Y. Kajiwara, T. Yoshino, K. Uchida, and E. Saitoh, IEEE Trans. Magn. **46**, 2202 (2010).

[149] C. W. Sandweg, Y. Kajiwara, K. Ando, E. Saitoh, and B. Hillebrands, Appl. Phys. Lett. **97**, 252504 (2010).

[150] A. J. P. Meyer and G. Asch, J. Appl. Phys. **32**, S330 (1961).

[151] F. Schreiber, J. Pflaum, Z. Frait, J. Heise, and J. Pelzl, J. Magn. Magn. Mater. **157-158**, 281 (1996).

[152] A. Gurevich and G. Melkov, *Magnetization oscillations and waves* (CRC Press, Boca Raton, 1996).

[153] D. T. Margulies, F. T. Parker, F. E. Spada, R. S. Goldman, J. Li, R. Sinclair, and A. E. Berkowitz, Phys. Rev. B **53**, 9175 (1996).

[154] L. R. Bickford, Phys. Rev. **78**, 449 (1950).

[155] A. Nielsen, *Magnetit - ein Material für die Spinelektronik*, Ph.D. thesis, Technische Universität München (2009).

[156] X. Liu, W. Lim, M. Dobrowolska, J. Furdyna, and T. Wojtowicz, Phys. Rev. B **71**, 035307 (2005).

[157] M. Oogane, T. Wakitani, S. Yakata, R. Yilgin, Y. Ando, A. Sakuma, and T. Miyazaki, Jpn. J. Appl. Phys. **45**, 3889 (2006).

[158] K. Ando, Y. Kajiwara, S. Takahashi, S. Maekawa, K. Takemoto, M. Takatsu, and E. Saitoh, Phys. Rev. B **78**, 014413 (2008).

[159] D. H. Hernando, Y. V. Nazarov, A. Brataas, and G. E. W. Bauer, Phys. Rev. B **62**, 5700 (2000).

[160] L. Vila, T. Kimura, and Y. Otani, Phys. Rev. Lett. **99**, 226604 (2007).

[161] K. Ando, S. Takahashi, K. Harii, K. Sasage, J. Ieda, S. Maekawa, and E. Saitoh, Phys. Rev. Lett. **101**, 036601 (2008).

[162] K. M. D. Hals, A. Brataas, and Y. Tserkovnyak, Europhys. Lett. **90**, 47002 (2010).

[163] H. Nakayama, K. Ando, K. Harii, Y. Kajiwara, T. Yoshino, K. Uchida, T. Ota, and E. Saitoh, J. Phys.: Conf. Ser. **200**, 062014 (2010).

[164] H. Kurt, R. Loloee, K. Eid, W. P. Pratt, and J. Bass, Appl. Phys. Lett. **81**, 4787 (2002).

[165] D. D. Stancil and A. Prabhakar, *Spin Waves* (Springer, New York, 2009).

[166] C. Bihler, *Magnetic Semiconductors*, Ph.D. thesis, Technische Universität München (2009).

[167] X. Liu, Y. Y. Zhou, and J. K. Furdyna, Phys. Rev. B **75**, 195220 (2007).

[168] B. Hoekstra, R. P. van Stapele, and J. M. Robertson, J. Appl. Phys. **48**, 382 (1977).

[169] S. Blundell, *Magnetism in Condensed Matter* (Oxford University Press, New York, 2001).

[170] A. Morrish, *The Physical Principles of Magnetism* (IEEE Press, New York, 2001).

[171] A. M. Portis, Appl. Phys. Lett. **2**, 69 (1963).

[172] A. Koeder, S. Frank, W. Schoch, V. Avrutin, W. Limmer, K. Thonke, R. Sauer, A. Waag, M. Krieger, K. Zuern, P. Ziemann, S. Brotzmann, and H. Bracht, Appl. Phys. Lett. **82**, 3278 (2003).

[173] W. Limmer, A. Koeder, S. Frank, V. Avrutin, W. Schoch, R. Sauer, K. Zuern, J. Eisenmenger, P. Ziemann, E. Peiner, and A. Waag, Phys. Rev. B **71**, 205213 (2005).

[174] K. M. Yu, W. Walukiewicz, T. Wojtowicz, I. Kuryliszyn, X. Liu, Y. Sasaki, and J. K. Furdyna, Phys. Rev. B **65**, 201303 (2002).

[175] K. W. Edmonds, P. Boguslstrokawski, K. Y. Wang, R. P. Campion, S. N. Novikov, N. R. S. Farley, B. L. Gallagher, C. T. Foxon, M. Sawicki, T. Dietl, M. B. Nardelli, and J. Bernholc, Phys. Rev. Lett. **92**, 037201 (2004).

[176] S. Mizukami, Y. Ando, and T. Miyazaki, Phys. Rev. B **66**, 104413 (2002).

[177] A. K. Bordoloi and S. Auluck, J. Phys. F **13**, 2101 (1983).

[178] N. W. Ashcroft and N. D. Mermin, *Solid State Physics* (Holt, Rinehart and Winston, New York, 1976).

[179] A. F. Lee, K. Wilson, and R. M. Lambert, Surf. Sci. **446**, 145 (2000).

[180] E. G. Colgan, J. Appl. Phys. **62**, 1224 (1987).

[181] S. P. Murarka, J. Appl. Phys. **47**, 5175 (1976).

[182] C. Brune, A. Roth, E. G. Novik, M. Konig, H. Buhmann, E. M. Hankiewicz, W. Hanke, J. Sinova, and L. W. Molenkamp, Nat. Phys. **6**, 448 (2010).

[183] G. Mihajlovic, J. E. Pearson, M. A. Garcia, S. D. Bader, and A. Hoffmann, Phys. Rev. Lett. **103**, 166601 (2009).

[184] C. Beenakker and H. van Houten, Solid State Phys. **44**, 1 (1991).

[185] L. J. van der Pauw, Philips Res. Rep. **13**, 1 (1958).

[186] J. Ku, J. Chang, H. Kim, and J. Eom, Appl. Phys. Lett. **88**, 172510 (2006).

[187] D. R. Lide, *CRC Handbook of Chemistry and Physics*, 76th ed. (CRC-Press, Boca Raton, 1995).

[188] S. O. Valenzuela and M. Tinkham, Nature **442**, 176 (2006).

[189] F. J. Jedema, H. B. Heersche, A. T. Filip, J. J. A. Baselmans, and B. J. van Wees, Nature **416**, 713 (2002).

[190] J. B. Johnson, Phys. Rev. **32**, 97 (1928).

[191] H. Nyquist, Phys. Rev. **32**, 110 (1928).

[192] P. Horowitz and W. Hill, *The art of electronics* (Cambridge University Press, Cambridge, 1989).

[193] D. Pollock, *Thermoelectricity: Theory, Thermometry, Tool* (ASTM International, Philadelphia, 1985).

[194] A. Daire, W. Goeke, and M. A. Tupta, White Paper: Keithley Instruments (2005).

[195] J. Zhou and J. Liu, IEEE Trans. Circuits Syst. II **52**, 49 (2005).

[196] J. Singleton, *Band Theory and Electronic Properties of Solids* (Oxford University Press, Oxford, 2001).

[197] D. K. C. MacDonald and K. Sarginson, Proc. R. Soc. Lond. A **203**, 223 (1950).

[198] R. B. Dingle, Proc. R. Soc. Lond. A **201**, 545 (1950).

[199] Y. Namba, Japan. J. Appl. Phys. **9**, 1326 (1970).

[200] G. Kästle, H. Boyen, A. Schröder, A. Plettl, and P. Ziemann, Phys. Rev. B **70**, 165414 (2004).

[201] A. Bietsch, M. A. Schneider, M. E. Welland, and B. Michel, J. Vac. Sci. Technol. B **18**, 1160 (2000).

[202] C. Durkan and M. E. Welland, Phys. Rev. B **61**, 14215 (2000).

[203] P. A. Smith, C. D. Nordquist, T. N. Jackson, T. S. Mayer, B. R. Martin, J. Mbindyo, and T. E. Mallouk, Appl. Phys. Lett. **77**, 1399 (2000).

[204] S. Karim, W. Ensinger, T. Cornelius, and R. Neumann, Physica E **40**, 3173 (2008).

[205] T. Kimura, J. Hamrle, and Y. Otani, Phys. Rev. B **72**, 014461 (2005).

[206] P. Monod and A. Janossy, J. Low Temp. Phys. **26**, 311 (1977).

[207] H. Haucke, S. Washburn, A. Benoit, C. Umbach, and R. Webb, Phys. Rev. B **41**, 12454 (1990).

[208] A. Geim, P. Main, P. Beton, P. Steda, L. Eaves, C. Wilkinson, and S. Beaumont, Phys. Rev. Lett. **67**, 3014 (1991).

[209] A. K. Geim, P. C. Main, P. H. Beton, L. Eaves, S. P. Beaumont, and C. D. W. Wilkinson, Phys. Rev. Lett. **69**, 1248 (1992).

[210] K. Kobayashi, H. Aikawa, S. Katsumoto, and Y. Iye, J. Phys. Chem. Solids **63**, 1301 (2002).

[211] H. Baranger, A. Stone, and D. DiVincenzo, Phys. Rev. B **37**, 6521 (1988).

[212] A. D. Stone, Phys. Rev. Lett. **54**, 2692 (1985).

[213] W. Skocpol, P. Mankiewich, R. Howard, L. Jackel, D. Tennant, and A. Stone, Phys. Rev. Lett. **58**, 2347 (1987).

[214] A. Benoit, C. P. Umbach, R. B. Laibowitz, and R. A. Webb, Phys. Rev. Lett. **58**, 2343 (1987).

[215] S. Lowitzer, M. Gradhand, D. Ködderitzsch, D. V. Fedorov, I. Mertig, and H. Ebert, Phys. Rev. Lett. **106**, 056601 (2011).

[216] M. Gradhand, private communication.

[217] Y. Takagaki and K. Ploog, Phys. Rev. B **49**, 1782 (1994).

[218] Y. Hirayama, A. D. Wieck, T. Bever, K. von Klitzing, and K. Ploog, Phys. Rev. B **46**, 4035 (1992).

[219] Y. Hirayama, Y. Tokura, A. D. Wieck, S. Koch, R. J. Haug, K. von Klitzing, and K. Ploog, Phys. Rev. B **48**, 7991 (1993).

[220] P. Schwab and M. Dzierzawa, private communication.

[221] J. Rammer and H. Smith, Rev. Mod. Phys. **58**, 323 (1986).

[222] J. M. Ziman, *Principles of the theory of solids*, 2nd ed. (Cambridge University Press, Cambridge, 1972).

[223] C. Gorini, P. Schwab, R. Raimondi, and A. L. Shelankov, Phys. Rev. B **82**, 195316 (2010).

[224] T. Kimura, Y. Otani, T. Sato, S. Takahashi, and S. Maekawa, Phys. Rev. Lett. **98**, 156601 (2007).

[225] T. McGuire and R. Potter, IEEE Trans. Magn. **11**, 1018 (1975).

[226] Y. Q. Jia, S. Y. Chou, and J. Zhu, J. Appl. Phys. **81**, 5461 (1997).

[227] J. Jorritsma and J. A. Mydosh, J. Appl. Phys. **84**, 901 (1998).

[228] C. Shearwood, S. J. Blundell, M. J. Baird, J. A. C. Bland, M. Gester, H. Ahmed, and H. P. Hughes, J. Appl. Phys. **75**, 5249 (1994).

[229] J. Kleiza, M. Sapagovas, and V. Kleiza, Informatica **18**, 253 (2007).

[230] W. L. V. Price, J. Phys. D: Appl. Phys. **5**, 1127 (1972).

[231] K. Uchida, J. Xiao, H. Adachi, J. Ohe, S. Takahashi, J. Ieda, T. Ota, Y. Kajiwara, H. Umezawa, H. Kawai, G. E. W. Bauer, S. Maekawa, and E. Saitoh, Nat. Mater. **9**, 894 (2010).

[232] C. M. Jaworski, J. Yang, S. Mack, D. D. Awschalom, J. P. Heremans, and R. C. Myers, Nat. Mater. **9**, 898 (2010).

[233] H. Adachi, J. Ohe, S. Takahashi, and S. Maekawa, Phys. Rev. B **83**, 094410 (2011).

[234] J. Xiao, G. E. W. Bauer, K. Uchida, E. Saitoh, and S. Maekawa, Phys. Rev. B **81**, 214418 (2010).

[235] M. S. Anwar, F. D. Czeschka, M. Hesselberth, M. Porcu, and J. Aarts, Phys. Rev. B **82**, 100501 (2010).

[236] G. Deutscher and P. G. de Gennes, in *Superconductivity*, edited by R. D. Parks (Dekker, New York, 1969).

[237] A. I. Buzdin, Rev. Mod. Phys. **77**, 935 (2005).

[238] T. M. Klapwijk, J. Supercond. **17**, 593 (2004).

[239] E. A. Demler, G. B. Arnold, and M. R. Beasley, Phys. Rev. B **55**, 15174 (1997).

[240] F. S. Bergeret, A. F. Volkov, and K. B. Efetov, Rev. Mod. Phys. **77**, 1321 (2005).

[241] G. Wild, C. Probst, A. Marx, and R. Gross, Eur. Phys. J. B **78**, 509 (2010).

[242] M. Weides, M. Kemmler, H. Kohlstedt, R. Waser, D. Koelle, R. Kleiner, and E. Goldobin, Phys. Rev. Lett. **97**, 247001 (2006).

[243] B. D. Josephson, Phys. Lett. **1**, 251 (1962).

[244] T. Kontos, M. Aprili, J. Lesueur, F. Genêt, B. Stephanidis, and R. Boursier, Phys. Rev. Lett. **89**, 137007 (2002).

[245] A. Bauer, J. Bentner, M. Aprili, M. L. D. Rocca, M. Reinwald, W. Wegscheider, and C. Strunk, Phys. Rev. Lett. **92**, 217001 (2004).

[246] M. D. Lawrence and N. Giordano, J. Phys.: Cond. Matter **8**, L563 (1996).

[247] M. Giroud, H. Courtois, K. Hasselbach, D. Mailly, and B. Pannetier, Phys. Rev. B **58**, 11872 (1998).

[248] V. T. Petrashov, I. A. Sosnin, I. Cox, A. Parsons, and C. Troadec, Phys. Rev. Lett. **83**, 3281 (1999).

[249] R. S. Keizer, S. T. B. Goennenwein, T. M. Klapwijk, G. Miao, G. Xiao, and A. Gupta, Nature **439**, 825 (2006).

[250] S. P. Lewis, P. B. Allen, and T. Sasaki, Phys. Rev. B **55**, 10253 (1997).

[251] L. Chioncel, H. Allmaier, E. Arrigoni, A. Yamasaki, M. Daghofer, M. I. Katsnelson, and A. I. Lichtenstein, Phys. Rev. B **75**, 140406(R) (2007).

[252] R. J. Soulen, J. M. Byers, M. S. Osofsky, B. Nadgorny, T. Ambrose, S. F. Cheng, P. R. Broussard, C. T. Tanaka, J. Nowak, J. S. Moodera, *et al.*, Science **282**, 85 (1998).

[253] G. Strijkers, Y. Ji, F. Yang, C. Chien, and J. Byers, Phys. Rev. B **63**, 104510 (2001).

[254] K. A. Yates, W. R. Branford, F. Magnus, Y. Miyoshi, B. Morris, L. F. Cohen, P. M. Sousa, O. Conde, and A. J. Silvestre, Appl. Phys. Lett. **91**, 172504 (2007).

[255] J. M. D. Coey and M. Venkatesan, J. Appl. Phys. **91**, 8345 (2002).

[256] F. Bergeret, A. Volkov, and K. Efetov, Phys. Rev. Lett. **86**, 4096 (2001).

[257] R. S. Keizer, *Singlet and triplet supercurrents in disordered mesoscopic systems*, Ph.D. thesis, Technische Universiteit Delft (2007).

[258] M. Eschrig, J. Kopu, J. Cuevas, and G. Schön, Phys. Rev. Lett. **90**, 137003 (2003).

[259] M. Eschrig and T. Lofwander, Nat. Phys. **4**, 138 (2008).

[260] G. E. Blonder, M. Tinkham, and T. M. Klapwijk, Phys. Rev. B **25**, 4515 (1982).

[261] R. Cheng, C. N. Borca, N. Pilet, B. Xu, L. Yuan, B. Doudin, S. H. Liou, and P. A. Dowben, Appl. Phys. Lett. **81**, 2109 (2002).

[262] G. Miao and G. Xiao, Phys. Rev. B **71**, 094418 (2005).

[263] N. A. Frey, S. Srinath, H. Srikanth, G. X. Miao, and A. Gupta, Phys. Rev. B **74**, 024420 (2006).

[264] A. Gupta, X. W. Li, S. Guha, and G. Xiao, Appl. Phys. Lett. **75**, 2996 (1999).

[265] M. S. Anwar and J. Aarts, Supercond. Sci. Technol. **24**, 024016 (2011).

[266] N. N. Iosad, A. V. Mijiritskii, V. V. Roddatis, N. M. van der Pers, B. D. Jackson, J. R. Gao, S. N. Polyakov, P. N. Dmitriev, and T. M. Klapwijk, J. Appl. Phys. **88**, 5756 (2000).

[267] R. Gross, private communication.

[268] G. X. Miao, A. Gupta, H. Sims, W. H. Butler, S. Ghosh, and G. Xiao, J. Appl. Phys. **97**, 10C924 (2005).

[269] C. Kittel, Phys. Rev. **73**, 155 (1948).

Acknowledgments

This work emerged in four years of work at the Walther-Meißner-Institute in Garching including several stays in Delft, The Netherlands. It would not have been possible without the help of many people who I would like to thank. These are in particular:

- *Prof. Dr. Rudolf Gross* for giving me the opportunity to do the Ph.D. in the magnetism group of the WMI; in particular for the stimulating discussions which always helped me, and for sharing his deep physical knowledge.
- *Dr. Sebastian T. B. Gönnenwein* for the great support, his enthusiasm for physics, the numerous ideas, and for his guidance.
- *Dr. Matthias Opel* for the encouragement, the help, and motivating words.
- *Dr. Hans Hübl* for asking the right questions.
- The "junior researchers" *Daniel Rüffer* and *Alexander Krupp* who I supervised during their Diploma thesis for their good ideas, helping hands and great work.
- The members of the magnetism group and all other Ph.D. students at the WMI for making the last years a great time both on the professional and on the private side. These are in particular: *Matthias Althammer, Andreas Brandlmaier, Johannes Büttner, Matthias Danner, Stephan Geprägs, Toni Helm, Elisabeth Hoffmann, Bernhard Muschler, Thomas Niemczyk, Manuel Schwarz,* and *Mathias Weiler.*
- The technical staff of the WMI for making impossible things possible and this, if needed, on shortest timescales. In particular *Thomas Brenninger, Robert Müller* and *Helmut Thies.*
- *Prof. Dr. Martin S. Brandt* for giving me the opportunity to use the ESR spectrometer and making always a time slot available. Moreover, I want to thank him for the many scientific discussions and a lot of good advice.
- *Lukas Dreher* for the support at the ESR machine, the simulation programming and for the many good suggestions concerning "applied mathematics".
- *Prof. Dr. Teun Klapwijk* for allowing me to work in his group, treating me as one of his students, and for many illuminating discussions.
- *Nathan Vercryssen, Tarun Bansal* and the other members of NF for giving me a nice time in Delft.
- *Dr. Peter Schwab* and *Dr. Michael Dzierzawa* for the transport simulations.
- *Prof. Dr. Gerrit E. W. Bauer* for interesting discussions.
- *Dr. Martin Gradhand* for his efforts to explain the non-local resistance.
- *Prof. Dr. Arunava Gupta* and his group for supplying CrO_2 samples.
- *Dr. Andi Thomas* and *Inga-Mareen Imort* for supplying Heusler samples.
- *Dr. Wolfgang Limmer* and *Dr. Wladimir Schoch* for supplying (Ga,Mn)As samples.
- In particular, I would like to thank my family for the unlimited support in any imaginable situation.
- *Britta* for her love, her support, and for constantly showing me that there is a life beyond physics.